STP 1429

PREDICTIVE MATERIAL modeling:

combining fundamental physics understanding, computational methods, and empirically observed behavior

Technical Editor(s):
Mark T. Kirk and M. Erickson Natishan

ASTM INTERNATIONAL
Standards Worldwide

STP 1429

Predictive Material Modeling: Combining Fundamental Physics Understanding, Computational Methods and Empirically Observed Behavior

M. T. Kirk and M. Erickson Natishan, editors

ASTM Stock Number: STP1429

ASTM International
100 Barr Harbor Drive
PO Box C700
West Conshohocken, PA 19428-2959

Printed in the U.S.A.

Library of Congress Cataloging-in-Publication Data

Predictive material modeling; combining fundamental physics understanding, computational methods and empirically observed behavior / M.T. Kirk and M. Erickson Natishan, editors.
p. cm. – (STP ; 1429)
Includes bibliographical references.
"ASTM Stock Number: STP1429."
ISBN 0-8031-3472-X
1. Steel--Metallurgy--Congresses. I, Kirk, Mark, 1961-II. Natishan, M. Erickson. III. ASTM special technical publication ; 1429.

2003062889

TN701.5.P74 2003
669'.142--dc22

Peer Review Policy

Each paper published in this volume was evaluated by two peer reviewers and at least one editor. The authors addressed all of the reviewers' comments to the satisfaction of both the technical editor(s) and the ASTM International Committee on Publications.

To make technical information available as quickly as possible, the peer-reviewed papers in this publication were prepared "camera-ready" as submitted by the authors.

The quality of the papers in this publication reflects not only the obvious efforts of the authors and the technical editor(s), but also the work of the peer reviewers. In keeping with long-standing publication practices, ASTM International maintains the anonymity of the peer reviewers. The ASTM International Committee on Publications acknowledges with appreciation their dedication and contribution of time and effort on behalf of ASTM International.

Printed in Mayfield, PA
January 2004

Foreword

The Symposium on Predictive Material Modeling: Combining Fundamental Physics Understanding, Computational Methods and Empirically Observed Behavior was held in Dallas, Texas on 7–8 November 2001. ASTM International Committee E8 on Fatigue and Fracture sponsored the symposium. Symposium chairpersons and co-editors of this publication were Mark T. Kirk, U. S. Nuclear Regulatory Commission, Rockville, Maryland and MarjoricAnn Erickson Natishan, Phoenix Engineering Associates, Incorporated, Sykesville, Maryland.

Contents

Overview

An ASTM International Symposium concerning *Predictive Material Modeling: Combining Fundamental Physics Understanding, Computational Methods, and Empirically Observed Behavior* was held on 7–8 November 2001 in Dallas, Texas in conjunction with the semi-annual meetings of ASTM International Committee E8 on Fracture and Fatigue. The symposium was motivated by the focus of many industries on extending the design life of structures. Safe life extension depends on the availability of robust methodologies that accurately predict both the fundamental material behavior and the structural response under a wide range of load conditions. Heretofore, predictive models of material behavior have been based on empirical derivations, or on fundamental physics-based models that describe material behavior at the nano- or micro-scale. Both approaches to modeling suffer from issues that limit their practical application. Empirically-derived models, while based on readily determined properties, cannot be reliably used beyond the limits of the database from which they were derived. Fundamental, physically-derived models provide a sound basis for extrapolation to other materials and conditions, but rely on parameters that are measured on the microscale and thus may be difficult and costly to obtain. It was the hope that this conference would provide an opportunity for communication between researchers pursuing these different modeling approaches.

The papers presented at this Symposium included six concerning ferritic steel; these address fracture in the transition regime, on the upper shelf, and in the creep range. Three of these papers used a combination of the Gurson and Weibull models to predict fracture performance and account for constraint loss. While successful at predicting conditions similar to those represented by the calibration datasets, all investigators found the parameters of the (predominantly) empirical Weibull model to depend significantly on factors such as temperature, strain rate, initial yield strength, strain hardening exponent, and so on. These strong dependencies make models of this type difficult to apply beyond their calibrated range. Natishan proposed the use of physically derived models for the transition fracture toughness of ferritic steels. While this approach shows better similarity of parameters across a wide range material, loading, and temperature conditions than does the Weibull approach, it has not yet been used to assess constraint loss effects as the Weibull models have.

Three papers at the Symposium addressed topics un-related to steels. One paper applied the Weibull models used extensively for steel fracture to assess the interfacial fracture of electronic components. As is the case for steel fracture, the Weibull models predict well conditions similar to the calibration dataset. In the remaining two papers researchers affiliated with the Naval Research Laboratory used advanced computational and experimental techniques to develop constitutive models for composite and shape memory materials.

We would like to close this overview by extending our thanks not only to the authors of the papers you find in this volume, but also to the many peer reviewers, and to the members of the ASTM International staff who made publication of this volume possible.

Mark T Kirk
Nuclear Regulatory Commission
Rockville, Maryland
Symposium chairperson and editor

MarjorieAnn Erickson Natishan
Phoenix Engineering Associates, Inc.
Sykesville, Maryland
Symposium chairperson and editor

Ferritic Steels

Mark T Kirk,[1] MarjorieAnn Erickson Natishan,[2] and Matthew Wagenhofer[3]

Transition Toughness Modeling of Steels Since RKR

Reference: Kirk, M. T., Natishan, M. E., and Wagenhofer, M., **"Transition Toughness Modeling Since RKR,"** *Predictive Material Modeling: Combining Fundamental Physics Understanding, Computational Methods and Empirically Observed Behavior, ASTM STP 1429,* M. T. Kirk and M. Erickson Natishan, Eds., ASTM International, West Conshohocken, PA, 2003.

Abstract: In this paper we trace the development of transition fracture toughness models from the landmark paper of Ritchie, Knott, and Rice in 1973 up through the current day. While such models have become considerably more sophisticated since 1973, none have achieved the goal of blindly predicting fracture toughness data. In this paper we suggest one possible way to obtain such a predictive model.

Keywords: Ritchie-Knott-Rice, cleavage fracture, transition fracture, modeling, ferritic steels.

Background and Objective

A longtime goal of the fracture mechanics community has been to understand the fracture process in the transition region of ferritic steels so that it may be quantified with sufficient accuracy to enable its confident use in safety assessments and life extension calculations. Watanabe et al. identified two different approaches toward this goal: the mechanics approach and the materials approach [1]. The classical mechanics, or *fracture* mechanics, approach is a semi-empirical one in which solutions for the stress fields near the crack tip are used to draw correlations between the near-tip conditions in laboratory specimens and fracture conditions at the tip of a crack in a structure. Conversely, the materials approach attempts to predict fracture through the use of models describing the physical mechanisms involved in the creation of new surface areas. Watanabe's "materials approach" is identical to what Knott and Boccaccini [2] refer to as a "micro-scale approach." Knott and Boccaccini also identify another approach to transition fracture characterization, the nano-scale approach, which attempts to describe the competition between crack propagation and crack blunting through the use of dislocation mechanics. In many ways, the micro-scale (or materials) approach provides a bridge between the classical fracture mechanics and nano-scale approaches.

1 Senior Materials Engineer, United States Nuclear Regulatory Commission, 11545 Rockville Pike, Rockville, MD, 20852, USA (mtk@nrc.gov). *(The views expressed herein represent those of the author and not an official position of the USNRC.)*
2 President, Phoenix Engineering Associates, Inc., 979 Day Road, Sykesville, MD, 21784, USA (mnatishan@aol.com).
3 Graduate Student, Department of Mechanical Engineering, University of Maryland, College Park, MD, 20742, USA.

Ritchie, Knott and Rice's [3] landmark 1973 paper (RKR) is a classic example of the micro-scale approach. The RKR model has gained widespread acceptance as an appropriate description of the conditions necessary for cleavage fracture (i.e., achievement of a critical value of stress normal to the crack plane over a characteristic distance ahead of the crack tip) at temperatures well below the transition temperature. Even though RKR themselves were unsuccessful in applying their model at higher temperatures (i.e. temperatures approaching the fracture mode transition temperature), the streamlined elegance of their model has prompted many researchers to expand on RKR in attempts to describe fracture up to the transition temperature. These modified / enhanced RKR approaches have produced varying degrees of success, yet they have never achieved the ultimate goal of being fully predictive because, being based on an underlying model that does not describe fully the precursors to cleavage fracture, the parameters of the modified/enhanced RKR models invariably must be empirically calibrated.

In this paper we trace the development of RKR-type models from 1973 through the present day, and provide our perspective on the steps needed to achieve a fully predictive transition fracture model for ferritic steels, a goal whose achievement can now be clearly envisaged.

RKR: The 1973 Model

Ritchie, Knott, and Rice (RKR) [3] were the first to link explanations for the cause for cleavage fracture based on dislocation mechanics with the concepts of *LEFM*. By 1973 both mechanistic [4] and dislocation-based [5-6] models suggested that cleavage fracture required achievement of a critical stress level. The RKR model combined this criteria with the (then) recently published solutions for stresses ahead of a crack in an elastic-plastic solid [7-9] to predict successfully the variation of the critical stress intensity factor with temperature in the lower transition regime of a mild steel (see Fig. 1). These researchers also introduced the concept that achievement of this critical stress at a single point ahead of the crack tip was not a sufficient criterion for fracture. They postulated, and subsequently demonstrated, that the critical stress value had to be exceeded over a micro-structurally relevant size scale (e.g., multiples of grain sizes, multiples of carbide spacing) for failure to occur.

The RKR model provides a description of cleavage fracture that, at least in the lower transition regime, is both consistent with the physics of the cleavage fracture process and successfully predicts the results of fracture toughness experiments. However, the model has limited engineering utility because the predictions depend strongly on two parameters (the critical stress for cleavage fracture, or σ_f, and the critical distance, ℓ_c, over which σ_f is achieved) that are both difficult to measure and can only be determined inferentially. In the following sections we discuss various refinements to RKR-type models that have been published since 1973. We define a *"RKR-type"* model as one that attempts to characterize and/or predict the cleavage fracture characteristics of ferritic steels and adopts the achievement of a critical stress over a critical distance ahead of the crack tip as the failure criterion. We begin by discussing early attempts to apply the RKR model to

temperatures higher in the transition regime than attempted by RKR themselves. We then review efforts undertaken in the 1990s and thereafter to extend the temperature regime over which RKR applies through the use of more accurate analysis of the stresses ahead of the deforming crack tip. We conclude the paper with a discussion of the advantages and limitations of these current modeling approaches, and provide a perspective on how these limitations can be overcome.

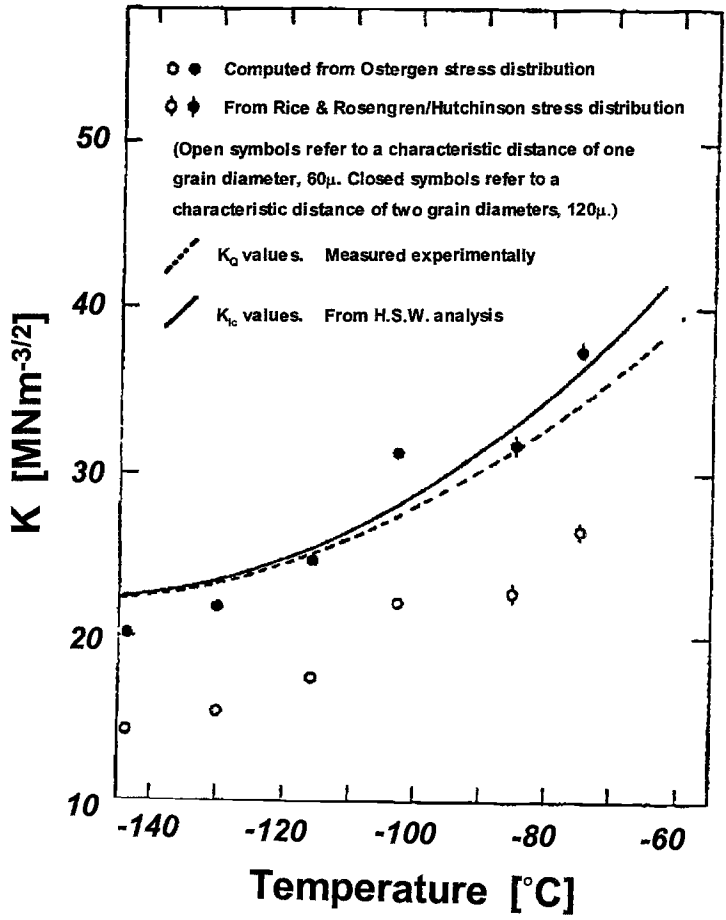

FIG. 1–*Comparison of RKR model prediction (symbols) with experimental K_{Ic} data (Solid Curve) showing good agreement for a characteristic distance of two-grain diameters. Note the low stress intensity factor values, indicating that these fracture toughness data are in the lower transition.*

Early Application of the RKR Model to Upper Transition

A paper by Tetelman, Wilshaw and Rau (TWR) [10] helps to provide a perspective on why the RKR model appears to be ineffective at temperatures approaching the fracture mode transition temperature. In their paper, TWR conclude that the microscopic fracture stress must be exceeded over a grain diameter and a half for fracture to occur. In arriving at this conclusion they identify three events that must occur prior to the onset of cleavage fracture in steel:

1. Microcrack nucleation,
2. Propagation of the microcrack through the grain in which the crack was nucleated (i.e. the crack remains sharp and does not blunt), and
3. Microcrack propagation through the boundaries that surround the nucleating grain.

TWR state that the first two events occur more easily when grain boundary carbides are present. The determination of a grain diameter and a half as a 'critical distance' comes from assuming that if the stress perpendicular to the plane of the crack is less than the microscopic fracture stress at the critical grain boundary of the 3rd event, then unstable crack growth will not occur.

RKR's work seems to build on these ideas from TWR. By setting their characteristic distance at two grain diameters, they place the focus of their model on the third TWR event. The RKR model thus assumes implicitly that the first and second TWR events occur with sufficient ease and frequency to make the third TWR event *alone* control the occurrence, or non-occurrence, of cleavage fracture. At the low temperatures (relative to the fracture mode transition temperature) that RKR were concerned with, these assumptions are appropriate. However, at temperatures higher in transition crack blunting becomes a more important issue to consider. Because cracks blunt due to emission of dislocations from the tip of the crack, blunting is controlled in large part by the friction stress of the material. Consequently, blunting is easier at higher temperatures (where the friction stress is lower). At these higher temperatures it cannot be assumed that TWR's second event can occur either easily or frequently so the potential for crack blunting needs to be addressed quantitatively. Thus, the assumptions made by RKR regarding crack tip blunting are seen to have greatly impaired both the model's accuracy and its physical appropriateness at temperatures approaching the fracture mode transition temperature. Attempts to "fix" the RKR model to work at higher temperatures by adjusting only the parameters of the RKR model (ℓ_c and σ_f) and not its fundamental nature have therefore never enjoyed success beyond the specific materials on which they were calibrated.

RKR-Type Models Featuring Improved Stress Analysis

By the late 1980s and early 1990s, much of the industrial infrastructure fabricated

from ferritic steels faced impending limitations – either design, economic, or regulatory – on its continued useful life. Examples include structures such as oil storage tanks [11] and petrochemical transmission pipelines [12]; i.e. structures fabricated long ago and/or using old techniques that sometimes experienced spectacular failures, and that invariably had toughness properties that were either not well quantified and/or feared to be low. Other examples include nuclear reactors, which while having well documented toughness properties faced regulatory limits on operability based on concerns about service related property degradation (i.e., neutron embrittlement) [13]. Also in this timeframe significant advances in computational power available to engineering researchers led to a renewed interest in the application of RKR-type models. Many researchers believed the Achilles' heel of the RKR model to be its use of an asymptotic solution for the crack-tip stress field (i.e. Hutchinson Rice Rosengren (HRR) solutions, or its close equivalents), and so viewed the advent of desktop finite element capability as a way to extend the temperature regime over which the model applies. In this Section we review the results of RKR-type models that seek improvements in predictive capabilities and/or range of applicability through the use of better near-tip stress solutions than were available to RKR in the early 1970s.

Two-Parameter Characterization of Cleavage Fracture Toughness

Initial efforts of this type borrowed from RKR the idea that the criterion for cleavage fracture is the achievement of a critical stress ahead of the crack-tip. These efforts focused on quantifying the leading non-singular terms in the near-tip stress field solution as a means to expand greatly (relative to the HRR solution used by RKR) the size of the region around the crack-tip over which the mathematical solution is accurate. This approach accurately described the deformation conditions associated with much higher toughness values thereby enabling application of the models to higher temperatures in the transition regime. Numerous approaches of this type were proposed, including the elastic-plastic, FE-based, J-Q approach [14], the elastic J-T approach [15], the elastic-plastic asymptotic solution for J-A_2 [16], and the "engineering" J-γ_g technique [17] to name just a few. These ideas differed in detail, but were similar in concept in that the second parameter was used to quantify the degree of constraint loss, which was invariably defined as a departure of the near-tip stresses from small scale yielding (SSY) conditions. All of these techniques succeeded at better parameterizing the conditions under which cleavage failure occurs, but none provided any improvement in predictive capabilities because of the requirement to perform extensive testing of specimens having different constraint conditions to characterize what came to be called the "failure locus" [18].

Prediction of Relative Effects on Fracture Toughness

Dodds, Anderson, and co-workers proposed improvements to these 2-parameter approaches [19]. Their finite element computations resolved the elastic-plastic stress state at the crack tip in detail, and used these results to evaluate the conditions for

cleavage fracture on the basis of the RKR failure criteria (i.e., achievement of a critical stress over a critical distance). By comparing the calculated near-tip stress fields for different finite geometries to a reference solution for a crack tip loaded under SSY conditions these investigators quantified the effect of departure from SSY conditions on the applied-J value needed to generate a particular driving force for cleavage fracture (as defined by a RKR-type failure criterion). This approach enabled prediction of the applied-J value needed to cause cleavage fracture in one specimen geometry based on toughness data obtained from another specimen geometry.

In the course of their research, Dodds and Anderson determined that the stress fields in finite geometries remain self-similar to the SSY reference solution to quite high deformation levels. Because of this, the particular values of the RKR parameters (i.e., the critical stress and critical distance, σ_f and ℓ_c, respectively) selected exerted no influence on the differences in fracture toughness predicted between two different crack geometries. This discovery that the difference in toughness between two different geometries did not depend on the actual values of the critical material parameters in the RKR model paved the way for the use of finite element analysis to account for geometry and loss of constraint effects. In this manner the Dodds/Anderson technique permitted toughness values to be scaled between geometries, thereby eliminating the extensive testing burden associated with the two-parameter techniques described earlier.

In spite of these advantages, the procedure proposed by Dodds and Anderson also had the following drawbacks:

- As the deformation level increased, the self-similarity of the stress fields in finite geometries to the SSY reference solution eventually broke down, making the results again dependent on the specific values of critical stress / critical distance selected for analysis.
- The Dodds / Anderson model assumes that an RKR-type failure criterion is correct, i.e. that cleavage fracture is controlled solely by the achievement of a critical stress at some finite distance ahead of the crack tip. In their papers, Dodds and Anderson admitted that this micro-mechanical failure criterion was adopted for its convenience, and its simplicity relative to other proposals. Nevertheless, as discussed earlier, the RKR failure criterion is in fact a special case of a more general criterion for cleavage fracture proposed by TWR. Thus, the Dodds/Anderson work did nothing to improve, relative to RKR, on the range of temperatures over which the model could be physically expected to generate accurate predictions of fracture toughness.
- Experimental studies demonstrated that the Dodds / Anderson technique successfully quantified the effect of constraint loss on fracture toughness for tests performed at a single temperature and strain rate [20]. However, such results could not be used to predict fracture toughness at other temperatures / strain rates due to the lack of an underlying physical relationship that included these effects in

the Dodds / Anderson model.

Prediction of Relative Effects on Toughness: Accounting for the Effects of Both Finite Crack-Front Length and Loss of Constraint

Because it was defined only in terms of stresses acting to open the crack plane, the Dodds / Anderson model cannot, by definition, characterize the well recognized "weakest link" effect in cleavage fracture, whereby specimens having longer crack front lengths exhibit systematically lower toughness values than those determined from testing thinner specimens [21]. Characterization of this inherently three-dimensional effect requires adoption of failure criteria that account for both volume effects and the variability of crack front stresses depending upon proximity to a free surface. Therefore in 1997 Dodds, et al. adopted the "Weibull Stress" developed by the Beremin research group in France as a local fracture parameter [22]. This model begins with the assumption that a random distribution of micro-scale flaws that act as cleavage initiation sites exists throughout the material, and that the size and density of these flaws constitute properties of the material. These flaws are further assumed to have a distribution of sizes described by an inverse power-law, as follows:

$$g(\ell_o) = \left\{\frac{\alpha}{\ell_o}\right\}^{\beta} \tag{1}$$

where ℓ_o is the carbide diameter and α and β are the parameters of the density function g. The probability of finding a critical micro-crack (i.e. one that leads to fracture) in some small volume V_o is then simply the integral of eq. (1), as illustrated graphically in Fig. 2(a) and described mathematically below:

$$p_f\left(\ell_o \geq \ell_o^c\right) = V_0 \int_{\ell_o^c}^{\infty} \left(\frac{\alpha}{\ell_o}\right)^{\beta} d\ell_o \tag{2}$$

where $\ell_o{}^c$ is the critical carbide diameter.

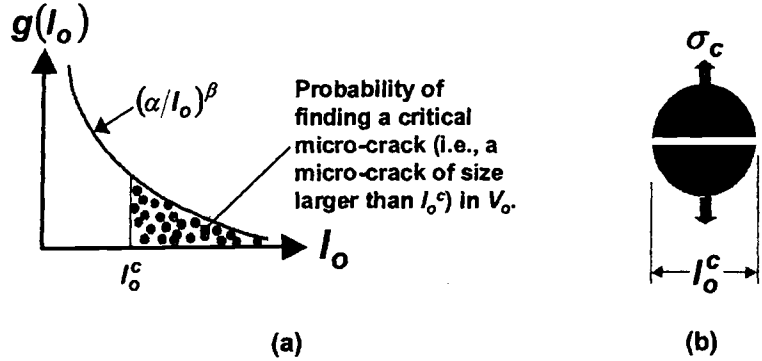

FIG. 2–*(a) Distribution of micro-scale flaws assumed by the BEREMIN model [22], and (b) illustration of Griffith fracture criterion applied to cracking of a carbide.*

The BEREMIN model further assumes that the Griffith fracture criterion [23] applies to the cracking of a carbide (see Fig. 2(b)), i.e., to one of the pre-existing flaws whose size density is characterized by eq. (1). Stress and flaw size are consequently related as follows:

$$\sigma_c = \frac{K_c Y}{\sqrt{l_o^c}}, \text{ or equivalently } l_o^c = \frac{K_c^2 Y^2}{\sigma_c^2} \tag{3}$$

where σ_c is the critical stress, K_c is the critical stress intensity factor, and Y is the geometry factor for a cracked carbide. Substituting eq. (3) into eq. (2) allows the failure probability to be expressed on a stress basis, as follows:

$$p_f(\sigma \geq \sigma_c) = V_0 \left(\frac{\sigma}{\sigma_u} \right)^m \tag{4a}$$

where m and σ_u are the parameters of a Weibull distribution, defined as follows:

$$m = 2\beta - 2 \tag{4b}$$

$$\sigma_u = (\beta - 1)^{\frac{1}{2\beta-2}} \alpha^{\frac{-\beta}{2\beta-2}} K_c Y \tag{4c}$$

For the simple case of uniaxial loading conditions when the total stressed volume, V, is very much larger than the small volume V_o eq. (4a) becomes

$$P_f(\sigma) = 1 - \exp\left[-\frac{V}{V_0} \left(\frac{\sigma}{\sigma_u} \right)^m \right] \tag{5}$$

However, to solve fracture problems one needs to evaluate eq. (5) for the highly non-uniform stress state ahead of a deforming crack-tip. In this situation the volumes (V_o) are made small enough that the assumption of a uniform stress state over the volume is reasonable, and the stresses are evaluated using the finite element technique. For the solution of crack problems, eq. (5) takes on the following form, with eq. (6d) being the analogue to the uniaxial version given in eq. (5):

$$P_f(\tilde{\sigma}) = 1 - \exp\left[-\frac{1}{V_0}\int_{\Omega}\left\{\frac{\tilde{\sigma}}{\sigma_u}\right\}^m d\Omega\right] \tag{6a}$$

$$\tilde{\sigma} = \tilde{\sigma}(\sigma_{ij}, \sigma_t, \sigma_m, \ldots) \tag{6b}$$

$$\sigma_w = \left[\frac{1}{V_0}\int_{\Omega}\tilde{\sigma}^m d\Omega\right]^{1/m} \tag{6c}$$

$$P_f(\sigma_w) = 1 - \exp\left[-\left\{\frac{\sigma_w}{\sigma_u}\right\}^m\right] \tag{6d}$$

Here Ω represents the "process zone," which is typically defined as either the plastic zone or as the region within which the maximum principal stress exceeds some integral multiple (usually 2 or 3) of the yield stress. Additionally, in the solution of cleavage fracture problems $\tilde{\sigma}$ is typically taken as to the maximum principal stress (σ_1). In this model, the parameters m and σ_u are taken to be characteristics of the material related, respectively, to the shape of the probability density function describing micro-crack size (see eq. (4b)), and to the characteristics of the probability density function describing micro-crack size *as well as* to the magnitude of the stress intensity factor required to fracture a carbide (see eq. (4c)). However, in practice m and σ_u are not defined from measurements of these micro-scale parameters, but rather are back-calculated from the results of multiple fracture toughness experiments [24].

This use of the maximum principal stress to define the BEREMIN Weibull stress in eq. (6c) identifies this approach as being a RKR-type model. Applications of this approach by Dodds and co-workers has successfully predicted toughness data for part-through semi-elliptic surface cracks from toughness data obtained using conventional straight-fronted fracture toughness test specimens [25] (see Fig. 3). This success would not have been possible using any of the models described previously because they had no mechanism to deal with the considerable variations in stress state around the crack front that characterize semi-elliptic surface cracks. However, Bass, et al. were unable to use this approach to predict successfully the toughness of cracks subjected to biaxial loading from conventional toughness results, needing instead to use of the mean stress (i.e., σ_m, the average of the three principal stresses) rather than the maximum principal stress in eq. (6b) to achieve a good prediction of experimental results (see Fig. 4) [26].

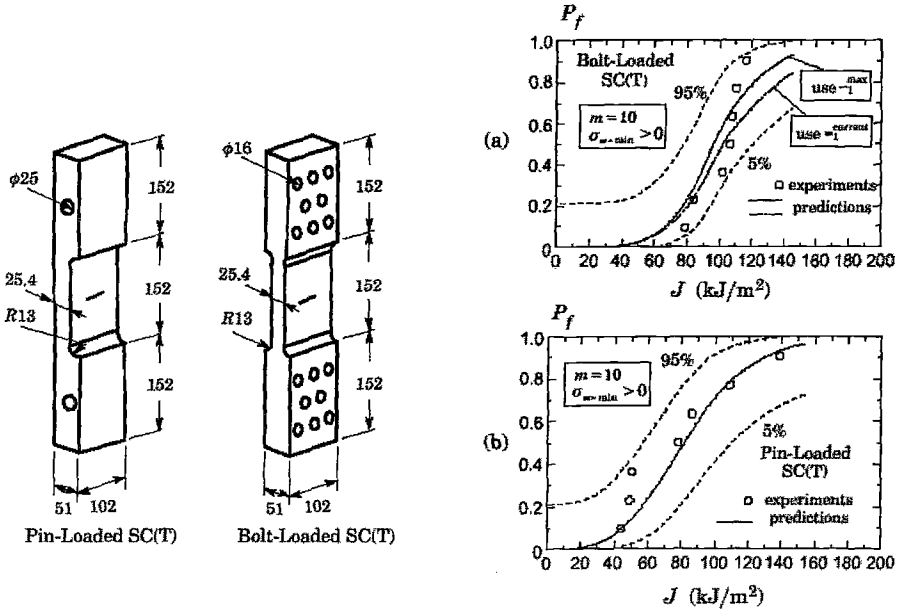

FIG. 3–*Successful prediction of critical J values reported by Gao, et al. for surface cracked specimens [25].*

Advantages and Limitations of the BEREMIN Modeling Approach, and a Proposed Way Forward

As detailed in the preceding Section, Dodds,' et al. implementation of the BEREMIN approach in the prediction of cleavage fracture successfully predicts the effects of complex changes in crack geometry on fracture toughness; predictions that had heretofore been impossible. However, in its current form the model does not capture the effects of relatively simple changes in applied loading. Specifically, under conditions of remote uniaxial loading the maximum principal stress (σ_1) must be taken as $\tilde{\sigma}$ in eq. (6) to obtain predictions that agree with experimental results, whereas under conditions of remote biaxial loading $\tilde{\sigma}$ must be set equal to the mean stress (σ_m). This inconsistency in the stress that appears to be controlling fracture suggests that, like its predecessors, the BEREMIN approach does not fully describe the physical processes responsible for cleavage fracture. Additionally, the Beremin approach contains no information regarding how the model parameters (m and σ_u) change with temperature and strain rate. These parameters can be back calculated from the results of replicate fracture toughness tests performed under the temperature and strain rate conditions of interest. However, the need to perform such detailed experimentation frustrates use of the Beremin model in a predictive capacity and, more practically, makes application of the model both costly and time-consuming.

To progress toward fully predictive models that are not as costly to implement, it seems important to enhance the Beremin model in two ways. First, it needs to incorporate a constitutive model that accounts for the physical phenomena responsible for temperature and strain rate dependency so that these trends don't have to be back calculated from toughness data. Secondly, a physically based criterion for cleavage fracture is needed so that the model can be applied with confidence to any condition of interest within the transition fracture regime. These refinements are discussed in the following Sections.

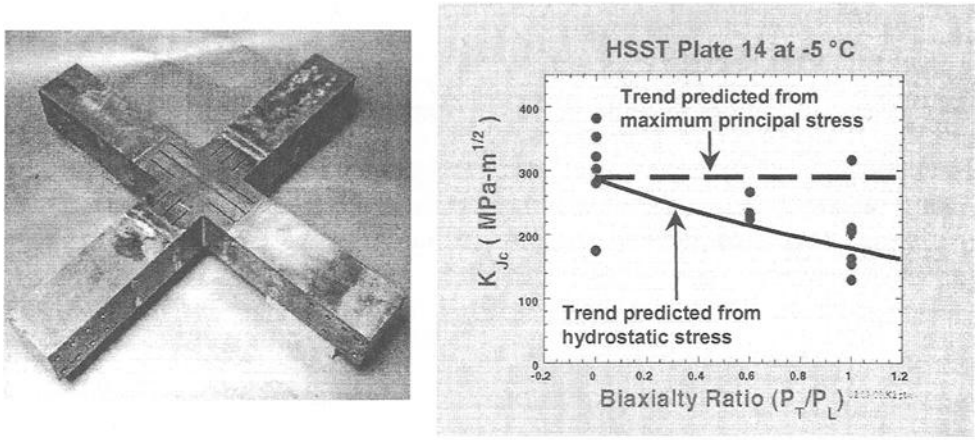

FIG. 4–*Four-inch thick biaxial load fracture specimen (left) and fracture toughness data (right) for biaxial loading reported by Williams, et al. [26] demonstrating that better prediction of the trends in toughness data is achieved by using the mean stress as $\tilde{\sigma}$ in eq. (6) rather than the maximum principal stress. The material tested is ASTM A533B that was given a special heat treatment to elevate its yield strength; it has a ASTM E1921 T_o value of -37°C.*

A Physically Based Constitutive Model for Ferritic Steels

Dislocation mechanics-based constitutive models describe how various aspects of the microstructure of a material control dislocation motion, and how these vary with temperature and strain rate. The microstructural characteristics of interest include short and long-range barriers to dislocation motion. The lattice structure itself provides the short-range barriers, which affect the atom-to-atom movement required for a dislocation to change position within the lattice. An inter-barrier spacing several orders of magnitude greater than the lattice spacing defines long-range barriers. Long-range barriers include point defects (solute and vacancies) precipitates (semi-coherent to non-coherent), boundaries (twin, grain, etc), and other dislocations in BCC materials.

As a stress is applied to a metal dislocations begin to move, which results in plastic deformation. For a dislocation to move it must shift from one equilibrium position in the

lattice to another, overcoming an energy barrier to do so. The wavelength of these barriers is equal to the periodicity of the lattice. The dislocation requires application of a force to overcome this energy barrier and the magnitude of this force is the Peierls-Nabarro stress, τ_{PN}. While moving the dislocation will also encounter other barriers such as solute atoms, vacancies, precipitates, inclusions, boundaries and other dislocations. Different spacings and size scales characterize these additional barriers.

At temperatures other than absolute zero, atoms vibrate about their lattice sites at a temperature-dependent amplitude. Additions of thermal energy (i.e., higher temperatures) act to increase the amplitude of atom vibration, increasing the probability that an atom will "jump" from one equilibrium site to another. This thermal energy thus acts to decrease the magnitude of the energy provided by the short range obstacles to dislocation motion at any moment in time, thereby decreasing the force required to move the dislocation from one equilibrium position to the next. The effect of strain rate (i.e., dislocation velocity) has a similar but opposite effect to that of temperature. As strain rate increases less time is available for the dislocation to overcome the short-range barriers provided by the lattice atoms. This decreases the effect of thermal energy, resulting in an increased force required for dislocation motion.

Long-range obstacles differ from short-range obstacles because changes in thermal energy do not greatly affect the ability of dislocations to move past them at the strain rates typically experienced by civil and mechanical structures that are not designed for creep service. This occurs because atomic vibration amplitude has little effect on the size of the long-range energy barrier presented to the dislocation, which is on the order of the inter-particle spacing. Consequently, the amount of energy required to move a dislocation past these large obstacles is orders of magnitude larger than that provided by the increased lattice vibration that results from increases in temperature. In their work, Armstrong and Zerilli concluded from carefully analyzed sets of Taylor experiments that overcoming the Peierls-Nabarro barriers was the principal thermally activated mechanism in BCC materials [27-30].

The fundamentally different nature of short- and long-range barriers to dislocation motion motivates a separate treatment in dislocation-based constitutive formulae. Consequently, the flow stress of a material is typically expressed as a sum of athermal and thermal components, associated with long-range and short-range barriers (respectively), as follows:

$$\sigma = \sigma_G(\text{structure}) + \sigma^*(T, \dot{\varepsilon}, \text{structure}) \tag{7}$$

The first term occurs due to the athermal or long-range barriers to dislocation motion while the second term described the action of thermally activated short-range barriers. The short-range barriers include the Peierls-Nabarro stress and dislocation forests. Peierls-Nabarro stresses (lattice friction stresses) are the controlling short-range barriers in BCC metals while dislocation forest structures are the controlling short-range barriers in FCC and HCP metals. This difference is responsible for the difference in strain rate sensitivity between BCC and FCC metals. Focusing attention on BCC metals, the

temperature dependence of the probability that a dislocation will overcome a short-range obstacle is given by:

$$P_B = \exp\left(\Delta G / kT\right) \tag{8}$$

where k is Boltzman's constant, T is the absolute temperature of interest, and ΔG is the activation energy of a barrier [31]. The strain rate effect shares a similar form:

$$\dot{\varepsilon} = \dot{\varepsilon}_o \exp\left(\Delta G / kT\right) \tag{9}$$

Solving eq. (9) for ΔG gives

$$\Delta G = kT \cdot \ln\left(\dot{\varepsilon} / \dot{\varepsilon}_o\right) \tag{10}$$

Equation (10) clearly shows that activation energy for dislocation motion decreases with temperature and increases with strain rate.

Using these equations as the basis for their model, Zerilli and Armstrong found that dislocations overcoming Peierls-Nabarro barriers are the principal thermally activated mechanism for deformation in BCC metals [32]. The spacing of these obstacles is equal to the lattice spacing and thus is not affected by prior plastic strain as are the dislocation forest structures in FCC metals. Zerilli and Armstrong developed the following expression for the thermal portion of the flow stress in eq. (7) (assuming a constant obstacle spacing for BCC):

$$\sigma^* = C_1 \exp(-\beta T) \tag{11}$$

where β depends on strain and strain rate as follows:

$$\beta = -C_2 + C_3 \ln \dot{\varepsilon} \tag{12}$$

Combining eqs. (11) and (12) with commonly accepted terms describing Orowan-type strengthening due to athermal barriers results in the following description of the flow behavior of BCC metals:

$$\sigma_f = \sigma_G + C_4 \varepsilon^n + \mu d^{-1/2} + C_1 \cdot \exp\left[-C_2 T + C_3 T \cdot \ln(\dot{\varepsilon})\right] \tag{13}$$

where C_1, C_2, C_3, C_4, μ, and n are material constants, and d is the grain diameter. The form of eq. (13) is consistent with dislocation-mechanics based constitutive models

developed by other researchers [33-34]. From the physical understandings that underlie eq. (13) the expectation arises that the temperature and strain rate dependence (i.e., $C_1 \cdot \exp[-C_2T + C_3T \cdot \ln(\dot{\varepsilon})]$) ***should be*** common to all ferritic steels. This is because the lattice structure is the same in all ferritic steels irrespective of their alloying, heat treatment, degree of cold work, degree of prior plastic strain, and degree of irradiation damage; factors whose influence are described by the terms $\sigma_G + C_4\varepsilon^n + kd^{-1/2}$. Fig. 5 demonstrates that experimental data validates this expectation. These figures display an excellent correspondence between the temperature and strain rate dependence of a wide variety of steel alloys and the predictions of eq. (13) for pure iron (i.e., $C_1 = 1033$ MPa, $C_2 = 0.00698$ / °K, and $C_3 = 0.000415$ / °K).

A Physically Based Criterion for Cleavage Fracture

Cottrell [35], Petch [36], Smith [5-6] and many other researchers have attempted to describe cleavage fracture mechanisms quantitatively. Here we examine the 1968 work of Tetelman, Wilshaw, and Rau (TWR) [10]. They describe the following sequence of three events that establish the necessary precursors for cleavage fracture:

Event #1. Cleavage fracture begins with micro-crack nucleation, which is well documented as resulting from dislocation motion and accumulation at long-range obstacles such as grain boundaries and second phase particles. The value of strain necessary to nucleate the micro-crack quantifies this event.

Event #2. Following nucleation, the micro-crack needs to propagate through the grain in which it was nucleated. A critical value of stress triaxiality is needed to keep the crack tip sharp. Otherwise dislocations will be emitted from the crack tip, thereby blunting it, which stops the cleavage fracture process and produces instead a non-propagating crack.

Event #3. The final event is the subsequent propagation of the micro-crack through the boundaries that surround the nucleating grain. This event occurs when the opening stress at the crack tip exceeds the microscopic cleavage fracture stress "over {a characteristic distance of} at least one grain diameter in the plastic zone ahead of the crack."

In 1973, RKR [3] expanded on TWR's hypothesis and developed their own "characteristic distance" of two grain diameters at lower transition region temperatures. However, the failing of the RKR model, and all of its subsequent progeny, has been its exclusive focus of TWR's Event #3, effectively implying that Events 1 and 2 are satisfied *a priori*. In specific, we mentioned earlier in this paper that the RKR model does not perform well at temperatures in the upper transition region. Additionally, application of the RKR-type BEREMIN model has been unsuccessful in the prediction of fracture in specimens that have an applied biaxial load. It is reasonable to postulate that both failings relate to RKR's assumed insignificance of Event #2 (adequate stress tri-axiality

to extend the micro-crack to the boundaries of the grain in which it initiated) for the following reasons:

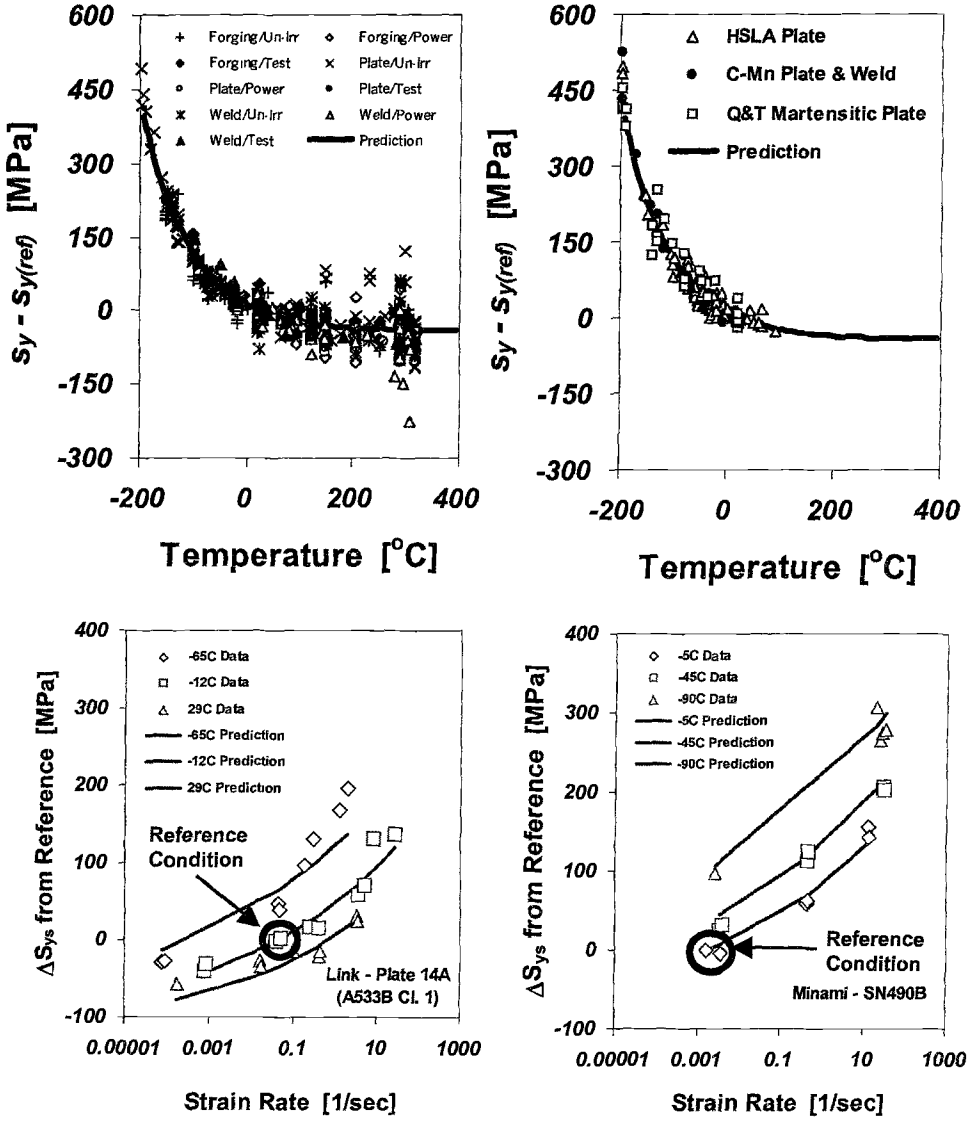

FIG. 5–*Experimental data demonstrates an excellent correspondence between the temperature and strain rate dependence of a wide variety of steel alloys and the predictions of eq. (13) for pure iron.*

- In Upper Transition: In the lower transition region that RKR investigated, the assumption that adequate tri-axiality exists under all conditions is appropriate because the lattice friction stress, which is temperature dependent, is high enough to prevent significant dislocation emission from the tip of the micro-crack and, consequently, is high enough to prevent significant crack tip blunting [37-38]. However, at temperatures higher in the transition region the friction stress decreases, allowing dislocation emission and motion to occur more easily. This leads to a greater possibility of micro-crack blunting, and a consequent failure to achieve Event #2. Thus, in upper transition the occurrence of Event #2 cannot be assumed and must be checked for independently.
- In the Presence of Applied Biaxial Loading: Most fracture mechanics test specimens are similar in that the applied loading acts only to open the crack. While specimens that have load applied parallel to the crack plane are rare, structures that apply load parallel to the crack plane are quite common. For example, any internally pressurized vessel generates a biaxial state of stress in the vessel wall, and thermal stresses are inherently two-or three dimensional in any restrained structure. A remotely applied multi-axial stress state clearly makes it easier to achieve Event #2 and, consequently, easier for cleavage fracture to occur. However, using the maximum principal stress as $\tilde{\sigma}$ in the BEREMIN model (eq. (6)) fails to provide any measure of stresses applied parallel to the crack plane, and thus cannot be expected to predict failure for loading conditions of this type.

In closing it is relevant to note that, in its current implementation, calculation of the Weibull stress following the approach suggested by the Beremin group involves an arbitrary selection of the parameter Ω. Ω represents the size of the "process zone" for cleavage fracture, which is typically defined as either the plastic zone, or as the region within which the maximum principal stress exceeds some integral multiple (usually 2 or 3) of the uniaxial yield stress. Thus, the current Beremin model includes an arbitrary and non-physically based definition of the process zone for cleavage fracture. This arbitrary selection can be replaced by appeal to TWR's Event #1, which suggests that the process zone for cleavage fracture is the region within which sufficient strain has developed to initiate a micro-crack.

Summary and Conclusions

In this paper we have reviewed the development of models that attempt to predict the transition fracture behavior of BCC metals, beginning with the landmark paper published by Ritchie, Knott, and Rice (RKR) in 1973 and working forward to the BEREMIN model, which is the focus of current research efforts. In the past three decades considerable progress has been made in prediction accuracy. Nevertheless, the best cleavage fracture models available currently still include coefficients back-calculated from fracture toughness experiments, these being necessary to incorporate into the models the temperature and strain rate dependency of ferritic steels. Moreover, experimental

evidence demonstrating that successful blind predictions of failure cannot be made even for the simple case of applied biaxial loading calls into question the robustness of these models to the prediction of the failure conditions in engineering structures.

To address these shortcomings and progress toward fully predictive models, two enhancements are needed to the BEREMIN model. First, it needs to incorporate a dislocation-mechanics based constitutive model such as that proposed by Zerilli and Armstrong. Such models account for the physical phenomena responsible for temperature and strain rate dependency in ferritic steels so that these trends don't have to be back calculated from toughness data; instead they become integral parts of the model. Secondly, a physically-based criterion for cleavage fracture is needed so that the model can be applied with confidence to any condition of interest within the transition fracture regime. To this end the use of a model proposed by Tetelman, Wilshaw, and Rau (TWR) is suggested. We demonstrate that the TWR 3-event cleavage fracture criterion is in fact a mode general expression of the critical stress / critical distance criteria popularized by RKR, and that this increased generality is expected to reconcile recognized deficiencies in RKR, and RKR-like cleavage fracture models (such as the BEREMIN model).

References

[1] Watanabe, J., Iwadate, T., Tanaka, Y., Yokoboro, T., and Ando, K., "Fracture Toughness in the Transition Region," *Engineering Fracture Mechanics*, 28, pp. 589-600, 1987.

[2] Knott, J.F. and Boccaccini, A.R., "The Fracture Mechanics-Microstructure Linkage," Mechanics and Materials: Fundamentals and Linkages, Meyers, M.A., et al., Eds., Wiley & Sons, pp. 399-424, 1999.

[3] Ritchie, R., Knott, J.F., and Rice, R., "On the Relationship Between Critical Tensile Stress and Fracture Stress in Mild Steels," *J Mech Phys Sol*, 21, pp. 395-410, 1973.

[4] Orowan, E., *Transactions of the Institute of Engineers and Shipbuilders in Scotland*, 89, p. 165, 1945.

[5] Smith, E., Physical Basis of Yield and Fracture, Conference Proceedings, Institute of Physics and the Physical Society, London, p. 36, 1966.

[6] Smith, E., "Cleavage Fracture in Mild Steels," *Int. J. Fract. Mech.*, Vol. 4, pp. 131-145, 1968.

[7] Rice, J.R., and Rosengren, G.F., "Plane Strain Deformation Near a Crack Tip in a Power-Law Hardening Material," *Journal of Mechanics and Physics of Solids*, 16, pp. 1-12, 1968.

[8] Hutchinson, J.W., "Singular Behavior at the End of a Tensile Crack in a Hardening Material," *Journal of Mechanics and Physics of Solids*, 16, pp. 13-31, 1968.

[9] Rice, J.R., and Johnson, M.A. in Inelastic Behavior of Solids, M.F. Kanninen, et al., Eds., McGraw Hill, New York, New York, pp. 641-672, 1970.

[10] Tetelman, A.S., Wilshaw, T.R., Rau Jr, C.A., "The Critical Tensile Stress Criterion for Cleavage," *Int. Jour. Frac. Mech.*, Vol. 4, No. 2, June 1968, pp. 147-157.

[11] Gross, J.L., et al., "Investigation of the Ashland Oil Storage Tank Collapse on January 2, 1988," National Bureau of Standards Report NBSIR 8-2792, 1988.

[12] Warke, R.W., Koppenhoefer, K.C. and Amend, W.E., "Case Study in Probabilistic Assessment: Seismic Integrity of Girth Welds in a Pre-World War II Pipeline," Proceedings of ICAWT '99: Pipeline Welding and Technology, Edison Welding Institute, Columbus, Ohio, October 1999.

[13] Code of Federal Regulation 10CFR50.61, "Fracture Toughness Requirements for Protection Against Pressurized Thermal Shock Events."

[14] O'Dowd, N.P., Shih, C.F., "Family of crack-tip fields characterized by a triaxiality parameter – I. Structure of fields," *Journal of Mechanics and Physics of Solids*, 39, pp. 989-1015, 1991.

[15] Hancock, J.W., Reuter, W.G., and Parks, D.M. "Constraint and Toughness Parameterized by T," *Constraint Effects in Fracture, ASTM STP 1171,* E.M. Hackett, K.-H. Schwalbe, and R.H. Dodds, Eds., American Society for Testing and Materials, Philadelphia, pp. 21-41,1993.

[16] Chao, Y.J., Yang, S., and Sutton, M.A., "On the Fracture of Solids Characterized by One or Two Parameters: Theory and Practice," *Journal of the Mechanics and Physics of Solids,* 42(4), pp.629-647, 1994.

[17] Newman, J.C. Jr., Crews, J.H., Bigelow, C.A., and Dawicke, D.S., "Variations of a Global Constraint Factor in Cracked Bodies Under Tension and Bending Loads," *Constraint Effects in Fracture, Theory and Applications: Second Volume, ASTM STP 1244,* Mark Kirk and Ad Bakker Eds., American Society for Testing and Materials, Philadelphia, pp. 21-42, 1995.

[18] O'Dowd, N.P., Shih, C.F., 'Family of crack-tip fields characterized by a triaxiality parameter – II. Fracture Applications," *Journal of Mechanics and Physics of Solids*, 40, pp. 939-963, 1992.

[19] Dodds, R.H., Anderson, T.L., and Kirk, M.T., "A Framework to Correlate a/W Ratio Effects on Elastic-Plastic Fracture Toughness (J_c)," *International Journal of Fracture,* 48, 1991, pp. 1-22,

[20] Kirk, M.T., Koppenhoefer, K.C., and Shih, C.F., "Effect of Constraint on Specimen Dimensions Needed to Obtain Structurally Relevant Toughness Measures", *Constraint Effects in Fracture, ASTM STP 1171,* E.M. Hackett, K.-H. Schwalbe, and R.H. Dodds, Eds., American Society for Testing and Materials, Philadelphia, pp. 79-103, 1993.

[21] Wallin, K., "The Size Effect in K_{Ic} Results," *Engineering Fracture Mechanics*, 22, pp. 149-163, 1985.

[22] Beremin, F.M., "A Local Criterion for Cleavage Fracture of a Nuclear Pressure Vessel Steel," *Metallurgical Transactions*, 14A, pp. 2277-2287, 1991.

[23] Griffith, A, "The Phenomena of Rupture and Flow in Solids," *Philosophical Transactions, Series A,* 221, pp. 163-198, 1920.

[24] Gao, X., Dodds, R.H., Tregoning, R.L., Joyce, J.A., and Link, R.E., "Effects of Loading Rate on the Weibull Stress Model for Simulation of Cleavage Fracture in Ferritic Steels," Proc. of the 2000 ASME Pressure Vessel and Piping Conference, ASME, July 2000.

[25] Gao, X., Dodds, R.H., Tregoning, R.L., and Joyce, J.A., "Cleavage Fracture in Surface Crack Plates: Experiments and Numerical Predictions," Proc. of the 1999 ASME Pressure Vessel and Piping Conference, ASME, July 1999.

[26] Williams, P.T., Bass, B.R., and McAfee, W.J., " Application of the Weibull Methodology to a Shallow-Flaw Cruciform Bend Specimen Under Biaxial Loading Conditions," *Fracture Mechanics, 31st Volume,* ASTM STP 1389, G. R. Halford and J. Gallagher, Eds., American Society for Testing and Materials, 2000.

[27] F.J. Zerilli and R.W. Armstrong, *J. Appl. Phys.*, 61, (1987) 1816.

[28] F.J. Zerilli and R.W. Armstrong, Shock and Compression of Condensed Matter, 1989, eds. S.C. Schmidt, J.N. Johnson, and L.W. Davison, Elsevier, Amsterdam, 1990, p357.

[29] F.J. Zerilli and R.W. Armstrong, *J. Appl. Phys.*, 68, (1990) 1580.

[30] F.J. Zerilli and R.W. Armstrong, *J. Appl. Phys.*, 40, (1992) 1803.

[31] Kocks, U.F., A.S. Argon, and M.F. Ashby, *Progr. Mater. Sci.,* 19, p. 1, 1975.

[32] Zerilli, F. J. and R. W. Armstrong, "Dislocation-mechanics-based constitutive relations for material dynamics calculations," *J. Appl. Physics,* Vol. 61, No. 5, 1 March 1987.

[33] Johnson, G.R., and W. H Cook, Proc. 7th Int. Symp. Ballistics, Am. Def. Prep. Org. (ADPA), The Netherlands, p. 541, 1983

[34] Follansbee, P.S. and Kocks, U.F., *Acta Met.,* 36, p.81, 1988.

[35] Cottrell, A.H., *Theoretical Aspects of Fracture,* Fracture, Averbach, B.L, et al., Eds., Wiley & Sons, p. 20-44, 1959.

[36] Petch N.J., "The Ductile-Cleavage Transition in Alpha Iron," Fracture, Averbach, B.L, et al., Eds., Wiley & Sons, p. 54-64, 1959.

[37] Rice, J.R. and Thomson, R. "Ductile versus brittle behaviour of crystals," *Phil Mag*, 1974:29(1):73-97.

[38] Weertman, J., Dislocation Based Fracture Mechanics, Singapore: World Scientific, 1996.

Anssi Laukkanen,[1] Kim Wallin,[2] Pekka Nevasmaa,[1] and Seppo Tähtinen[1]

Transferability Properties of Local Approach Modeling in the Ductile to Brittle Transition Region

Reference: Laukkanen, A., Wallin, K., Nevasmaa, P., and Tähtinen, S., **"Transferability Properties of Local Approach Modeling in the Ductile to Brittle Transition Region,"** *Predictive Material Modeling: Combining Fundamental Physics Understanding, Computational Methods and Empirically Observed Behavior, ASTM STP 1429,* M. T. Kirk and M. Erickson Natishan, Eds., ASTM International, West Conshohocken, PA, 2003.

Abstract: Qualitative descriptive potential of local approach models for upper shelf and transition region has been well established. Models such as the Gurson-Tvergaard-Needleman and the Beremin model have been demonstrated to enable characterization of fracture phenomena over the entire transition regime. The foundation for consistent local approach characterization of material failure has been set, but quantitative application is still at developing stages. Current work addresses properties of a modified Beremin model in terms of material parameter consistency and transferability, which are taken as measures of performance with respect to quantitative applicability. Three-point bend specimen fracture toughness data of sizes 3×4×27 mm, 5×5×27 mm, 5×10×55 mm and 10×10×55 mm are simulated in the ductile to brittle transition region using finite element methods and inference of local approach parameters is performed using pointwise collocation and stochastic methods. The suitability of the calibration methods and overall model performance are evaluated and demonstrated.

Keywords: Brittle Fracture, Beremin model, Miniature Specimens, Local Approach, Transferability.

Introduction

The use of fracture mechanics in design and failure assessment is in some practices impeded by the difficulties in quantifying the structure related constraint and transferability properties of experimental test data. It is well known that specimen size, crack depth and loading conditions may effect the materials fracture toughness. Transferability of small specimen toughness data to real structures has long been the key issue in fracture mechanics research. Methods based on the Weibull statistic, such as the "Master Curve" methodology and local approach methods of fracture have been developed and are able to characterize the scatter of fracture toughness test results and the effects of specimen dimensions on the data distribution, making it possible to define

[1] Research Scientists and [2] Research Professor, VTT Industrial Systems, P.O. Box 1704, FIN-02044VTT, Finland.

fracture toughness parameters for a given probability of failure and develop scaling models for toughness transferability.

Ongoing development of local approach methods for cleavage fracture has led to the introduction of several different types of material models and parameter calibration procedures. The feasibility of these methods to practical purposes has usually been demonstrated by performing parameter inference on the basis of attainable experimental data and in many cases it can be argued that even limited generality of the used methods is doubtful. It can be stated that qualitative descriptive potential of local approach and damage mechanics models has been well authenticated, but quantitative properties are a completely different matter.

The current work contributes to the matter by analyzing a relatively extensive fracture toughness dataset using a modified Beremin model [1,2,3]. This collection of fracture toughness data in the ductile to brittle transition region consists of both irradiated and reference data of A533B Cl. 1 (JRQ) over a wide temperature range and with different size bend type fracture mechanics specimens. The experimental results are processed using the Master Curve method and two fundamentally differing local approach parameter calibration methods are applied on the basis of the dataset. Dependencies in the calibrated parameters are describes and discussed, and on the basis of the results, a calibration methodology producing the widest range of property transferability is presented.

Testing and material

The material and experimental procedures are described in detail in [4], where the fracture toughness data is applied to demonstrate performance of small fracture mechanics specimens in the ductile to brittle transition region. A533B Cl.1 (JRQ) in T-L orientation has a yield strength of 486 MPa and a tensile strength of 620 MPa. Irradiation of the steel was performed approximately 15 years ago at a temperature of 265°C with a neutron fluency of approximately 1.5×10^{19} n/cm^2 (E > 1 MeV). At the irradiated condition the yield strength is 687 MPa and tensile strength 815 MPa. The T28J transition temperatures are -29°C and +84°C and upper shelf Charpy-V energies are 210 J and 129 J, respectively.

The investigated specimen geometries were of three-point bend type (3PB) with sizes 10-10-55 mm, 5-10-55 mm, 5-5-27 mm and 3-4-27 mm, respectively. The specimens are presented schematically in Fig.1. Reference orientations were that of T-L while the irradiated were L-T. The specimens were tested in three point bending with a span to specimen width ratio of 4. Initial crack length to specimen width was 0.5 and the specimens were side-grooved 10% on each side. The testing and analyses routines followed ASTM standard E1820-1999a (Test Method for Measurement of Fracture Toughness) and E1921-2002 (Standard Test Method for Determination of Reference Temperature, T_0, for Ferritic Steels in the Transition Range).

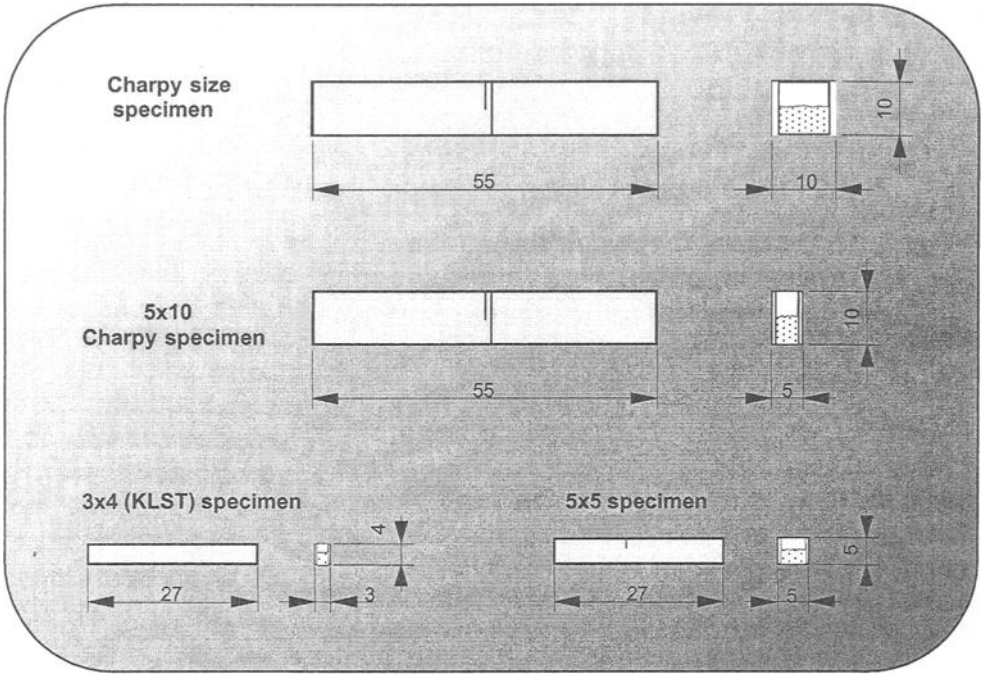

Fig. 1—*Three-point bend specimens used in material characterization and numerical analysis.*

Master Curve Analysis

The Master Curve analysis followed the ASTM Test Method for Determination of Reference Temperature, T_0, for Ferritic Steels in the Transition Range (E1921-2002). Two levels of censoring were4 applied. First, for all data referring to "non-cleavage" (ductile end of test) it was prescribed that $\delta_i = 0$. Second, all data violating the specimen size validity criterion were assigned the toughness value corresponding to the validity criterion with $\delta_i = 0$.

A plastic η-factor of 2 was used instead of 1.9 as prescribed in E1921. The reason for this was that the testing and J-analysis followed E1820. The effect of using the η-factor of 2 instead of 1.9 is a 1-2°C bias of the T_0 values towards lower temperatures.

For the comparison of different size specimen data, and for the calculation of the Master Curve transition temperature T_0, all data were thickness-adjusted to the reference flaw length (thickness) $B_0 = 25$ mm with Eq. 1 as prescribed in E1921:

$$K_{25mm} = K_{\min} + (K_{JC} - K_{\min}) \cdot \left(\frac{B}{B_0} \right)^{1/4} \tag{1}$$

The thickness, B, refers to the nominal thickness, regardless of side-grooving.

For all data sets, T_0 was estimated from the size-adjusted K_{Jc} data using a multi-temperature randomly censored maximum likelihood expression (Eq. 2) [5]:

$$\sum_{i=1}^{n}\frac{\delta_i \cdot \exp\{0.019[T_i - T_0]\}}{11+77\cdot\exp\{0.019[T_i - T_0]\}} - \sum_{i=1}^{n}\frac{(K_{IC_i}-20)^4 \cdot \exp\{0.019[T_i - T_0]\}}{(11+77\cdot\exp\{0.019[T_i - T_0]\})^5} = 0 \quad (2)$$

The transition temperature, T_0, was solved by iteration from Eq. 2. Yield strength temperature dependency was evaluated following the SINTAP-procedure as $\sigma_{ys}^{T} = \sigma_{ys}^{RT} + 1e5/(491+1.8T) - 189MPa$, where RT denotes room temperature and temperature is given in degrees Celsius.

Ideally, the Master Curve should not be fitted to data below T_0 - 50°C, i.e. data close to or on the lower shelf, where a temperature fit becomes highly inaccurate and where deviation in the lower shelf toughness from the Master Curve assumption may bias the results. Also, the effect of extensive ductile tearing should be avoided. Therefore, in the determination of T_0 the data were limited to $-50°C<T-T_0<+50°C$. This is in harmony with the latest revision of the Master Curve standard, ASTM E1921-2002.

In order to perform local approach parameter calibration on the basis of Master Curve scatter, the normalization fracture toughness, K_0, was estimated. The Master Curve scatter is described by Eq. 3 according to ASTM E1921-2002:

$$P_f = 1 - \exp\left(-\left(\frac{K_{Jc}-K_{min}}{K_0 - K_{min}}\right)^4\right). \quad (3)$$

The estimation of the normalization fracture toughness K_0, corresponding to a 63.2% failure probability was carried out on the basis of randomly censored Maximum Likelihood, Eq. 4 [6]:

$$K_0 = \left(\frac{\sum_{i=1}^{n}(K_i - K_{min})^4}{\sum_{i=1}^{n}\delta_i - 1 + \ln 2}\right)^{1/4} + K_{min}, \quad (4)$$

where the censoring parameter δ_i is 1 for uncensored and 0 for censored data, the limiting fracture toughness having a fixed value of 20 $MPa\sqrt{m}$.

Numerical analysis

Numerical analyses at temperatures corresponding to experimental fracture toughness data were carried out using the WARP3D research code version 13.9 developed by University of Illinois [2]. The computations presented in the current paper were carried out in 2D plane strain conditions. The elastic-plastic material behavior was modeled with an incremental isotropic hardening formulation. The deformation description was presented in a finite strain Lagrangian framework. Meshes were generated for 10×10×55 mm, 5×10×55 mm, 5×5×27 mm and 3×4×27 mm small 3PB specimens. 8 node bbar-stabilized 3D solid elements were used in the computations. A mesh for a CVN size specimen is presented in Fig. 2.

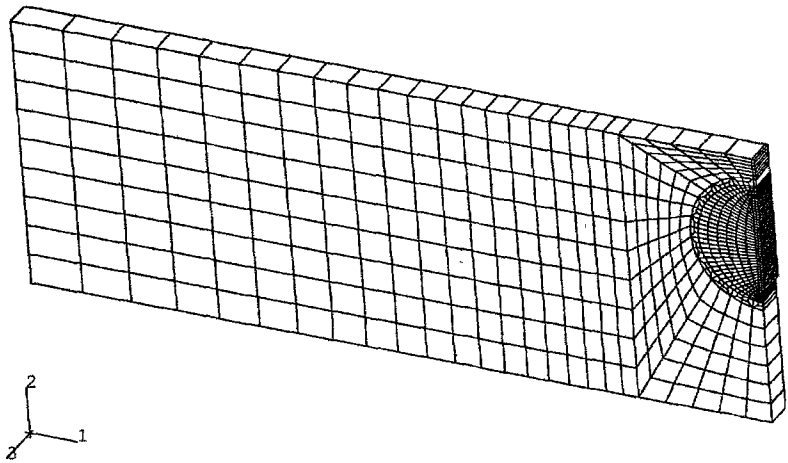

Fig. 2—*Mesh used for CVN size specimen.*

The temperature dependency of yield strength was evaluated in accordance with the Master Curve method. Strain hardening exponent was evaluated on the basis of yield to tensile strength ratio using an expression developed by Auerkari [7]: $\left(\sigma_0/\sigma_{ts} = (30 \cdot 1/N)^{-1/N}\right)$, where σ_0 is the yield strength, σ_{ts} the tensile strength and N the strain hardening exponent.

On the basis of numerical and experimental fracture toughness results for the transition region the parameters of a three-parameter Weibull distribution were fitted using a maximum likelihood (MML) scheme. This was performed using the WSTRESS [3] code and MatLab built evaluation routines. The three parameter Weibull model/modified Beremin model for cleavage initiation is presented as

$$P_f = 1 - \exp\left[-\left(\frac{\sigma_w - \sigma_{th}}{\sigma_u - \sigma_{th}}\right)^m\right], \tag{5}$$

where σ_w is the Weibull stress, σ_u the scale parameter, m the shape parameter and σ_{th} the threshold stress. The Weibull stress is presented as

$$\sigma_w = \left\{ \frac{1}{V_0} \int_\Omega \sigma_1^m d\Omega \right\}^{\frac{1}{m}}, \tag{6}$$

where σ_1 is the first principal stress, V_0 is a reference volume set to unity and Ω is the fracture process zone. The process zone was defined as $\Omega : \sigma_1 \geq \lambda \cdot \sigma_0$, where two values of λ were used, 1 and 2, to evaluate results process zone dependency. σ_{th} was identified with K_{min}, i.e. it corresponds to a Weibull stress at $K = K_{min}$.

The calibration of the shape and scale parameters was carried out using a MML routine. The form of used MML for a Weibull probability density function of Eq. 5 was

$$L(m, \sigma_u) = \left(m\sigma_u^{-m}\right)^r \prod_{i=1}^{r} \sigma_{wi}^{m-1} \exp\left[-\sigma_u^{-m} \sum_{i=1}^{r} \sigma_{wi}^m\right] \exp\left[-(n-r)\sigma_u^{-m}\sigma_{wc}^m\right], \tag{7}$$

where $n-r$ is the number of censored samples. The parameters were determined by iteratively finding the maxima of Eq. 7.

The calibration process consists of determining the variation of the Weibull stress with different values of the shape parameter to find the maximum of Eq. 7 by inputting the experimental fracture toughness results. Two different philosophies were adopted for this process. First, a direct approach by using the actual experimental samples at a fixed temperature was utilized. Second, the Master Curve normalization toughness was determined and the resulting distribution was used to stochastically generate the sample for parameter inference. In this case Monte-Carlo sampling is used to generate a large number of datapoints using Eq. 8:

$$K_{generated} = (K_0 - K_{min}) \cdot -LN\{1-U\}^{1/4} + K_{min}, \tag{8}$$

where $U \in [0,1]$ is randomly sampled. The first method is simpler and can be used even to "ill-behaving" fracture toughness data, while the second method requires a reliable estimate of the normalization data and as such, the necessary number and quality of valid experimental data.

Experimental results

The Master Curve analysis results for different specimens and irradiated and reference materials are presented in Figs. 3 and 4.

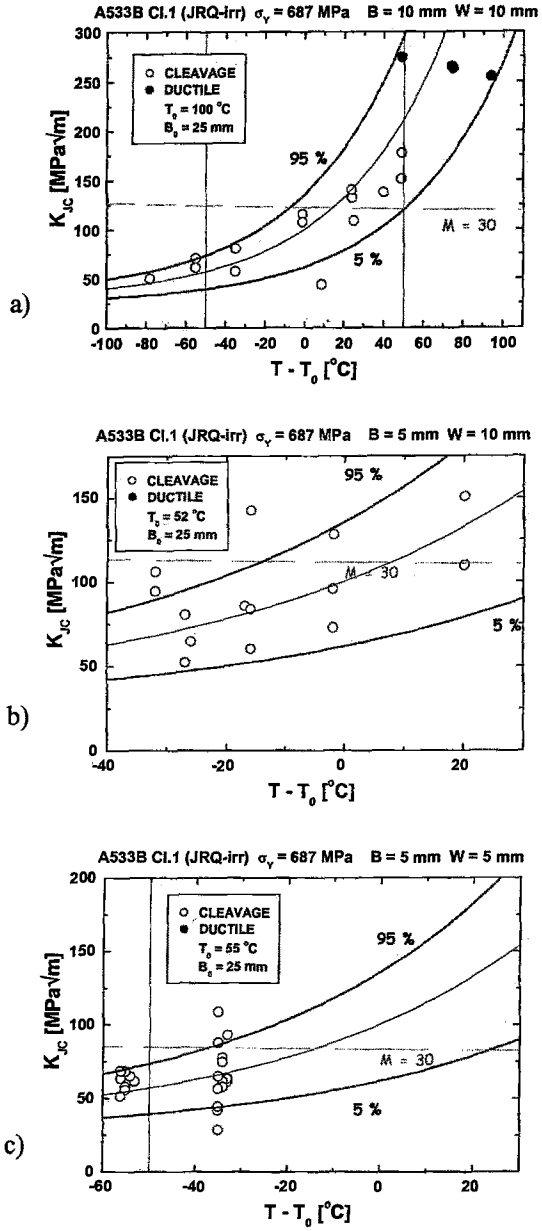

Fig. 3—*Master Curve analysis results for A533B Cl.1 (JRQ) in irradiated condition. Results for a) 10-10-55 mm, b) 5-10-55 mm and c) 5-5-27 mm specimens.*

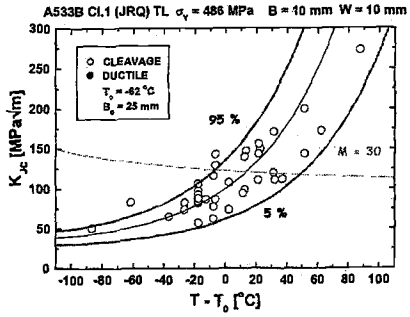

a)

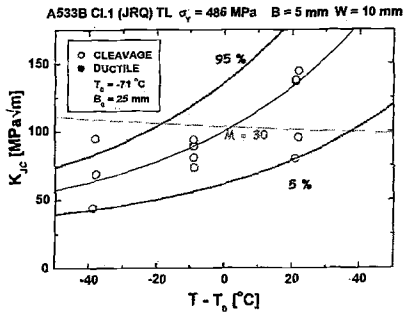

b)

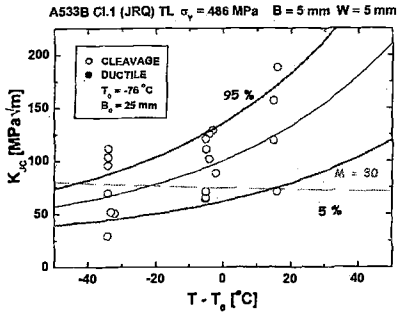

c)

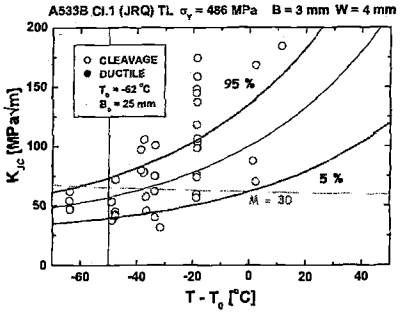

d)

Fig. 4—*Master Curve analysis results for A533B Cl.1 (JRQ) in reference condition. Results for a) 10-10-55 mm, b) 5-10-55 mm, c) 5-5-27 mm and d) 3-4-27 mm specimens.*

It can be noted from Figs. 3 and 4 that the differences between the irradiated and reference state materials are quite high, the reference temperature differences being of the order of 100°C. The old irradiated 10-10-55 mm specimen results deviated from the other irradiated ones (also new irradiated 10-10-55 mm specimens [4]). The reference temperature differs by nearly 40°C, which cannot be understood via any common means and probably results from deficiencies or mishandling during some stages of experimental testing or macroscopic material inhomogeneity, since the results still follow the Master Curve. The differences in results of other specimen sizes are of commonly observed order, the 3-4-27 mm results differing from this trend by exhibiting to some extent a larger than expected scatter.

The normalization fracture toughness was evaluated at temperatures and with specimens where enough datapoints were available (nominally 6 or more in order to have a number of samples to identify distribution properties). The results of this evaluation are presented in Figs. 5 and 6 and the fitted temperature dependencies in Fig. 7. The minimum fracture toughness was fixed in all evaluations.

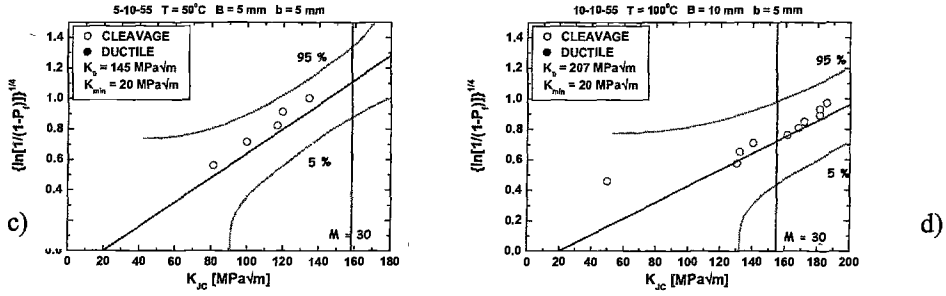

Fig. 5—*Results for normalization toughness, K_0, for irradiated A533B Cl.1 (JRQ). a) 5-5-27 mm ,20°C, b) 5-5-27 mm ,0, c) 5-10-55 mm , 50°C, d) 10-10-55 mm, 100°C.*

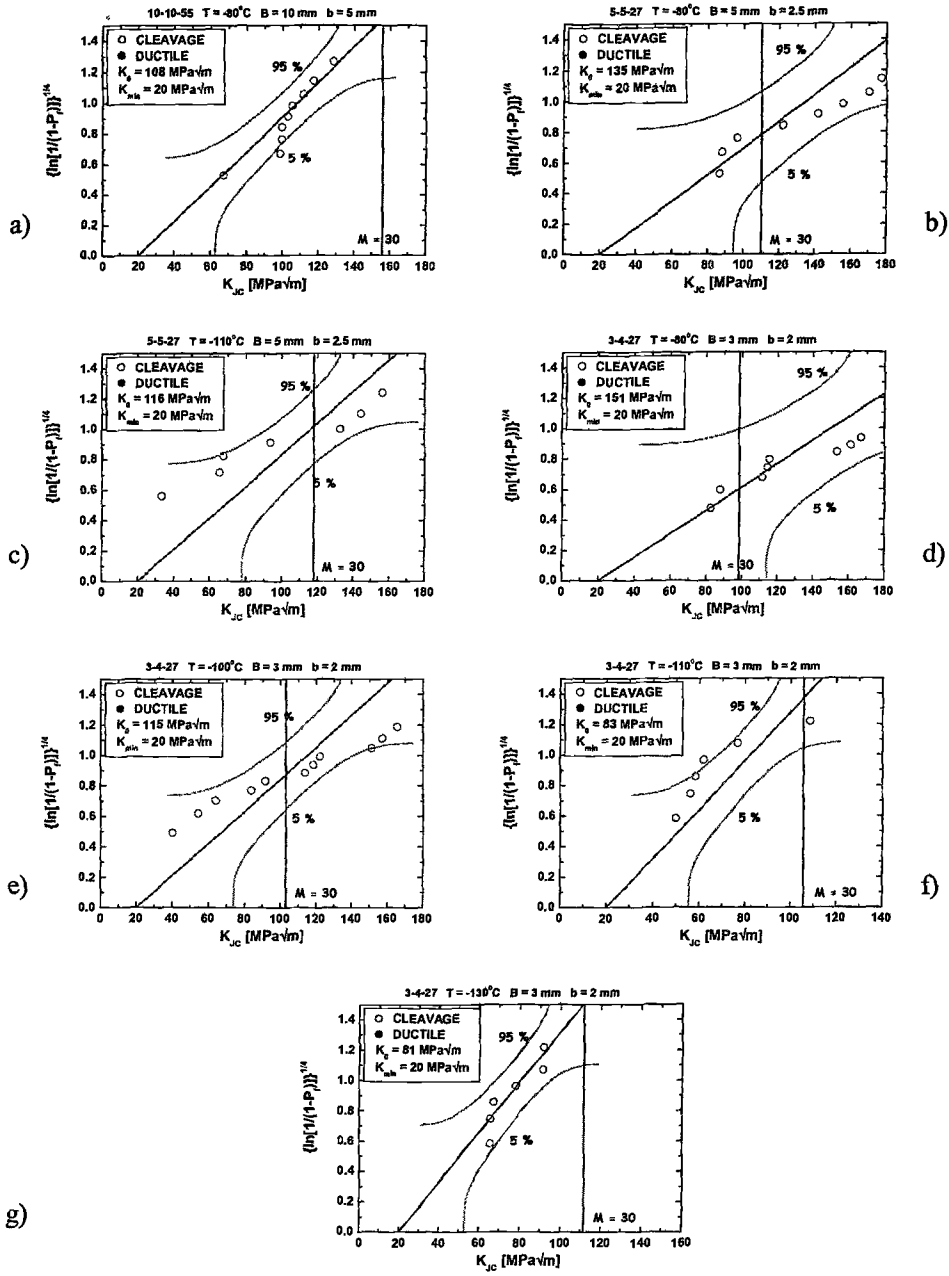

Fig. 6—*Results for normalization fracture toughness, K_0, for reference A533B Cl.1 (JRQ). a) 10- 10-55 mm, -80 °C, b) 5-5-27 mm, -80 °C, c) 5-5-27, -110 °C, d) 3-4-27 mm, -80 °C, e) 3-4-27 mm, -100 °C, f) 3-4-27 mm, -110 °C and g) 3-4-27 mm, -130 °C.*

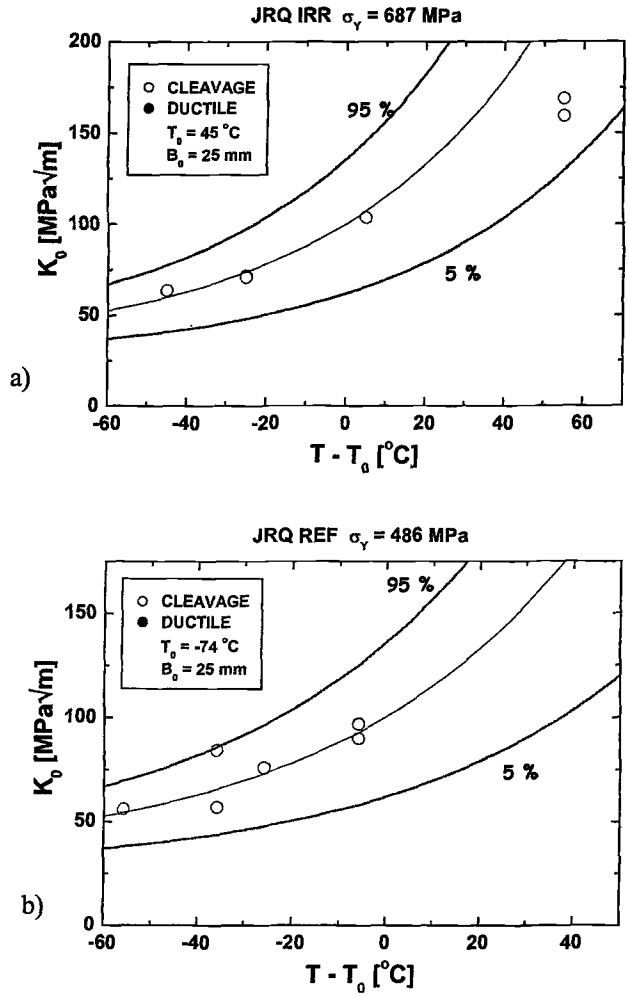

Fig. 7—*Temperature dependency of the normalization fracture toughness, K_0. a) irradiated and b) reference.*

Numerical results - calibration

The numerical results comprise of calibrated parameters, estimates of failure probability, evaluation of dependencies and transferability of results over temperatures and specimens, and comparison of simulated to actual Master Curves.

The cleavage fracture initiation stress, the Weibull stress, is presented in Figure 8 for two cases, one irradiated and another for reference steel. The results are based on MML collocation estimation directly on the basis of fracture toughness datapoints. The different process zone measures are indicated in the legends along with temperature. The effect of

decreasing temperature with increasing stress for crack initiation is noted. Scatter of fracture toughness results is seen to affect the estimation results such that in some cases even though the temperature decreases, the cleavage crack driving stress appears to decrease as well.

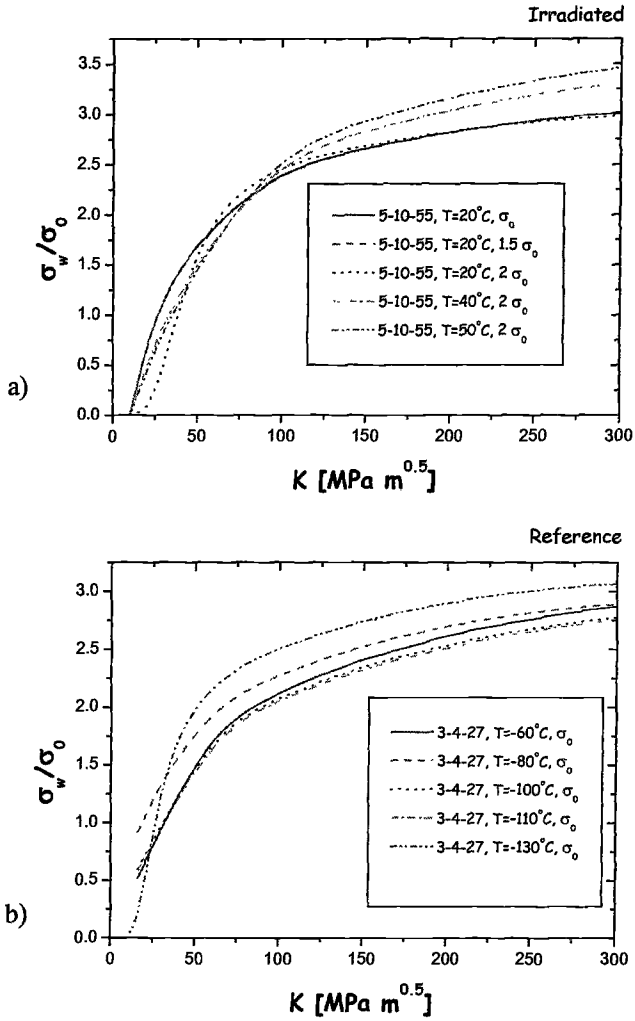

Fig. 8—*Weibull stress for a) irradiated 5-10-55 mm specimen and b) reference 3-4-27 mm specimen.*

The calibrated Weibull shape and scale results using point collocation are presented in Figs. 9 and 10 as a function of temperature, respectively. The results for the shape parameter include 5% and 95% reliability bounds, for the scale and threshold parameters the scatter in the values is low enough to make them unnecessary.

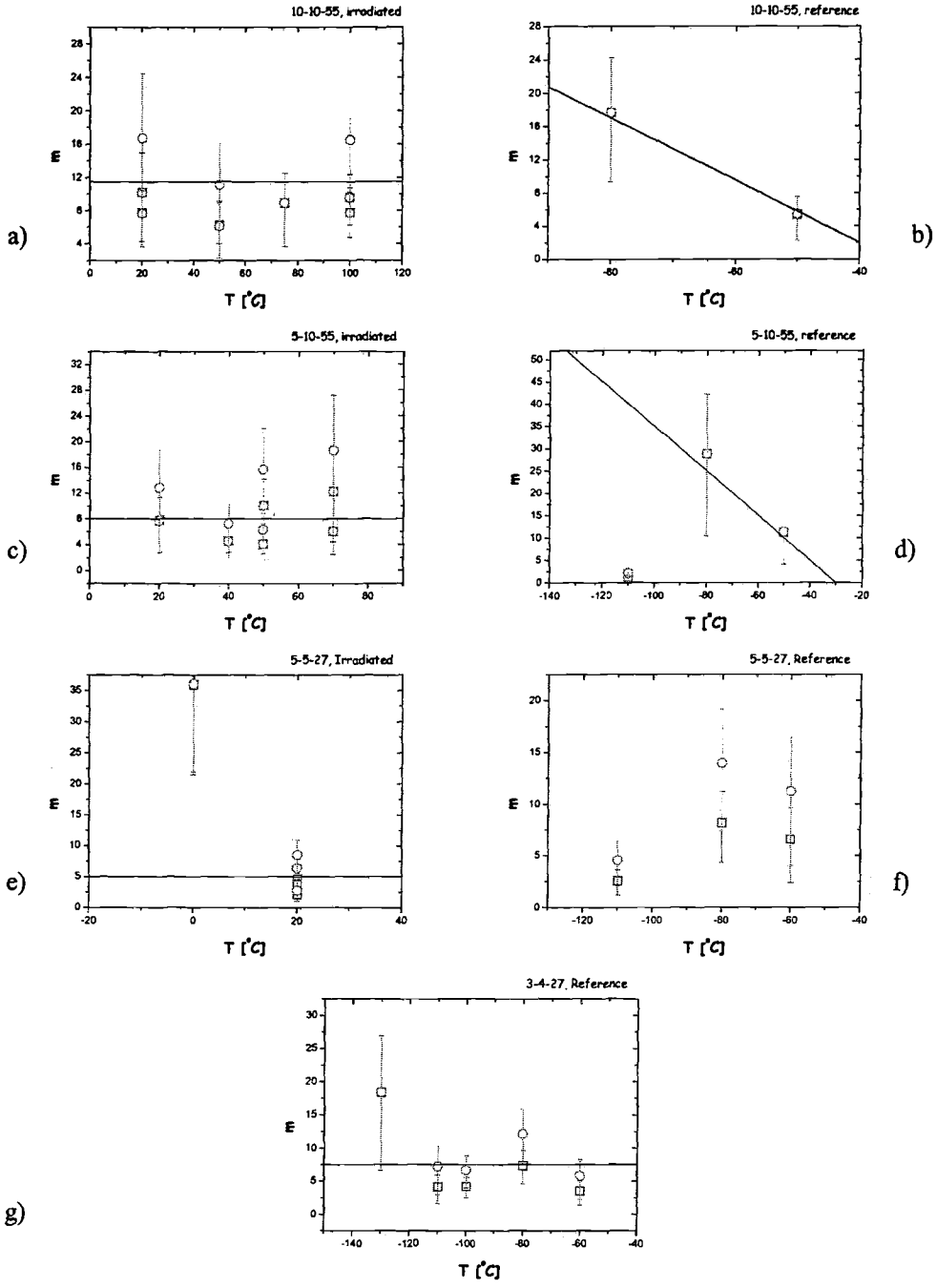

Fig. 9—*Weibull shape parameter for a) irradiated 10-10-55 mm, b) reference 10-10-55 mm, c) irradiated 5-10-55 mm, d) reference, 5-10-55 mm, e) irradiated 5-5-27 mm, f) reference 5-5-27 mm, g) reference 3-4-27 mm. Boxes, $\lambda = 1$, circles, $\lambda = 2$.*

The results of Fig. 9 imply that material fracture toughness scatter, at least to some extent, handicaps the calibration performance with respect to the Weibull shape parameter. On some instances the trends do appear decreasing with temperature before increasing again as one approaches lower shelf, but on some instances the results also display continuously increasing trends as a function of temperature. The fact that some of the calibrations have been made to irradiated and other to reference state materials does not appear to play a part. In addition to the shape parameter being dependent on the closeness of lower and upper shelves, the actual transition temperature dependency appears quite moderate and on some parts even negligible.

The shape and threshold parameters of Fig.10 display a clear, even to some extent linear, temperature dependency. The effects of different process zones are seen quite clear in limiting the range of the Weibull stress as dependent on applied loading.

Comparison between experimental and collocation based numerical cumulative failure properties is given in Fig.11, where the failure probabilities of experimental results have been evaluated according to ASTM E1921-2002. Overall, even though the results for the shape parameter are seen to contain a large scatter, the predictions for the cumulative failure probability are seen to perform quite well and consistently, the median fracture toughness being simulated to a good accuracy.

The analyses were all repeated using normalization fracture toughness based stochastic inference. The results for the Weibull shape and scale parameters are presented in Figs.12 and 13, respectively. Since in the Monte-Carlo based generation of fracture data for the calibration the scatter is treated by the pre-existing Master Curve analysis instead of the fitting routine itself, the trends in the results can be seen without the interfering scatter. The shape parameter is seen to be nearly linearly dependent on temperature as well as the scale and threshold parameters. Selection of process zone is seen to affect the results, this occurring via the corresponding magnitude of the Weibull stress values in larger/smaller process zone, introducing a shift in the calibration results. The threshold parameter is seen to attain very small values for smaller process zones, understood by the same analogy as above.

The dependencies related to K_0 are portrayed in Fig.14. The results for K_0 do contain a similar temperature effect evident during increase of the normalization fracture toughness, but since the results are given as a function of specimen size corrected K_0 they also imply that the results are dependent on specimen size. It is seen that for smaller specimen sizes smaller process zone leads to smaller shape parameter, and vise versa for larger process zones. The specimen ligament dependencies of the scale and threshold parameters are smaller than those of the shape parameter. The dependency on ligament size in Fig.14 is presented by the fact that the specimens are proportional in thickness and width, and the thickness naturally does not explicitly come into play in two-dimensional analyses.

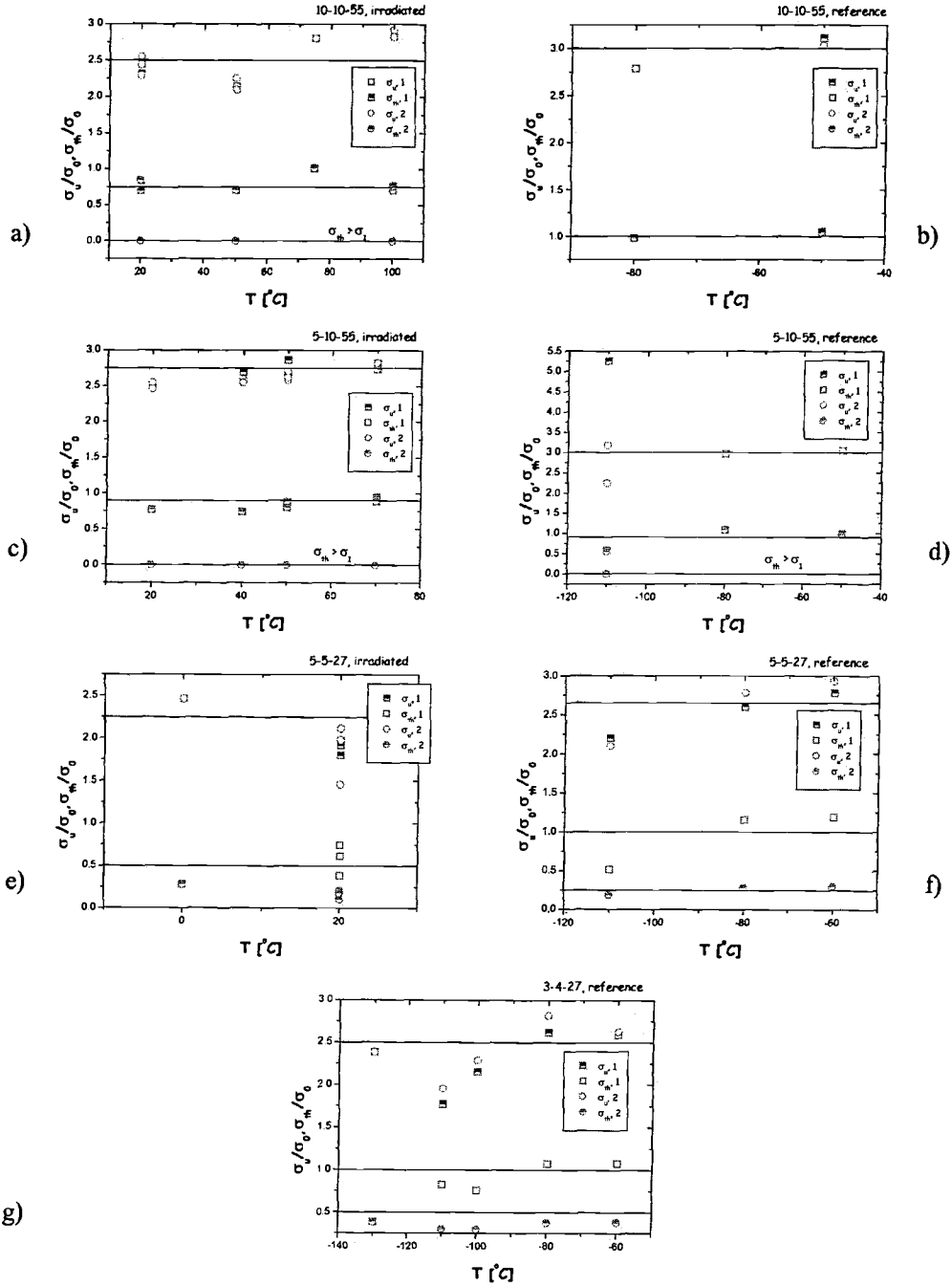

Fig.10—*Weibull scale and threshold parameters for a) irradiated 10-10-55 mm, b) reference 10-10-55 mm, c) irradiated 5-10-55 mm, d) reference, 5-10-55 mm, e) irradiated 5-5-27 mm, f) reference 5-5-27 mm, g) reference 3-4-27 mm.*

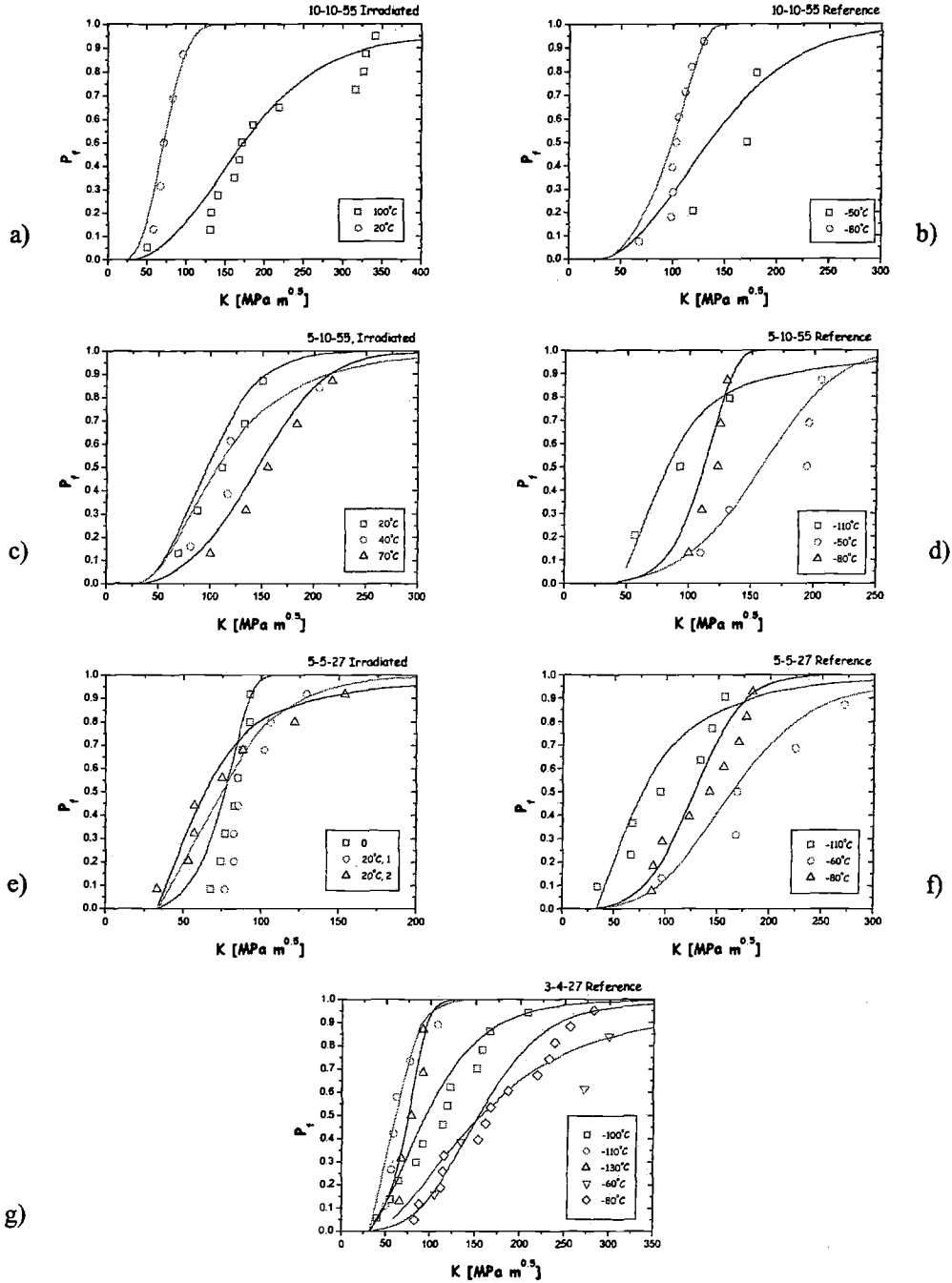

Fig.11—*Comparison of numerical cumulative failure probabilities to those of experiments: a) irradiated 10-10-55 mm, b) reference 10-10-55 mm, c) irradiated 5-10-55 mm, d) reference, 5-10-55 mm, e) irradiated 5-5-27 mm, f) reference 5-5-27 mm, g) reference 3-4-27 mm.*

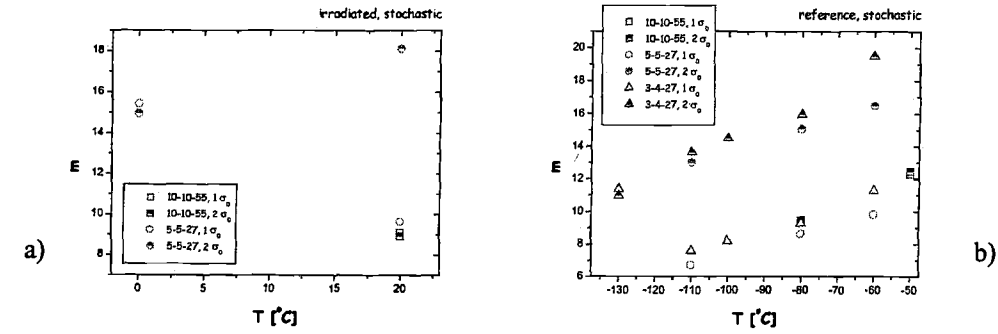

Fig.12—*Weibull shape parameters using stochastic inference for a) irradiated and b) reference materials.*

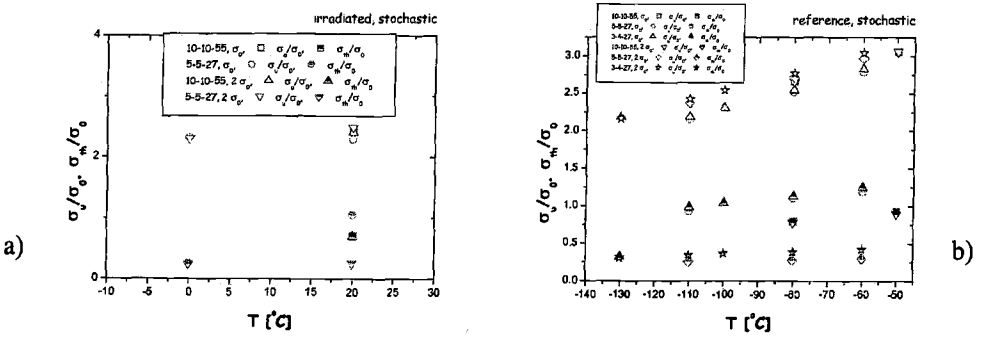

Fig.13—*Weibull scale and threshold parameters using stochastic inference for a) irradiated and b) reference materials.*

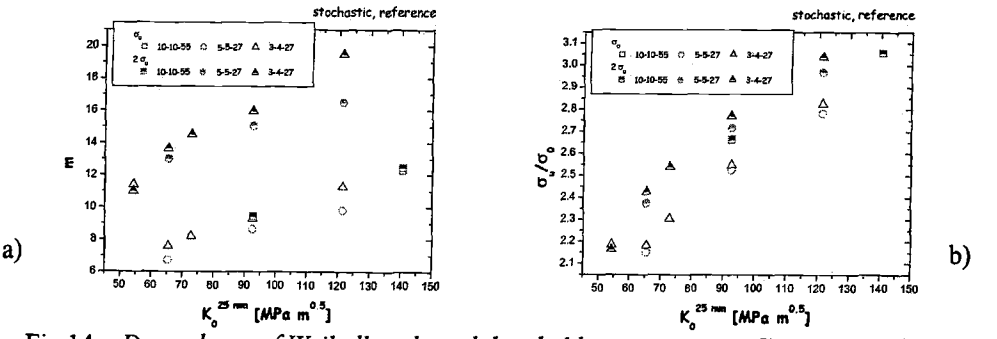

Fig.14—*Dependency of Weibull scale and threshold parameters on K_0 using stochastic inference for a) irradiated and b) reference materials.*

Numerical results - comparison between different calibration methods

Results pertaining the relative performance of the two applied calibration methods are presented in Figs.15 and 16. The differences are quite considerable, especially for the shape parameter, and are naturally reflected then onto the scale parameter, but not to extent of similar magnitude. The results overall display that the stochastic inference based methodology for attaining the parameters performs quite a lot better than the pointwise collocation type of an approach. The trends are clear and continuous, differences between process zone specification being particularly non-existent for 10-10-55 mm size specimens, while for the smaller specimens the steeper local stress-fields produce a greater dependency on definition of fracture process zone. Overall, the scatter is effectively eliminated by using K_0 and the Master Curve scatter expression as a basis of calibration.

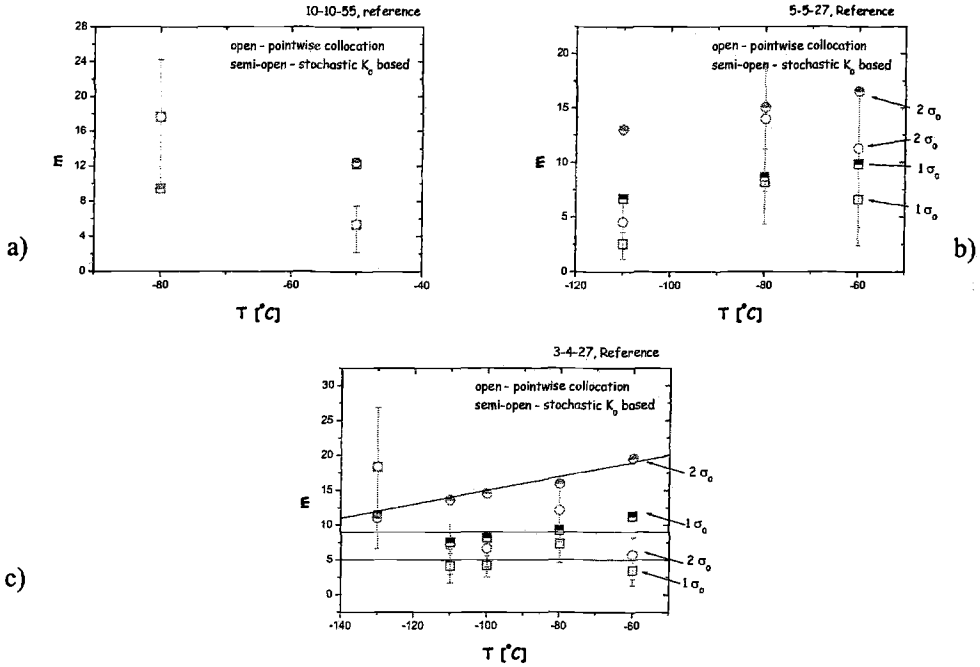

Fig.15—*Comparison of shape parameters attained using different calibration methods. a 10-10-55 mm, b) 5-5-27 mm and c) 3-4-27 mm.*

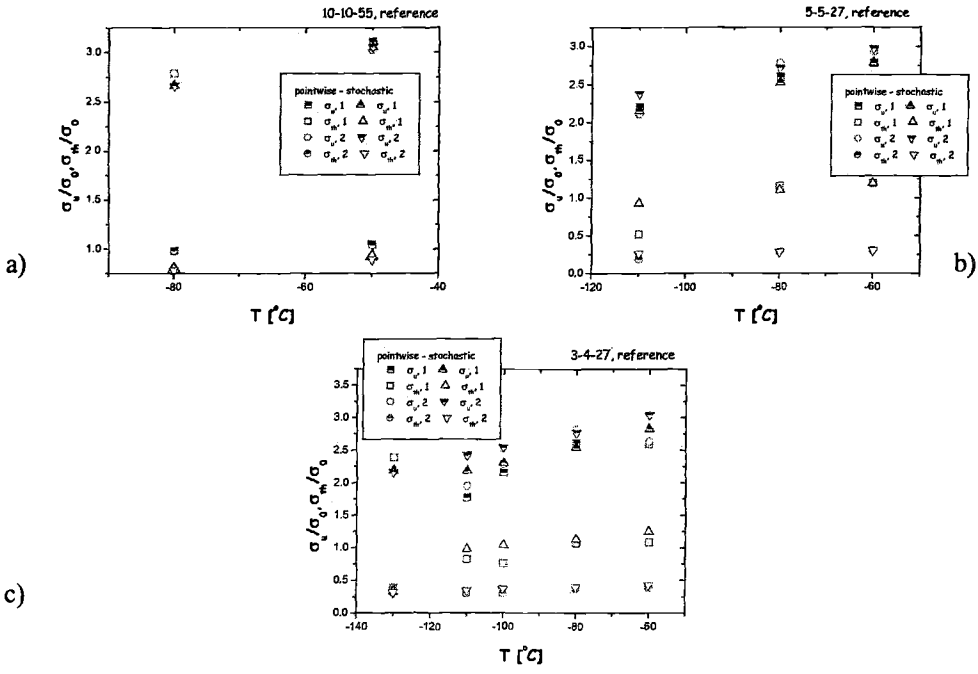

Fig.16—*Comparison of scale and threshold parameters attained using different calibration methods. a) 10-10-55 mm, b) 5-5-27 mm and c) 3-4-27 mm.*

Numerical results - evaluation of parameter transferability

To evaluate the performance of calibration performed specifically at a single temperature against a single specified value for the whole temperature range, the different datasets were averaged with respect to the shape parameter and the cumulative failure probabilities were compared. These analyses were performed on the basis of the stochastically attained values, since they displayed overall a quality notably better than the pointwise ones. As such, for the reference material and for a process zone specified by $\lambda = 1$ a value of $m = 9$ was chosen, while for $\lambda = 2$ $m = 14$ resulted. The irradiated cases were considered as well, but the results did not display anything differentiating from those attained for the reference case.

The results of the transferability evaluation are collected in Fig.17. Since the temperature related trends of all calibrated parameters are nearly linear, the differences are bound to be the greatest at both ends to the temperature spectra. Also, the differences are naturally expected to be higher at the end of the increasing transition where the change of toughness with temperature is higher, and following, the error ought to be greatest at such temperatures. This is also observed from the results, i.e. the largest discrepancies between the temperature specific results and 'generic' results are observed for all cases at temperatures of -50°C and -60°C. At other parts of the transition the results are

surprisingly good, the differences between the specific and generic results being practically negligible, especially for median fracture toughness.

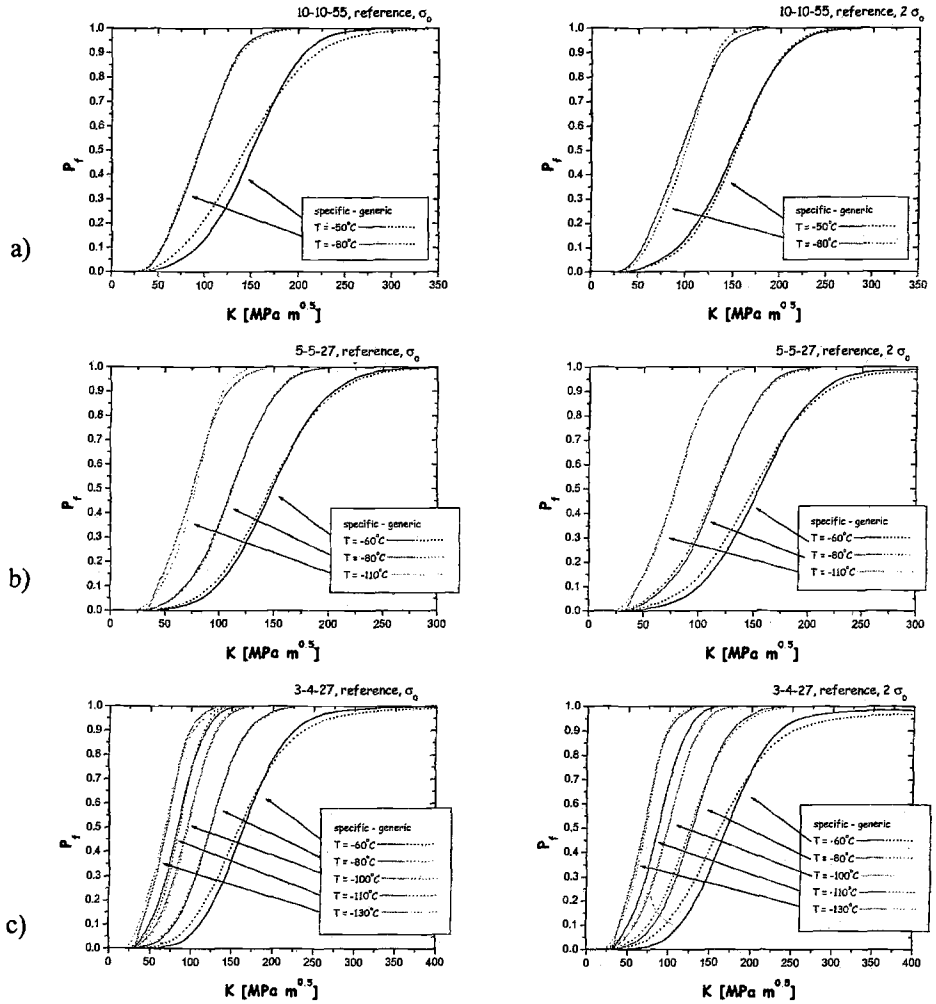

Fig.17—*Comparison of temperature specific and general parameter results for cumulative failure probability for different process zone definitions. a) 10-10-55 mm, b) 5-5-27 mm and c) 3-4-27 mm.*

Numerical results - comparison between Master Curves

A complete view of the results is attained by comparing the results to the corresponding Master Curve analysis results. This is presented for the 5-5-27 mm and 3-4-27 mm specimens in Figs.18 and 19, respectively.

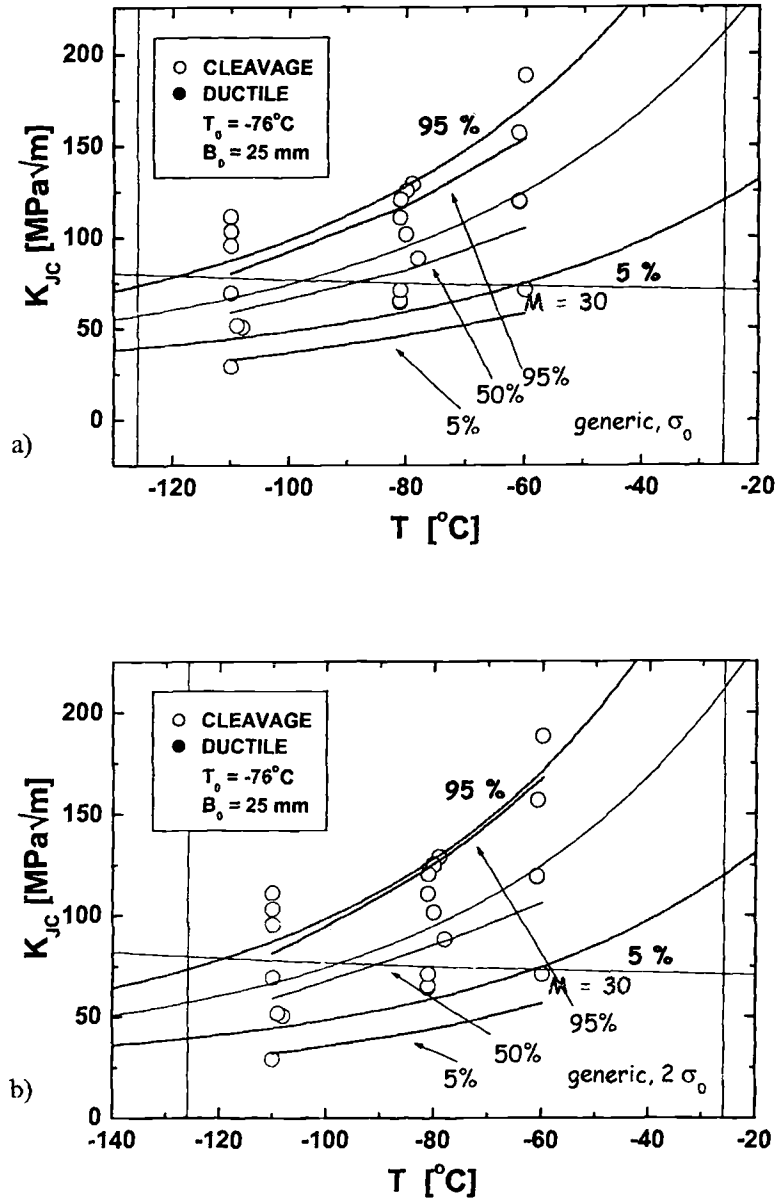

Fig.18—*Comparison of simulated and experimental Master Curves for 5-5-27 mm specimens for a reference state A533B Cl.1 (JRQ). a) process zone* $\lambda = 1$ *and b) process zone* $\lambda = 2$.

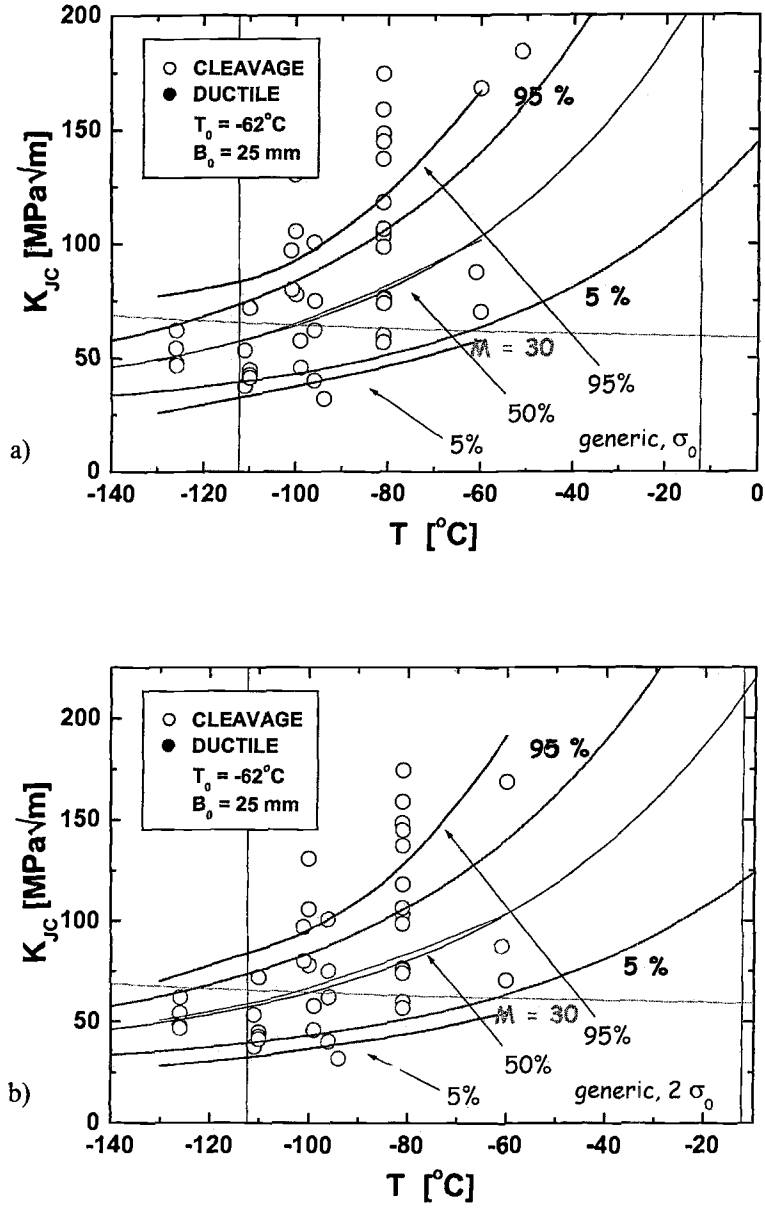

Fig.19—*Comparison of simulated and experimental Master Curves for 3-4-27 mm specimens for a reference state A533B Cl.1 (JRQ). a) process zone* $\lambda = 1$ *and b) process zone* $\lambda = 2$.

The comparability of Master Curve results to simulated results is good in general, but as it was noted in the previous chapter the generality of the calibrated single set of parameters does not quite carry to the upper parts of the modeled transition region, i.e. the simulations and the Master Curve start to deviate as one moves towards higher temperatures. In any case, it does appear that a validity range of approximately 50°C can be attained.

Discussion

The calibration of modified Beremin model parameters on the basis of pointwise fracture toughness data produced results with considerable scatter. Since in many cases the number of different temperatures was considerably higher than typically in such analyses, a synthesis on probable parameter values and their trends could be made, but on the other hand, several cases persisted which would have led to ill-mannered conclusions. Such situations occurred in particular when approaching temperatures lower than the reference temperature for a specific case. This is not to be inferred as a theoretical deficiency of the used local approach model, but rather a consequence of sample scatter, which in such cases were attributed to scarcity in number of data and the values of fracture toughness. In some cases when using the collocation type of an approach this led to severe ill conditioning when the analyses were performed at a low temperature (with respect to T_0) combined to large scatter of fracture toughness and a limited sample size. Overall, it can be stated that reliable analyses can be performed for a typical fracture toughness dataset (which the current data was to establish and present) but calibrations performed for inhomogeneous datasets or at temperatures significantly differing from the reference temperature may produce unexpected problems. This can be interpreted such that the calibration ought to be performed where the fundamentals of weakest link principles apply best. In using the calibrated collocation data specific to temperature, the calibration naturally produces a decent estimate in terms of cumulative failure probability. This is primarily related to the corresponding values for the Weibull scale parameter, which adjusts accordingly to produce a description of the failure probability.

The calibration using stochastic inference produced clearly defined trends with minimal scatter, the remaining inaccuracies primarily related to the numerical modeling process as a whole. The Weibull shape parameter had a consistently decreasing trend with temperature, which obeys its understanding as a damage rate parameter, i.e. as the temperature and the associated fracture toughness decrease, the demands set to initiating a cleavage crack decrease, overcoming the threshold for initiation with a lower value of the shape parameter. The scale parameter can be treated as the normalization Weibull stress, and in a sense, is a ductility property for the sample at a specific temperature. As such, its decrease as a function of temperature was clearly defined even for the collocation type of results. As a scaling parameter it also adjusts the calibration such that independently of m a decent fit for the specific sample in question results. The temperature dependency of this parameter has been observed e.g. in [8]. The calibrated parameters displayed specimen size dependencies, which in the current work were apparent as specimen ligament size was considered. By considering the trends exhibited as a function of normalization fracture toughness it became apparent that for typical process zone definitions smaller specimens produce higher

estimates for the Weibull shape. This is logical if one considers the differences associated with near crack-tip fields in the studied 3PBs, reported in published literature e.g. in [9]. If the states of constraint in the different specimens are inferred by using e.g. Q-trajectories for characterization, it becomes apparent that the smallest of the 3PB specimens have a much more local and steeper stress field than that of the 10-10-55 mm specimen (i.e. a lower state of constraint). As such, the failure process zone becomes smaller necessitating an increase in the damage rate as the normalization toughness is decreasing with temperature. In such terms, there are differences between the predicted measuring capacities of the modified Beremin model and those of experimental findings, even though quantitatively the correspondence of the results may be satisfactory. The same analogy applies to explaining process zone dependencies, except that in some cases a 'too large' process zone can suffocate all trends in general and decrease evaluation performance.

As it was noted the use of stochastically generated fracture data and the temperature dependency of the normalization fracture toughness to produce the parameter calibration was able to produce clearly defined dependencies between the parameters and temperature. This has much to do with the underlying Master Curve method, i.e. the superiority of using the scatter expression in the calibration is explained by the fact that the Master Curve analysis eliminates the uncertainties in analysis of the experimental fracture toughness results, while the large sample generated using a Monte-Carlo method takes care of the rest. With respect to the parameters of the modified Beremin model, this evidently appears to be the most robust and statistically sound approach. The problem relies in analysis of the normalization fracture toughness. The experimental data of the current study barely enabled such an evaluation, and the number of fracture toughness experiments typically performed to specify the reference temperature can be too stringent to enable sound determination.

The evaluations using specific temperature dependent modified Beremin model parameters and those averaged over a range of temperatures enabled quantification of transferability properties as a function of temperature. Except for the far ends in the studied temperature ranges the results were proven quite satisfactory with respect to cumulative failure probability. This was witnessed by the comparison of simulated fracture toughness temperature dependency and scatter to those of the Master Curve method. At the far ends, in particular towards the increasing end of the temperature range, the temperature independence of the parameters of the modified Beremin model started to lose their hold. This was seen as significant differences in failure probabilities erupted and can be expected since any temperature related effects are neglected. The range of application was, however, quite large, and for the 3-4-27 mm and 5-5-27 mm specimens studied in detail one can conclude that approximately 50°C was covered by a single mean valued set of parameters using stochastic inference. Relying on the temperature dependency of the normalization fracture toughness is crucial in this matter for the performance of the modified Beremin model, otherwise the explicit dependencies on temperature and stress need to be modified.

Summary and Conclusions

Master Curve analyses of experimental fracture toughness results were assessed using a modified Beremin model. The model parameters were calibrated using two fundamentally differing methods and transferability of the results evaluated. Simulated fracture toughness transition Curves were compared to the Master Curve ones. The results of the work can be concluded as follows:

- Calibration of modified Beremin model parameters was reliably performed using methodology based on stochastic inference.
- Pointwise collocation type of an approach suffered from intrinsic scatter of the fracture toughness samples. This lead to uncertainties in calibration results, unidentifiable trends and some ill-conditioned estimates highlighted in small sample statistics.
- The Weibull shape and scale parameter temperature dependencies were identified for the current fracture toughness results. In general, both were found nearly linearly dependent on temperature, whereas the temperature dependency can be expected in the used local approach model.
- Process zone definitions and states of near crack tip constraint produce a 'ligament' dependency on calibration results. For typically used process zones lower state of constraint necessitates a higher value for the shape parameter, vice versa for larger process zones. Too large of a process zone can decrease the accuracy of the estimates by adding 'bulk' stress fields to the prediction of failure event, decreasing prediction performance and the requirements set to the scale parameter and/or normalization fracture toughness.
- The reference temperature itself does not have a primary effect on the calibration results, but rather defines suitable surroundings for the temperatures where most reliable results are attained.
- Using the temperature dependency of the normalization fracture toughness and stochastic generation of the calibration sample reliable estimates of failure behavior in the ductile to brittle transition behavior can be attained. In the current study the range of feasible use of a determined parameter set was approximately 50°C, where the results were practically identical to those produced by the Master Curve method.

Acknowledgements

This work is a part of the Structural Integrity Project (STIN) belonging to the Finnish Research Programme on Nuclear Power Plant Safety (FINNUS) and the European Fusion Technology Programme (Association Euratom-Tekes). The work is performed at VTT Industrial Systems and financed by the Ministry of Trade and Industry, the Technical Research Centre of Finland (VTT), the National Technology Agency and the Radiation and Nuclear Safety Authority (STUK).

References

[1] Beremin, F. M., "A Local Criterion for Cleavage Fracture of a Nuclear Pressure Vessel Steel," *Metallurgical Transactions.*, Vol. 14a, 1983, pp. 2277-2287.

[2] WARP3D, "WARP3D-Release 13.9. 3-D Dynamic Nonlinear Fracture Analysis of Solids Using Parallel Computers and Workstations," *University of Illinois Report UILU-ENG-95-2012,* University of Illinois at Urbana-Champaign, Urbana, Illinois, 2000.

[3] WSTRESS, "WSTRESS 2.0, Numerical Computation of Probabilistic Fracture Parameters," *University of Illinois Report UILU-ENG-95-2013,* University of Illinois at Urbana-Champaign, Urbana, Illinois, 1998.

[4] Wallin, K., Planman, T., Valo, M., and Rintamaa, R., "Applicability of Miniature Size Bend Specimens to Determine the Master Curve Reference Temperature T_0," *Engineering Fracture Mechanics*, Vol. 68, 2001, pp. 1265-1296.

[5] Wallin, K., "Validity of Small Specimen Fracture Toughness Estimates Neglecting Constraint Corrections," *Constraint Effects in Fracture Theory and Applications: Second Volume, ASTM STP 1244,* M. Kirk and A. Bakker, Eds., ASTM International, West Conshohocken, PA, 1995, pp. 519-537.

[6] Wallin, K., "Recommendations for the Applications of Fracture Toughness Data for Structural Integrity Assessment," *Proceedings of the Joint IAEA/NEA International Specialists' Meeting on Fracture Mechanics Verification by Large Scale Testing,* C. E. Pugh, B. R. Bass and J. A. Keeney, Eds., Oak Ridge, OECD, NUREG/CP-0131, ORNL/TM-12413 RF, 1993, pp. 465-494.

[7] Auerkari, P., "On the Correlation of Hardness with Tensile and Yield Strength," *VTT Research Reports No. 416,* Technical Research Centre of Finland, Espoo, 1986, pp. 24.

[8] Gao, X., Dodds, R. H., Tregoning, R. L., Joyce, J. A., and Link, R. E., "Weibull Stress Model to Predict Cleavage Fracture in Plates Containing Surface Cracks," *Fatigue and Fracture of Engineering Materials and Structures*, Vol. 22, 1999, pp. 481-493.

[9] Laukkanen, A. "Consistency of Damage Mechanics Modeling of Ductile Material Failure in Reference to Attribute Transferability," 1999, *First MIT Symposium in Computational Fluid and Solid Mechanics*, K. J. Bathe, Ed., Elsevier, 2001, pp. 310-313.

Fumiyoshi Minami [1] and Kazushige Arimochi [2]

Constraint Correction of Fracture Toughness CTOD for Fracture Performance Evaluation of Structural Components

Reference: Minami, F. and Arimochi, K., **"Constraint Correction of Fracture Toughness CTOD for Fracture Performance Evaluation of Structural Components,"** *Predictive Material Modeling: Combining Fundamental Physics Understanding, Computational Methods and Empirically Observed Behavior, ASTM STP 1429*, M. T. Kirk and M. Erickson Natishan, Eds., American Society for Testing and Materials, West Conshohocken, PA, 2003.

Abstract: A correction of CTOD for constraint loss in large-scale yielding conditions is made on the basis of the Weibull stress fracture criterion, that eliminates an excessive conservatism in the conventional fracture assessment and material fracture toughness requirement. A CTOD ratio $\beta = \delta_{3P} / \delta_{WP}$ (< 1) is proposed, where δ_{WP} is the CTOD of a wide plate component and δ_{3P} is an equivalent CTOD of the fracture toughness specimen at which the toughness specimen gives a compatible Weibull stress with the wide plate. The CTOD ratio β is decreased to a large extent after full yielding of the wide plate component, which is more significant for a high yield ratio *YR* and a deep surface crack in the wide plate. The Weibull modulus m exerts a marginal influence on β. A case study is presented on the application of the CTOD ratio β to the fracture performance assessment of full-scale column-to-beam connections subjected to cyclic and dynamic loading.

Keywords: brittle fracture, constraint effect, transferability analysis, fracture toughness, fracture performance, equivalent CTOD, Weibull stress criterion, structural steels

Introduction

Fracture mechanics approaches to the defect assessment, the structural integrity evaluation and the material qualification rely on the stress intensity factor K, crack tip opening displacement (CTOD) and J integral as the mechanical parameters controlling stress fields near the crack tip. It is known, however, that in large-scale yielding (LSY) conditions the actual stress fields do not necessary follow the K- and J-controlled fields and depend significantly on the crack size and geometry of specimens employed. This is due to a loss of plastic constraint around the crack tip. In notched tension panels and bend specimens with

[1] Associate Professor, Department of Manufacturing Science, Graduate School of Engineering, Osaka University, 2-1 Yamada-Oka, Suita, Osaka 565-0871, Japan.
[2] General Manager, Plate & Structural Steel Project Promoting Department, Sumitomo Metal Industries, LTD., 1-8, Fuso-Cho, Amagasaki, Hyogo 660-0891, Japan.

a shallow crack, a marked growth of plastic zone decreases the crack tip constraint to a large extent while the standard fracture toughness specimen with a deep crack maintains a high level of constraint even in the LSY state. Such constraint loss relaxes the near-crack tip stress fields, which leads to an apparently increased fracture toughness K_c, δ_c and J_c at brittle fracture initiation.

In order to characterize the constraint loss effect on the stress fields, the T-stress and Q-parameter were developed in the K- and J-controlled fields, respectively [1-5]. Fracture toughness results for different specimen geometries are scaled with the T-stress and Q-parameter at fracture. Nevertheless, the K-T and J-Q characterizations posed a problem in the fracture assessment; the T-stress and Q-parameter at fracture can not be estimated in advance because they change with the load level as a function of the specimen geometry. A series of fracture tests using different specimen configurations are required for the transferability analysis of test results [6].

On the other hand, Anderson and Dodds [7, 8] have proposed a toughness scaling model (TSM) to correct the fracture toughness for constraint loss in the LSY conditions. This model insists on a similarity between near-tip stress contours in different yielding conditions, and transfers the fracture toughness in large-scale yielding to one under small-scale yielding with equivalent stressed areas ahead of a crack. For simplicity, the TSM does not reflect the variation of stresses within near-tip stress contours and not consider a statistical aspect of cleavage fracture. In order to overcome limitations of the TSM, a modified toughness scaling with the Weibull stress was attempted [9, 10], that requires the attainment of a specified Weibull stress to cause cleavage fracture at the same probability in different specimen geometries.

Those methodologies focus the attention on toughness scaling in small-scale yielding conditions. From a structural design point of view, however, the fracture toughness to be used for the fracture performance evaluation in service conditions should be quantified in conjunction with the constraint condition. This paper addresses the constraint correction of CTOD as a function of the deformation level of structural components. The Weibull stress is used as a medium of the fracture transferability analysis. A parametric study is performed on the CTOD correction ratio β, that includes the effects of the work hardening property, the crack size assumed in components and the Weibull modulus m related to a scatter of the material fracture toughness. As a practical application, the fracture performance of full-scale models of column-to-beam connections subjected to large plastic deformation is analyzed with the CTOD ratio β.

CTOD Toughness Scaling with the Weibull Stress

This paper introduces a CTOD toughness scaling methodology to correct the constraint loss in large-scale yielding conditions. The Weibull stress σ_W is used as a driving force for cleavage fracture of ferritic materials. The Weibull stress σ_W is derived from a statistical characterization of instability of microcracks in the local approach [11, 12], and given by the integration of a near-tip stress σ_{eff} over the fracture process zone V_f in the form

$$\sigma_W = \left[\frac{1}{V_0} \int_{V_f} [\sigma_{eff}]^m \, d V_f \right]^{1/m} \tag{1}$$

where V_0 and m are a reference volume and a material parameter, respectively, and V_f almost corresponds to the plastic zone near the crack tip. The m-value reflects the distribution of microcracks for the material, and generally is in the range 10 to 40 [11, 13-19]. The critical Weibull stress $\sigma_{W,cr}$ at brittle fracture initiation obeys the Weibull distribution with two parameters m and σ_u

$$F(\sigma_{W,cr}) = 1 - exp\left[-\left(\frac{\sigma_{W,cr}}{\sigma_u}\right)^m\right] \tag{2}$$

that is considered as a material property independent of the size and geometry of specimens. This feature enables the fracture transferability analysis among different specimen configurations. In fact, the thickness effect [13, 14], the crack depth effect [15-17] and the specimen type and geometry effects [13, 18, 19] on the cleavage resistance of fracture mechanics specimens were successfully predicted on the basis of the Weibull stress criterion.

Figure 1 illustrates the CTOD toughness scaling between the standard fracture toughness specimen (three-point bend specimen with a deep crack is considered in this study) and a wide plate component with a crack. This paper defines the CTOD ratio β [19] as

$$\beta = \delta_{3P} / \delta_{WP} \tag{3}$$

where δ_{WP} is the wide plate CTOD, and δ_{3P} is an equivalent CTOD at which the fracture toughness specimen gives the same Weibull stress as the wide plate. In structural engineering fields, the CTOD design curve (= relationship between applied strain ε_∞ and δ_{WP}) is conventionally used for the fracture assessment of notched components. Because a direct connection of the material fracture toughness with the CTOD design curve may lead to a very conservative estimation of the fracture performance due to a constraint loss, the CTOD ratio β will pronounce a fair judgement of the incidence of brittle fracture. This paper quantifies the CTOD ratio β as a function of the applied strain ε_∞ of the wide plate, aiming at a reasonable fracture assessment as the:

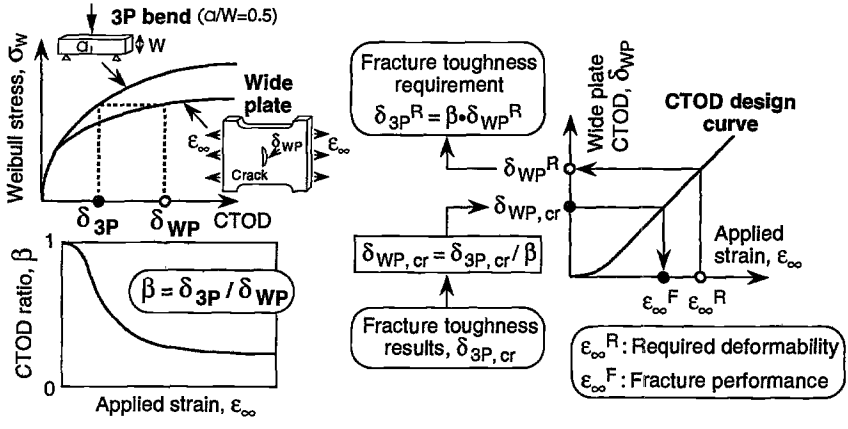

Figure 1 — *CTOD toughness scaling between wide plate component and fracture toughness specimen by way of the Weibull stress.*

- Determination of minimum required fracture toughness $\delta_{3P}{}^{R}$ to meet a design solution $\varepsilon_{\infty}{}^{R}$ of structural components, and the
- Accurate estimation of fracture performance $\varepsilon_{\infty}{}^{F}$ of structural components from fracture toughness test results $\delta_{3P,\,cr}$.

As for the near-tip stress σ_{eff} in Eq 1 to calculate the Weibull stress, an effective stress [14] considering a random spacial distribution of microcracks is employed in this paper. The selection of the reference volume V_0 does not affect the fracture transferability analysis, although the absolute value of the Weibull stress depends on V_0. Furthermore, the Weibull modulus m has no relation with V_0. Hence, a unit volume is adopted as V_0 for convenience [14]. The Weibull stress in this paper is numerically evaluated by the Gaussian quadrature using the isoparametric representation of finite elements [20].

Transferability Analysis of Fracture Mechanics Test Results

Experiments and numerical analysis were conducted to demonstrate the advantage of the Weibull stress criterion for the fracture transferability analysis. Two high-strength structural steels, HT490 and HT950, with different work hardening properties were used. The plate thickness of each steel was 25 mm. Table 1 shows the chemical composition and mechanical properties of these steels. Low and extremely high *YR*s (yield-to-tensile ratios) are noted for HT490 and HT950 steels, respectively. Figure 2 shows the configuration of test specimens employed. Fracture toughness tests were conducted with the compact and three-point bend (3PB) specimens. The compact and deep-notch 3PB specimens with $a/W = 0.5$ (a: notch length, W: specimen width) were of a standard type specified in the British Standard of Fracture Mechanics Toughness Tests - Part 1, Method for Determination of K_{Ic}, Critical CTOD and Critical J Values of Metallic Materials (BS7448-Part 1 : 1991). A shallow notch of $a/W = 0.1$ was also prepared for the bend specimen of HT950 steel. Tension specimens had a double-edge notch (DENT) of $a/W = 0.3$ for both steels, where the specimen width $2W = 100$ mm. The notch tip of each specimen was finished with a fatigue precrack of length 2.0 ~ 2.5 mm. Fracture tests were conducted at -100 °C for both steels in a lower range of the fracture transition.

Test results were given in Figure 3 in terms of a cumulative distribution of the critical CTOD at brittle fracture initiation. The fracture mode of the HT490 steel was almost pure cleavage. By contrast, the HT950 steel exhibited a small amount of the crack growth before

Table 1 — *Chemical composition and mechanical properties of high strength steels used* [1].

	Chemical composition (mass %)										
	C	Si	Mn	P	S	Ni	Cr	Mo	Cu	V	Ceq
HT490	0.17	0.33	1.22	0.012	0.004	0.02	0.03	0.01	-	-	0.40
HT950	0.12	0.19	0.89	0.004	<0.001	2.61	0.58	0.55	0.30	0.05	0.60

	Mechanical properties (Rolling direction)			
	σ_Y (MPa)	σ_T (MPa)	YR=σ_Y/σ_T (%)	ε_T (%)
HT490	356	520	68.3	13.8
HT950	1026	1036	99.1	6.2

[1] Ceq=C+Mn/6+Si/24+Ni/40+Cr/5+Mo/4+V/14, σ_Y : Yield stress, σ_T : Tensile strength, ε_T : Uniform elongation

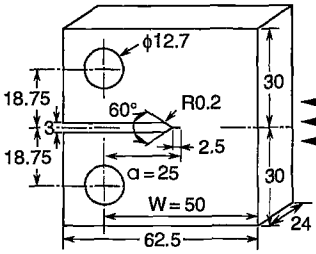

(a-1) *Compact specimen for HT490 steel*

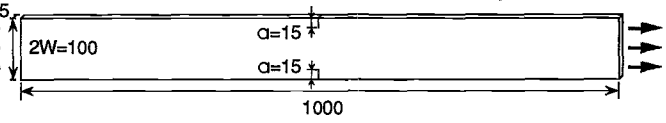

(a-2) *Double-edge notched tension specimen for HT490 steel*

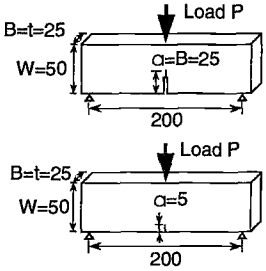

(b-1) *Three-point bend specimens for HT950 steel*

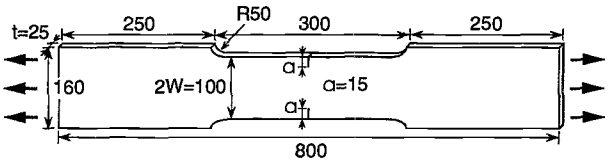

(b-2) *Double-edge notched tension specimen for HT950 steel*

Figure 2 — *Fracture mechanics specimens used in experiments.*

brittle fracture. The CTOD values were calculated according to BS7448-Part 1 for the compact and deep-notch 3PB specimens and by the Dugdale model [21] for the DENT specimen. One for the shallow-notch 3PB specimen was evaluated by a method proposed by Wang and Gordon [22], that is based on the area under the load versus CMOD record (CMOD: crack mouth opening displacement). A marked effect of constraint loss is observed in the DENT and shallow-notch 3PB test results; apparently higher critical CTOD values than those of the compact and deep-notch 3PB specimens (standard fracture toughness specimens).

Using the CTOD test results of the standard fracture toughness specimens, the critical CTODs of the DENT and shallow-notch 3PB specimens were predicted on the basis of the Weibull stress criterion; independence of $\sigma_{W,cr}$ on the specimen geometry. The near-crack tip stress fields were addressed by a three-dimensional FEM with the FE-code, ABAQUS ver. 5.8. The minimum element size at the crack tip was $0.01 \times 0.01 \times 0.05$ mm, that was common to all specimen geometries. An iteration procedure [14] was employed for the determination of the Weibull modulus m. The m-values determined from the standard toughness specimens were 17 and 20 for HT490 and HT950 steels, respectively. With these m-values, the evolution of the Weibull stress with the CTOD was calculated for the DENT and shallow-notch 3PB specimens. According to the Weibull stress criterion, the critical CTODs of these specimens are estimated as the CTOD level at which these specimens exhibit the same Weibull stress as the standard toughness specimen at any cumulative frequency. The estimated results are drawn with a solid line in Figure 3. A good agreement is observed between the prediction and experimental data. One may argue the reliability of

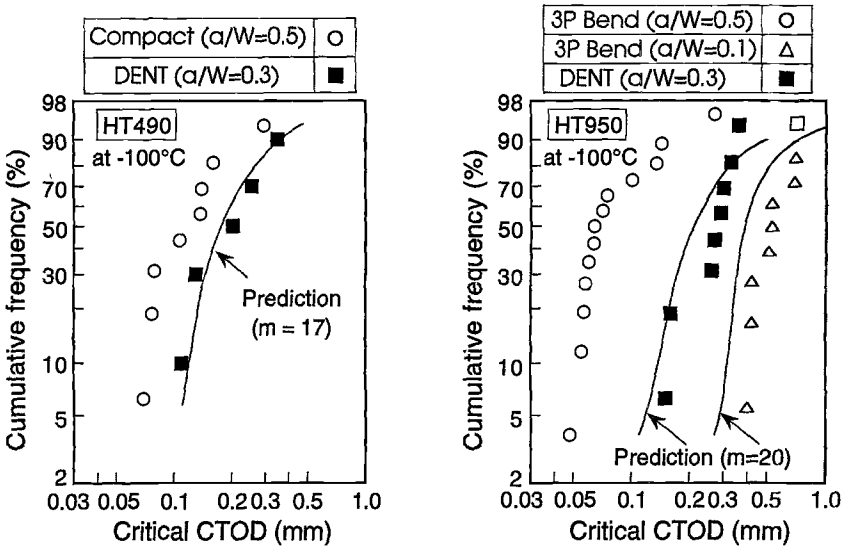

(a) *HT490 steel* (b) *HT950 steel*

Figure 3 — *CTOD test results and estimation of critical CTODs of tension and shallow-notch bend specimens based on the Weibull stress criterion.*

the m-value determined by the iteration procedure; non-uniqueness in small-scale yielding conditions [9]. In order to address this subject, a bias was introduced in the range $0.5\hat{m} \le m \le 1.5\hat{m}$, where $\hat{m}$ is the Weibull modulus determined by the iteration method ($\hat{m}$=17, 20 in this case). The numerical investigation with $m = \hat{m} \pm 0.5\hat{m}$ indicated that such bias hardly affected the prediction of the critical CTOD. It is demonstrated [18, 19] that the Weibull stress criterion is also applicable to the fracture transferability analysis of welded joints, where the Weibull stress is calculated over a specific region responsible for fracture initiation.

CTOD Toughness Scaling Diagram

Parametric FE-Analysis

As an engineering application of the Weibull stress criterion, a framework begins in this study to construct the CTOD toughness scaling diagram that corrects the constraint loss in the fracture assessment in large-scale yielding conditions.

A tension wide plate with a surface crack and a standard three-point bend (3PB) specimen with a deep notch of $a/W = 0.5$ are considered (Figure 4). For these specimens, a parametric FE-analysis was conducted to investigate the controlling factors of the CTOD ratio β. Table 2 gives basic variables employed in the FE-analysis, which include the work hardening property of the material, the size of a surface crack in the wide plate, and the Weibull modulus m.

Work hardening property: The work hardening properties affect the near-crack tip stress fields to a large extent. In this study, the YR ($=\sigma_Y/\sigma_T$) was varied in the range 0.60 to 0.95

with a given yield stress σ_Y= 583 MPa. For comparison, the *YR* was also varied with a given tensile strength σ_T= 711 MPa. The uniform elongation ε_T (nominal strain at attainment of σ_T) was kept constant, ε_T= 11.4 %. These σ_Y, σ_T and ε_T values were referred to the mechanical properties of a high strength pipeline steel of grade 550 MPa [23].

Crack size: The Weibull stress of the wide plate component depends on the crack tip constraint as well as the process zone size of the surface crack. The former controls the intensity of the stress fields, and the latter has a volume effect on the Weibull stress. In the FE-analysis, the length *2a* and depth *b* of a surface crack were varied in the range $16 \le 2a \le 100$ mm and $1 \le b \le 6$ mm.

Weibull modulus m: The Weibull stress includes the shape parameter *m* in the form of Eq 1. The *m*-value ranged from 15 to 40 in the numerical analysis, where $m = 20$ was used as a standard value.

The parametric FE-analysis was conducted with the FE-code, JOH-NIKE3D. The minimum element size at the crack tip was 0.067 × 0.067 × 0.5 mm, that was common to the 3PB specimen and wide plate component. The crack tip opening displacement of the

Table 2 — *Basic variables in parametric FE-analysis of CTOD ratio β.*

		Mechanical properties				Crack size			Weibull modulus m
		σ_Y (MPa)	σ_T (MPa)	YR $=\sigma_Y/\sigma_T$ (%)	ε_T (%)	Length 2a (mm)	Depth b (mm)	$2\bar{a}$ (mm)	
Effect of YR	σ_T: const.	427~675	711	60~95	11.4	40	6	13.8	20
	σ_Y: const.	583	614~972	60~95	11.4	40	6	13.8	20
Effect of crack size	Crack length effect	583	711	82	11.4	100	6	18.2	20
						40		13.8	
						30		12.0	
						16		7.4	
	Crack depth effect					40	1	2.5	20
							3	7.4	
							6	13.8	
Effect of Weibull modulus		583	711	82	11.4	100	6	18.2	15~40
						40		13.8	

σ_Y: Yield stress, σ_T: Tensile strength, ε_T: Uniform elongation, $2\bar{a}$: Equivalent through-thickness crack size

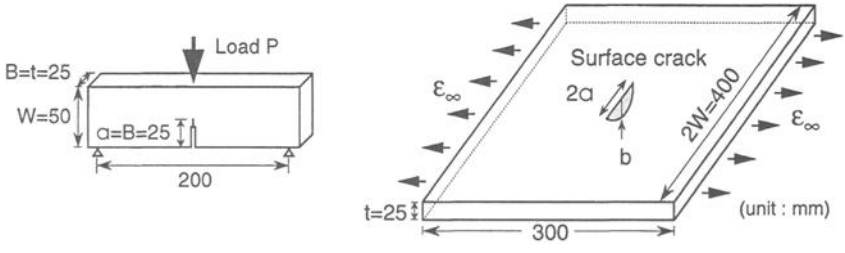

Figure 4 — *Three-point bend specimen with a deep notch and wide plate with a surface crack used for parametric study of CTOD ratio β.*

surface crack was evaluated at the center of the crack, and calculated by a tangential method [24]. The CTOD of the 3PB specimen was calculated according to the procedure in BS 7448-Part 1: 1991.

Effect of Work Hardening Properties

The yield-to-tensile ratio YR ($=\sigma_Y/\sigma_T$) had a large influence on the CTOD ratio β. Figure 5 shows the change in β with YR for the surface crack of $2a = 40$ mm and $b = 6$ mm, where the results are given as a function of the non-dimensional overall strain $\varepsilon_\infty/\varepsilon_Y$ of the wide plate (ε_Y: yield strain). In the Weibull stress calculation, a standard m-value of 20 was used. As described earlier on, the CTOD ratio β corrects the CTOD δ_{WP} for constraint loss in the wide plate so as to give the identical Weibull stress with the 3PB specimen. Namely, the wide plate CTOD of $\beta\delta_{WP}$ is equivalent to the 3PB CTOD δ_{3P} in terms of the Weibull stress. It can be seen that the CTOD ratio β is considerably reduced after full yielding of the wide plate, which is more significant for a high YR. This is mainly related to a crack tip opening behavior of the wide plate, as described below. The change in YR under a constant σ_Y condition gave substantially the same results as in a constant σ_T condition. Similar dependence of β on YR was observed for other crack size and m-values.

Figure 6 shows a comparison of the maximum crack opening stresses $(\sigma_{yy})_{max}$ near the crack tip for the 3PB specimen and the wide plate with a surface crack of $2a = 40$ mm and $b = 6$ mm, where the results for $YR = 0.60$ and 0.82 are shown. Due to a constraint loss, the wide plate component gives a lower near-crack tip stress $(\sigma_{yy})_{max}$ than the 3PB specimen at a large CTOD level. The increase in YR increases the near-tip stress $(\sigma_{yy})_{max}$ under a constant σ_T condition (Figure 6(a)), but decreases $(\sigma_{yy})_{max}$ under a constant σ_Y condition (Figure 6(b)), respectively. Nevertheless, the difference between the Weibull stresses for the 3PB specimen and wide plate is nearly independent of the yield ratio YR.

The work hardening properties also affect the crack opening behavior. Figure 7 shows the effect of YR on the CTOD δ_{WP} of the wide plate with a surface crack of $2a = 40$ mm and $b = 6$ mm. A definite dependence of δ_{WP} on YR is observed; increasing δ_{WP} with increasing YR in both σ_T-constant and σ_Y-constant conditions. This is related to a localization of plastic strain: Low work hardening (= high YR) yields a marked strain localization in the crack tip region, which produces a large CTOD δ_{WP} [25-28].

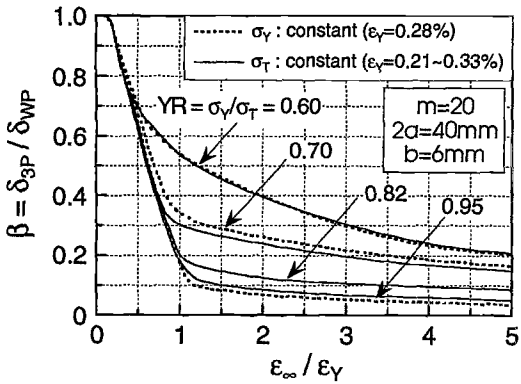

Figure 5 — *Effect of yield ratio YR on CTOD ratio β.*

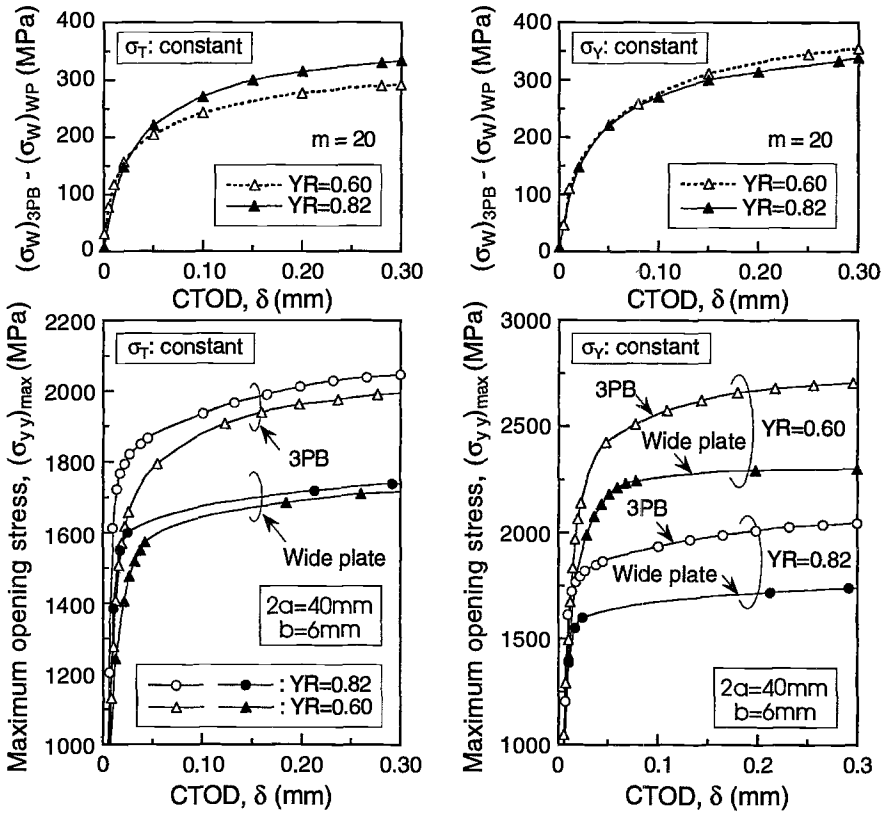

(a) σ_T *-constant condition* (b) σ_Y *-constant condition*

Figure 6 — *Effect of yield ratio YR on evolution of near-crack tip maximum stress and Weibull stress for 3PB specimen and wide plate.*

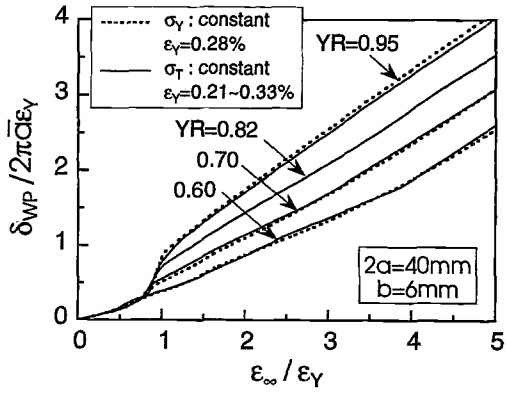

Figure 7 — *CTOD - overall strain ε_∞ relationship for wide plate with different yield ratios.*

It can be understood from Figures 6 and 7 that the dependence of the CTOD ratio β on YR is mainly dominated by the crack opening behavior of the wide plate. Remember that the difference between critical CTODs of the DENT and deep-notch 3PB specimens for HT950 steel with $YR = 0.99$ was apparently larger than one for HT490 steel with $YR = 0.68$ (Figure 3). This is consistent with the numerical results in Figure 5, small β for a high YR.

Effect of Crack Size in Wide Plate Component

(a) Effect of Crack Length —The size of a surface crack exerts an influence on the Weibull stress of the wide plate in two aspects; the near-crack tip stress σ_{eff} and the volume V_f of the fracture process zone. In addition, the crack size governs directly the crack opening behavior of the wide plate. The CTOD ratio β is determined by the combined effects of these properties.

Figure 8 shows the effect of surface crack length $2a$ in the wide plate on the CTOD ratio β for $YR = 0.82$. The crack depth b is fixed at 6 mm. The CTOD ratio β seems to be not so sensitive to the crack length. With different YR, the results were almost similar. The little effect of the crack length $2a$ on β on is discussed below.

Figure 9 shows the evolution of the near-crack tip maximum stress $(\sigma_{yy})_{max}$ for different

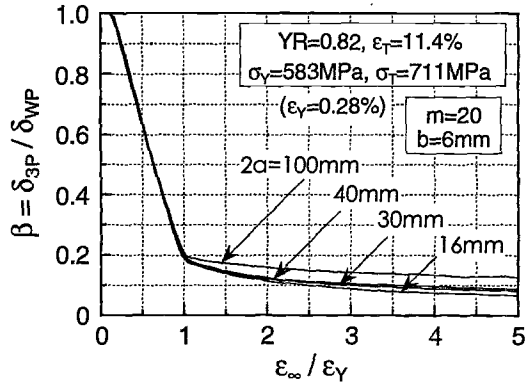

Figure 8 — *Effect of surface crack length 2a in wide plate on CTOD ratio β.*

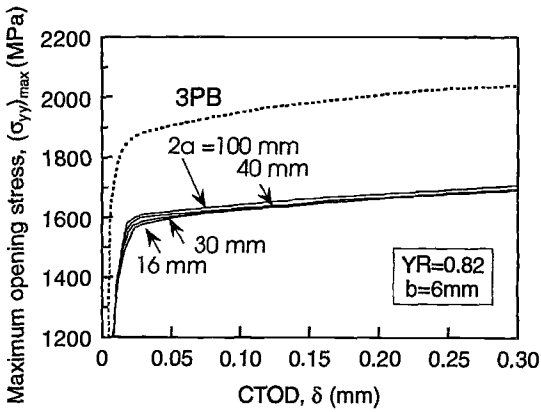

Figure 9 — *Effect of crack length on near-crack tip maximum opening stress of wide plate.*

crack length in the wide plate. The $(\sigma_{yy})_{max}$ for the 3PB specimen is also presented as a reference. It is found that the near-tip stress $(\sigma_{yy})_{max}$ is not affected very much by the crack length $2a$. However, the Weibull stress for the wide plate is increased with increasing the crack length $2a$, as shown in Figure 10. This is due to a volume effect of the surface crack. Provided that the near-tip stress $(\sigma_{yy})_{max}$ is independent of the crack length and uniform along the crack front, the Weibull stresses for crack length $2a_1$ and $2a_2$ are related in the form

$$\sigma_{W(2a_1)} = (a_1/a_2)^{1/m} \cdot \sigma_{W(2a_2)} \tag{4}$$

The Weibull stress in Figure 10 is slightly larger than one estimated by Eq 4 for $a_1 > a_2$. Such volume effect may lead to a larger β for a longer crack. On the other hand, a long surface crack produces a large CTOD δ_{WP}, as shown in Figure 11. This contributes to decreasing β for a long crack. Namely, the crack length $2a$ brings about two opposite influences on the CTOD ratio β. The positive and negative effects are almost evenly balanced, so that the CTOD ratio β seems to be insensitive to the crack length $2a$ in the range of calculations in this paper ($16 \le 2a \le 100$ mm, $b = 6$ mm). As an example, the CTOD

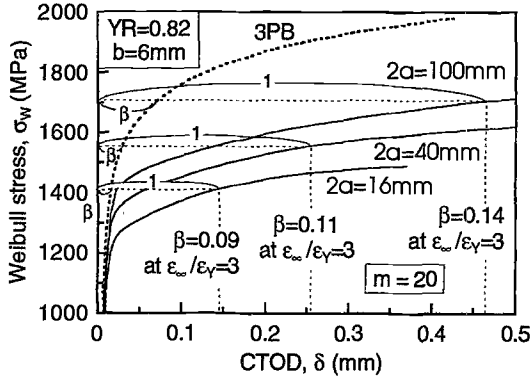

Figure 10 — *Effect of surface crack length 2a on evolution of the Weibull stress for wide plate.*

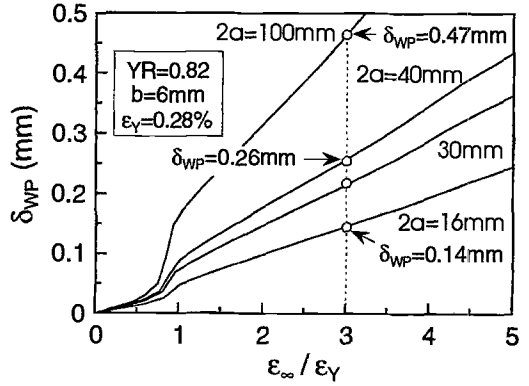

Figure 11 — *CTOD - overall strain ε_∞ relationship for wide plate as a function of surface crack length 2a.*

ratio β at the overall strain of $\varepsilon_\infty / \varepsilon_Y = 3$ is given in Figure 10.

For a small m-value, say $m \leq 15$, the crack length effect on β is slightly enlarged. This is discussed later (Figure 16).

(b) Effect of Crack Depth — The effect of surface crack depth b on the CTOD ratio β is investigated in Figure 12 under a condition of $YR = 0.82$ and $2a = 40$ mm. The CTOD ratio β is decreased with increasing the crack depth. This tendency is determined by a competition between the crack depth effects on the stress fields and on the crack opening behavior, as discussed below.

Figure 13 shows the effect of crack depth b on the evolution of the near-tip maximum stress $(\sigma_{yy})_{max}$ for the wide plate. A deep crack elevates the near-tip stress $(\sigma_{yy})_{max}$ definitely, as informed by the study of Newman and Raju [29]. This may lead to a larger β for a deeper crack, but the results in Figure 12 are opposite. It should be remembered at the same time that the wide plate CTOD δ_{WP} is enlarged with increasing the crack depth, as exhibited in

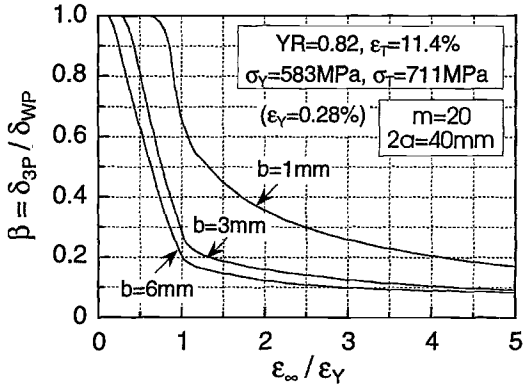

Figure 12 — *Effect of surface crack depth b in wide plate on CTOD ratio β.*

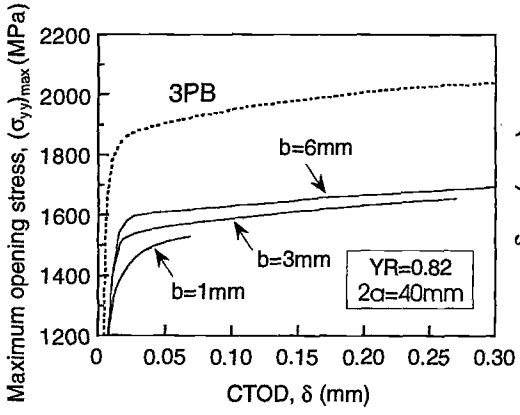

Figure 13 — *Effect of surface crack depth b on near-crack tip maximum opening stress of wide plate.*

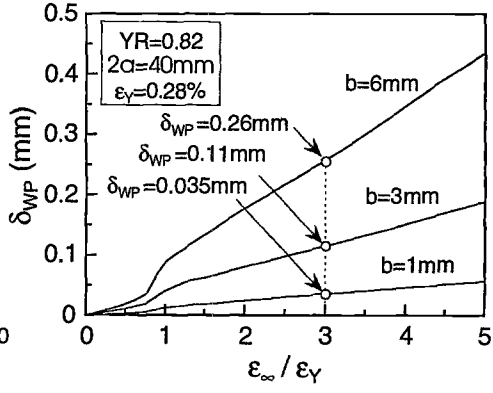

Figure 14 — *CTOD - overall strain ε_∞ relationship for wide plate as a function of surface crack depth b.*

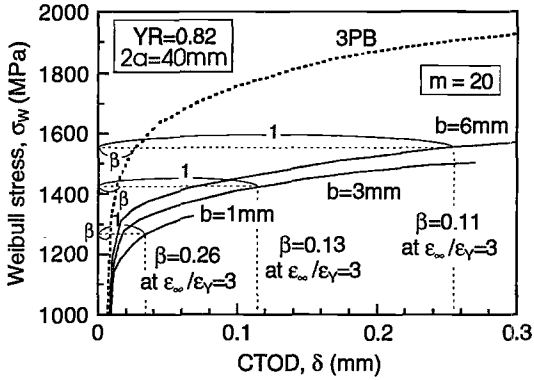

Figure 15 — *Effect of surface crack depth b on evolution of the Weibull stress for wide plate.*

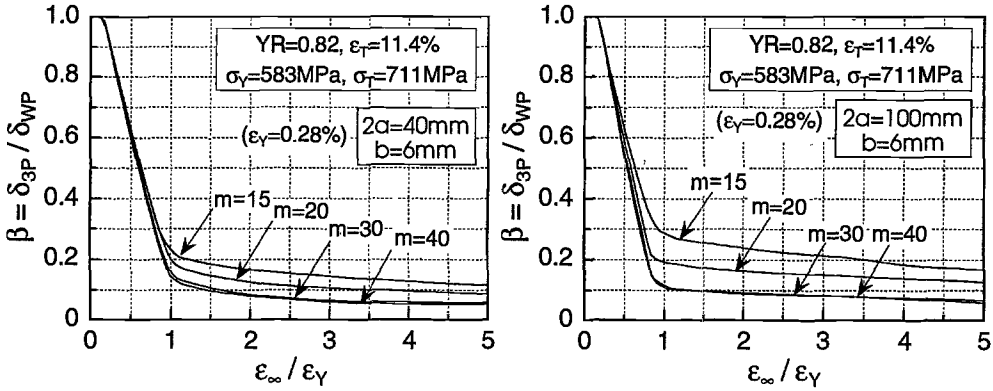

(a) Crack length $2a$ = 40 mm (b) Crack length $2a$ = 100 mm

Figure 16 — *Effect of Weibull modulus m on CTOD ratio β.*

Figure 14, which decreases the CTOD ratio β. A smaller β for a deeper crack, that is shown in Figure 12, suggests that the crack depth exerts a larger effect on the CTOD δ_{WP} than on the near-tip stress intensity of the wide plate. Figure 15 shows the evolution of the Weibull stress for different crack depth, where the CTOD ratio β at the overall strain of $\varepsilon_\infty / \varepsilon_Y = 3$ is calculated as an example. The deep crack results in a small CTOD ratio β. At a large deformation level, however, the crack depth effect on β seems to be weakened (Figure 12).

Effect of Weibull Modulus

The influence of the Weibull modulus m is exhibited in Figure 16 for the surface crack of $2a$ = 40 and 100 mm. The CTOD ratio β is slightly increased with decreasing m. This is explained as follows: The Weibull stress σ_W consists of a stress term and a volume term. The stress term is expressed as $(\sigma_{eff}{}^m)^{1/m}$ and almost independent of m. On the other hand, the volume term includes the shape parameter m in the form $V_f{}^{1/m}$. The latter becomes active, when a large process zone V_f is combined with a small m. However, the effect of shape parameter m on β is marginal for $m \geq 20$.

Fracture Assessment of Steel Structures Using CTOD Ratio β

The CTOD ratio β proposed in this paper has been implemented in the fracture assessment guideline, Method for Assessing Brittle Fracture in Steel Weldments Subjected to Large Cyclic and Dynamic Strain (WES-TR 2808 : 2000) published by the Japan Welding Engineering Society. In WES-TR 2808, a practical application of β is included in the fracture performance assessment of large-scale components. In the following, the results are described briefly.

A series of large-scale fracture tests of column-to-beam connections have been carried out [30]. Materials used were high strength structural steels (rolled H-shape steels) of 490 MPa strength class. A typical example of the specimen configuration is shown in Figure 17. Various details of connection were applied, that included the type of weld access hole, different curvature of the access hole, with/without expansion of the beam flange at the beam end, and the extension of diaphragm from the column etc. Cyclic loading was applied to the specimens at 0 °C. Some tests were conducted in a dynamic loading condition; the strain rate at the beam end was in the order of 10 %/s. A total of 30 large-scale specimens were tested. During the tests, the history of the load and strain (macro-strain) at the beam end was recorded. It was observed that brittle fracture was originated at the bottom of the access hole or from the weld bond near weld start/end of the column-to-beam joints.

The fracture assessment guideline, WES-TR 2808, is characterized by two key ides; 1) a temperature shift concept for fracture toughness evaluation in cyclic and dynamic loading conditions and 2) the CTOD ratio β to correct a constraint loss in structural components subjected to large plastic deformation.

The cyclic loading causes a prestrain effect, which elevates the flow stress and deteriorates the fracture toughness of materials. The dynamic loading also brings about a similar effect, although the mechanism is different from the prestrain effect. The temperature shift concept (Figure 18) enables the fracture toughness evaluation in cyclic and dynamic conditions from the static toughness results without prestrain. Authors' recent study [31] has derived the relationship between the temperature shift ΔT_{PD} and the flow stress elevation $\Delta\sigma_f^{PD}$

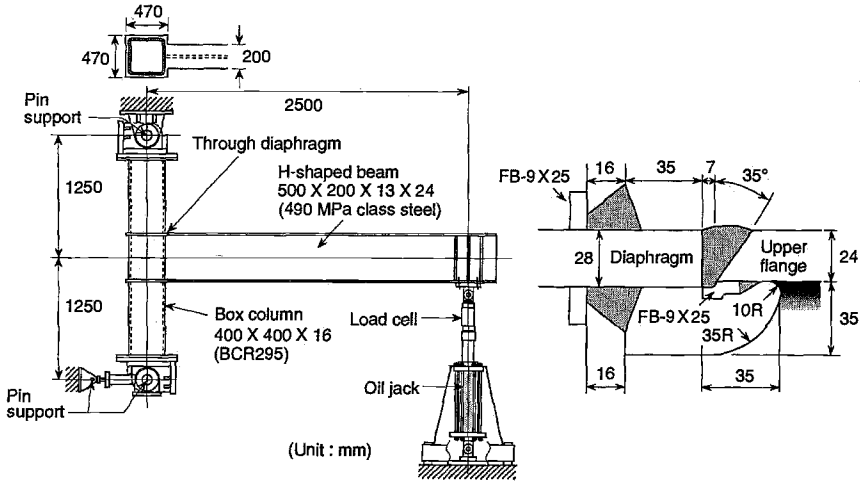

Figure 17 — *Large-scale test specimen of column-to-beam connection.*

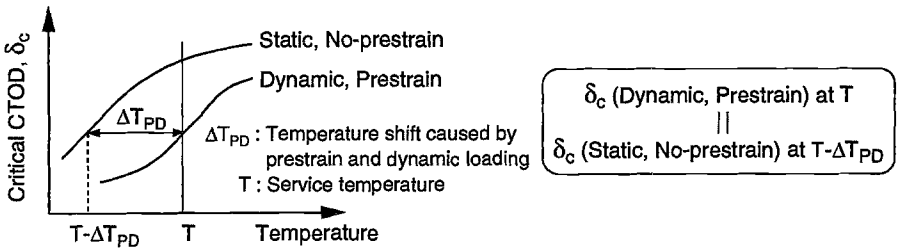

Figure 18 — *Temperature shift concept for fracture toughness evaluation in cyclic and dynamic loading conditions.*

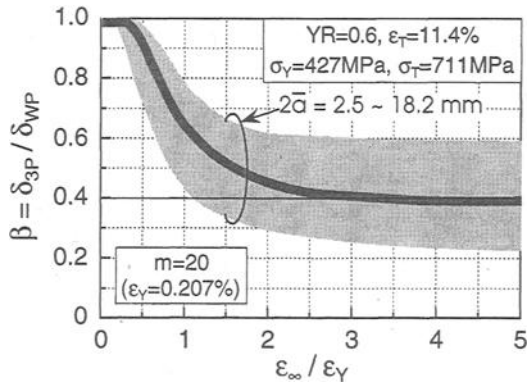

Figure 19 — *CTOD ratio β for fracture assessment of column-to-beam connections.*

from the analysis based on the Weibull stress criterion. In WES-TR 2808, the ΔT_{PD} - $\Delta\sigma_f^{PD}$ relationship is more simplified as

$$\Delta T_{PD}\,(°C) = \begin{cases} 0.4\,\Delta\sigma_f^{PD} & : 0 \le \Delta\sigma_f^{PD} \le 100\ (\text{MPa}) \\ 40 & : 100 \le \Delta\sigma_f^{PD} \le 300\ (\text{MPa}) \end{cases}, \quad \Delta\sigma_f^{PD} = (\Delta\sigma_Y^{PD} + \Delta\sigma_T^{PD})/2 \qquad (5)$$

for structural steels of 400 to 490 MPa strength class, where $\Delta\sigma_Y^{PD}$ and $\Delta\sigma_T^{PD}$ are the increase in the yield stress and tensile strength, respectively, by prestrain and dynamic loading at the service temperature T. An empirical formula for estimating $\Delta\sigma_Y^{PD}$ and $\Delta\sigma_T^{PD}$ as a function of the prestrain and strain rate is given in WES-TR 2808.

The yield-to-tensile ratio, YR, of the high strength structural steels tested was nearly 0.7 in as-rolled conditions. Nevertheless, the CTOD ratio β for the column-to-beam connections was evaluated with $YR = 0.6$ considering a reduction of YR due to the Bauschinger effect during cyclic loading. Figure 19 shows the change in β with the applied strain ε_∞ for the wide plate component. The $m = 20$ was employed in the light of m-values of recent Japanese steels [16, 18, 19]. The size of a surface crack was varied in the range of $2\bar{a} = 2.5$ to 18.2 mm, where $\bar{a}$ is a half of the equivalent through-thickness crack size. Since the column-to-beam connections failed at large strains exceeding $3\varepsilon_Y$ (ε_Y: yield strain) in the fracture region, the CTOD ratio of $\beta = 0.4$ was applied to all specimens as a mean value.

The CTOD δ of the column-to-beam connections was evaluated with the CTOD design curve in WES 2805-1997 (Method for Assessment for Flaws in Fusion Welded Joints with Respect to Brittle Fracture and Fatigue Crack Growth)

$$\frac{\delta}{\varepsilon_Y \bar{a}} = \begin{cases} (\pi/2)(e_{local}/\varepsilon_Y)^2 & (e_{local} < \varepsilon_Y) \\ (\pi/2)\left[9\,(e_{local}/\varepsilon_Y) - 5\right] & (e_{local} \geq \varepsilon_Y) \end{cases} \tag{6}$$

where e_{local} is a local strain in the crack region. The local strain e_{local} is converted from a macro-strain e_{macro} using a strain concentration factor K_ε

$$e_{macro} = e_{local} / K_\varepsilon \tag{7}$$

Typical values of K_ε for the column-to-beam connections are given in WES-TR 2808.

The fracture strain (macro-strain) at the beam end of the column-to-beam connections was estimated as follows:

1) Evaluation of the material fracture toughness $\delta_{3P,\,cr}$ at a temperature of $T - \Delta T_{PD}$ in the static condition without prestrain (T : test temperature = 0 °C). The temperature shift ΔT_{PD} was calculated with Eq 5, where the prestrain accumulated up to the fracture load cycle and the strain rate in the fracture load cycle were used for the estimation of $\Delta\sigma_f^{PD}$.
2) Correction of the fracture toughness for constraint loss in the column-to-beam connections using the CTOD ratio β. Namely, $\delta_{WP,\,cr} = \delta_{3P,\,cr} / \beta$, where $\beta = 0.4$ was applied to all specimens.

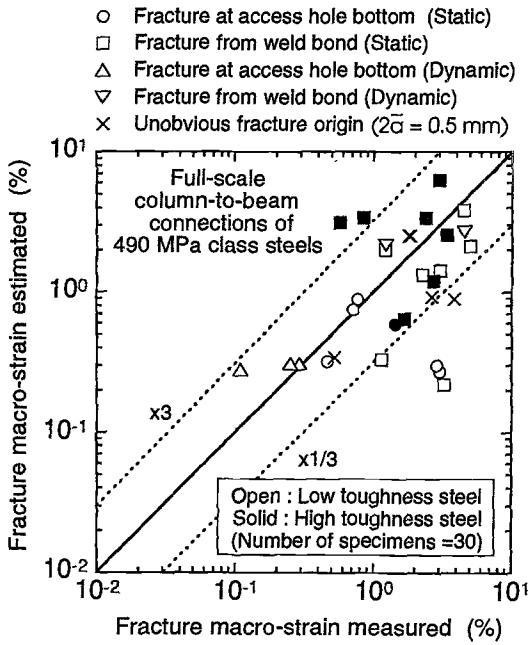

Figure 20 — *Comparison between fracture macro-strains of column-to-beam connections estimated with CTOD ratio β and measured in experiments.*

3) Evaluation of a local strain at fracture, $e_{local,F}$, with the CTOD design curve (Eq 6). The corrected fracture toughness $\delta_{WP,cr}$ was substituted for δ in Eq 6. The equivalent crack size $\bar{a}$ was calculated from a pre-existing flaw or a ductile crack nucleated during cyclic loading.

4) Determination of the fracture macro-strain at the beam end, as $e_{macro,F} = e_{local,F} / K_e$.

Figure 20 compares the fracture macro-strain estimated with one measured in the tests. The estimated results are almost consistent with the experimental data.

It is expected that the CTOD ratio β proposed in this paper will exclude an excessive conservatism in the conventional fracture assessment and material fracture toughness requirement. Further work is in progress to make a monograph for a simple evaluation of β for engineering applications.

Conclusions

This paper focused on the CTOD toughness scaling between structural components and fracture toughness specimens. A CTOD ratio $\beta = \delta_{3P} / \delta_{WP}$ (< 1) was introduced on the basis of the Weibull stress criterion, where δ_{WP} is the CTOD of a wide plate component and δ_{3P} is an equivalent CTOD of the standard fracture toughness specimen at which the toughness specimen presents the same Weibull stress as the wide plate. The CTOD ratio β corrects the CTOD of structural components for constraint loss in large-scale yielding conditions. The CTOD toughness scaling with β was conducted as a function of the applied strain of the wide plate component and the CTOD δ_{3P} of the toughness specimen. Major factors controlling β were the work hardening property of materials and the depth of a surface crack in the component. A low β was found for a low work hardening (= high yield-to-tensile ratio *YR*) and a deep surface crack. The length of a surface crack and the Weibull modulus *m* did not exert a large influence on β within the range of calculations in this paper.

Acknowledgments

This study was performed as a sub-task of the LDF Committee in the Japan Welding Engineering Society, that aims at establishing the procedure for fracture performance assessment of steel structures subjected to large cyclic and dynamic strain. The authors acknowledge useful discussions from engineering viewpoints and cordial supports by the Committee members. The fracture test of a structural steel of 950 MPa strength class steel was conducted in Nippon Steel Corporation as an investigation of fracture properties of high strength steels for future applications. The courteous permission to analyze the test data is also highly acknowledged.

References

[1] Larsson, S. G. and Carlsson, A. J., "Influence of Non-Singular Stress Terms and Specimen Geometry on Small-Scale Yielding at Crack Tips in Elastic-Plastic Materials," *Journal of the Mechanics and Physics of Solids*, Vol. 21, 1973, pp. 263-277.

[2] Betegón, C. and Hancock, J. W., "Two-Parameter Characterization of Elastic-Plastic Crack-Tip Fields," *Journal of Applied Mechanics*, Vol. 58, 1991, pp. 104-110.

[3] Wang, Y.-Y., "Two-Parameter Characterization of Elastic-Plastic Crack-Tip Fields and Applications to Cleavage Fracture," Ph. D. Thesis, Department of Mechanical

Engineering, Massachusetts Institute of Technology, 1991.

[4] O'Dowd, N. P. and Shih, C. F., "Family of Crack-Tip Fields Characterization by a Triaxiality Parameter - I. Structure of Fields," *Journal of the Mechanics and Physics of Solids*, Vol. 39, 1991, pp. 989-1015.

[5] O'Dowd, N. P. and Shih, C. F., "Family of Crack-Tip Fields Characterization by a Triaxiality Parameter - II. Fracture Applications," *Journal of the Mechanics and Physics of Solids*, Vol. 40, 1992, pp. 939-963.

[6] Dodds, Jr. R. H., "Constraint Effects on Fracture Initiation Loads in HSST Wide-Plate Tests," *NUREG/CR-6259, UILU-ENG-94-2009, ORNL/TM-12796*, University of Illinois, 1994.

[7] Anderson, T. L. and Dodds, Jr. R. H., "Specimen Size Requirements for Fracture Toughness Testing in the Transition Region," *Journal of Testing and Evaluation*, Vol. 19, 1991, pp. 123-134.

[8] Dodds, Jr. R. H., Anderson, T. L. and Kirk, M. T., "A Framework to Correct *a/W* Ratio Effects on Elastic-Plastic Fracture Toughness," *International Journal of Fracture*, Vol. 48, 1991, pp. 1-22.

[9] Gao, X., Ruggieri, C. and Dodds, Jr. R. H., "Calibration of Weibull Stress Parameters using Fracture Toughness Data," *International Journal of Fracture*, Vol. 92, 1998, pp. 175-200.

[10] Miyata, T., Tagawa, T. and Hongkai, Y., "A Proposal for Specimen Size Requirements in Toughness Qualification with the Weibull Stress Criterion, " *Journal of Testing and Evaluation*, Vol. 28, 2000, pp. 62-65.

[11] Beremin, F. M., "A Local Criterion for Cleavage Fracture of a Nuclear Pressure Vessel Steel," *Metallurgical Transactions A*, Vol. 14A, 1983, pp. 2277-2287.

[12] Mudry, F., "A Local Approach to Cleavage Fracture," *Nuclear Engineering and Design*, Vol. 105, 1987, pp. 65-76.

[13] Bakker, A. and Koers, R. W. J., "Prediction of Cleavage Fracture Events in the Brittle-Ductile Transition Region of a Ferritic Steel," *ESIS/EGF 9*, Mechanical Engineering Publications, 1991, pp. 613-632.

[14] Minami, F., Brückner-Foit, A., Munz, D. and Trolldenier, B., "Estimation Procedure for the Weibull Parameter Used in the Local Approach," *International Journal of Fracture*, Vol. 54, 1992, pp. 197-210.

[15] Di Fant, M. and Mudry, F., "Interpretation of Shallow Crack Fracture Mechanics Tests with a Local Approach to Fracture," *Proceedings of International Conference on Shallow Crack Fracture Mechanics, Toughness Tests and Applications*, TWI, Abington, Cambridge, Paper 27, 1992.

[16] Ruggieri, C., Minami, F., Toyoda, M., Hagiwara, Y. and Inoue, T., "Local Approach to Notch Depth Dependence of CTOD Results," *Journal of the Society of Naval Architects of Japan*, Vol. 171, 1992, pp. 493-499.

[17] Moinereau, D. and Frund, J. M. et al., "Local Approach to Fracture Applied to Reactor Pressure Vessel: Synthesis of a Cooperative Programme Between EDF, CEA, Framatome and AEA," *Journal de Physique IV, Colloque C6, supplément au Journal de Physique III,* Vol. 6, 1996, pp. C6/243-C6/257.

[18] Minami, F. and Toyoda, M., "Evaluation of Fracture Toughness Results and Transferability to Fracture Assessment of Welded Joints," *Fatigue and Fracture Mechanics*, Vol. 29, *ASTM STP 1332*, American Society for Testing and Materials, 1999, pp. 315-340.

[19] Minami, F., Katou, T., Nakamura, T. and Arimochi, K., "Equivalent CTOD Concept for Fracture Toughness Requirement of Materials for Steel Structures," *Proceedings of 18th International Conference on Offshore Mechanics and Arctic Engineering (OMAE)*, St. John's, Newfoundland, 1999, OMAE99/MAT-2130, pp. 1-12.

[20] Ruggieri, C., Minami, F. and Toyoda. M., "Effect of Strength Mismatch on Crack Tip Stress Fields of HAZ-Notched Joints Subjected to Bending and Tension," *Journal of the Society of Naval Architects of Japan*, Vol. 174, 1993, pp. 543-549.

[21] Bilby, B. A., Cottrell, A. H., Smith, E. and Swinden, K. H., "The Spread of Plastic Yield from a Notch," *Proceedings of the Royal Society of London*, Vol. A272, 1963, pp. 304-314.

[22] Wang, Y.-Y. and Gordon, J. R., "The Limits of Applicability of *J* and CTOD Estimation Procedures for Shallow-Cracked SENB Specimens," *Proceedings of International Conference on Shallow Crack Fracture Mechanics, Toughness Tests and Applications*, TWI, Abington, Cambridge, Paper 28, 1992.

[23] Minami, F., Ohata, M., Toyoda, M., Tanaka, T., Arimochi, K., Glover, A. G. and North, T. H., "The Effect of Weld Metal Yield Strength on the Fracture Behavior of Girth Welds in Grade 550 Pipe," *Pipeline Technology*, Vol. 1, 1995, pp. 441-461.

[24] Harrison, J. D., "The State-of-the-Art in Crack Tip Opening Displacement (CTOD) Testing and Analysis, Part 1 - Background and Testing Methods," *Metal Construction*, Vol. 12, 1980, pp. 415-422.

[25] Tracey, D. M., "Finite Element Solutions for Crack-Tip Behavior in Small-Scale Yielding," *Transactions of the ASME, Journal of Engineering Materials and Technology*, Vol. 98, 1976, pp. 146-151.

[26] McMeeking, R. M., "Finite Deformation Analysis of Crack-Tip Opening in Elastic-Plastic Materials and Implications for Fracture," *Journal of the Mechanics and Physics of Solids*, Vol. 25, 1977, pp. 357-381.

[27] Rice, J. R. and Sorensen, E. P., "Continuing Crack-Tip Deformation and Fracture for Plane-Strain Crack Growth in Elastic-Plastic Solids," *Journal of the Mechanics and Physics of Solids*, Vol. 26, 1978, pp. 163-186.

[28] Sorensen, E. P., "A Numerical Investigation of Plane Strain Stable Crack Growth Under Small-Scale Yielding Conditions," *Elastic-Plastic Fracture, ASTM STP 668*, American Society for Testing and Materials, 1979, pp. 151-174.

[29] Newman Jr., J. C. and Raju, I. S., "Stress Intensity Factor Equations for Cracks in Three-Dimensional Finite Bodies Subjected to Tension and Bending Loads," *NASA Technical Memorandum 85793,* 1984.

[30] Morita, K., "Fracture of Column-to-Beam Joints, " *Proceedings of Seminar on Brittle Fracture Incidence in Steel Framed Structures and Fracture Toughness Properties of Structural Steels*, Tokyo, The Japan Welding Engineering Society, JWES-IS-9901, 1999, pp. 33-42 (in Japanese).

[31] Minami, F. and Arimochi, K., "Evaluation of Prestraining and Dynamic Loading Effects on the Fracture Toughness of Structural Steels by the Local Approach," *Transactions of the ASME, Journal of Pressure Vessel Technology*, Vol. 123, 2001, pp. 362-372.

Marjorie E. Natishan,[1] *Matthew Wagenhofer,*[2] *and Stan T. Rosinski*[3]

A Physics-Based Predictive Model for Fracture Toughness Behavior

Reference: Natishan, M. E., Wagenhofer, M., and Rosinski, S. T., **"A Physics-Based Predictive Model for Fracture Toughness Behavior,"** *Predictive Material Modeling: Combining Fundamental Physics Understanding, Computational Methods, and Empirically Observed Behavior, ASTM STP 1429,* M. T. Kirk and M. Erickson Natishan, Eds., ASTM International, Philadelphia, PA 2003.

Abstract: Using the Zerilli-Armstrong (ZA) constitutive model for BCC materials and a combined strength-strain model of fracture, a physics model suitable for predicting the fracture toughness transition behavior of ferritic steels has been developed. The model predicts an exponential dependence of the plastic work on temperature and thus is comparable to the exponential dependence of plastic work predicted by Wallin et al. for the Master Curve. Exploring the limits of applicability of the ZA equation used as the basis for this model provides the information required to firmly establish the limits of material condition applicability of the Master Curve. Calculations based on limited data provide validation of the proposed model. The models ability to predict shifts in transition temperature with irradiation and its application to RP vessel integrity assessment will also be discussed.

Keywords: Cleavage fracture; Steels; Transition temperature; Dislocation mechanics; Characteristic distance

Introduction

The goal of most any model development program is confident prediction of material behavior over a wide range of material and load conditions. If the model is well understood and accurately reflects the mechanisms controlling material behavior then the limits of applicability are well defined. It is also desirable that the input parameters be readily obtained.

Two approaches to model development have been defined; one that looks to understand and define material behavior at a very basic level (the so-called *Physics or Local Approach*) and one that seeks to use trends in experimental data to predict material behavior (the so-called *Empirical Approach*). The Physics Approach seeks to derive mathematical expressions of material behavior from an understanding of the basic physical phenomena controlling the behavior to be predicted. Often, assumptions are made that many properties (strength, ductility, and toughness) are interrelated through

[1] President, Phoenix Engineering Associates, Inc., Davidsonville, MD 21035.
[2] Graduate Research Assistant, Mechanical Engineering Department, University of Maryland, College Park, MD 20742.
[3] Program Manager, Electric Power Research Institute, Charlotte, NC.

their dependence on only a few, basic phenomena, such as dislocation motion. The Empirical Approach makes no such assumptions, but instead, depends on statistical analysis of data against test conditions to identify and derive mathematical expressions for trends exhibited by the material.

Each of these types of models can have an underpinning in a physical understanding of the mechanical deformation and fracture process and each requires some level of empirical calibration. The differences lie in the approach. The Physics models look to tie all global properties to a basic, physical, phenomena that can be mathematically described with aknowledge of microstructural parameters that control all material behavior in some way. In the Empirical Approach, it is often assumed that properties are controlled by some combination of physical phenomena that are not necessarily related. Problems arise in each due to the methodology and assumptions made. The Physics Approach models tend to require input of parameters that are often difficult to obtain; those requiring high resolution, detailed microscopy. Therefore, the models often need recalibration each time a microstructural feature is changed. It is often difficult to translate the local parameters to the global properties. And often, we cannot predict the scatter in the data. The Empirical Approach also has its limitations. Typically model parameters are back-calculated from experimental data. This requires that every condition of interest be tested so as to determine these calibration factors. This requires testing of all new material conditions of interest to bound the data, resulting in a model that is not really predictive at all! Considering all effects independently can result in very complicated models with many calibration factors and the need to measure data on the material and service condition of interest is burdensome.

The objective of this study is to develop a relatively simple, predictive model of material fracture toughness transition behavior that combines the best of both model approaches. More specifically, our goal was to define the temperature and strain rate dependence of the fracture toughness. The general approach taken in developing this sort of model was to combine an appropriate constitutive model describing the basic physical phenomena controlling fracture resistance with mathematical descriptions of the failure criteria (cleavage). We started with the assumption that the temperature and strain rate dependence of plastic behavior is controlled by the temperature and strain rate dependence of dislocation motion within the material. This assumption only holds for properties within the temperature and strain rate region for which the mechanism of plasticity is dominated by dislocation motion.

The temperature region of interest in the current study is the lower transition region of the fracture toughness transition curve. In this region the fracture mode is predominantly cleavage with little or no gross plastic deformation prior to cleavage fracture. The Master Curve method (ASTM 1921-97) for identifying the fracture toughness transition temperature for ferritic steels defines this temperature as that at which the fracture toughness is 100 MPa$\sqrt{m}$. This value occurs just above the lower shelf region and thus is well within the temperature region for which plasticity is expected to be dislocation-dominated.

Temperature Dependence

Natishan and Kirk [1] utilized dislocation mechanics to provide the physical basis for the existence of a universal curve shape for the fracture toughness transition behavior

of ferritic steels. They suggested that the shape of the toughness versus temperature curve for BCC metals, such as ferritic steel, is governed by the Peierls-Nabarro stress describing the effects of lattice atoms on dislocation motion. This stress is, therefore, a function of the lattice spacing. Work conducted by Zerilli and Armstrong showed that as a result of the favorable comparison between the spacing of the lattice atoms and the magnitude of thermally induced lattice atom vibrations, the lattice presents itself as the only temperature dependent obstacle to dislocation motion in BCC metals [2]. All other obstacles, including precipitates, solute atoms and other dislocations, have inter-obstacle spacings that are orders of magnitude larger than the thermally induced atomic vibration amplitudes, making their effect on dislocation motion independent of temperature. This behavior is well described by the constitutive flow stress equations proposed by Zerilli and Armstrong [2] for materials of various crystal structures. The equation proposed for BCC materials is given by:

$$\sigma_{ZA} = c_0 + B_0 e^{-\beta T} + K\varepsilon^n \tag{1a}$$

where

$$\beta = \beta_0 - \beta_1 \ln \dot{\varepsilon} \tag{1b}$$

and

$$c_0 = \sigma_G + kd^{-1/2}. \tag{1c}$$

Strain is denoted by ε, $\dot{\varepsilon}$ is the strain rate, T is the absolute temperature, d is the average grain diameter and σ_G is the contribution to the flow stress from solutes, precipitates, and the initial dislocation density. The values k, β_0, β_1, B_0, K and n are constants specific to a material. In the case of most BCC metals, the ZA temperature AND strain rate dependence of the flow stress is contained entirely in the yield stress and is due to Peierls-Nabarro stress interactions. As such, the thermal constants for all ferritic steels should be statistically similar to those of pure iron, leading to a uniform transition region curve shape. Natishan et al. [3] showed that the temperature dependence of the yield strength of a wide range of ferritic steels is well represented by the thermal terms of the ZA equation using ARMCO iron values for β_0, β_1, and B_0, Figure 1. This helps validate the proposed origin of a single toughness transition curve shape.

Fracture Toughness Model

Recognizing the potential of combining dislocation mechanics with the Master Curve Method [ASTM E1921], Natishan and Kirk [1] proposed a predictive, dislocation mechanics based description of the plastic work term used by Wallin et al.[4] to describe the temperature dependence of fracture toughness. Similar to Wallins proposed Master Curve Approach their approach assumed that the temperature dependence of the plastic work per unit area of crack surface created controls the temperature dependence of the fracture toughness. They represented this plastic work term as:

$$w_p = \int_0^{\varepsilon_c} \sigma_{flow} d\varepsilon \cdot \ell \tag{2}$$

where the integrand is a measure of the strain energy density calculated from a uniaxial tension test and ℓ is the length scale over which the strain energy density is applicable The flow stress was taken as Eqn. (1).

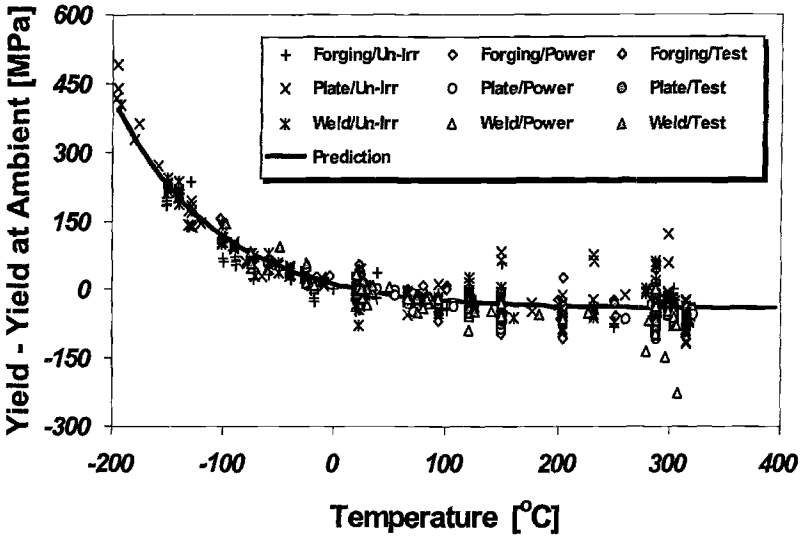

Fig. 1 — *Yield stress versus temperature for a variety of ferritic steels in various irradiation enbrittled conditions.*

The incremental theory of plasticity provides justification for describing the plastic work with a constitutive relationship, such as the ZA equation, that is based on a uniaxial tension test. If the material is assumed to be isotropic then the von Mises criteria can be used to define its yield surface. It can then be shown [5] that the increment of plastic work per unit volume defined in terms of the stress and incremental plastic strain tensors

$$dW_p = \sigma_{ij} d\varepsilon_{ij}^p \tag{3}$$

is equivalent to that defined in terms of the effective stress and incremental effective strain

$$dW_p = \bar{\sigma} d\bar{\varepsilon} . \tag{4}$$

In order for Eqn. (4) to be useful, a relationship between the effective stress and effective strain must be defined. Generally, this is done by correlating the following simple relation,

$$d\bar{\sigma} = H_p(\bar{\sigma}) d\bar{\varepsilon} \tag{5}$$

to the results of a uniaxial tension test. The plastic modulus, $H_p(\bar{\sigma})$, is defined as the slope of the uniaxial stress-plastic strain curve at the current effective stress value. In the current work, however, Eqns. (1) are used to represent the effective stress-effective strain relationship. By so doing, Natishan and Kirk's [1] approach to a physically based model

is preserved while at the same time it is justified for use in a multiaxial stress state application such as plane strain fracture.

With the constitutive stress-strain relationship taken as Eqn. (1,) the other parts of Eqn. (2), specifically the limit of integration and the length scale, can be examined in detail. Definition of these components first requires an understanding of the mechanisms involved in transition region cleavage fracture. Many researchers [6-9] have studied these mechanisms and attempted to describe them quantitatively to various degrees. In this instance we choose to examine the 1968 work of Tetelman, Wilshaw and Rau (TWR) [10]. They state that three events must occur for cleavage fracture to take place in mild steel. The first event is microcrack nucleation. This is well documented to be the result of dislocation motion and accumulation at long-range obstacles such as grain boundaries and second phase particles. The stress fields of these immobile dislocations are additive and the net effect is a stress concentration that reaches the level of the cleavage stress of the second phase particle in question. The second event is the propagation of the microcrack through the grain in which it was nucleated. The third event is the subsequent propagation of the microcrack through boundaries surrounding the nucleating grain. TWR then state that the first two events occur more easily in materials such as mild steel where brittle grain boundary carbides are present leading to the observation of non-propagating cracks [11]. The last criteria for fracture is stated as:

$$\sigma_{22} \geq \sigma_f \tag{6}$$

"over at least one grain diameter in the plastic zone ahead of the notch" [10]. In this case the fracture stress is the microscopic cleavage fracture strength and σ_{22} is the normal stress perpendicular to the crack plane. If this tensile stress is just equal to or lower than the level of the fracture stress at the critical boundary of TWR's third event, then unstable crack growth will not occur.

A measurable quantity can be associated with each of TWR's three events. There is a value of strain necessary to nucleate the microcrack that leads to unstable fracture, given by ε_c in Eqn. (2). There is a stress triaxiality ratio that describes the ability of the microcrack to propagate through the first grain and there is a strength value that must be achieved at the next grain boundary in order for unstable fracture to occur. These three quantities were examined in detail in a series of papers from 1991 to 1993 by Chen et al. [11], Chen and Wang [12] and Chen et al. [13]. Through careful metallographic examination of a variety of C-Mn base and weld steel specimens tested at various temperatures, they measured the distance from the crack tip to the cracked carbide that caused unstable fracture. They proposed a model of transition region cleavage fracture that did not contain a characteristic distance such as the RKR model [14], but instead required that the material achieve critical values of each of the three quantities just mentioned ahead of the crack tip for unstable fracture to occur. We feel that as the temperature increases through the transition region it becomes increasingly necessary to quantitatively account for the ability of TWR's second event to occur and that the Chen model provides a solid starting point for developing a physically based expression for the plastic work involved in fracture.

The constants in Eqns. (1) necessary for the calculations in this paper were gathered from literature reporting tensile data for similar C-Mn steels and are listed in Table 1. The thermal coefficients were taken from Armstrong et al. [15] for C-Mn steel

and are very close to the ARMCO iron coefficients used by Natishan and Kirk [1]. The c_0 value was the result of a best-fit calculation to the Chen and Wang [12] yield data.

Table 1 — *Coefficients used in Eqn. (2).*

c_0 (MPa)	B_0 (MPa)	β_0 (K^{-1})	β_1 (K^{-1})	K (MPa)	n
176	1000	0.0075	0.0004	1198	0.23

Fracture Stress and the Effective Energy

Equation (2) is now rewritten here as the effective energy to reflect TWR's required events in addition to the use of the ZA equation as the effective stress and the Chen model's critical strain:

$$\gamma_{eff} = \int_0^{\varepsilon_c} \sigma_{ZA} d\bar{\varepsilon} \cdot \ell . \tag{7}$$

At this point, Eqn. (7) does not accurately represent the plastic work in a fully constrained toughness specimen. Said constraint causes an artificial elevation of up to three times the yield and subsequent flow stresses of the material [16]. Thus smaller strains are required to reach the fracture stress as compared to uniaxial behavior. The ZA equation, being representative of the uniaxial stress-strain curve, is not equipped to describe this constraint effect. Cottrell [7] described the necessity for a ratio that compares the normal stress to the shear stress. Following Petch [6], the stress triaxiality ratio is introduced to Eqn. (7) as a scalar multiplier

$$\gamma_{eff} = \left(\frac{\sigma_m}{\sigma_i}\right)_f \int_0^{\varepsilon_c} \sigma_{ZA} d\bar{\varepsilon} \cdot \ell \tag{8}$$

Here the subscript on the triaxiality ratio refers to the value at fracture at the critical microcrack location. The ratio itself is altered from that described by Chen et al. [11] in that the material's friction stress, σ_i, is used instead of the effective shear stress. The numerator of the ratio remains the mean stress, σ_m, defined as

$$\sigma_m = \frac{\sigma_{11} + \sigma_{22} + \sigma_{33}}{3} \tag{9}$$

The extent of microcrack blunting is directly related to the ease with which dislocations can migrate away from the crack tip. By using the friction stress, the triaxiality ratio compares the ability of the stress-state to propagate the microcrack to the material's resistance to dislocation motion. In the Hall-Petch definition of the yield stress,

$$\sigma_y = \sigma_i + kd^{-1/2}, \tag{10}$$

the friction stress represents all resistance to dislocation motion that does not arise from grain boundaries. Analogously in the ZA equation for the yield stress, the friction stress is represented by all the terms in Eqns. (1) that are not associated with grain boundaries, i.e.

$$\sigma_i = \sigma_G + B_0 e^{-\beta T} + K\varepsilon^n \tag{11}$$

Incorporation of the above form of the triaxiality ratio thus serves two purposes: 1) to properly account for the elevated stresses ahead of the crack tip and 2) to quantitatively represent the ability of TWR's second event, propagation of the microcrack through the first grain, to occur.

Tetelman and Wilshaw [17] calculated values of the fracture strain in three-point bending for a carbon manganese steel. Like Chen and Wang's data [12], Tetelman and Wilshaw's displayed an exponential temperature dependence. This dependence is seen explicitly by solving Eqn. (1a) for the strain:

$$\varepsilon = \left[\frac{1}{K}\left(\sigma_{ZA} - c_0 - B_0 e^{-\beta T}\right)\right]^{1/n}. \tag{12}$$

In the current methodology, the strain of interest is that necessary to raise the stress sufficiently at the critical carbide to cleave it. The cleavage stress of an Fe_xC_y carbide is independent of temperature. Plastic strain, being the product of dislocation motion, is controlled by the friction stress, which as previously mentioned, decreases with increasing temperature. So as the temperature is increased, greater strains and thus more strain hardening is required to develop the stress necessary to crack the carbide. With Eqns. (1) describing the material behavior, the strain will increase exponentially with temperature. Figure 2 shows the Chen and Wang [12] strain data and corresponding values of the integrand of Eqn. (8).

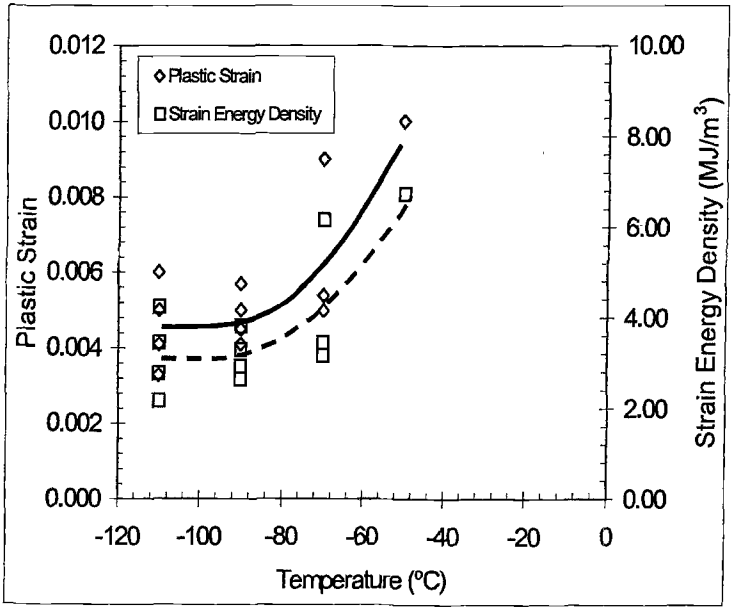

Fig. 2 — *Chen and Wang [12] effective plastic strain to fracture and corresponding strain energy density (integrand of Eqn. (8)) versus temperature.*

Now we look at the length term at the end of Eqn. (8). In 1973, RKR [14] suggest a characteristic distance or length scale over which the stress at the crack tip must exceed the fracture stress of the material. They expanded on TWR's hypothesis and were able to confirm their own 'characteristic distance' of two grain diameters at lower transition region temperatures. The RKR model does not perform well at higher temperatures. This is because both TWR and RKR assume the insignificance of event two in the fracture process. At lower transition region temperatures, this is a safe assumption in large part because the friction stress, which is temperature dependent, is high enough to prevent significant dislocation emission from the tip of the microcrack and its subsequent blunting [18-19]. When the temperature is raised, however, the friction stress decreases and allows dislocation emission and motion to occur more easily. This leads to a greater possibility of microcrack blunting and failure of event two. So if the microcrack is to successfully traverse the grain in question, the constraint at its tip, which can be represented by the hydrostatic stress, must be significantly large as compared to the friction stress so that dislocation emission and motion is suppressed. The microcrack is thus allowed to grow to the next grain boundary.

The length scale of Eqn. (8) can now be described by turning attention to the following conceptual description of the fracture process zone. Tetelman and McEvily [20] suggested that the region of material in front of the notch of a toughness specimen could be represented as a series of small tensile 'specimens' of gage length 2ρ where ρ is the notch root radius. Assuming that the crack tip strains remain small ($\varepsilon < 0.25$, $\rho = 0.25$ mm), then all of the notch tip opening displacement will be concentrated in the 'specimen' adjacent to the tip [17]. Thus the critical crack tip opening displacement can be written as

$$2V_c = 2\rho\varepsilon_f \tag{13}$$

where ε_f is the tensile strain at fracture corresponding to the point ahead of the notch tip where the maximum triaxial stress is first reached [17, 21-22]. The energy, G_{Ic}, needed to cause plastically induced Mode I cleavage fracture is then:

$$K_{Ic} = \sqrt{\frac{EG_{Ic}}{(1-\nu^2)}} \text{ (plane-strain)} \tag{14a}$$

$$G_{Ic} \cong 2\sigma_Y V_c \tag{14b}$$

$$G_{Ic} \cong 2\rho\sigma_Y\varepsilon_f . \tag{14c}$$

Equation (14c) is valid for perfectly plastic materials [20]. When strain hardening occurs, Tetelman and McEvily suggest that the area under the stress-strain curve is more appropriate than the product of the yield strength and the fracture strain. A comparison of Eqns. (8) and (14c) leads to the conclusion that the length scale is twice the notch root radius. This is a temperature dependent quantity, however, since increased temperature leads to crack-tip blunting and an increased root radius. Thus an analogous, but different, length scale is needed to fit into Eqn. (8).

The fracture process zone for a carbide must include the material to the left of the carbide as shown in Figure 3 for it is in this region that the dislocations accumulate to crack the carbide. Above and below the carbide, dislocations will move and accumulate at grain boundaries and other obstacles. However, these 'pile-ups' only affect the overall stress state of the material through the grain size term of Eqn. (2c) and do not contribute to the stress concentration needed to crack the carbide. So in a manner similar to the Tetelman and McEvily approach, the region to the left of the carbide can be viewed as a tensile specimen with a gage length that is, as shown in Figure 3, the diameter of the carbide, D_o. Taking this gage length as the length scale gives the final form of the equation for the effective energy:

$$\gamma_{eff} = \left(\frac{\sigma_m}{\sigma_i}\right)_f \int_0^{\varepsilon_c} \sigma_{ZA} d\bar{\varepsilon} \cdot D_0 . \tag{15}$$

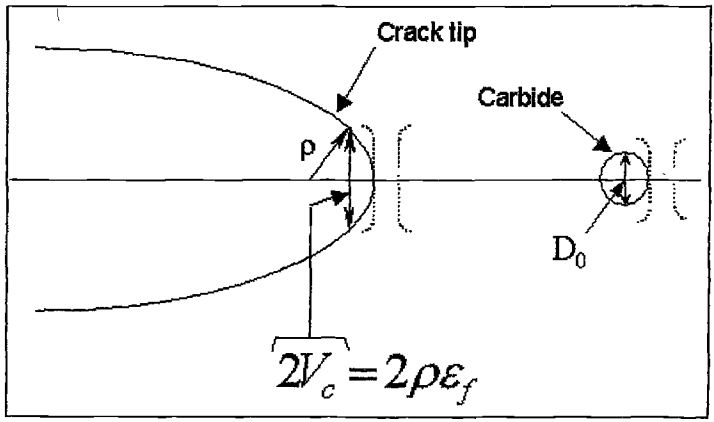

Fig. 3 — *Schematic of Tetelman and McEvily's hypothetical tensile specimen concept as they applied it to the macrocrack. The concept is extended to the microcrack to illustrate the current choice of length scale in Eqn (15).*

The fracture stress of a material can be written using the modified Griffith equation for the fracture stress,

$$\sigma_f = \left[\frac{\pi E \gamma_{eff}}{2(1-\nu^2) r_0}\right]^{1/2}, \tag{16}$$

where E is the elastic modulus, ν is Poisson's ratio, r_0 is the size of the fracture-causing microstructural feature and γ_{eff} is the effective surface energy of the material that is dominated in the transition region by the plastic work consumed in moving dislocations. Inserting Eqn. (15) into the Griffith fracture equation leads to the elimination of the carbide radius from the Griffith equation:

$$\sigma_f = \left[\frac{\pi E \gamma_{sed}}{(1-\nu^2)}\right]^{1/2} \tag{17}$$

In their metallographic observations, Chen et al. measured the sizes of the cleavage initiators. Numeric results for Eqn. (15) are shown in Figure 4 using their median carbide diameter of 1.1 μm. As can be seen, the values calculated from Eqn. (15) exhibit a curve shape that is very similar to the shape produced by Wallin et al.'s, empirically-derived, γ_s+w_p equation. The difference in values at the various temperatures arises from the difference in yield strengths of the two steels. Wallin et al.'s curve is based on a tool steel that has a higher yield strength than the C-Mn steel used in the current calculations. It is well known that in a comparison between two similar materials, the one with the higher yield strength will have a lower toughness at a given temperature.

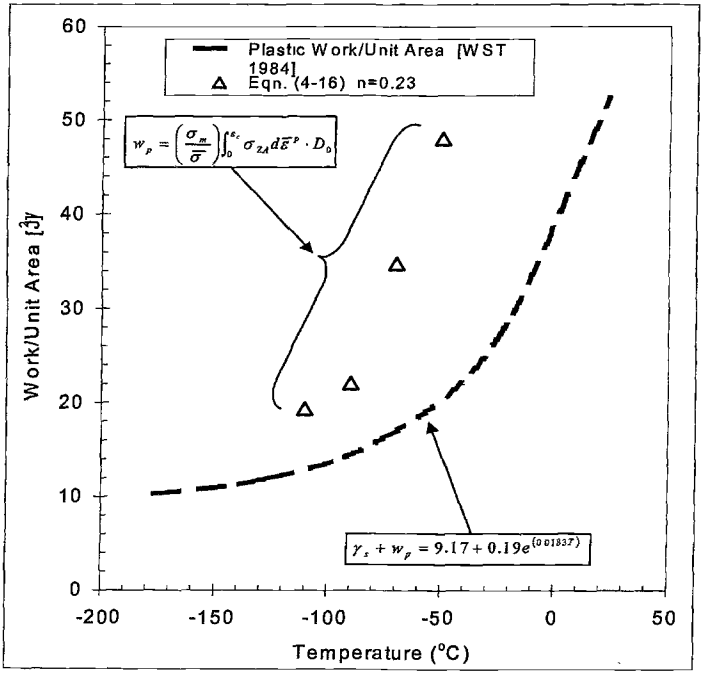

Fig. 4 — *Plot of plastic work versus temperature for results predicted from Eqn. (15) versus the equation derived by Wallin et al. [4].*

Values can be calculated for K_{Ic} and compared to the measured Chen and Wang [12] values. Fracture toughness values can be calculated based on the current methodology through the use of the following equation

$$K_{SSY} = \sqrt{\frac{E\gamma_{eff}}{2(1-\nu^2)}}. \tag{18}$$

Some rearranging is necessary before coherent results can be obtained from Eqn. (18). First, rewrite the fracture stress as

$$\sigma_f = \sqrt{\frac{\pi}{r_0}}\sqrt{\frac{E\gamma_{SED}}{(1-\nu^2)}}. \tag{19}$$

Now substitute Eqn. (16) into Eq. (17) and solve for K to get:

$$K_{SSY} = \sqrt{\frac{\pi E\gamma_{SED}}{(1-\nu^2)}}\sqrt{\frac{r_0}{\pi}} = \sigma_f\sqrt{\frac{r_0}{\pi}}. \tag{20}$$

The fracture stress is defined by Eq. (17) in which the length scale, r_0, was removed and the strain energy density involved in fracture is defined by Eqn. (15). In Eq. (20), r_o cancels leaving a length scale that can be interpreted as a crack length. In this way, values of K_{SSY}, can be calculated. In Figure 5 values of K_{SSY} calculated from the Chen and Wang [12] trend and average data with a crack length of 0.006 m are superposed on the Wallin et al. data [4]. Additionally, K values calculated from *CTOD* data [12] are shown for comparison to the current model. The correlation between the measured data and the current model is quite good despite the limited amount of data. Turning attention to the comparison between the two steels, it can be seen that the current model's values do not rise as sharply at the higher temperatures as Wallin's data. This is most likely the result of scatter in the Chen and Wang [12] data. Fracture initiated in their test specimens at different distances in the crack plane ahead of the notch and application of finite element stress analysis to such results yields different critical strains for the same temperatures. Since the current methodology has a very strong dependence on the shape of the critical strain versus temperature curve, it is important to know where any data lies with respect to the overall scatter.

Also, Chen and Wang [12] state that their fracture model represents the lower bound of toughness versus temperature and does not account for statistical scatter. As such, lower bound data was chosen for use in the current study. Inclusion of the scatter data for the higher temperatures would certainly cause the curve in Figure 5 to rise more sharply with temperature as the critical strain values are greater. In spite of these concerns, the current results for the C-Mn steel indicate a lower transition temperature, about –70°C at 100 MPa·$m^{1/2}$, than that shown by the ferritic tool steel of Wallin et al., about –47°C at 100 MPa·$m^{1/2}$. Since the yield strength of the C-Mn steel is approximately 100 MPa lower than that of the tool steel at all temperatures, this is indeed a positive indicator that the current methodology can predict the shape of the curve as well as the shift in transition temperature.

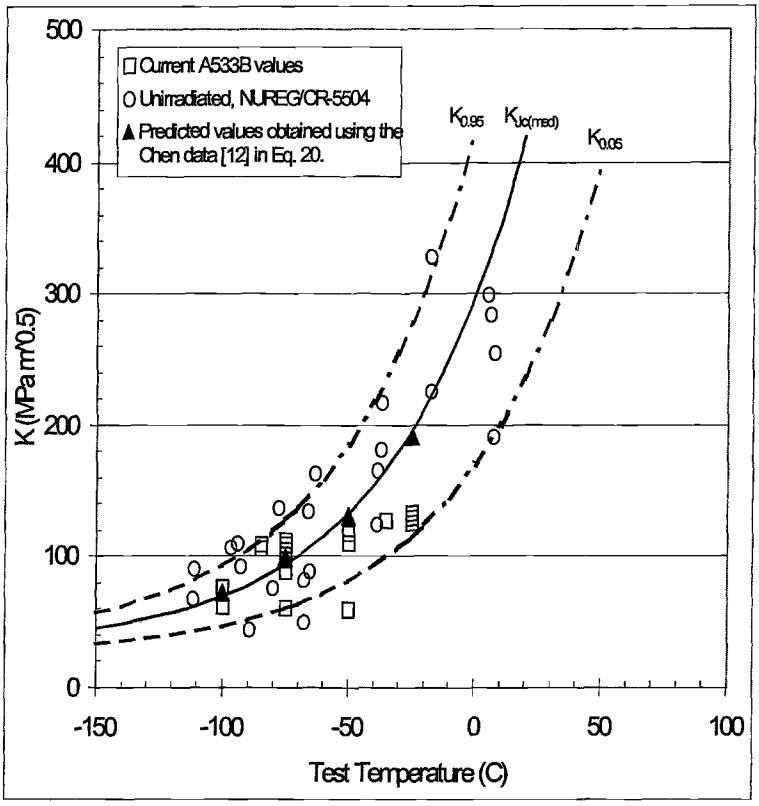

Fig. 5 — *Results of fracture toughness testing compared to results predicted using Eq. 20 and data from NUREG/CR-5504.*

Summary

Significant strides have been made in developing a physically-based model that can predict the shape of the fracture toughness versus temperature curve. Natishan and Kirk's original proposal for the form of the energy involved in fracture has been expanded to include the three requirements for cleavage fracture detailed by Tetelman, Wilshaw and Rau. The question of the appropriate length scale has been resolved by considering the size of the fracture process zone carbide. The calculated values of the effective energy compare favorably in both value and trend to the 1984 results of Wallin et all whose work forms the basis of the current ASTM Master Curve Method. Overall the results presented here are positive indicators that a complete model, utilizing finite element calculations is close at hand.

References

1. Natishan, M. E. and Kirk, M. T., "A Micromechanical Evaluation of the Master Curve," *Fatigue and Fracture Mechanics, Vol. 30, ASTM STP1360*, Jerina, K. L., Paris, P. C., Eds., ASTM International, West Conshohocken, PA, 2000.

2. Zerilli, F. J. and Armstrong, R. W., "Dislocation-Mechanics-Based Constitutive Relations for Material Dynamics Calculations," *J App Phys*, 1987;61(5):1816-1825.

3. Natishan, M. E., Wagenhofer, M., and Kirk, M. T., "Dislocation Mechanics Basis and Stress State Dependency of the Master Curve," *Fatigue and Fracture Mechanics, Vol. 31, ASTM STP1389*, G. R. Halford and J. P. Gallagher, Eds., ASTM International, West Conshohocken, PA, 2000.

4. Wallin, K., Saario, T., and Törrönen, K., "Statistical Model for Carbide Induced Brittle Fracture in Steel," *Metal Science*, 1984;18:13-16.

5. Chen, W. F. and Han, D. J., *Plasticity for Structural Engineers*, New York: Springer-Verlag, 1988.

6. Petch, N. J., "The Ductile-Cleavage Transition in Alpha Iron," Averbach, B. L., et al., Eds, *Fracture*, Wiley & Sons, 1959. p. 54-64.

7. Cottrell, A. H., "Theoretical Aspects of Fracture," Averbach, B. L. et al., Eds., *Fracture*, Wiley & Sons, 1959. p. 20-44.

8. Smith, E., "The Nucleation and Growth of Cleavage Microvoids in Mild Steel," *Proc of Conf on Physical Basis of Yield and Fracture*, 1966:36-46.

9. Stroh, A. N., "A Theory of the Fracture of Metals," *Advances in Physics* 1957;6.

10. Tetelman, A. S., Wilshaw, T. R., Rau, Jr., C. A., "The Critical Tensile Stress Criterion for Cleavage," *Int Jour Frac Mech*, 1968;4(2):147-157.

11. Chen, J. H., Wang, G. Z., Wang, Z., Zhu, L., Gao, Y. Y., "Further Study on the Scattering of the Local Fracture Stress and Allied Toughness Value," *Met Trans A*, 1991;22A:2287-2296.

12. Chen, J. H., Wang, G. Z., "Study of Mechanism of Cleavage Fracture at Low Temperature," *Met Trans A*, 1992;23A:509-517.

13. Chen, J. H., Zhu, L., Wang, G. Z., Wang, Z., "Further Investigation of Critical Events in Cleavage Fracture of C-Mn Base and Weld Steel," *Met Trans A*, 1993;24A:659-667.

14. Ritchie, R. O., Knott, J. F., Rice, R., "On the Relationship Between Critical Tensile Stress and Fracture Stress in Mild Steels," *J Mech Phys Sol*, 1973;21:395-410.

14. Ritchie, R. O., Knott, J. F., Rice, R., "On the Relationship Between Critical Tensile Stress and Fracture Stress in Mild Steels," *J Mech Phys Sol*, 1973;21:395-410.

15. Armstrong, R. W., Zerilli, F. J., Holt, W. H., Mock, Jr., W., "Dislocation Mechanics Based Constitutive Relations for Plastic Flow and Strength of HY Steels," Schmidt, S. C., Shaner, J. W., Samara, G. A., Ross, M., Eds,. *High-Pressure Science and Technology – 1993*, AIP Press, 1993. p. 1001-1004.

16. Dowling, N. E., *Mechanical Behavior of Materials*, 2nd ed., Upper Saddle River: Prentice-Hall, 1999.

17. Tetelman, A. S., Wilshaw, T. R., "A Criterion for Plastically Induced Cleavage After General Yield in Notched Bend Specimens," *Proc 2nd Intl Conf on Fracture*, 1968:18/1-18/10.

18. Weertman, J., *Dislocation Based Fracture Mechanics*, Singapore: World Scientific, 1996.

19. Rice, J. R., Thomson, R., "Ductile Versus Brittle Behavior of Cyrstals," *Phil Mag*, 1974;29:73-96.

20. Tetelman, A. S., McEvily, A. J., Jr., *Fracture of Structural Materials*, New York: Wiley & Sons, 1967.

21. Koide, M., Kikuchi, A., Yagi, T., Nagumo, M., "Brittle fracture initiation in low carbon steels at the ductile-brittle transition temperature region," *Matls Sci Eng*, 1994;176(1-2):171-175.

22. Chan, J.H., Yan, C., Sun, J., "Further Study on the Mechanism of Cleavage Fracture at Low Temperatures," *Acta Metal, Mater*,1994;42(1):251-261.

K. M. Nikbin[1]

Sensitivity in Creep Crack Growth Predictions of Components due to Variability in Deriving the Fracture Mechanics Parameter C^*

Reference: Nikbin, K. M, **"Sensitivity in Creep Crack Growth Predictions of Components due to Variability in Deriving the Fracture Mechanics Parameter C^*,"** *Predictive Materials Modeling: Combining Fundamental Physics Understanding, Computational Methods, and Empirically Observed Behaviour,* ASTM *STP 1429,* M. T. Kirk and M. Erickson Natishan, Eds., ASTM International, West Conshohocken, PA, 2003.

Abstract: In this paper the uncertainties in estimating C^* creep fracture mechanics parameter, on component defect assessment, is considered. Comparisons of reference stress σ_{ref} and the stress intensity factor K for a surface cracked plate under tension and bending and a pipe geometry under internal pressure and external bending using formulae from available codes of practices such as the R5/R6 [1-2], BS7901 [3] and A16 [4] are made with three-dimensional Finite Element (3D FE) analysis calculations. It is shown, using the same material properties and specimen dimensions, that the uncertainty associated with calculating σ_{ref} could be as much as ±40% whereas for the stress intensity K it is about ±10%. The σ_{ref} values are used to calculate C^* using the mean properties of a base 316LN type stainless steel plate tested at 650 °C and a cross-weld P22 circumferentially welded pipe tested at 565 °C. Both the pipe and the plate were tested within a European collaborative programme 'HIDA' between (1996-2000) [5]. The tendency is that 'global' limit load analysis will give a lower and more conservative C^* than the 'local' analysis. From the comparisons of the pipe and plate initial cracking rates, using different C^* estimations, with standard creep crack growth rate data on compact tensions (CT) specimens, using the ASTM E1457-2002 to evaluate C^*, it is shown that predictions of cracking rates could vary by as much as two decades in magnitude. This inconsistency yields itself to an analysis based on an empirical model for predicting crack growth in components.

Keywords: creep, crack growth rate, fracture mechanics, k, c*, limit analysis, reference stress, high temperature testing, life assessment, steels, constraint

Introduction

[1] Dr K. M. Nikbin, Imperial College, Mechanical Engineering Department, London, SW7 2BX, UK.

In order to predict, with confidence, creep crack growth rates in engineering structures both material properties and the fracture mechanics models used need to be examined in detail. Material properties vary in creep crack growth and are reflected as scatter in test data [5,6]. The fracture mechanics parameters K, C^* and σ_{ref} [5-10] will also contain a certain degree of uncertainty since the analytical and numerical methods for their derivations vary. High performance and parallel computing has allowed non-linear and time dependant calculations of 3D geometries to be modelled faster and more efficiently. In some cases 2D calculations can now be performed interactively with the results of finite element calculations being incorporated into an assessment code.

Defect assessment codes [1-4] in the power generation industry use linear and non-linear fracture mechanics parameters to predict initiation and crack growth of components at elevated temperatures. It is clear in these assessment methods that the correct evaluation of the relevant fracture mechanics parameters, for which the lifetime prediction times are dependent upon, will largely determine the accuracy of the life predictions. In this paper a comparison of solutions of K, C^* and σ_{ref} are presented using three Dimensional Finite Element (3D FE) analysis and analytical modelling of collapse loads. Three dimensional meshes are used to model a plate under bending and tension, pre-cracked pipes under internal pressure and bending with an axial elliptical crack, and a longitudinal pipe under pressure and four-point bend containing a circumferential crack. Results of standard CT specimens are also presented and compared to the experimental tests n the plate and the pipe geometry. Emphasis is placed on the differences in results that are obtained from seemingly perfectly acceptable methods and boundary conditions using the same material properties. The differences are discussed in the light of life assessment methods for cracked components operating at elevated temperatures.

High Temperature Fracture Mechanics

The arguments for correlating high temperature crack growth data essentially follow those of elastic-plastic fracture mechanics methods. For creeping situations [5-10] where elasticity dominates K may be sufficient to predict crack growth. However as creep is a non-linear time dependent mechanism even in situation where small scale creep may exist linear elasticity my not be the answer. By using the J definition to develop the fracture mechanics parameter C^* it is possible to correlate time-dependent crack growth using non-linear fracture mechanics concepts.

A simplified expression for stress dependence of creep is given by a power law equation which is often called the Norton's creep law and is comparable to the power law hardening material giving;

$$\varepsilon = A'\sigma^N \tag{1}$$

and by analogy for a creeping material

$$\dot{\varepsilon} = A\sigma^n \tag{2}$$

where A', A,N, n, are material constants ε, $\dot{\varepsilon}$ and σ are the strain, creep strain rate and applied stress respectively. Equation (2) is used to characterise the steady state (secondary) creep stage where the hardening by dislocation interaction is balanced by recovery processes. The typical value for n is between 5 and 12 for most metals. When N=n for creep and plasticity it is assumed that the state of stress is characterised in the same manner for the two conditions. The stress fields characterised by K in elasticity will be modified to the stress field characterised by the J integral in plasticity in the region around the crack tip. In the case of large scale creep where stress and strain rate determine the crack tip field the C^* parameter is analogous to J. The C^* integral has been widely accepted as the fracture mechanics parameter for this purpose [5-10]. The experimental derivation for C^* for standard laboratory CT estimates the parameter under steady state [6-9] or under small scale creep [10].

In cases where the load-line deformation rates are available, such as in laboratory Compact Tension tests, the creep load-line displacement is used for estimating C^*, as described in ASTM E1459-02. The data is used as 'benchmark' for materials creep crack growth properties in the same way as creep strain rate and rupture is in uniaxial creep tests. However the engineering method available to calculate C^*, for component shaped tests, is based on the reference stress concepts [1-4, 11-15] using;

$$C^* = \sigma_{ref} . \dot{\varepsilon}_{ref} \left(\frac{K}{\sigma_{ref}} \right)^2 \tag{3}$$

where $\dot{\varepsilon}_{ref}$ is the unaxial creep strain rate at the appropriate σ_{ref}. Usually it is convenient to employ limit analysis [13-15] to obtain σ_{ref} from

$$\sigma_{ref} = \sigma_y \frac{P}{P_{lc}} \tag{4}$$

where P_{lc} is the collapse load of a cracked body and σ_y is the yield stress. The value of P_{lC} will depend on the collapse mechanism assumed and whether plane stress or plane strain conditions apply. The collapse loads solutions are available for some geometries [1-4,13] and in some cases need to be numerically derived.

It is also evident from previous work [1-10] that for most creeping materials there exists a relationship between crack growth rate and C^* so that

$$\dot{a} = DC^{*\phi} \tag{5}$$

where D and $\phi \cong n/(n+1)$ are material constants depending on temperature and stress state. In general equation (5) is used in the codes of practice for high temperature defect assessment [1,3,4] to predict crack growth rate under steady state conditions.

Materials, Geometry and Test Information

The main object of the present exercise is to highlight and compare the differences that exist in the calculated results of σ_{ref} for cracked components using available analytical collapse load solutions [1-4] and comparing them with 3D FE calculations. For this reason specific σ_{ref} values are used to calculate C^* using the appropriate material properties, dimensions and loading taken from a pre-cracked pipe and a plate component tests.

The first specimen is a P22 circumferentially welded pipe tested at 565 °C by SPG in Dresden, Germany, and the second is a type 316LN stainless steel plate tested at 650 °C by CEA in Saclay, France. Both tests were performed within a European collaborative programme called 'HIDA' [7]. In addition, for validation of results, standard creep crack growth test on CT specimens were also performed by partners [7] in the programme using the same batch of material and test temperatures. The details of the materials properties, geometries, and creep crack tests for these specimens have been reported elsewhere by [7]. It is therefore sufficient to identify the relevant data that will be used in the present analysis.

Table 1—*The chemical composition of the test material P22.*

C	Si	Mn	P	S	Cr	Mo	Ni	Cu	Sn
0.10	0.21	0.44	0.013	0.002	2.31	0.97	0.10	0.17	0.014

Table 2—*The chemical composition of the test material 316 LN- batch SD.*

C	Mn	Si	S	P	Cr	Ni	Mo	Ti	Nb	N	Cu
0.038	1.830	0.313	0.02	0.036	17.3	11.9	2.46	<0.01	<0.01	0.067	0.27

Table 3—*Tensile properties of P22 at 565 °C, and 316 L(N) at 650 °C.*

Material (parent)	*Strain rate (/s)*	*Young's modulus (GPa)*	*0.2% yield (MPa)*	*A' (MPa^n)*	*N*	*UTS (MPa)*	*Failure strain (%)*
P22	4e-3	157	282	5.8e-30	10.8	365	27
316 LN	5.8e-3	161	170	2.3e-24	9.4	412	65

Table 4—*Uniaxial creep deformation properties.*

Material	Material Condition	*Temp °C*	*A*	*n*	*failure strain ε_f*	*RA%*
P22	base	565	3.0E-27	10.7	0.37	0.65
P22	XW	565	2.7E-27	10.7	0.02	0.19
316 LN	base	650	9.0E-24	8.7	0.59	0.55

Tables 1 and 2 show respectively the material composition of the alloys. Table 3 shows the tensile properties of the steels at the relevant test temperature. This information is used in the 3D FE limit load analysis. Table 4 gives the uniaxial creep properties for both materials used in the evaluation of C^* from the reference stress method. Since the pipe test contained a crack in the region of the heat affected zone (HAZ) of the specimen, table 4 also gives the information related to cross-weld (XW) uniaxial properties of P22. It should be noted that the XW properties are shown to be very similar to the base material properties.

The nominal dimensions for the pipe and the plate tested are shown in Figs. 1 and 2 respectively. Both geometries contained pre-machined semi-elliptical EDM (electro-discharged machined) cracks with the notch tip diameter of 0.2 mm. The crack was placed in the HAZ region for the pipe as well as in the parent, making sure that they were sufficiently apart not to allow interaction. The present analysis only deals with the cracking in the HAZ notch as there was insufficient growth in the base material. The pipe was internally pressurized and was loaded under four-point bend as described in Fig. 1. The bending and axial stresses are comparable in magnitude in the cracked section of the pipe whereas the plate was loaded under a primarily bending load, as shown in Fig. 2, at 1 cycle/hour dwell at peak load.

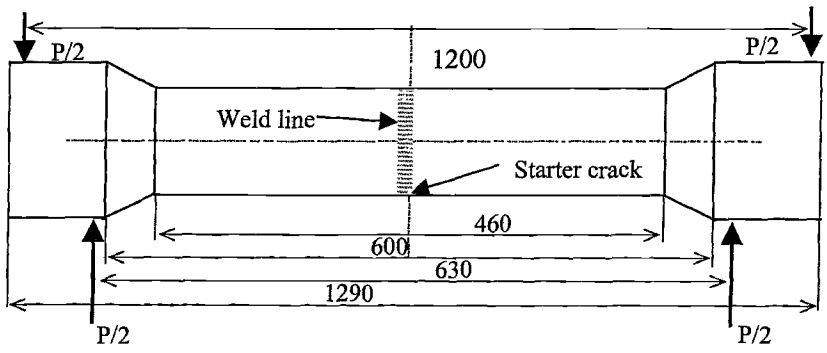

Fig.1— *SPG's four-point-bend pipe dimensions in (mm) showing the loading points. Containing a circumferential crack with initial crack depth a_o=5.7mm, surface crack length 2c=43mm mm, pipe thickness W=20mm, internal/external radius R_i/R_o=80/100mm, internal pressure of 20 MPa and bending moment of 25.7KNm giving a bending stress of 100.7 MPa.*

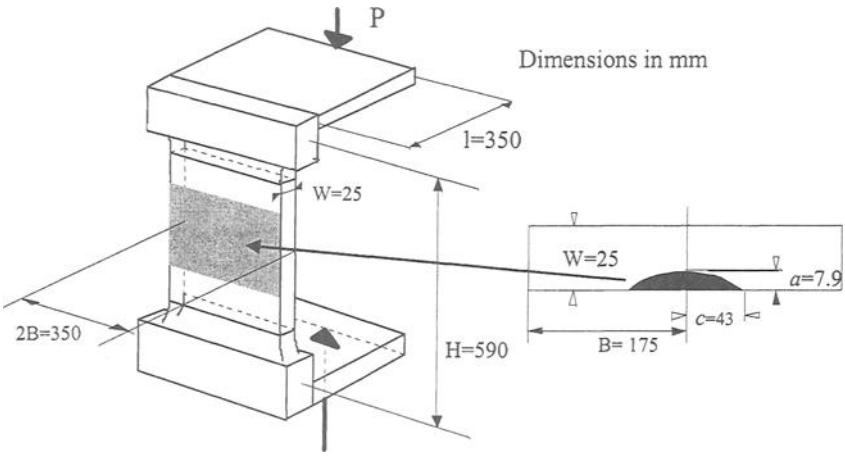

Fig. 2— *CEA's plate specimen dimensions in (mm) showing the loading points. Initial crack depth a_o=7.9mm, surface crack length 2c=86mm mm, plate thickness=20mm, width =175mm and slow dwell (1cycle/hour) bending moment of ±14.0 KNm.*

Given the slow cycle dwell on the plate it has been shown [11] that the mechanism for failure is predominantly intergranular and creeps dominant. It has been observed that fatigue, at low frequencies of less than 0.1 Hz [5-11], does not make a major contribution to the growth of the crack. The present analysis therefore disregards fatigue and is carried out at maximum load where creep damage is at a maximum.

Finite Element Analysis

The ABAQUS package [16] was used in the FE analysis to derive K and the collapse loads for the pipe and the plate geometries. Essentially for deriving σ_{ref} from equation (4) calculations for collapse load of the cracked geometries need to be performed. It is also important to note from equation (3) that the important factors determining C^* for the component case is the correct employment of the material properties given the extent of scatter in the data [5-6] and the interpretation of the collapse load.

Since material properties data always contain an inherent variability and creep properties in equation (2) are sensitive to the creep index n, they will both contribute to an increased uncertainty in C^* estimations. However for the present purposes the mean material properties, as shown in tables 3 and 4 will be used and differences derived only from σ_{ref} solutions will be considered.

The plate and the pipe meshes were modeled around a generic 20-noded three dimensional (3D) mesh structure containing a crack shaped out of a series of collapsed elements as shown in Fig. 3. Therefore the extended mesh in Fig. 3 was shaped circular for the pipe and flat for the plate using the dimensions given in Figs. 1 and 2 respectively. Only a quarter section of the geometries were modeled due to symmetry. It was assumed that the material was made up of elastic perfectly plastic material as required for the

calculation of σ_{ref}. Perfect plasticity in ABAQUS was modeled using the *PLASTIC option. The material properties used for the plate and the pipe analysis are shown in tables 3 and 4.

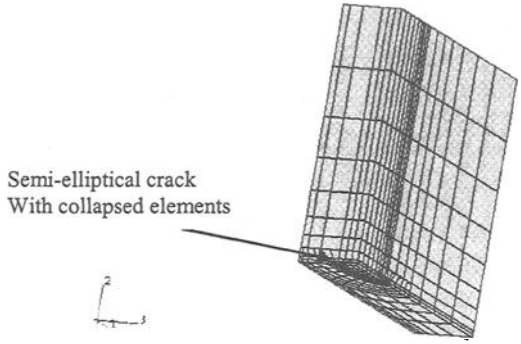

Fig. 3—*3D FE mesh region local to the crack straight pipe with circumferential external surface semi-elliptical crack and the plate mesh with surface semi-elliptical crack were shaped around this mesh form.*

For the plate, two options were tested in order to apply a uniformly distributed bending load on the top surface of the mesh. The first option necessitated the creation of 8-noded shell elements using the top surface nodes of the 3D mesh. A linearly distributed pressure (*DLOAD) was applied to the shell elements simulating the remote stress distribution in the plate. The pressure on the shell elements could then be transmitted to the plate. The second option consisted in linking a remote node to the node set containing the nodes on the top surface of the plate using the subroutine *EQUATION. A bending moment could then be applied to that remote node, of half the magnitude of the experimental bending moment (because of symmetry). This bending moment would then be transmitted evenly to the nodes on the top surface.

The second loading option proved to be the best. In a purely elastic analysis run, to validate the mesh, stresses in the far-field (away from the crack) were linearly distributed and were null at the neutral axis of the plate, as predicted by simple beam theory. It was then decided to apply the load using the remote node option. The elastic-plastic plate and pipe were then collapsed by applying an incrementally increasing bending moment for the plate and a bending and pressure for the pipe.

Bending solutions for the reference stress were also investigated using finite element analysis. The mesh used in the plate analysis was modified in order to fit the shape and dimensions of the four-point bend pipe with a circumferential semi-elliptical defect (a=5.7 mm, c=43mm). The load was applied using the same procedure as for the plate. Two measures of collapse were made. The first one, local, in the net section of the defect when plasticity covered the section, and the second, global measured at a remote point using the load displacement diagram giving rise to global plasticity in the pipe's section.

Stress Intensity Factor K Calculations

A survey in the literature shows that there are several formulae to determine the stress intensity factor for the semi-elliptical crack. However, all of them are based on Raju and Newman [17]. The codes [1-4] all use a closed form solution and for the present comparison, the Raju and Newman formulae [17] are compared to the 3D FE calculations for the pipe and the plate. The K from Raju and Newman were also obtained for a surface crack by using a three-dimensional finite-element stress analysis and is defined as:

$$K_{I\,Raju} = p \cdot \frac{R_i}{W} \sqrt{\pi \cdot \frac{a}{Q}} \cdot F_e\left(\frac{a}{2c}, \frac{a}{W}, \frac{W}{R_i}\right) \tag{6}$$

where Q is approximated by:

$$Q = 1 + 1.464 \cdot \left(\frac{a}{c}\right)^{1.65} \tag{7}$$

and F_e is the boundary-correction factor of an external surface crack, which can be written as:

$$F_e = \frac{W}{R_i} \cdot \left(\frac{R_i^2}{R_e^2 - R_i^2}\right) \cdot \left[2 \cdot G_0 + 2 \cdot \left(\frac{a}{R_e}\right) \cdot G_1 + 3 \cdot \left(\frac{a}{R_e}\right)^2 \cdot G_2 + 4 \cdot \left(\frac{a}{R_e}\right)^3 \cdot G_3\right] \tag{8}$$

where the G_j are dependent on $a/2c$, a/W and W/R_i and are given in the literature [17]. The G_j relevant to this investigation were obtained from interpolation or extrapolation according to the dimensions in Figs. 1 and 2.

Validation of the mesh for the pipe and the plate was made by comparing values of the J-integral calculated numerically using the *CONTOUR INTEGRAL with the above Raju-Newman solution used for the stress intensity factor of a surface semi-elliptical plate. An elastic FE analysis was performed for the pipe and the plate and the results are compared to table 5. The variation in K is shown to be small (about ±10%) when comparing different methods for its derivation.

This validation was an important prerequisite in using the meshes, with sufficient confidence, for limit load and reference stress calculations. Also since the subsequent FE runs were non-linear elastic-plastic and the meshes were modeled with cracks it was necessary to try different boundary conditions and loads in order to see the effect on the calculations.

Table 5—*Comparison of the 3D FE, K calculations and the Raju-Newman solution for the pipe and the plate assuming initial defect dimensions shown in Figs. 1 and 2.*

Geometry	*Raju and Newman: (K in MPa.m$^{1/2}$)*	*3D FE analysis: (K in MPa.m$^{1/2}$)*
Plate: At deepest point *a=7.9 mm*	17.78	18.02
Pipe: At deepest point *a=5.7 mm*	20.2	21

Reference Stress Calculations

The reference stress is a unique value of stress in a loaded body associated with a specific failure mechanism. It can be derived from the limit load of a component (see equations (3) and (4)) which is the value of the load parameter that corresponds to the end of the restricted plastic flow and to the initiation of the unrestricted plastic flow and collapse is the global failure mechanism associated with the attainment of the limit load [1-4, 7,13]. Analytical expressions exist [13] for collapse solutions or the 'global' limit load can be performed numerically using a load versus displacement curve as shown in Fig. 4a.

However in cracked components the relevant parameter for limit load may not be global collapse but 'local' collapse. The various life assessment codes suggest that σ_{ref} should be taken from the collapse of the crack region [1-4]. Fig. 4b shows a schematic example of the regions of local collapse around the crack tip that would constitute a relevant reference stress for a cracked body. The grey 'local' regions do not necessarily correspond to 'global' collapse (as shown in Fig. 4a). The choice of the local collapse region is therefore 'judgmental' and will give differences in the value for collapse loads reflecting on the reference stress calculations.

Comparison of C solutions*

In order to determine the significance of the different methods of calculating σ_{ref}, from equation (3) σ_{ref} is estimated for the initial crack length of the pipe and the plate test using the relevant material properties data shown in tables 3 and 4 and the applied loads set out in Figs. 1 and 2. The solutions for σ_{ref} have been taken from appropriate codes [1-4] and are shown in the Appendix. The various solutions for σ_{ref} and C^* are then compared to the local and global solutions of the 3D FE analysis for the pipe and plate that use the same material properties. The results at a fixed initial crack length are tabulated in tables 6 and 7. The finite element calculations show that the 'local' reference stress evaluated in the ligament is higher by almost 40-50% compared to the reference stress calculated form the 'global' collapse for both the plate and the pipe. Also since 3D FE analysis used the actual material and specimen condition, no assumption had to be made concerning the state of stress. It should be noted that generally global collapse solutions from the codes tend to give a lower C^* values than local solutions as shown in tables 6 and 7.

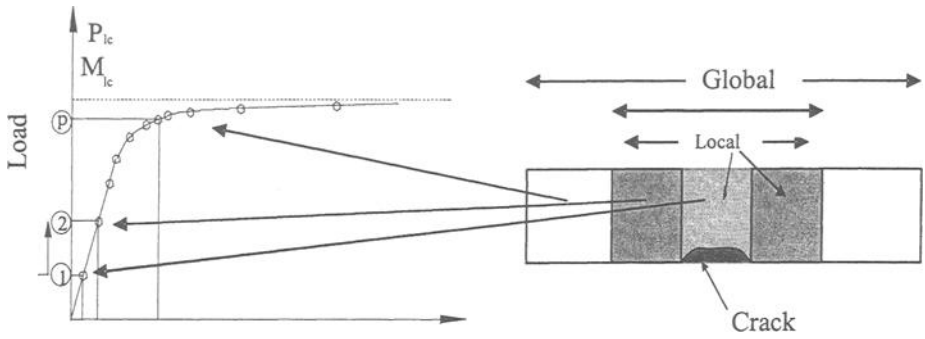

Fig. 4— *a) Schematic diagram of the global with respect to local displacement in a cracked component, b) Cross-section showing regions of local and global collapse.*

Analysis of crack growth rate predictions in components

Testing of component sized specimens is both costly and the data difficult to obtain. Therefore a comparatively few tests have been performed [7]. For the purposes of this study an example comparison is therefore made between the experimental compact tension crack growth data and the pipe and plate data of the same batches of material [7]. Since material and specimen specific 3D FE analysis for the pipe and the plates were performed for one crack length only the present comparison with σ_{ref} is made on one specific load and initial crack length where test data exists.

The experimental creep crack growth data, chosen to highlight the sensitivity of C^* to the choice of σ_{ref}, is shown in Figs. 5 and 6 for P22 pipe and 316 LN plate respectively. The Figs. show, in both cases, that initiation of the cracks from the EDM notches occur instantly.

The crack growth versus time for the pipe and plate, shown in Figs. 5 and 6, give an initial crack rate of 1.36 E-3 and 1.42 E-3 mm/h respectively. These are plotted, as specific points for both geometries, in Figs. 7 and 8 versus the different calculations of C^* values derived from the various σ_{ref} solutions shown in the Appendix and detailed in tables 6 and 7. For the case of the pipe, with the starter crack in the HAZ region, C^* was estimated from the XW data in table 4. Figs. 7 and 8 also compare the CT data crack growth data for both alloys exhibiting the usual degree of scatter. Fig. 7 also shows that the CT data for P22 exhibits little difference between the crack growth rates for the base and cross-weld, XW, P22 material.

Table 6—*Reference stresses and C* evaluated for P22 HAZ material properties, at 565 °C comparing different solutions for an Initial crack depth a_o=5.7mm, combining Internal Pressure of 20 MPa and Bending moment of 25.7KNm giving an initial experimental cracking rate of 1.3E-3 mm/h.*

Reference	σ_{ref} (MPa)	Initial C* [MJ/m^2 h]
BS7910 -Local [3]	137	8.0 E-5
R5/6 – No defect-Global [1,2]	105	3.0 E-6
A16 - Global [4]	149	1.5E-4
3D FE -Global	78	9.0E-7
3D FE - Local	116	7.0E-6

Table 7— *Reference stresses and C* evaluated for 316LN steel at 650 °C comparing different solutions for an Initial crack depth a_o=7.9mm, Bending moment ±14 KNm giving an initial experimental cracking rate of 1.4.2E-3 mm/h.*

Reference	σ_{ref} [MPa]	*Initial C** [MJm^{2}h]
BS7910 - Local [3]	144	1.2E-4
R5/R6 - Local [1,2]	140	9.1E-5
A16 - Global [4]	93	3.5E-6
Global - 3D FE	109	8.1E-6
Local – 3D FE	143	1.4E-4

a)

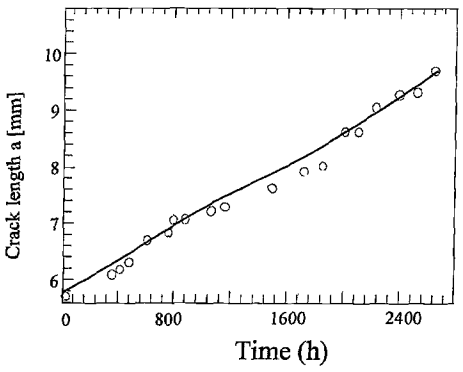

Fig. 5—*Crack length versus time on first loading of 316 LN plate, tested at 650 °C. Initial cracking rate 1.36E-3.*

b)

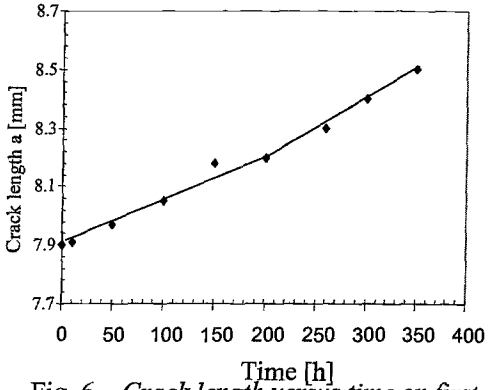

Fig. 6—*Crack length versus time on first loading of P22 pipe, tested at 565 °C. Initial cracking rate 1.42E-3.*

In Fig. 7 for the pipe the 3D FE results show the right trend of a lower σ_{ref}, for the global analysis but when compared to the analytical solutions the local solution from the 3D FE is substantially below the rest. At the same time what is termed as 'global' in A16 gives C* values higher that the 'local' BS7910 solution. These differences are likely due to the modeling of the large bending/tensile loading ratio that exists in the pipe test. The details of the solutions are shown in the appendix. It is clear that a detailed sensitivity analysis is required to fully quantify the differences in this case.

Fig. 8, for the plate, shows the plot of C^*, derived from the codes and the 3D FE analysis, versus initial cracking rates measured from Fig. 6. From the different C^* solutions and the 3D FE calculations there is a clearer trend for the global σ_{ref}, solutions of giving a lower C^* values than the local solutions. The 3D FE solutions also compare better to the analytical solutions in the plate than the pipe. It should be noted that the plate was predominantly loaded in bending.

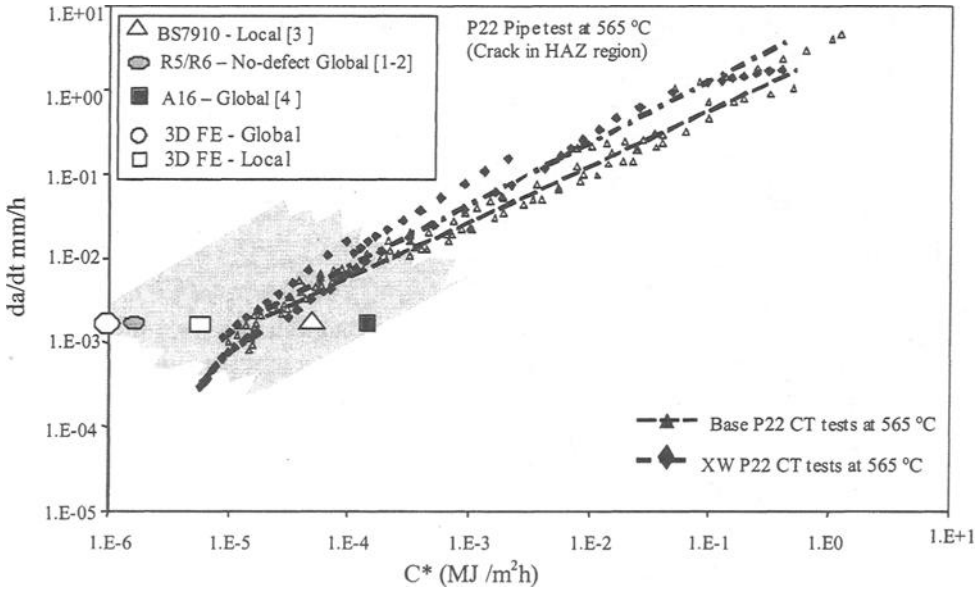

Fig. 7—*Comparison of crack rate versus C* for P22 parent and HAZ material at 565 °C, tested as CT specimens, with the initial crack growth rate of P22 Pipe material (in the HAZ region) using different reference stresses and 3d FE analysis.*

Comparing the 'benchmark' CT data with the pipe and plate data it can be seen both in Figs. 7 and 8 that the CT data can be described as conservative or not depending on which solution of C^* is chosen. Any comparison in this way should therefore be treated with caution. Effectively the range of C^* solutions extend to two orders of magnitude. The highlighted grey region in Figs. 7 and 8, drawn parallel to the mean slope of the CT data, gives a tentative indication of how far predictions for crack growth would diverge depending on the choice of the C^* solution. The grey region also highlights the region where the pipe data lie with respect to the CT data. The tendency is for the pipe to span over the CT data in Fig. 7 and for the plate data in Fig. 8 to generally show higher cracking rates compared to the CT. It is clear that additional data over a wider range of cracking rates would be needed to establish these trends precisely.

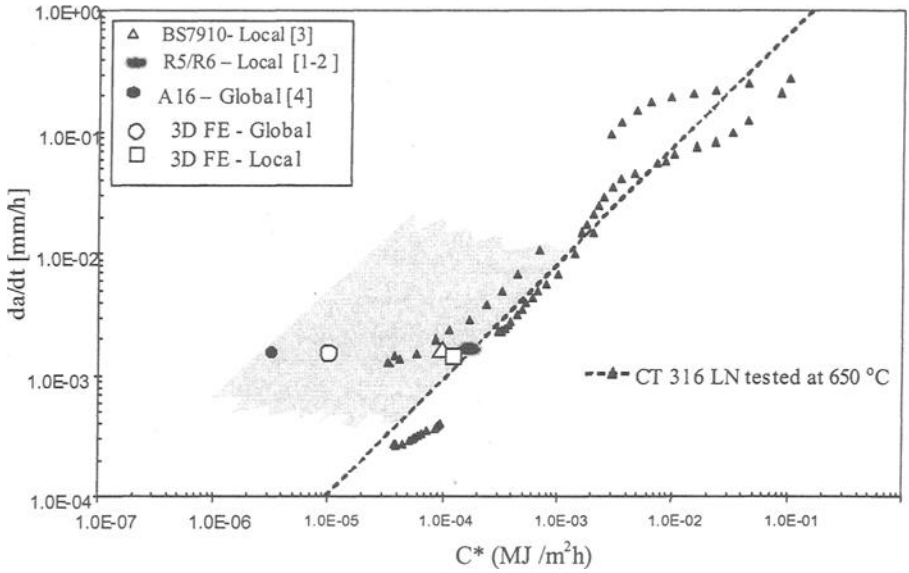

Fig. 8—*Comparison of crack rate versus C* for 316 LN parent material, tested as CT specimens, with the initial cracking rate of the plate tested at 650 °C using different reference stresses and 3D FE analysis.*

Discussion and a Proposed Method

It is difficult to dissociate the intrinsic problems involved in deriving crack growth predictions using reference stress solutions and relating the data to different geometries. Since the standard CT data is used to derive the crack growth properties of the material as proposed in ASTM E1457-02 and is taken as the 'benchmark' data in equation (5) for crack growth prediction it is important to be able to quantitatively relate it to component crack growth behaviour using the C* reference stress solutions. A scaling method is proposed which links the appropriate laboratory test data for crack growth to predict

crack extension in components. In order to deal with this problem the following should be taken into consideration

1. Laboratory tests specimens should reflect the stress state of the component under investigation. Both size and geometry should match the component as closely as possible. Therefore the differences in constraint on testing geometries other than the CT used in ASTM E1457-02 needs evaluation.

2. If crack growth data for the relevant geometry is not available data derived from CT tests performed according to ASTM E1457-02 could be taken as the benchmark for any crack growth analysis prediction. However caution is advised as the specimen size and mode of loading may be different between the CT and the component. Therefore compensation, in the calculations, should be allowed for these differences. At present this is only possible if a sample component shape is tested to validate the difference that exists in the CT data.

3. Reference stress is a convenient approximation for simplifying the evaluation of the appropriate stresses at the crack tip being relatively insensitive to creep properties of the material. The choice of the reference stress solution for the component should therefore satisfy the failure mechanism relevant to the component. Furthermore an agreed solution specific to the geometry and mode of loading if universally implemented would reduce the problems associated with differences between solutions.

4. Since capability to perform 3D FE analysis has increased substantially in recent years a wide ranging non-linear 3D numerical analysis should be undertaken to tabulate the reference stress and C^* for a range of crack lengths and geometries and components using both collapse load solution and actual derivation of C^* from the contour integral. In this way these solutions, once validated experimentally, could act as benchmark solutions for every geometry.

Once these steps are considered it may then be appropriate to use a scaling method to ensure a way to predict component crack growth similar to the method suggested for crack initiation in R5 [1]. Provided that crack growth is in steady state and the value of ϕ in equation (5) and the creep index n in equation (2) is the same for the CT as well as the component then by using

$$\frac{\dot{a}_{comp}}{\dot{a}_{spec}} = \frac{D_{comp}}{D_{spec}} \left(\frac{C^*_{comp}}{C^*_{spec}} \right)^K \tag{9}$$

where D_{spec} and D_{comp} are the respective constants in equation (5) for the specimen and the component. $\dot{a}_{spec}$ is the crack growth rate in the laboratory specimen, $\dot{a}_{comp}$ is the crack growth rate in the component, C^*_{spec} is the experimental C^* solution for the specimen using ASTM E1457-02 and C^*_{comp} in the validated reference stress solution for the component and κ is the constraint factor. The predictions will be conservative if $C^*_{spec} < C^*_{comp}$ for the same cracking rate.

If κ=1 when the component under test has the same constraint as the test specimen. The value of κ is linked to the range of crack growth that could occur over the plane stress/plane strain range of crack growth [8-10]. This difference can be as much as a factor of 30 for a wide range of material properties and sizes. However for comparison between the same materials and similar size specimens, under creep ductile conditions, this factor could be about 5 [18]. Once the appropriate reference stress is established and C^* for the component is calculated then equation (9) can be used and crack growth rates for the component data can be scaled with the CT benchmark data.

It follows if the codes provide an agreed reference stress, taking into account validated results, for evaluating C^* equation (9) may be used to empirically predict crack growth in components based on laboratory tests. This method will need knowledge of the crack growth rate for the generic component to establish the constants in equation (9). Subject to the results and the appropriate safety factors the reference stress solution can be adopted by identifying the relevant values of D_{spec} and D_{comp}.

Material Variability

There is an additional factor other than parameter variability that is important in defect life assessment of components. Scatter in creep properties and creep crack growth data are well known [5-7]. Figs. 7 and 8 shows the scatter in the same batch of P22 and 316 LN data. The scatter in the data is a reflection of the time dependent creep damage and crack growth development and any other differences in deviation in specified testing procedures and specified specimen geometries. Since the slopes in Figs. 7 and 8 is given by equation (5) as ϕ and in the NSW predictive model [8-9] $\phi = n/(n+1)$ it is clear that variability in n will also have an affect. If batch specific data is not available and generic data were needed to be used for the defect assessment analysis it would be self-evident that a less accurate assessment analysis would be produced.

Conclusions

In this paper the σ_{ref} values are used to calculate C^* using the appropriate properties of a 316LN type stainless steel plate tested at 650 °C and a P22 circumferentially welded pipe tested at 565 °C. These were tested within a framework of a European collaborative programme 'HIDA' between (1996-2000) [7]. It is shown from the comparisons of the

pipe and plate cracking rates, using different reference stress estimations, with standard creep crack growth rate data on compact tensions specimens, using the ASTM E1457-02 to evaluate C^*, that a very wide range of C^* values can be achieved. The analysis of the plate and the pipe has highlighted the range of reference stresses that can be calculated from either analytical formulae or numerical results, based on different assumptions of the extent and mode of collapse. No account has been taken in this paper regarding material variability.

It appears generally from the present analysis that the global solution of reference stress produces the lower C^* solutions compared to the local solutions. However more experimental data on component type tests at different cracking rate as well as full 3D FE solutions at different crack lengths are needed in order to quantify this trend with the variation in, ligament size and a wider range of cracking rates.

For the differences found in reference stress and hence C^* solutions in components it is suggested that the codes should choose specific solutions on the basis correct crack tip conditions. These should be validated using experimental, analytical and FE solutions. On this basis any differences found between component crack growth and standard laboratory crack growth should be dealt with using a scaling technique taking into account the differences in constraint between the laboratory test and the component test and adding appropriate safety factors. The advantage of this approach is that users of the codes can compare data and crack growth predictions of their data in a unified fashion. The methods bypasses the fundamental problem of the disunity that exist in the evaluation or the estimation of the C^* parameter which needs further analysis.

Acknowledgments

The author would like to thank the partners in the European Commission funded 'HIDA' collaborative project (1996-2000) for the provision of the plate and pipe data which were tested at CEA in Saclay, France and APG, Dresden, Germany. Thanks is also due to Dr N. J. C. Celard for performing parts of the calculations.

References

[1] Ainsworth, R. A, "Assessment Procedure for the High Temperature Response of Structures," Nuclear Electric procedure R5 Issue2, 1999.

[2] "Assessment of the Integrity of Structures Containing Defects," Revision 3, British Energy Generation, 2000.

[3] British Standards—7910, 1999, "Guide to Methods of Assessing the Acceptability of Flaws in Fusion Welded Structures," BSI, London, 1999.

[4] AFCEN (1985) "Design and Construction Rules for Mechanical Components of FBR Nuclear Islands" RCC-MR, Appendix A16, AFCEN, Paris.

[5] Tan, M., Celard, N. J. C, Nikbin, K. M., Webster, G. A., "Comparison of Creep Crack Initiation and Growth in Four Steels Tested in the HIDA Project: Advances in Defect Assessment in High Temperature Plan," MPA Stuttgart, Germany 4 - 6 October 2000.

[6] Nikbin, K. M., "Consideration of Safety Factors in the Life Extension Modelling of Components Operating at High Temperatures," *Effects of Product Quality and Design Criteria on Structural Integrity, ASTM STP 1337*, R. C. Rice, D. E. Tritsch, Eds., ASTM International, West Conshohocken, PA, 1998.

[7] "Creep and Fatigue Crack Growth in High Temperature Plant," International HIDA Conference, *Journal of Materials at High Temperature*, Vol. 15, 1998.

[8] Nikbin, K. M., Smith, D. J., and Webster, G. A., "Prediction of Creep Crack Growth from Uni-axial Creep Data," Proceedings of the Royal Society, Series A, 396, 1984, pp.183-193.

[9] Nikbin, K. M., Smith, D. J., and Webster, G. A., "An Engineering Approach to the Prediction of Creep Crack Growth," *Journal of Engineering Material and Technology*, ASME, 108, pp.186-191, 1986.

[10] Saxena, A., "Evaluation of Crack Tip Parameters for Characterizing Crack Growth: Results of the ASTM Round-Robin Program," Materials at High Temperatures, Vol.10, 1992, pp. 79-91.

[11] Webster, G. A, Nikbin, K., Chorlton, M. R, Cellard, N. J. C, Ober, M, "A Comparison of High Temperature Defect Assessment Methods," *Journal of Materials at High Temperature*, Vol. 15, 1998.

[12] Ainsworth, R. A., "Approximate Non-Linear Fracture Mechanics Calculations Using Reference Stress Technique," Proc. Joint ASME/JSME PVP Conf., Honolulu, Hawaii, ASME PVP, 170, July 23-27, 1989, pp. 13-20.

[13] Miller, A. G., "Review of Limit Loads of Structures Containing Defects," *International Journal of Pressure Vessel and Piping*, 32, 1899, pp. 197-267.

[14] Ainsworth, R. A. and Budden, P. J. "Design and Assessment of Components Subjected to Creep," *Journal Strain Analysis*, 29, 1994, pp. 201-208.

[15] Webster, G. A., Nikbin, K. M., Chorlton, M. R., Celard, N. J. C., Ober, M., "A Comparison of High Temperature Defect Assessment," *Journal of Materials at High Temperature*, 15(3/4) 1998, pp.337-347.

[16] ABAQUS, HKS, " Non-linear finite element package," 2000.

[17] Raju, I. S. and Newman, J. C. "Stress-Intensity Factors for Internal and External Surface Cracks in Cylindrical Vessels," *Journal of Pressure Vessel Technology*, Vol. 104,1982, pp. 293-298.

[18] Bettinson, A, Nikbin, K. M., N. O'Dowd, N, Webster, G. A., "The Influence of Constraint on Creep Crack Growth in 316H Stainless Steel," *Structural Integrity in the 21st Century*, Eds. J. H. Edwards et.al., EMAS, 219-22, Sept., Cambridge, 2000, pp. 149-159.

Appendix A: Expressions for Reference Stress

Loading and Stresses for the Pipe under Pressure and Bending

The four-point loaded pressurized pipe gives rise to bending (σ_b) and tensile stresses (σ_{xx}) at the crack tip. Internal pressure gives rise to axial, hoop and radial stresses in the nominal section of the component. In this instance, both hoop and radial stresses are neglected since they do not contribute to crack opening in the axial direction (only mode I is considered). Axial stresses (σ_{xx}) are obtained from

$$\sigma_{xx}(r) = const = P \cdot \frac{R_i^2}{\left(R_o^2 - R_i^2\right)} \tag{A1}$$

The four-point bend condition has been chosen to obtain a constant global bending moment between the supports. The bending moment M over the length of the pipe is given by

$$M(x) = P \cdot \langle x \rangle - P \cdot \langle x - A \rangle \tag{A2}$$

with x is the distance from the centre of the pipe and A the length from the centre of the pipe to the loading point as shown in Fig. 1 giving

$$\left.\frac{\partial M}{\partial x}\right|_{x \geq A} = 0 \tag{A3}$$

Bending stress resulting from the application of this global bending moment can be obtained by the integration of

$$M = -\int_0^{2\pi R_o} \int_{R_i} r^2 \cdot \cos\theta \cdot \psi(r,\theta)\, dr \cdot d\theta \tag{A4}$$

where

$$\psi(r,\theta) = \sigma(r,\theta) - \frac{N}{A} \tag{A5}$$

and

$$N = \int_0^{2\pi R_o} \int_{R_i} r \cdot \sigma(r,\theta) \cdot dr \cdot d\theta \tag{A6}$$

where r is the distance from the crack tip and θ is the polar co-ordinate. For pure cantilever, $N=0$ and $\psi = \sigma$ assuming a linear stress distribution (i.e. if the pipe remains elastic) defined by $p(r,\theta)$ *gives*

$$p(r,\theta) = -\frac{\sigma_b}{R_o} \cdot r \cdot \cos\theta \tag{A7}$$

$$M = -\frac{\sigma_b}{R_o} \cdot \int_0^{2\pi} \int_{R_i}^{R_o} r^3 \cdot \cos^2\theta \cdot dr \cdot d\theta \tag{A8}$$

The outer fiber bending stress is then given by

$$\sigma_b = \frac{4 \cdot R_o}{\pi \cdot \left(R_o^4 - R_i^4\right)} \cdot M \tag{A9}$$

The Codes of Practice [1-4] propose a number of formulae for the reference stress in various forms: separately for pressure loading or for bending or in the form of a combined pressure and bending formula. Under combined loading a conservative estimate to the limit load could be obtained from [11]:

$$\frac{P}{P_{LC}} + \frac{M}{M_{LC}} \leq 1 \tag{A10}$$

$$\sigma_{refC}^{T} + \sigma_{refC}^{B} \leq \sigma_{mat} \tag{A11}$$

$$\sigma_{ref}^{TB} = \sigma_{ref}^{T} + \sigma_{ref}^{B} \tag{A12}$$

where superscripts T and B are for P_{LC} and M_{LC} are the collapse load and collapse moments.

A16 [4] however, uses a different formula for combining references stresses in tension and bending. The expression for the reference stress takes into account on the one hand the membrane and local bending stress through the thickness of the pipe and on the other hand the global bending moment of the pipe giving

$$\sigma_{refC}^{TB} = \sqrt{\left(\sigma_{refC}^{T}\right)^2 + \left(\sigma_{refC}^{B}\right)^2 + \frac{1}{\sqrt{3}} \cdot \sigma_{refC}^{T} \cdot \sigma_{refC}^{B}} \tag{A13}$$

The use of either formula to combine the reference stress in tension and bending gives rise to two distinct loci for the equivalent reference stress under combined.

For pipes under internal pressure, the A16 [4] formula given below assumes a defect of rectangular shape with characteristic lengths a and c. It also assumes a plane stress thin shell solution with global collapse

$$\sigma_{ref}^{T} = \sqrt{\left[\frac{P\cdot\left(R_i^2+1/2\cdot a\cdot c\right)}{\left(R_o^2-R_i^2\right)-1/2\cdot a\cdot c}\right]^2+\left[\frac{P\cdot R_m}{W}\right]^2+\frac{1}{\sqrt{3}}\cdot\frac{P\cdot\left(R_i^2+1/2\cdot a\cdot c\right)}{\left(R_o^2-R_i^2\right)-1/2\cdot a\cdot c}\cdot\frac{P\cdot R_m}{W}} \tag{A14}$$

For bending, A16 suggests a formula validated for thin pipes (plane stress) and with the same assumptions for the extent of collapse and the yield criterion so that

$$\sigma_{ref}^{B} = \frac{M\cdot R_o}{\pi\cdot\left(R_m+\frac{a}{2}\right)^3\cdot(W-a)\cdot\left(cos\left(\frac{\beta}{2}\cdot\frac{a}{W}\cdot\frac{\pi}{4}\right)-0.5\frac{a}{W}\cdot sin\left(\beta-\frac{\pi}{4}\right)\right)\cdot\gamma} \tag{A15}$$

where M is the bending moment and P is the pressure.

R5 [1] refers to the R6 [2] manual for reference stress calculations. It contains a very comprehensive compendium of solutions for limit loads, where all variables (extent of collapse, state of stress, yield criterion and loading conditions) are represented for a wide range of configurations. In order to keep the analysis simple at this stage of the procedure, the chosen reference stress solution for internal pressure was based on an axisymmetric external defect. Axisymmetry also implies global collapse. Under such conditions, the limit load is given by:

$$P_{LC} = \frac{(R_o-a)^2-R_i^2}{R_i^2}\cdot\sigma_y \tag{A16}$$

$$\sigma_{refC} = \frac{P\cdot R_i^2}{(R_o-a)^2-R_i^2} \tag{A17}$$

and the bending solution under the same assumptions:

$$M_{LC} = \frac{4}{3}\cdot\sigma_y\cdot\left((R_o-a)^3-R_i^3\right) \tag{A18}$$

$$\sigma_{refC} = \frac{M}{\frac{4}{3}\cdot\left((R_o-a)^3-R_i^3\right)} \tag{A19}$$

where σ_{refC} is the reference stress of a cracked component. In Fig. 7 the same formulae were used but assuming that no defect is present in pipe (setting a=c=0). The growth of the defect is then taken into account by the stress intensity factor solution only.

BS 7910 [3] uses the reference stress solution given as

$$\sigma_{ref} = \frac{\left\{(\sigma_m + \sigma_b)\cdot\pi\cdot\left(1-\frac{a}{W}\right)+2\cdot\frac{a}{W}\cdot sin\left(\frac{c}{R_m}\right)\right\}}{\left(1-\frac{a}{W}\right)\cdot\left\{\pi-\left(\frac{c}{R_m}\right)\cdot\left(\frac{a}{W}\right)\right\}} \qquad \text{(A20)}$$

where σ_m is the membrane and σ_b is the bending stress. This formula is valid under combined tension and bending. The formula is based on a circumferential internal surface flaw and can be used for external surface flaws in cylinders. It assumes local collapse

Although all the solutions for defect dimension a/W<0.4 are broadly in agreement, for larger crack depths (a/W=0.8) 'local' estimates of σ_{ref} can be up to about 70% greater than 'global' values which can report in a substantially different prediction in crack growth.

Collapse solutions for the plate

For cracked plates subjected to primary membrane and primary bending stress, information on recommended reference stresses may be obtained from BS 7910 [3], R6 [2] and A16 [4]. For more complex geometries, with and without defects, valuable sources of information are also given in the compendia produced by Miller [11].

It should be noted that usually for partially penetrating defects in plate structures, the recommended calculations are often based on a so-called 'local' limit load, which seeks to reflect the limited strain capacity of the ligament ahead of the crack tip. The intent is to define a limited region over which the 'local' limit load is determined. This is the region shown as local in Fig. (4b).

The reference stress from BS7910 [3], which is termed the effective 'net section stress' is given by:

$$\sigma_{ref} = \frac{\sigma_b + 3\sigma_m\alpha\left[(\sigma_b + 3\sigma_m\alpha)^2 + 9\sigma_m^2(1-\alpha)^2\right]^{0.5}}{3(1-\alpha)^2} \qquad \text{(A21)}$$

where,

$$\sigma_b = \frac{6M}{2BW^2} \quad \text{and} \quad \sigma_m = \frac{P}{2BW} \qquad \text{(A22)}$$

$$\alpha = \begin{cases} \dfrac{a/W}{1+W/c} & \text{for} \quad 2B \geq (c+W) \\ \left(\dfrac{a}{W}\right)\left(\dfrac{c}{2B}\right) & \text{for} \quad 2B < (c+W) \end{cases} \tag{A23}$$

where σ_m and σ_b is the membrane and the bending stresses respectively. It can also be seen that an average crack depth is selected in this case.

A summary of the reference stress given in R6 [2], using pure bending and the Tresca criterion, gives the reference stress by the following equation:

$$\sigma_{ref} = \frac{6M/2BW^2}{\dfrac{1}{2\xi+2c}\left(\dfrac{6}{W^2}\right)\left\{2\xi\dfrac{W^2}{4}+2c\dfrac{W^2}{4}\left(1-\dfrac{a}{W}\right)^2\right\}} \tag{A24}$$

where for global collapse the geometric constant $\xi = W$ and for local collapse $\xi = (W-a)$.

Finally for A16 [4] the reference stress is given by

$$\sigma_{ref} = \frac{\sigma_b}{3}\sqrt{\left(\frac{\sigma_b}{3}\right)^2 + \sigma_m^2} \tag{A25}$$

where,

$$\sigma_b = \frac{6M}{2BW^2} \quad \text{and} \quad \sigma_m = \frac{P}{2BW - \pi a c/2} \tag{A26}$$

The above are examples of relevant reference stresses that have been applied in the analysis. There are however many other options which may also affect the calculations. This highlights the difficulty of producing a uniform, agreed and validated set of closed solutions for generic component shapes.

Christophe Poussard,[1] Claude Sainte Catherine,[2] Pierre Forget,[3] and Bernard Marini[4]

On the Identification of Critical Damage Mechanisms Parameters to Predict the Behavior of Charpy Specimens on the Upper Shelf

Reference: Poussard, C., Sainte Catherine, C., Forget, P., and Marini, B., **"On the Identification of Critical Damage Mechanisms Parameters to Predict the Behavior of Charpy Specimens on the Upper Shelf,"** *Predictive Material Modeling: Combining Fundamental Physics Understanding, Computational Methods, and Empirically Observed Behavior, ASTM STP 1429,* M. T. Kirk and M. Erickson Natishan, Eds., ASTM International, West Conshohocken, PA, 2003.

Abstract: The use of sub-sized Charpy-V specimens to monitor the mechanical properties of reactor pressure vessel (RPV) steels is receiving increasing attention. It is motivated by the fact that a smaller amount of material can be used to obtain the fracture properties, which can be of great economical interest when dealing with activated materials. Prior to use reduced-size specimens, investigations are still necessary to verify that the properties obtained from sub-sized specimens are comparable to those obtained from standard size specimens. Amongst the approaches that are available, the local approach to failure, which combines a description of the material microstructure (void density, distance between inclusions...) and empirical observations, is a promising way to investigate the transferability of mechanical properties. It has been successfully used to describe the macroscopic behavior of a wide range of cracked or notched specimens and components of various dimensions but restricted so far to quasi-static loading conditions.

The results discussed in the paper are focused on the upper shelf behavior of the French RPV material, equivalent to the American ASTM A508 Cl.3 material. Modeling of the material is achieved using the Rousselier coupled damage constitutive equations. This model is implemented in CAST3M, a general-purpose finite element code developed by the French Atomic Energy Agency. Comparisons between the numerical results and the experimental observations are given and the computed local temperature elevations and plastic strain rates discussed to explain the behavior of the specimens.

Keywords: Damage fracture mechanics, RPV steel, upper shelf, conventional and sub-sized Charpy specimens, finite element modeling

[1] Research Engineer, COMMISSARIAT A L'ENERGIE ATOMIQUE, DEN/DMN, Nuclear Material Department, F-91191 GIF SUR YVETTE CEDEX, FRANCE.

[2] Head of Laboratory, COMMISSARIAT A L'ENERGIE ATOMIQUE, DEN/DMN, Nuclear Material Department, F-91191 GIF SUR YVETTE CEDEX, FRANCE.

[3] Research Engineer, COMMISSARIAT A L'ENERGIE ATOMIQUE, DEN/DMN, Nuclear Material Department, F-91191 GIF SUR YVETTE CEDEX, FRANCE.

[4] Head of Laboratory, COMMISSARIAT A L'ENERGIE ATOMIQUE, DEN/DMN, Nuclear Material Department, F-91191 GIF SUR YVETTE CEDEX, FRANCE.

Introduction

The use of sub-sized Charpy-V specimens to monitor the mechanical properties of RPV steels is receiving increasing attention. This is motivated by the fact that a smaller amount of material can be used to obtain fracture properties, which can be of great economic interest when dealing with activated materials. Also, specimens may be machined from broken halves of previously tested conventional Charpy specimens which, at the end, allows increasing substantially the number of experimental results that may be collected for a given volume of material.

Before using reduced-size specimens, investigations are still necessary to verify that the properties obtained from sub-sized specimens are comparable to those obtained from standard size specimens. It is known that absolute ductile to brittle transition temperatures and upper shelf energies depend strongly upon the geometry and the size of the specimens. Amongst the approaches that are available, the local approach to failure, which combines a description of ductile damage (void density, growth and coalescence) and empirical observations is a promising way to investigate the transferability of mechanical properties. It has been successfully used to describe the macroscopic behavior of a wide range of cracked or notched specimens and components of various dimensions but restricted so far to quasi-static loading conditions.

The results discussed in the paper are focused on the upper shelf behavior of the French RPV material, equivalent to the American ASTM A508 Cl.3 material. Modeling of the material is achieved using the Rousselier coupled damage constitutive equations [1] implemented in CAST3M [2], a general-purpose finite element code developed by the French Atomic Energy Agency to support its research investigations. This model accounts for the presence of voids in the matrix of the material that may grow and coalesce when subjected to external loading.

The purpose of the work is to identify and model the different physical phenomena that may affect the results obtained from impact testing on the upper shelf. Dynamic effects including striker impact, imposed specimen bending vibrations and wave propagation as well as friction effects will not be discussed in this paper because it has been shown in an earlier work [3] that, on the lower shelf, it is sufficient to account for strain rate effects on the material stress-strain curve to reproduce the specimen behavior successfully. However, on the upper shelf, both strain rate effects and temperature elevation during impact are likely to influence locally the mechanical behavior of the material, the material at the notch root, ductile crack extension and therefore the global response of the specimens.

Material

Material Origin

The material investigated in this project is a low alloy Manganese ferritic steel with Nickel and Molybdenum additions. It is referenced as 16MND5 in the French designation and is very close to from the American ASTM A508 Cl.3. The batch of material originates from the nozzle opening of a real nuclear pressure vessel forged by Creusot Loire Industry for Electricité de France. It is therefore perfectly representative of the

material used to manufacture the vessel of 1300 MW PWRs. This batch of material has already been largely investigated in preceding studies and in particular in [4-8]. The chemical composition is given in Table 1.

Table 1 - *Chemical composition for PWR 16MND5 steel.*

		C	Mn	Si	Ni	Cr	Mo	Cu	S	P	Al	V
Mes. 3/4 thickness		0.159	1.37	0.24	0.70	0.17	0.50	0.06	0.008	0.005	0.023	<0.01
Imposed	Min		1.15	0.10	0.50		0.43					
RCC-M [9]	Max	0.22	1.60	0.30	0.80	0.25	0.57	0.20	0.015	0.02	0.04	0.03

Thermal treatment of this steel includes three different steps:

- Quenching : after austenitization at 865/895°C during 4h40, water quenching by product immersion was performed. This step was repeated two times.
- Recovering : 630/645°C during 7h30 followed by a cooling step in free air.
- Stress relief : was performed at 610°C for 8h00.

The specimens were machined at 3/4 of the nozzle thickness. For tensile specimens, the direction is axial (T) whilst for Charpy and toughness tests, the direction is axial-radial (T-S).

Microstructure

Metallographical observation of the material achieved using an optical microscope [6] reveals a bainitic microstructure (Figure 1a, after Nital chemical attack) and the presence of manganese sulfides (MnS) inclusions (Figure 1b, without chemical attack). Figure 1c shows the microstructure along the three orientations.

An analysis of the material microstructure has been performed [5, 6] in order to determine average inclusion parameters such as the initial void volume fraction and the spatial distribution of the inclusions used for the micro-mechanical modeling. The analysis has revealed ellipsoidal MnS inclusions (12x10x8 μm) that can be reasonably assumed to be spherical with an average diameter of 10 μm. Franklin's [10] formula gives a value void volume fraction of 3.9×10^{-4}, which is approximately two times lower than the value resulting from image analysis (9.4×10^{-4} in the T direction). The analysis has also shown that the average distance between inclusions (determined from the number of inclusions per surface unit assuming an homogeneous inclusion distribution) is close to 100μm. Another analysis (based upon a Delaunay triangulation) gave a larger value (about 270 μm), which supports the view that the spatial distribution of the inclusions is non-uniform and that most MnS inclusions are gathered in clusters.

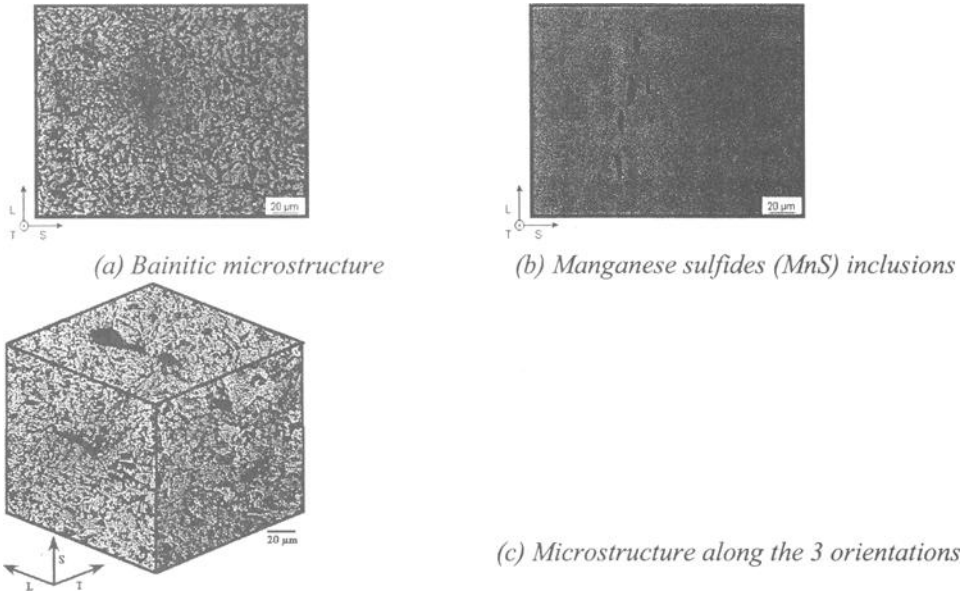

Figure 1 – *Material microstructure (from [6]).*

Basic Mechanical Properties

The material characterization of the steel has been performed with round tensile specimens over a range of temperatures between –196°C and 30°C. The standard tensile material properties (strain rate of 4.10^{-4} s^{-1}) are shown in Figure 2. The material yield stress σ_y, the ultimate tensile stress σ_{UTS} and the uniform elongation A_g% decrease with temperature whilst the total elongation A% and reduction of area at rupture Z% increase between –196°C up to –125°C.

Although not shown here, fractographic examination of NT (notched tensile) specimens has been performed [6], and ductile damage initiated on MnS inclusions prior to cleavage fracture has been almost systematically observed above –100°C.

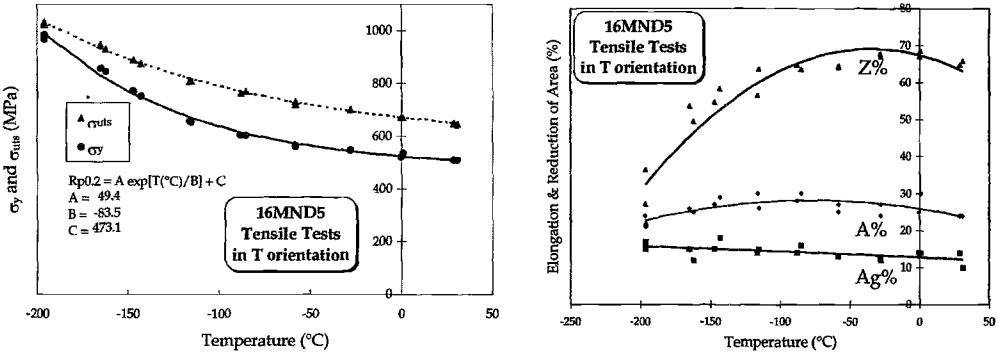

Figure 2 – *16MND5 basic mechanical properties.*

Impact Strength

The geometry and the main dimensions of the conventional and sub-size Charpy-V specimens are shown in Figure 3. The test device used for conventional Charpy-V tests is an instrumented 350 J impact machine. Both the testing machine and the specimen geometry are in conformity with the EN-10045 standard [11]. For the sub-size specimens, the test device used is a 50 J sub-size pendulum equipped with an automatic specimen positioning system. The striker is instrumented with strain gauges, and an optical sensor is installed on the pendulum mass for displacement measurement. Specimens, striker and anvil geometries are in accordance with ESIS TC5 Draft 9 [12].

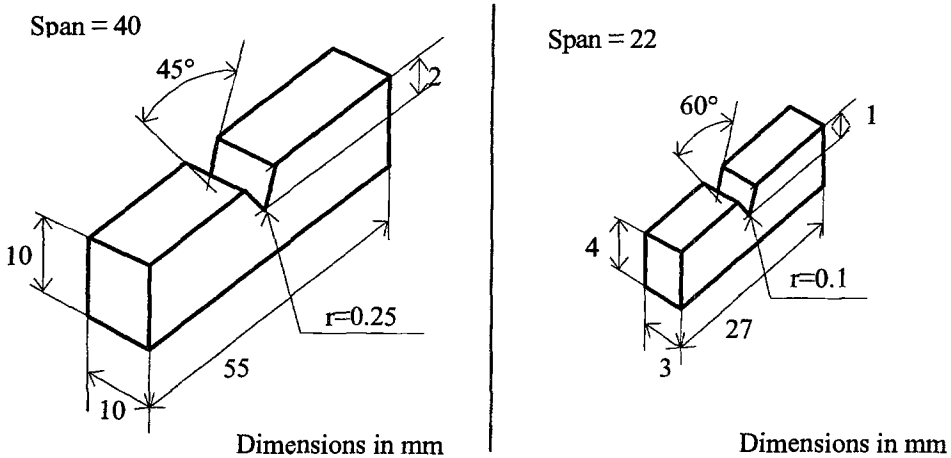

(a) Charpy-V specimen *(b) Sub-size Charpy specimen*

Figure 3 - *Main dimensions of (a) Charpy-V specimen (from [11]) and (b) sub-size Charpy specimen (from [12]).*

A careful calibration of the temperature losses during specimen transfer from the furnace to the support until impact has then been performed for sub-size Charpy specimens. It has been shown that during transfer (1.85 seconds), the temperature correction varies respectively from +3°C at –150°C down to -10°C at 300°C. Additional detailed information on the experimental procedure and calibration of the load cells can be found in reference [3].

More than 100 Charpy-V specimens have been used to establish the transition curve (Figure 4a). This gives a reliable shape and well-identified characteristic points. It is also of great value to perform a confidence interval evaluation. For the sub-size geometry, more than 60 specimens have been broken, which also gives a good definition of the transition curve (Figure 4b). Characteristic values have then been determined using the Oldfield hyperbolic tangent adjustment [13]:

$$E(J) = A + B \cdot tgh\left[\frac{(T - T_0)}{C}\right] \quad (1)$$

The results are summarized in Table 2. The temperature index (TK) corresponding to a particular energy level, which is commonly equal to 68 J for Charpy-V and 3.1 J for sub-size Charpy, is also indicated. It can be noticed that the ductile to brittle transition

temperature shift (ΔDBTT) is equal to 66.7°C, and the temperature index shift (ΔTK) equals to 62.5°C. The ratio between upper shelf energies is 23.8 but 6.3 only for lower shelf energies. Finally, the results show that the scatter associated with sub-size Charpy appears to be greater than the one observed for Charpy-V. This however requires further confirmation.

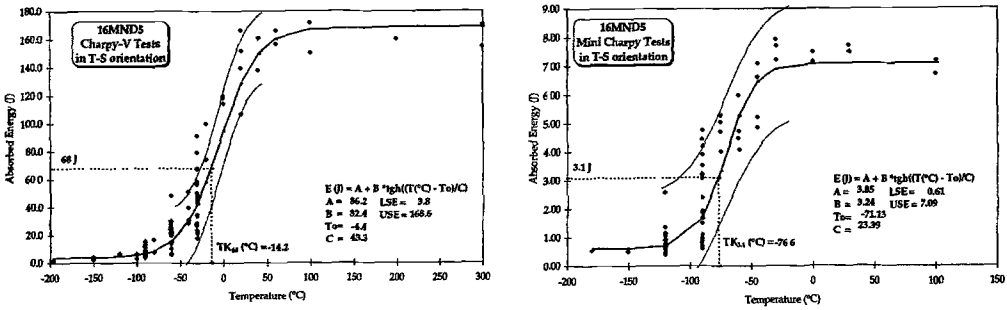

(a) Charpy-V specimens *(b) Sub-sized specimens*

Figure 4 - *16MND5 absorbed energy transition curve for (a) Charpy-V and (b) sub-size specimens.*

Table 2 - *Characteristic parameters of the hyperbolic tangent adjustments.*

E (J)	A (J)	B (J)	To (°C)	C (°C)	LSE (J)	USE (J)	TK (°C)
Charpy-V	86.2 ± 4.3	82.4 ± 5.0	-4.4 ± 4.0	43.3 ± 6.4	3.8 ± 9.3	168.6 ± 9.3	-14.2
Sub-size	3.8 ± 0.46	3.2 ± 0.63	-71.1 ± 7.4	23.4 ± 15.0	0.6 ± 1.1	7.1 ± 1.1	-76.6

Material Modeling

Rousselier Model Constitutive Equation

The model used for the simulation is the Rousselier model [1] as implemented in CAST3M [2], a general Finite Element (FE) code developed by CEA. This model is based on a thermodynamic approach of porous media in which both the current void volume fraction f and the effective plastic strain p are considered as internal variables. It allows one to account for the presence of voids in the matrix of the material as well as for the influence of the hydrostatic stress responsible for the fracture mechanism. The constitutive equations of this model are based upon the Von Mises yield condition extended for porous media:

$$f(\sigma,R,f)=\frac{\sigma_{eq}}{\frac{1-f}{1-f_0}}+D.\sigma_1.f.\exp\left(\frac{\sigma_h}{(1-f).\sigma_1}\right)-R(p) \qquad (2)$$

where f_0 is the initial void volume fraction, $R(p)$ is the tensile stress-strain curve of the material, σ_{eq} is the Von Mises equivalent stress, σ_h is the hydrostatic stress, D is an

integration constant for the model and σ_1 characterizes the flow stress of the material matrix, which is related to the yield strength and the hardening of the material. The evolution of the void volume fraction depends upon the plastic strain rate and is defined by $\dot{f}=(1-f)tr\dot{\varepsilon}_P$ where $\dot{\varepsilon}_P$ is the effective plastic strain rate. In this model, no account is given to nucleation and an initial void volume fraction f_0 has to be specified. The Rousselier model, as implemented in CAST3M, includes a modification proposed by Seidenfuss [14] to account for the coalescence of voids. This modification allows to perform fracture mechanics calculations [15] and consists in comparing the current value of f to a critical value, f_c. If $f=f_0$, the material is damage-free, if $f_0<f<f_c$, the material is damaged and if $f=f_c$, the material is fully damaged and void coalescence occurs (the stresses at the Gauss points are forced to 0).

Quasi-static Material Behavior

The quasi-static temperature dependent material stress-strain curves as determined by Renevey [6] have been used as an input in the FE calculation (Figure 5). Poisson ratio is equal to 0.3 and Young's modulus depends upon temperature [4].

Strain Rate Effects

Since the Charpy test is a dynamic test, strain rate hardening effects are likely to occur in the steel depending upon strain rate fields. Rossoll et al. [7, 8] have shown that strain rate is a significant parameter for this RPV steel, even at low temperatures such as -90°C. Static and dynamic compression tests (with Hopkinson bars), achieved over a wide range of temperatures, have allowed to identify the parameters (p_0=12 and $\dot{\varepsilon}_0=10^8\ s^{-1}$) of the following Cowper and Symonds relationship:

$$\sigma_{DYN}=\sigma_{STAT}\cdot\left[1+\left(\frac{\dot{\varepsilon}_p}{\dot{\varepsilon}_0}\right)^{1/p_0}\right] \tag{3}$$

Figure 6 represents the true stress-strain curve of the material resulting from the Cowper and Symonds relationship at 0°C. It shows that strain hardening has a pronounced effect on the material behavior.

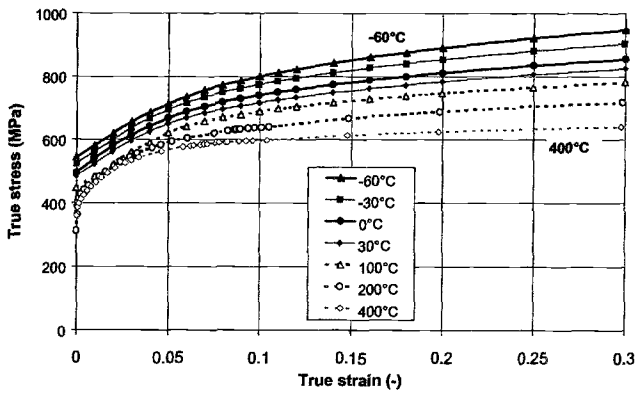

Figure 5 - *16MND5 quasi-static true stress-strain curves* ($\dot{\varepsilon}=4.10^{-4}\ s^{-1}$).

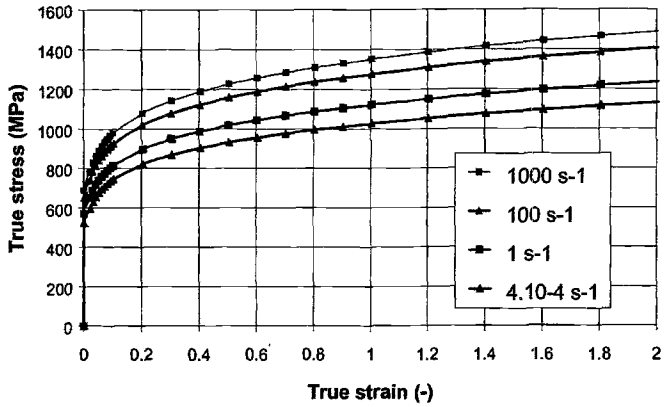

Figure 6 - *16MND5 true stress-strain curves at 0°C.*

Identification of Critical Damage Parameters to Model Ductile Tearing on The Upper Shelf at 0°C

Outline of the Model Parameters Identification Procedure

The procedure developed and adopted by CEA [16] to identify micro-mechanical damage parameters for ductile crack extension in ferritic or austenitic steels was used in these investigations. It results from a wide number of computations applied to a number of structures and components made of various steels for which however only quasi-static loading conditions have been considered. Some of these investigations have been performed via Round Robins organized within the ESIS (European Structural Integrity Society) Technical Committee on Numerical Methods [17] which will serve as baseline data to draft an extension to the already existing ESIS guideline [18], restricted so far to crack free specimens and components with uncoupled damage models and quasi-static loading conditions.

For the present investigations, this procedure was therefore modified to account for the strain rate dependence of the material stress-strain curve. The damage parameters to identify are the initial void volume fraction f_0 and the dimension of the square elements L_c (average distance between inclusions) to be used to model the material at the crack tip and along the crack growth path. Both of these parameters can be reasonably assumed to be independent upon temperature and strain rate. The σ_1 parameter of the Rousselier model however, which characterizes the flow stress of the material matrix has to be strain rate and temperature dependent. In contrast to the multiplicative form of the Gurson-Tveergaard and Needleman [19, 20] constitutive equation, the additive form adopted by Rousselier (eq. 2) implies that both the stress-strain curve and σ_1 have to be corrected to account for strain rate or temperature effects. Tanguy et al. [21, 22] have proposed modifying the original Rousselier model to account for such effects and have succeeded in predicting the ductile behavior of Charpy specimens. Another possibility, exposed below, consists in defining σ_1 as a function of temperature and strain rate, identified from

uniaxial NT tests results performed at different temperatures and imposed strain rate conditions. In the present work, the model was simply updated to account for a strain rate dependency of σ_1, the influence of temperature being much less pronounced over the range of temperatures under consideration. Further work is however underway to account for both effects simultaneously to model the brittle to ductile transition.

Identification of f_0 from NT Specimens Subjected to Quasi-static Loading Conditions

For the material investigated in this work, f_0 has been first estimated with Franklin's formulae [10] and the material chemical composition (Table 1). This gives a value of $f_0=3.9\times10^{-4}$ that was then adjusted by comparing the result of computations to experimental test results obtained from NT specimens subjected to quasi-static loading conditions. In these calculations, the Rousselier damage parameters were assumed to be constants for strain rate independent materials (σ_1=445MPa, D=2 and f_c=0.05). Three different specimen geometries have been used with notch radii equal to 2, 4 and 6 mm for NT 2-6, 4-6 and 10-6, respectively. Also, test results obtained at temperatures ranging between –60°C and 0°C have been considered to evaluate the dependence of f_0 upon temperature.

Figure 7 shows that at 0°C, a value of $f_0=2\times10^{-4}$ describes well the influence of geometry whilst for a given geometry (Figure 8), it is shown that the temperature (ranging between –60°C and 0°C) has little influence on crack initiation. On these two figures, the plain lines represent the computed values and the lines with marks represent the experimental data. This value of f_0 is found to be in good agreement with the value derived from the chemical composition of the material but approximately four times less than the value arising from the microstructure analysis.

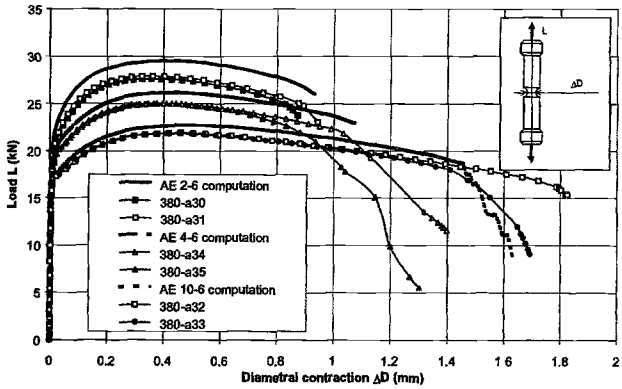

Figure 7 - *Calculated and experimental load versus diametrical contraction curves at 0°C with $f_0=2\times10^{-4}$ under quasi-static loading conditions - Influence of the geometry.*

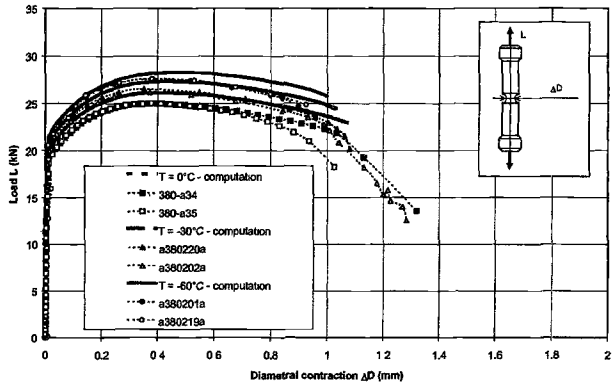

Figure 8 – *Calculated and experimental load versus diametrical contraction curves at 0°C with $f_0=2\times10^{-4}$ under quasi-static loading conditions -Influence of temperature.*

Identification of L_c from CT Specimens Subjected to Quasi-static Loading Conditions

The test results used for the identification of L_c have been obtained from two 20% side grooved (SG) CT25 specimens tested at 0°C and 30°C subjected to quasi-static loading conditions. With the side-grooved specimens, a 2D plane strain analysis is sufficient to reproduce the experimental observations. Crack extension is computed using a post-processing procedure that consists of comparing, at each load step and for the Gauss points of the elements in the remaining ligament, the value of f to f_c. As a Gauss point of an element reaches the critical void volume fraction, one half of the element length is considered to be damaged. Figures 9 and 10 show the comparison between calculated and experimental load versus CMOD and CMOD versus crack extension curves, respectively. It is shown that a very good correlation between the calculation and the observations is obtained with a *Lc* value of 200μm, a value close to that resulting from the microstructure observations of the mean distance between inclusions [6].

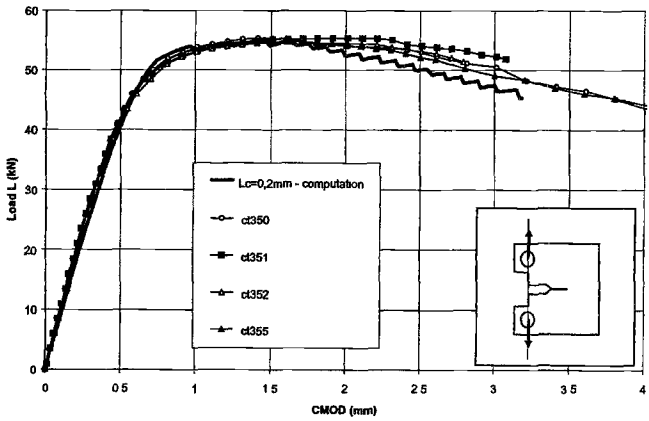

Figure 9 - *Calculated and experimental load versus CMOD curves at 0°C*

with $f_0=2\times10^{-4}$ and $L_c=0.2mm$.

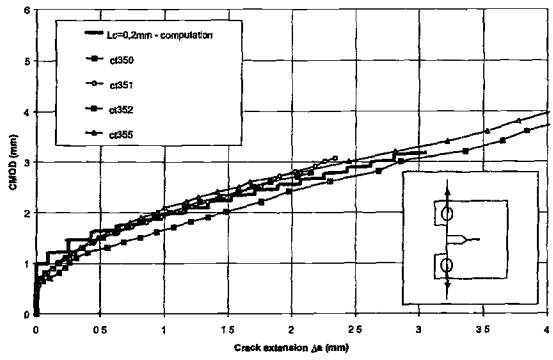

Figure 10 - *Calculated and experimental CMOD versus crack extension curves at 0°C with $f_0=2\times10^{-4}$ and $L_c=0.2mm$.*

Identification of σ_1

The dependency of σ_1 with respect to strain rate was calibrated from an analysis of the strain rate material yield strength (Figure 11). At 0°C, the temperature of interest for the Charpy and subize specimen computations, for low strain rates close to quasi-static loading conditions (less than $5\text{x}10^{-4}$ s^{-1}), the value of σ_y is indeed close to 445 MPa, the value of σ_1 commonly used to simulate quasi-static tests. At higher strain rates (greater than $1\text{x}10^{3}$ s^{-1}), σ_y approaches 700 MPa. In the computations, it was therefore assumed that σ_1 would vary as σ_y with strain rate. Figure 12 shows the results of mechanical computations of a NT specimen (NT10-6) performed for strain rates between $4\text{x}10^{-4}$ s^{-1} up to $1\text{x}10^{4}$ s^{-1}. It shows that as the strain rate increases, a constant σ_1 value leads to a decrease of the diametrical contraction at initiation (Figure 12a) whereas with a strain rate dependent σ_1, the load bearing capacity of the specimen increases (Figure 12b), but the diametrical contraction at crack initiation remains almost constant. This is in good agreement with the experimental results obtained by Tanguy et al. [21, 22] for the same geometry but for another cast of the material (Figure 2c). The drop of diametrical contraction at initiation observed experimentally for load line velocities greater than 10mm/mn corresponds to a significant increase of temperature.

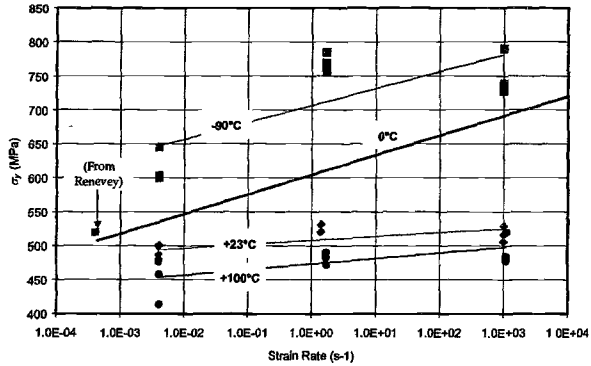

Figure 11 - *Strain rate dependence of yield strength (σ_y).*

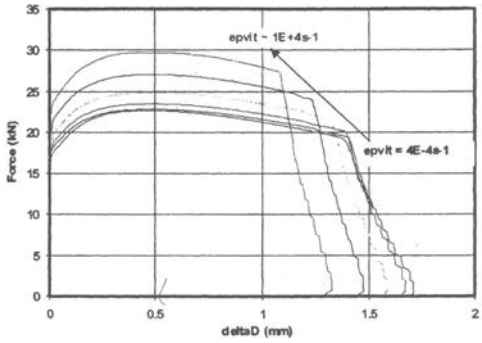

(a) Global NT specimen response with constant σ_l (σ_l=445MPa)

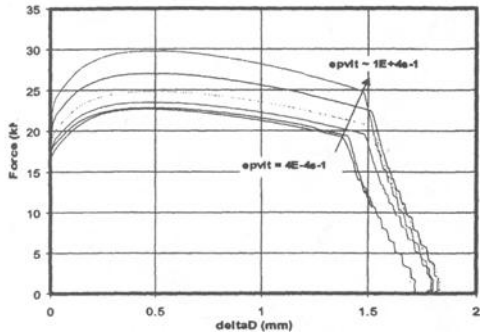

(b) Global NT specimen response with calibrated σ_l

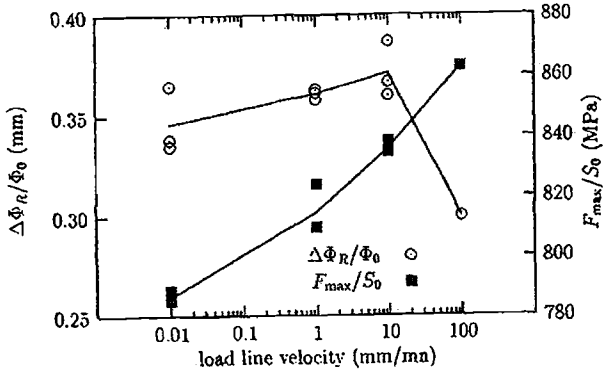

(c) Experimental diametrical contraction at crack initiation (from [21, 22])

Figure 12 – *Rousselier model computation of a NT 10-6 specimen at 0°C.*

Discussion

Meshes Used to Simulate Ductile Tearing in Charpy-V and Sub-size Charpy Specimens

Both 2D and 3D simulations have been carried out in this work to investigate the influence of adiabatic heating and strain rate effects. For the 3D modeling, the symmetry planes allow modeling only 1/4 of the specimen. CUB20 reduced integration elements with 20 nodes and 8 Gauss points are used to model the specimen, the striker and the anvil, the latter two being considered as perfectly rigid. Contact conditions without any inter-penetration nor friction are imposed to the specimen, anvil and striker. The anvil is fixed on the back in the vertical direction and at one point in horizontal direction. A displacement is imposed at the back face of the striker. The ligament is modeled with calibrated elements along the crack growth path with the L_c value identified from the CT specimen. In total, the meshes are composed of 2560 and 1365 elements with 13220 and 7451 nodes for the Charpy-V and sub-size Charpy specimens, respectively.

Influence of Strain Rate and Adiabatic Heating (2D Modeling)

Figure 13 compares 2D FE computations with the result of two sub-size Charpy tests performed at 0°C. The results reported in this figure refer to quasi-static computations and strain-rate dependent computations including adiabatic heating or not. Perfect adiabatic heating is assumed in the calculation, i.e., conduction was neglected since the test duration is less than 2ms, which corresponds to a conduction distance of 190μm. At this stage of the analysis, the influence of strain rate on σ_I was neglected.

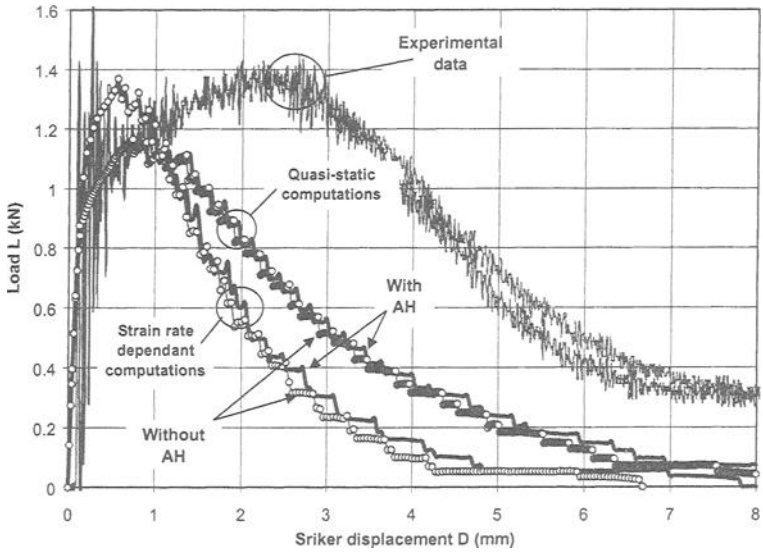

Figure 13 - *Comparison between 2D FE calculations and sub-size Charpy test results at 0°C.*

The results show that the strain rate affects the results significantly. It increases the maximum load and the crack growth rate once initiation has occurred. Figure 14 shows the temperature elevation that arises in both specimens at different imposed striker displacements. It indicates that at the early stages of impact, the maximum temperature is obtained at the notch root. The temperature increases rapidly in the material under the striker and becomes greater than at the notch root as the crack propagates. A maximum of 133°C and 110°C for the conventional and sub-sized geometry, respectively, is obtained at the notch root whilst in the ligament, the temperature elevation remains negligible. In the material located under the striker, the temperature elevations reach 280 and 241°C, respectively.

Despite these large values of temperature elevation, adiabatic heating has only a minor influence on the global behavior, as shown in Figure 13. This is attributed to the fact that the temperature rises are very localized and are negligible for the ligament, therefore not sufficient to affect the global mechanical specimen behavior nor crack propagation. It is however important to bear in mind that at lower temperatures, in the ductile-brittle

transition, adiabatic heating may be sufficient to shift locally at the crack tip from a cleavage failure mode to a ductile failure mechanism.

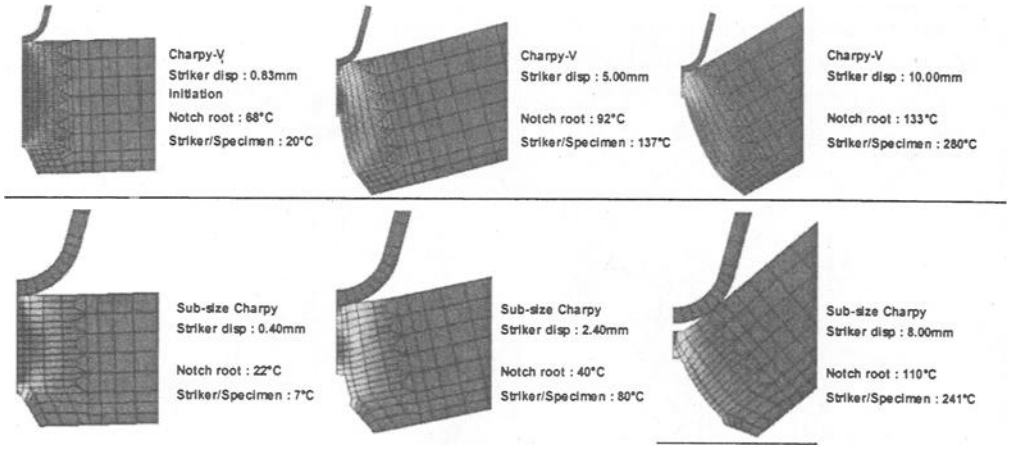

Figure 14 – *Adiabatic temperature rise for Charpy-V and sub-sized specimens at 0°C.*

3D FE Simulations With Strain Rate Dependent σ_1 Parameter

Figures 15 and 16 compare the global response of the specimens resulting from 3D FE computations with experimental data. The 3D modeling was achieved since from Figure 13, it is clear that the 2D modeling does not allow to predict satisfactorily the load-displacement curves. The results obtained with a constant value of σ_1 and a variable value are given for both geometries. The results clearly indicate that the dependence of the σ_1 parameter with strain rate allows one to describe well the observed behaviors. An excellent agreement is obtained for the sub-size specimen whilst for the conventional Charpy specimen, the correlation between the computation and the experimental data is acceptable.

Also shown for the sub-sized specimen is the result of a 3D computation that includes both the influence of strain rate and temperature on the stress-strain curve. At this temperature, adiabatic heating does not influence the global mechanical behavior of the specimen as much as the strain rate. Figures 17 and 18 give the temperature elevation and the plastic strain rate in the ligament of the conventional Charpy specimen for a 4 mm striker displacement. On these figures, the fully damaged elements have been removed, allowing one to visualize crack growth. A pronounced tunneling effect is predicted, which favorably compares with the experimental observations. As expected, the maximum temperature elevation (183°C) is obtained at the crack front on the shear lips that forms on the free surfaces due to high plastic deformation localization. High temperatures are also predicted in the material under the striker (about 140°C) whilst at the crack front on the mid-thickness, the temperature elevation does not exceed 80°C, in agreement with the 2D results.

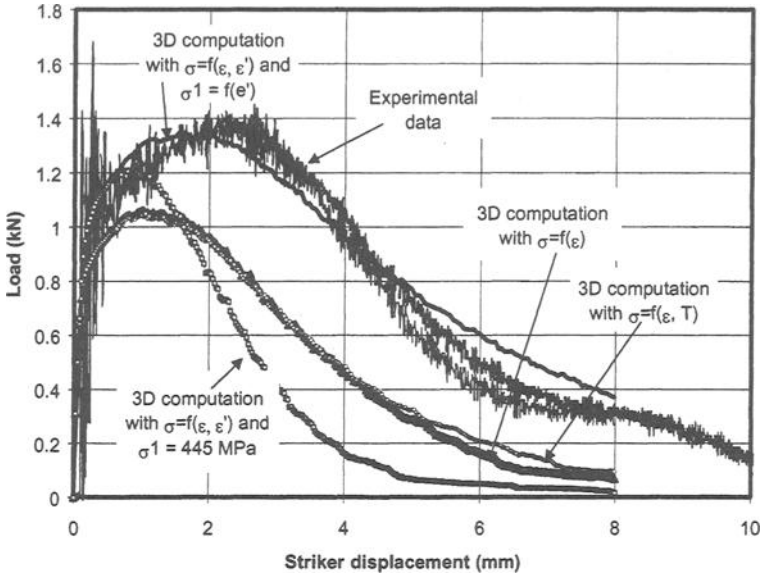

Figure 15 - *3D sub-size Charpy computational results at 0°C.*

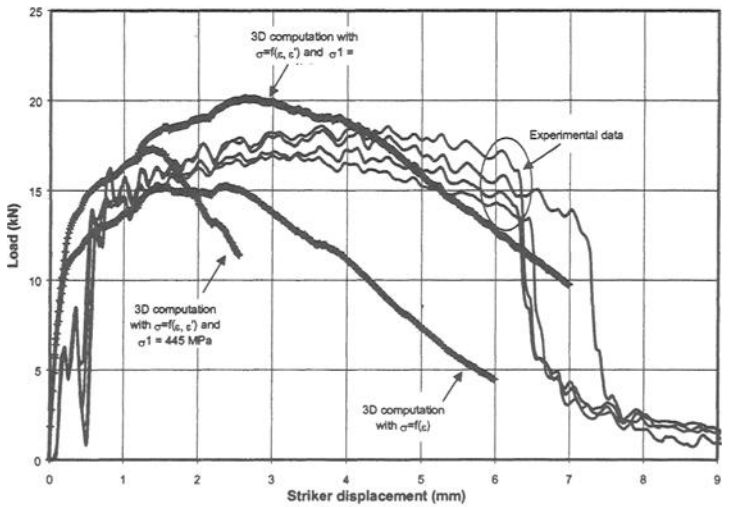

Figure 16 - *3D Charpy computational results at 0°C.*

Isovalues of the plastic strain rate (Figure 18) show that, in contrast to the temperature elevations, the maximum value is obtained at the crack front at the mid-thickness position (4830 s^{-1}). Large values of plastic strain rate are also obtained in the material under the striker (around 4000 s^{-1}). The main difference, however, with the temperature field is that the whole ligament has a high average plastic strain rate (about 100 s^{-1}), which necessarily influences significantly the global behavior of the specimens.

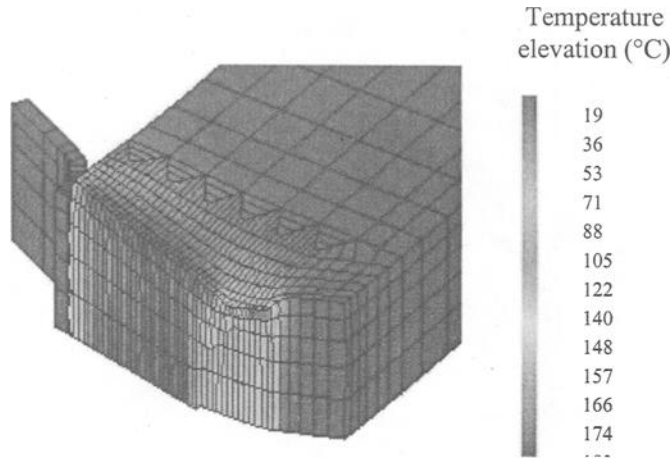

Figure 17 – *Computed temperature elevation for the conventional Charpy specimen at 0°C with a 4 mm striker displacement.*

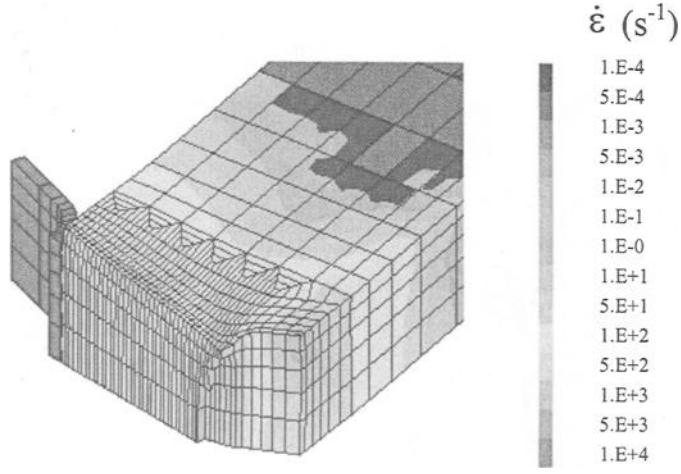

Figure 18 – *Computed plastic strain rate for the conventional Charpy specimen at 0°C with a 4 mm striker displacement.*

Concluding Remarks

This paper has reviewed both experimental and numerical investigations that have been performed to investigate the behavior of un-irradiated sub-size Charpy and conventional Charpy-V specimens made of the French 16MND5 RPV steel, a steel equivalent to the American ASTM A508 Cl.3. The purpose of the work was to verify that the local approach to failure could be used to describe the behavior of such specimens.

Ductile tearing at 0°C was computed using the Rousselier coupled damage model for which the damage parameters have determined with an identification procedure that uses both uniaxial tensile specimens (smooth and notched) data and conventional ductile

tearing tests resulting from CT specimen. All these tests have been performed under quasi-static loading conditions and do not reflect the hardening or softening of the material due to strain rate or temperature for example that prevails in impact testing.

It has been demonstrated that the original Rousselier model can however successfully predict the behavior of the dynamic tests provided that strain rate effects are accounted for, both on the stress-strain curve of the material and on the σ_1 parameter which, in this model, characterizes the mechanical resistance of the matrix of the material. 2D and 3D modeling has shown that the ligament undergoes an average plastic strain rate of about $100s^{-1}$ which significantly influences the global mechanical behavior of the specimen. It was also shown that despite high temperature elevation (greater than 100°C), adiabatic heating has little influence on the global mechanical behavior and crack propagation on the upper shelf since it remains localized at the shear lips of the specimen and in the material under the striker. However, it may have to be taken into account at lower temperatures in the ductile-brittle transition region.

References

[1] Rousselier, G., "Les Modèles de Rupture Ductile et leurs Possibilités Actuelles dans le Cadre de l'Approche Locale", EDF, Service Réacteurs Nucléaires et Echangeurs, Les Renardières, BP 1, F-77250, Moret-Sur-Loing, France, (1986).

[2] CAST3M, Finite element code developed by CEA, DEN/DM2S/SEMT/LM2S, F-91 191 Gif sur Yvette, France, http://www.castem.org:8001, (2001).

[3] Sainte Catherine, C., Poussard, C., Vodinh, J., Schill, R., Hourdequin, N., Galon, P., And Forget, P., "Finite Element Simulations and Empirical Correlation for Charpy-V and Subsize Charpy Tests on an Unirradiated Low-Alloy RPV Ferritic Steel", *Small Specimen Test Techniques: Fourth Volume, ASTM STP 1418,* M. A. Sokolov, J. D. Landes, and G.E. Lucas, Eds, American Society for Testing Materials, West Conshohocken, PA, 2002.

[4] Genty, A., "Etude Expérimentale et Numérique de l'Amorçage et de l'Arrêt de Fissure, sous Choc Thermique dans un Acier Faiblement Allié (16MND5)", PhD Thesis, Ecole des Mines de Paris, France (1989).

[5] Bauvineau, L., "Approches Locale de la Rupture Ductile : Application à un Acier Carbone-Manganèse", PhD Thesis, Ecole des Mines de Paris, France, (1996).

[6] Renevey, S., "Approches Globales et Locales de la Rupture dans le Domaine de la Transition Fragile-Ductile d'un Acier Faiblement Allié", PhD Thesis, CEA Report R-5784, (1998).

[7] Rossoll, A., Berdin, C. , Forget P., Prioul, C. And Marini, B., "Mechanical Aspects of the Charpy Impact Test", *Nuclear Engineering and Design*, Vol. 188, pp. 217-229, (1999).

[8] Rossoll, A., "Fracture Toughness Determination of a Low Alloy Steel by Instrumented Charpy Impact Test", Ph.D. Thesis, CEA and Ecole Centrale de Paris, France, November, (1998).

[9] RCC-M, "Design and Construction Rules for Mechanical Components of PWR Nuclear Islands", AFCEN, Paris, (1985).

[10] Franklin, A.G., "Comparison Between a Quantitative Microscope and Chemical Methods for Assessment of non Metallic Inclusions", *J. of the Iron and Steel Institute*, (1969).

[11] EN 10045, "Essai de Flexion par Choc sur Eprouvette Charpy", Parties 1 et 2, AFNOR, Octobre (1990).

[12] ESIS TC 5, European Structural Integrity Society, Technical Committee n°5 on Dynamic Testing Standards, "Proposed Standard Method for Instrumented Impact Testing of sub-size Charpy-V Notch Specimens of Steels", Draft 9, March, (2000).

[13] Oldfield, W., "Curve Fitting Impact Test Data : A Statistical Procedure", *ASTM Standardization News*, November, (1975), pp. 24-29.

[14] Seidenfuss, M., "Untersuchungen zur Beschreibung des Versagensverhaltens mit Hilfe von Schadigungsmodellen am Beispiel des Werkstoffes 20 MnMoNi 5 5", PhD Thesis, MPA Stuttgart, GERMANY, (1992).

[15] Poussard, C. And Seidenfuss, M., "On the Simulation of Ductile Crack Growth using the Rousselier Model", *Transaction of the 14th SMIRT conference*, GW/7, pp. 673-680, Lyon, France, (1997).

[16] Poussard, C., Sainte Catherine, C. And Miannay, D., "Finite Element Modeling of a Smooth Tensile Specimen and a Compact Tension Specimen with the Gurson-Tveergard-Needleman and Rousselier Micro-mechanical Models", ECF 13, San Sebastian, Spain, September, (2000).

[17] Bernauer, G. And Brocks, W., "Micro-Mechanical Modelling of Ductile Damage and Tearing – Result of a European Numerical Round Robin", GKSS Report Nb 2000/15, GKSS, Geesthacht, GERMANY, (2000).

[18] ESIS, "ESIS P6-98 : Procedure to measure and calculate material parameters for the local approach to fracture using notched tensile specimens", European Structural Integrity Society, Eds Karl-Heinz Schwalbe, GKSS, Geesthacht, GERMANY, (1998).

[19] Gurson, A.L., "Continum Theory of Ductile Rupture by Void Nucleation and Growth - Part I : Yield Criteria and Flow Rules for Porous Ductile media", *Transaction of the ASME*, January (1977).

[20] Needleman, A; And Tvergaard, V., "An Analysis of Ductile Rupture in Notched Bars", *J. Mech; Phys. Solids*, Vol. 32, No 6, pp 461-490, (1984).

[21] Tanguy, B., "Modélisation de l'Essai Charpy par l'Approche Locale de la Rupture. Application au Cas de l'Acier16MND5 dans le Domaine de la Transition", PhD Thesis, Ecole des Mines de Paris, France, (2001).

[22] Tanguy, B. And Besson, J., "An Extension of the Rousselier Model to Predict Viscoplastic Temperature Dependant Materials", To be published in International Journal of Fracture, (2001).

Electronic Materials

Fumiyoshi Minami,[1] *Wataru Takahara,*[1] *and Tetsuya Nakamura*[1]

Interface Strength Evaluation of LSI Devices Using the Weibull Stress

Reference: Minami, F., Takahara, W., and Nakamura, T., **"Interface Strength Evaluation of LSI Devices Using the Weibull Stress,"** *Predictive Material Modeling: Combining Fundamental Physics Understanding, Computational Methods, and Empirically Observed Behavior, ASTM STP 1429,* M. T. Kirk and M. Erickson Natishan, Eds., ASTM International, West Conshohocken, PA, 2003.

Abstract: Interface fracture strength is evaluated by the Weibull stress criterion for LSI devices composed of epoxy resin and Fe-Ni alloy sheet. The difference in coefficient of thermal expansion of the epoxy resin and Fe-Ni sheet causes a stress singularity at the corner ends of the device in the cooling process during LSI packaging, which is responsible for the interface fracture of the device. It is shown that the critical Weibull stress, an integrated stress over the stressed body along the interface, at fracture initiation is almost independent of the package geometry, although both the local stresses and the singularity parameters in the LSI device significantly depend on it. Shape design to decrease the Weibull stress values would be effective to improve the LSI devices reliability.

Keywords: interface strength, delamination, dissimilar material joints, LSI devices, package geometry, local approach, Weibull stress

Introduction

Interface fracture evaluation is important not only for fundamental fracture mechanics [1-7] but also for electronics industry [8-17]. Electronic devices consist of multi-layered structures of different materials. Mismatch of the thermal coefficients of expansion often causes delamination at the interface in electronic packaging because of the high thermal stresses near the bond edge [8, 9, 12, 15-18]. Simple but accurate evaluation of interface strength is required to improve the reliability of electronic packages. Considerable progress has been made toward understanding the interfacial strength. However, a clear assessment procedure has not yet emerged because the stresses have a singularity near the idealized interface edge [1]. Hattori et al. proposed a stress singularity parameter approach using two stress singularity parameters, λ and K in

$$\sigma = K / r^{\lambda} \tag{1}$$

where σ is the thermal stress, r is the distance from the singularity point of bond edge, K is the intensity of stress singularity, and λ is the order of stress singularity [8-11]. They

[1]Professor, Research Associate and Graduate Student, respectively, Department of Manufacturing Science, Graduate School of Engineering, Osaka University, 2-1 Yamada-Oka, Suita, Osaka 565-0871, Japan.

evaluated delamination criteria using these two parameters, λ and K in plastic-encapsulated LSI device models composed of epoxy base resin and Fe-Ni alloy sheets [8-10]. In resin-molded electronic material, the molding material becomes an adhesive and the delamination might be caused by the thermal stress under the cooling process. The analytical model proposed by Hattori et al. [8, 9] is based on two-dimensional joints. Xu and Nied discussed the stress singularity for three-dimensional corners [15]. However, the singularity order λ changes with the specimen geometry in both two- and three-dimensional edges. Consequently, the criterion $K=K_{cr}$ loses the physical meaning for the evaluation of fracture strength of bonded joints with different geometries.

Here we reanalyze the fracture data reported by Hattori et al. [8, 9] for plastic encapsulated LSI devices composed of epoxy base resin and Fe-Ni alloy sheets. Interface strength is evaluated by the Weibull stress in the local approach [18-23], which is a singularity independent parameter.

Delamination Test of Resin and Fe-Ni Alloy Bonding Specimens

Experimental details on the delamination test were reported in the literature [8, 9]. Two materials bonding specimens composed of epoxy base resin and Fe-Ni sheets were used. Figure 1 shows the three metal-resin models used for the delamination tests. Two materials were bonded at the curing temperature 170°C for five hours. During the cooling process from the curing temperature to room temperature, thermal stress generated and delamination occurred at the corners. The delamination was detected using two strain gauges mounted on both the resin and the metal surfaces. Temperature of the models was measured with thermocouples. Figure 2 shows the test results of the temperature changes to initiation of delamination ΔT from the curing temperature [8, 9].

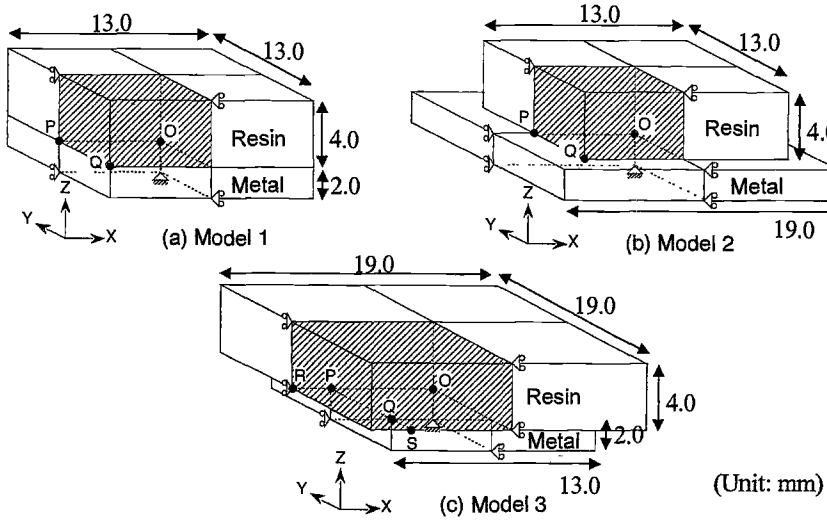

Figure 1 – *Models for metal-resin bonded specimens.*

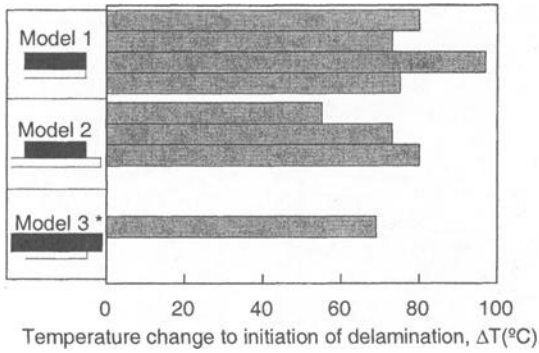

Figure 2 – *Delamination test results of metal-resin bonded specimens* [8,9] (*Model 3: Average data).

Thermal Stress Analysis

In order to evaluate the thermal stress distribution, three-dimensional elastic FE-analysis was conducted. The FE-code employed was ABAQUS ver.5.8. Figure 3 shows the FE-model used for the analysis of Model 1. Because of symmetry, one quarter model was used. The material constants of Fe-Ni alloy are as follows: Young's modulus E=148GPa, Poisson's ratio ν=0.3 and coefficient of thermal expansion α=5.0 × 10^{-6}/°C. Those of resin are E=14.7GPa, ν=0.25 and α=19.0 × 10^{-6}/°C. These material constants were assumed to be independent of the temperature in the analysis. The two-dimensional plane strain analysis was also performed for comparison with the three-dimensional analysis. The minimum element size was assumed to be 0.01mm×0.01mm×0.01mm for all three models. It was confirmed that analysis with the smaller mesh also gives the same λ value of stress singularity parameter.

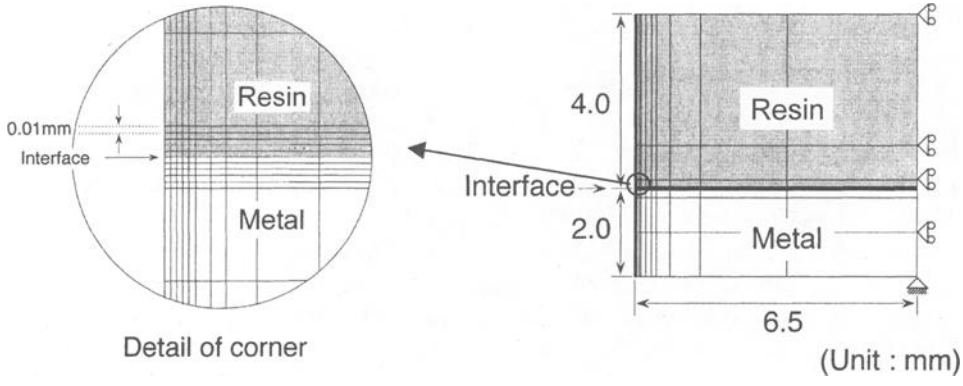

Figure 3 – *FEM mesh of model 1 (Z-X plane).*

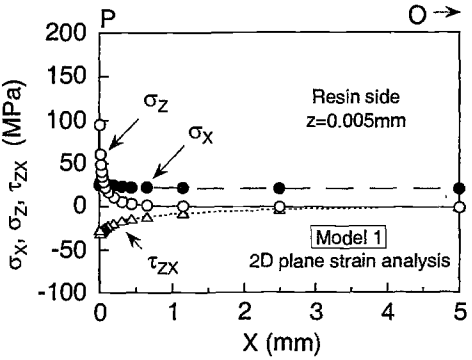

Figure 4 – *Stress distributions in resin side close to bonded interface obtained by 2D plane strain FE-analysis (Model 1, ΔT=100°C).*

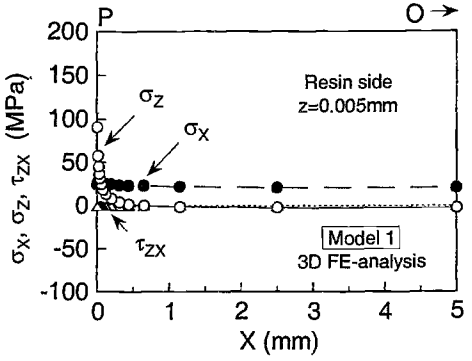

Figure 5 – *Stress distributions in resin side close to bonded interface obtained by 3D FE-analysis (Model 1, along P-O line, ΔT=100°C).*

Results of Thermal Stress Analysis

The delamination criteria using stress singularity parameters by Hattori et al. is based on two-dimensional analysis [8, 9]. However, the package is actually a three-dimensional object and has corners. It is necessary to make clear an essential difference in the two- and three-dimensional analysis [15]. Figure 4 and Figure 5 show the stress distribution in the resin side close to bonded interface obtained by FE-analysis when the temperature decreases to 70°C from 170°C (ΔT=100°C). Figure 4 and Figure 5 are the results of two-dimensional plane strain and three-dimensional analysis, respectively. In the three-dimensional model of Figure 5, the distribution is along the P-O line in Model 1 of Figure 1. Although the normal stress components σ_z and σ_x have similar distribution both in two- and three-dimensional models, the shearing stress component τ_{zx} is largely different in two- and three-dimensional analysis. As shown in Figure 5, the shearing stress τ_{zx} is sure not to be caused by the symmetry of the three-dimensional object in Figure 1. In two-dimensional analysis, τ_{zx} is caused by the constraint on the deformation in y-direction perpendicular to the P-O line direction. It is necessary to consider the three-dimensional analysis in the dissimilar material joints.

Figures 6, 7 and 8 show the stress distribution under the temperature decrease into 70°C from 170°C (ΔT=100°C) in resin side close to bonded interface along the Q-P line of model 1, 2 and 3, respectively. The normal stress σ_z distribution level around the Q point in the P-Q line of Figure 6 is higher than the level around P point in the O-P line of Figure 5 in Model 1. Further, the shearing stress τ_{zx} clearly generates at the Q point in the P-Q line of Figure 6 although the τ_{zx} is zero in Figure 5. These results indicate that the stress environment near the three-dimensional corner is more severe than that near the two-dimensional edge [15]. So, the actual three-dimensional analysis is very important to investigate the delamination criteria. Comparing the effect of model geometry on stress around the Q point, normal stress σ_z of Model 2 is largest and that of Model 3 is smallest. On the other hand, the absolute value of shearing stress τ_{zx} is large in Model 3. Outside

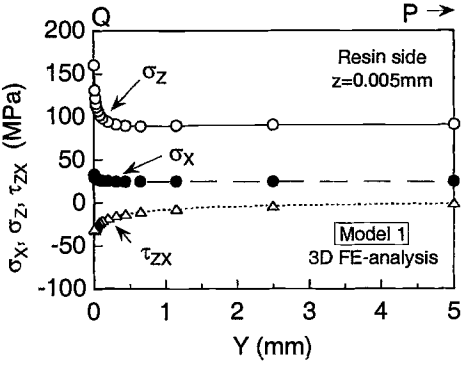

Figure 6 – *Stress distributions in resin side close to bonded interface obtained by 3D FE-analysis (Model 1, along Q-P line, ΔT=100°C).*

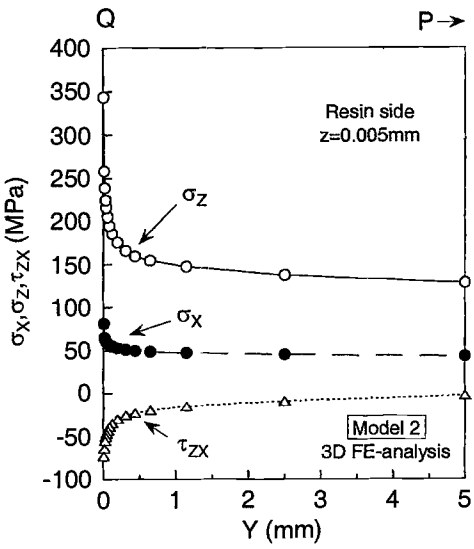

Figure 7 – *Stress distributions in resin side close to bonded interface obtained by 3D FE-analysis. (Model 2, along Q-P line, ΔT=100°C).*

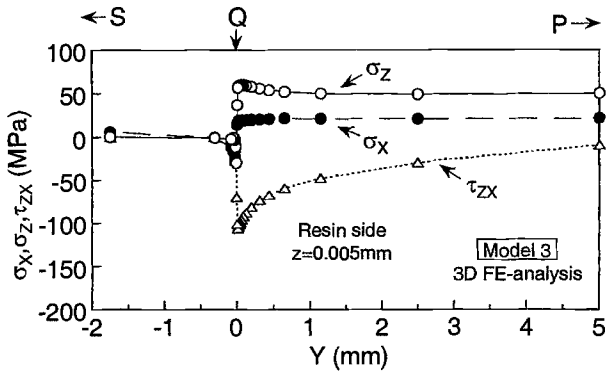

Figure 8 – *Stress distributions in resin side close to bonded interface obtained by 3D FE-analysis (Model 3, along S-Q-P line, ΔT=100°C).*

resin has a large coefficient of thermal expansion in Model 3. In cooling process a large amounts of resin shrink and this causes the increase of shearing stress component.

Evaluating the Delamination Strength

Figures 9, 10 and 11 show the dalamination strength evaluated by normal, shearing and maximum principal stress, respectively. Every kind of critical stress varies remarkably in

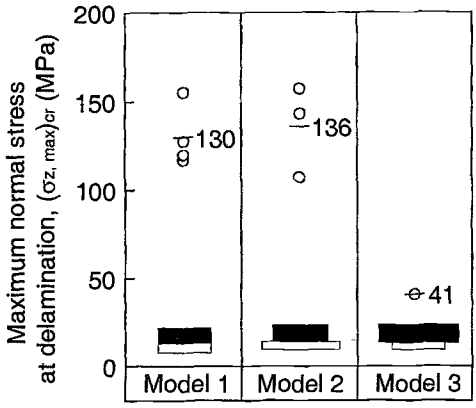

Figure 9 – *Delamination criteria using maximum normal stress.*

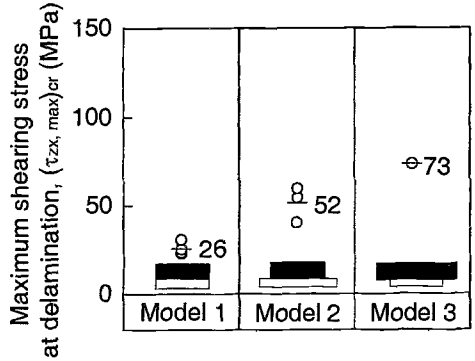

Figure 10 – *Delamination criteria using maximum shearing stress.*

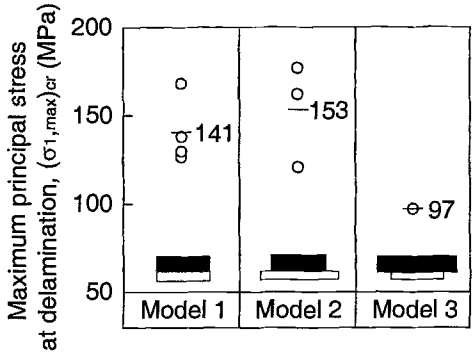

Figure 11 – *Delamination criteria using maximum principal stress.*

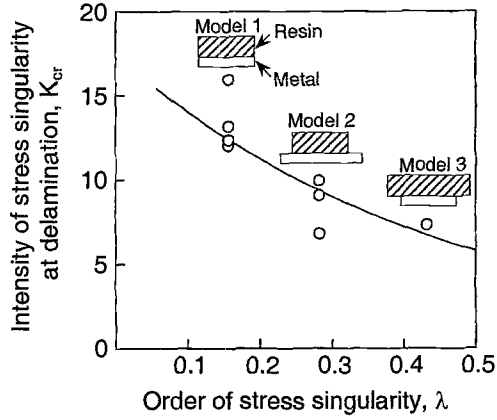

Figure 12 – *Delamination criteria using stress singularity parameters K and λ.*

the three models of 1,2 and 3. These local stresses can be confirmed not to be evaluation parameters for delamination strength. Figure 12 shows the delamination criteria using stress singularity parameter [8, 9]. Although one can draw a critical curve as shown in this figure proposed by Hattori et al. [8, 9], not only the order of stress singularity λ but also the intensity of stress singularity at delamination K_{cr} are different in these three models. The different order of λ leads the different dimension of the stress singularity parameter and one does not know the physical meaning of the dimensional difference.

Application of the Weibull Stress Criterion

This paper applies the Local Approach [18, 19] to estimate the delamination strength [22, 23]. The local approach employs the Weibull stress σ_w as a fracture driving force. The Weibull stress σ_w is given by the integration of an effective stress σ_{eff} over a fracture process zone in the form

$$\sigma_W = \left[\frac{1}{V_0} \int_{V_f} \left[\sigma_{eff} \right]^m dV_f \right]^{1/m} \tag{2}$$

where m is the Weibull shape parameter of the material, and V_0 and V_f are a reference volume defined in the local approach and the volume of the fracture process zone, respectively. The local approach assumes that the onset of unstable fracture is controlled by the instability of the weakest microcrack in the fracture process zone.

The glass transition temperature T_g of the present resin is about 170°C. The delamination temperatures are much lower than the T_g. The resins show glass-brittle behavior because the resins consist of a network of carbon atoms covalently bonded together to form a rigid solid. The debonding seemed to occur in the resin side by examination using a scanning electron microscope and an energy dispersive X-ray spectroscopy [2] and only the resin side region is considered as the V_f to calculate the Weibull stress σ_W. Since the crack plane is parallel to the interface, the effective stress σ_{eff} is given by

$$\sigma_{eff} = \sqrt{\sigma_y^2 + \frac{4\tau_{xy}^2}{(2-\nu)^2}} \tag{3}$$

where σ_y and τ_{xy} are the normal stress and the shear stress, respectively.

The critical Weibull stress $\sigma_{W,cr}$ at fracture obeys the Weibull distribution with two paraneters m and σ_u

$$F(\sigma_{W,cr}) = 1 - \exp\left[-\left(\frac{\sigma_{W,cr}}{\sigma_u} \right)^m \right] \tag{4}$$

which is expected to be a material property independent of the specimen geometry. Since the m-value does not depend on the reference volume V_0, a unit volume is convenient to V_0 for calculating the Weibull stress [21]. The iteration procedure using the maximum likelihood method was employed for the determination of the m-value [21]. The likelihood estimate of m is obtained when the moment m-value derived from a statistical sample of $\sigma_{W,cr}$ is consistent with an assumed m-value used for the calculation of $\sigma_{W,cr}$ [23].

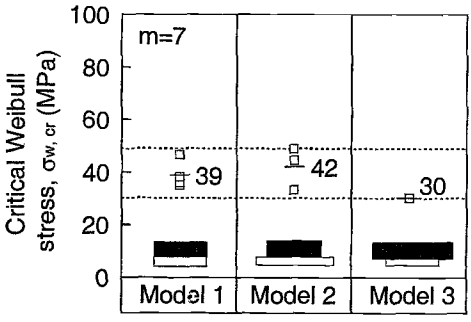

Figure 13 – *Delamination criteria using Weibull stress values.*

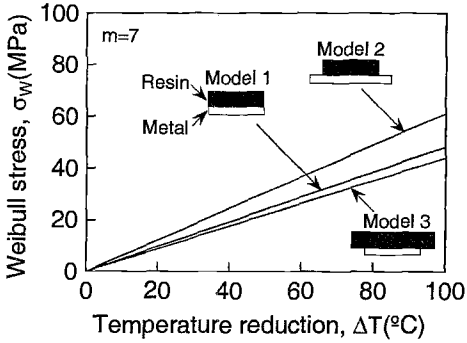

Figure 14 – *Weibull stress values generated by the thermal loading.*

[2] Iwasa, M., and Httori, T., personal communication, May 2000.

From the experimental delamination data of Figure 2, m = 7 and σ_u = 39MPa were obtained. Figure 13 shows the delamination strength evaluated by the Weibull stress. The critical Weibull stresses at delamination occurrence are almost the same in all models with different package geometry. Some uncertainty might remain regarding the m-value since the experimental sample is limited. Assuming other m-values such as m=5, 10, 20, absolute Weibull stresses change. However, we confirmed that the critical Weibull stresses are independent of the specimen geometry in package under each m-value. This means that the delamination strength of dissimilar material joint by the Weibull stress is a material property independent of the geometrical condition of the specimen.

Figure 14 shows the relationship between Weibull stress and the reduction temperature from the curing temperature for the three models. This is the elastic analysis and a linear dependence is observed in this figure. Because the Weibull stress is largest, Model 2 seems to be most severe. To improve the reliability of the dissimilar material joints, it would be effective to avoid the geometry pattern of Model 2 in LSI devices design if the plastic material region would be a fracture origin. That is to say, shape design concept to decrease the Weibull stress field would be effective to improve the LSI devices reliability.

Conclusions

Interface fracture strength of plastic encapsulated LSI devices is analyzed by the Weibull stress criterion. Thermal stress of epoxy base regin and Fe-Ni alloy sheets are calculated by three-dimensional FE-analysis. The stress environment near the three-dimensional corner is more severe than near the two-dimensional edge. The actual three-dimensional analysis is very important to investigate the delamination criteria. Both the local stresses and singularity parameters depend strongly on the package shape. On the other hand, the Weibull stress criterion is almost independent of package geometry. The geometry pattern where the Fe-Ni alloy sheet extends outside seems to be most severe. Shape design concept to decrease the Weibull stress field would be effective to improve the LSI devices reliability.

Acknowledgment

The authors gratefully acknowledge Dr. Hattori and Dr. Iwasa of Hitachi, Ltd. for permission to use their experimental delamination data of this work.

References

[1] Bogy, D. B., "Two Edge-Bonded Elastic Wedges of Different Materials and Wedge Angles Under Surface Tractions," *ASME Journal of Applied Mechanics*, Vol. 38, 1971, pp. 377-386.

[2] Banks-Sills, L., and Ashkenazi, D., "A Note on Fracture Criteria for Interface Fracture," *International Journal of Fracture*, Vol. 103, 2000, pp. 177-188.

[3] Penado, F. E., "Analysis of Singular Regions in Bonded Joints," *International Journal of Fracture*, Vol. 105, 2000, pp. 1-25.

[4] Glushkov, E. V., Glushkova, N. V., Munz, D., and Yang, Y. Y., "Analytical Solution for Bonded Wedges under Thermal Stresses," *International Journal of Fracture*, Vol. 106, 2000, pp. 321-339.

[5] Klingbeil, N. W., and Beuth, J. L., "On the Design of Debond-Resistant Bimaterials Part I: Free-Edge Singularity Approach," *Engineering Fracture Mechanics*, Vol. 66, 2000, pp. 93-110.

[6] Klingbeil, N. W., and Beuth, J. L., "On the Design of Debond-Resistant Bimaterials Part II: A Comparison of Free-Edge and Interface Crack Approach," *Engineering Fracture Mechanics*, Vol. 66, 2000, pp. 111-128.

[7] Li, Y. L., Hu, S. Y., and Yang, Y. Y., "Stresses Around the Bond Edges of Axisymmetric Deformation Joints," *Engineering Fracture Mechanics*, Vol. 66, 2000, pp. 153-170.

[8] Hattori, T., Sakata, S., and Watanabe, T., "A Stress Singularity Parameter Approach for Evaluating Adhesive and Fretting Strength," *ASME Advances in Adhesively Bonded Joints* - MD-Vol. 6, Book No. G00485, 1988, pp. 43-50.

[9] Hattori, T., Sakata, S., and Murakami, G., "A Stress Singularity Parameter Approach for Evaluating the Interfacial Reliability of Plastic Encapsulated LSI Devices," *ASME Journal of Electronic Packaging*, Vol. 111, 1989, pp. 243-248.

[10] Kawai, S., Nishimura, A., Hattori, T., Kitano, M., and Shimizu, T., "Reliability Evaluation of Electronic Devices," *Materials Science and Engineering*, Vol. 143A, 1991, pp. 247-256.

[11] Nishimura, A., Hirose, I., and Tanaka, N., "A New Method for Measuring Adhesion Strength of IC Molding Compounds," *ASME Journal of Electronic Packaging*, Vol. 114, 1992, pp. 407-412.

[12] Xie, W., and Sitaraman, S. K., "Interfacial Thermal Stress Analysis of Anisotoropic Multi-Layered Electronic Packaging Structures," *ASME Journal of Electronic Packaging*, Vol. 122, 2000, pp. 61-66.

[13] Yeung, D. T. S., Lam, D. C. C., and Yuen, M. M. F., "Specimen Design for Mixed Mode Interfacial Fracture Properties Measurement in Electronic," *ASME Journal of Electronic Packaging*, Vol. 122, 2000, pp. 67-72.

[14] Hui, C. Y., Conway, H. D., and Lin, Y. Y., "A Reexamination of Residual Stresses in Thin Films and of the Validity of Stoney's Estimate," *ASME Journal of Electronic Packaging*, Vol. 122, 2000, pp. 267-273.

[15] Xu, A. Q., and Nied, H. F., "Finite Element Analysis of Stress Singularities in Attached Flip Chip Packages," *ASME Journal of Electronic Packaging*, Vol. 122, 2000, pp. 301-305.

[16] Ghaffarian, R., "Accelerated Thermal Cycling and Failure Mechanisms for BGA and CSP Assemblies," *ASME Journal of Electronic Packaging*, Vol. 122, 2000, pp. 335-340.

[17] Gu, Y., Nakamura, T., Chen, W. T., and Cotterell, B., "Interfacial Delamination Near Solder Bumps and UBM in Flip-Chip Packages," *ASME Journal of Electronic Packaging*, Vol. 123, 2001, pp. 295-301.

[18] Beremin, F. M., "A Local Criterion for Cleavage Fracture of a Nuclear Pressure Vessel Steel," *Metallurgical Transactions A*, Vol. 14A, 1983, pp. 2277-2287.

[19] Mudry, F., "A Local Approach to Cleavage Fracture," *Nuclear Engineering and Design*, Vol. 105, 1987, pp. 65-76.

[20] Minami, F., Brückner-Foit, A., and Trolldenier, B., "Numerical Procedure for Determining Weibull Parameters Based on The Local Approach," *Proceedings of the 8th Biennial European Conference on Fracture, ECF8*, Torino, Vol. 1, 1990, pp. 76-81.

[21] Minami, F., Brückner-Foit, A., Munz, D., and Trolldenier, B., "Estimation Procedure for the Weibull Parameters Used in the Local Approach," *International Journal of Fracture*, Vol. 54, 1992, pp. 197-210.

[22] Satoh, S., Tsukamoto, M., Minami, F., and Toyoda, M., "Evaluation of Interface Strength of Plasma Sprayed Coating by the Local Approach," *Proceedings of the 15th International Conference on Offshore Mechanics and Arctic Engineering (OMAE)*, Florence, Book No. G00987, Vol. 3, 1996, pp. 157-164.

[23] Satoh, S., Minami, F., Tsukamoto, M., and Toyoda, M., "Evaluation of Adhesive Strength of T-Notched Plasma Sprayed Coating by the Local Approach," Proceedings of the *17th International Conference on Offshore Mechanics and Arctic Engineering (OMAE)*, Lisbon, OMAE98-2183, 1998, pp. 1-8.

Computational Techniques

Andrew B. Geltmacher,[1] Richard K. Everett,[1] Peter Matic,[1] and Carl T. Dyka[2]

Computational Estimation of Multiaxial Yield Surface Using Microyield Percolation Analysis

Reference: Geltmacher, A. B., Everett, R. K., Matic, P., and Dyka, C. T., **"Computational Estimation of Multiaxial Yield Surface Using Microyield Percolation Analysis,"** *Predictive Material Modeling: Combining Fundamental Physics Understanding, Computational Methods and Empirically Observed Behavior, ASTM STP 1429*, M. T. Kirk and M. Erickson Natishan, Eds., ASTM International, West Conshohocken, PA, 2003.

Abstract: Measurements of multiaxial properties of materials, such as yield surfaces, damage surfaces and fracture limit surfaces, are a time and resource intensive problem. For three-dimensional (3D) multiaxial yield of a complex microstructure, hundreds of points are required at different 3D strain states to define a full yield surface to the resolution required for constitutive model implementation. Experimental determination of the effects generated by a specific microstructure on a multiaxial yield surface is hindered by the inability to produce multiple specimens with the exact same microstructure or the inability to subject the same specimen to multiple stress or strain states without changing its response. Full nonlinear analysis of a specific microstructure for such a large set of points is also prohibitive, due to the time constraints of solving large, 3D nonlinear problems. A technique has been developed that uses high resolution 3D tomographic images and finite element simulations to track the development of microplastic connectivity for actual material microstructures in an 1100 aluminum/TiB_2 particle composite. This information is then used to estimate the 3D multiaxial yield surface of the material in strain space for the imaged microstructures. The multiaxial yield surface is estimated using linear superposition and load scaling of three orthogonal displacement basis loads. Macroscopic yielding is defined as the percolation of microplastic elements across the model. Interval halving is used to solve for the scaling parameter, iterating to the value at which plastic flow percolation occurs and defining a point on the yield surface. Percolation can occur across one or more of the three directions defined by the model, but it need not occur simultaneously. A small selected set of nonlinear analyses is used as calibration for the estimated yield surface. The aim of this approach is to accelerate the process of building 3D multiaxial yield surfaces from microstructures and to gain insight into the material microstructure performance.

Keywords: Multiaxial yield surfaces, material properties, X-ray computed microtomography, image-based modeling, percolation analysis

[1]Materials Scientist, Section Head, and Branch Head, respectively, Multifunctional Materials Branch, Code 6350, Naval Research Laboratory, 4555 Overlook Ave. SW, Washington, DC, 20375.
[2]Mechanical Engineer, GEO-Centers, Inc., P. O. Box 441340, Fort Washington, MD, 20749.

Introduction

Materials properties, such as yield, damage, and fracture limit surfaces, are examples of important multiaxial data required for structural analyses. Current measurement techniques involve specialized and time-consuming experiments. Furthermore, the measurements are affected by and vary with the microstructure of the material. A rapid estimation technique for multiaxial material yield properties would allow cost-effective sensitivity analyses of structures and provide a new tool with which to examine microstructural performance.

Previous researchers has examined the role of microstructure on the effective elastoplastic response of materials, especially fiber and particle reinforced composites. A number of these studies were performed on two-dimensional (2D) periodic and random arrays of particles, for example see References [1-3]. Some of this work has been expanded into 3D by producing periodic arrays unit cell models [4,5]. These studies generally underestimate the role of second phase distributions by ignoring particle shape and clustering. Brockenbrough and co-authors examined the effect of actual microstructures in 2D by using Voronoi tessellations of aluminum/silicon alloy [6]. They examined the development of local stress and strain states due to particle clustering.

In this paper, we report on efforts to develop a procedure to translate 3D microstructural information into practical nonlinear material response predictions suitable for use by designers and analysts. Yield surface estimates are obtained from linear superposition and load scaling of three orthogonal displacement basis loads, as applied to a three dimensional image-based model. The estimation technique uses percolation analysis to generate the material yield surface.

A schematic example of a 2D percolation process is shown in Figure 1. This illustrates a notional two-phase material (e.g. a particulate reinforced composite) being loaded to yielding. As the specimen is loaded, small regions of microplasticity are formed around particles (or voids). Upon further loading, these regions of microplasticity grow, link up, and percolate across the specimen to produce macroscopic yielding.

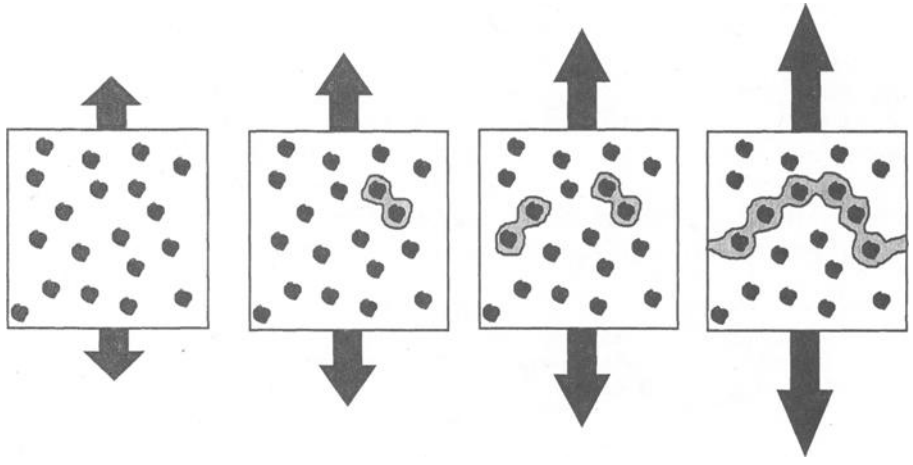

Figure 1 – *Schematic illustration of plasticity percolation in composite material.*

The procedure will be described in four steps: X-ray computed microtomography (XCMT), model generation, finite element modeling, and percolation analysis. In addition, comparisons to full nonlinear analyses and statistical results from the percolation analysis will be reported.

Material

The aluminum/TiB_2 composite material selected for this study is an excellent model system. The nominally 20 volume percent composite was manufactured using standard powder metallurgical techniques (cold isostatic pressing followed by hot extrusion). The median TiB_2 particle size was measured to be 10.4 μm. This processing produced the microstructure shown in Figure 2. The composite offers high particle-matrix contrast for X-ray computed microtomography (XCMT).

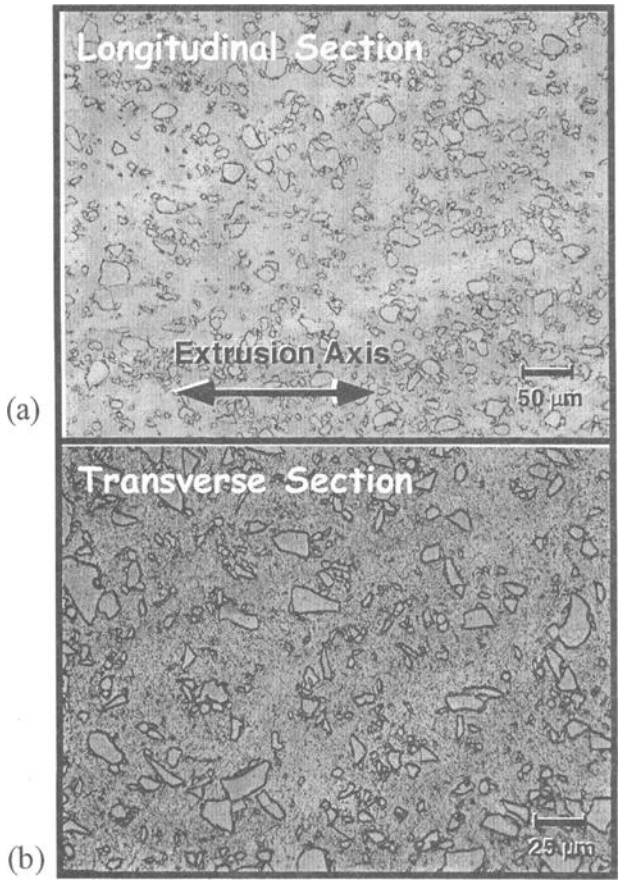

Figure 2 – *Micrographs of hot extruded 1100 aluminum/TiB_2 composite material in (a) longitudinal section and (b) transverse section.*

X-Ray Computed Microtomography (XCMT)

X-ray computed microtomography is a non-destructive 3D characterization technique used to examine second phase and defect distributions with a micron level resolution. Previous tomography work has examined defects from material processing, thermal cycling and deformation [7-12] as well as second phase distributions and defects in Al/SiC composites [13,14]. High resolution XCMT data was obtained at the National Synchrotron Light Source (NSLS). The specialized hardware and software required for XCMT has been developed in previous research [15]. The current instrument is capable of producing 3D voxel data of 1 to 2 μm resolution over a 2 to 3 mm field of view. A voxel is the 3D volumetric equivalent to a 2D image pixel. A specimen is placed on a rotational stage where it is exposed to a high intensity X-ray beam produced by the synchrotron. This x-ray beam can be either a "white" beam or monochromatic with the energies ranging from 6 to 36 keV. The X-rays pass through the sample to be converted to visible light through a scintillator crystal composed of either yttrium aluminum garnet (YAG) or cesium iodide (CsI). A folding mirror and objective lens are used to focus the radiograph on a charge-coupled device (CCD) camera. In order to generate a tomogram, a series of radiographs are needed at specific angular orientations determined by the size and resolution of the tomogram. This is performed under computer control of the rotary stage and camera. The radiographs are then converted to 3D images with specialized reconstruction software that uses a Fast Filtered Fourier Back Transformation algorithm. Essentially, the tomograms are 3D maps of the x-ray attenuation exhibited by the sample.

The images produced from the composite were collected with both 4.5 μm and 3.6 μm resolutions. An example of the tomograms is shown in Figure 3. Individual slices of the tomograms were normalized to allow for the selection of a single intensity value to delineate between the aluminum and the TiB_2 particles using a Fourier transform slice normalization procedure. This procedure reduces ring artifacts in the voxel intensities by removing the low frequency portion of the reconstructed data.

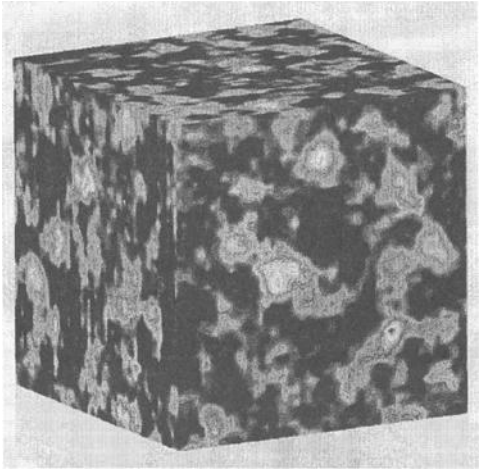

Figure 3 – *Example of tomography image of 1100 aluminum/TiB_2 composite material. The volume is 180 μm on a side. The voxel size is 3.6 μm.*

Three-Dimensional Image-Based Models of the Composite Microstructure

Model Generation

The XCMT data was used to generate realistic finite element models of the composite microstructures. Due to the size of the tomograms, subsections of the XCMT data were transposed onto a regular finite element mesh with each element the size of an individual tomogram voxel. Thus each element was either a 4.5 or 3.6 μm cube depending on the resolution of the tomogram. The material identification for each element was determined by binarizing the XCMT data into two different material types; 1100 aluminum or TiB_2 particles. The threshold was selected to produce approximately 19 volume percent of the TiB_2 particles, consistent with experimental measurements. These image-based models represent the actual spatial and size distributions of the TiB_2 composites measured by XCMT. Two different sizes of solid models were generated, a 20x20x20 element model (8000 elements total) from the 4.5 micron data and a 50x50x50 element model (125000 elements total) from the 3.6 micron data. Thus the 50x50x50 model examines a volume eight times greater than the 20x20x20 model. Both models are shown in Figure 4, where only the TiB_2 elements are distinctly represented to show the particle distributions. Element sets were created to translate the voxel data material types to different material properties in the finite element model.

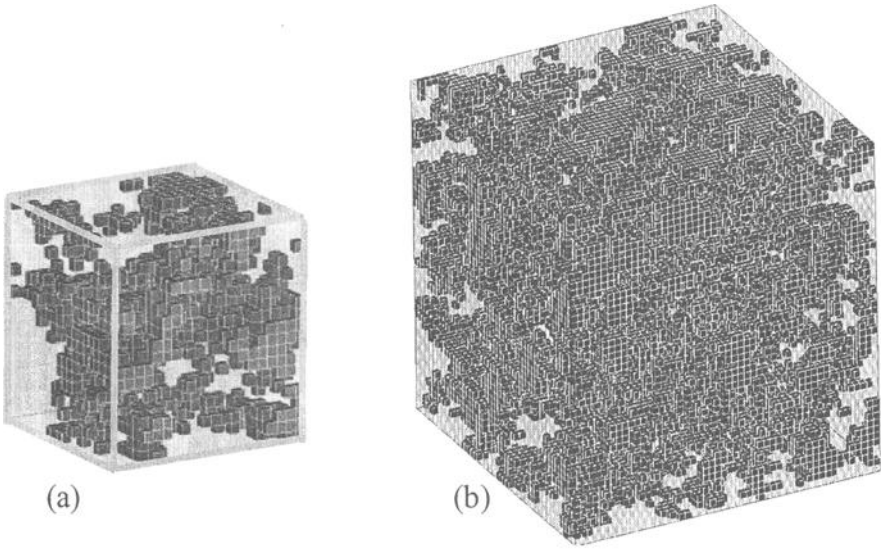

Figure 4 – *Image-based finite element models of aluminum/TiB_2 composite with (a) 20x20x20 element model volume 90.6 μm on a side and (b) 50x50x50 element model volume 180 μm on a side.*

The smaller 20x20x20 element model was used to facilitate postprocessing software development of percolation evaluation algorithms, plasticity cluster statistics, and yield surface estimation. The larger 50x50x50 element model was more representative of a

statistically relevant model size, given the particle size and volume fraction of the composite, and it was used to examine the cluster statistics during the yield surface estimation.

The physical nonlinear response of particulate composites generally involves a combination of matrix plasticity, particle debonding, and/or particle fracture. Particle debonding and particle fracture are void initiating mechanisms. This can produce a complex state of affairs, due to the statistical nature of these mechanisms. Two limiting cases exist: perfectly bonded and fracture resistant particles, which produce no voids, and weakly bonded particles which immediately debond to produce voids upon loading. For the purposes of this study, both limiting cases have been examined. In both cases, elements marked as 1100 aluminum matrix were given material properties of 1100 aluminum. The effects of perfectly bonded particles were modeled by giving the particles TiB_2 properties. The effects of voids were implemented in a simple manner by replacing the particle finite elements with very low stiffness properties, forcing them to behave essentially like voids.

The elastic material properties for the three element types are shown in Table 1. The models were run with the elastic properties for the given element type. In the case of void microstructure, the particle elements were assigned void properties using a significantly reduced elastic modulus value of 0.001 times the modulus of the aluminum. This modulus was used instead of an effective zero modulus to facilitate model convergence and eliminate the potential for overlapping deformation of elements in the model. The reduction of elastic modulus effectively carries through to the shear modulus, using the same value of Poisson ratio. The impact of the value of Poisson ratio is relatively inconsequential at these moduli reductions.

Table 1 – *Elastic material properties.*

Material	Young's Modulus (GPa)	Poisson Ratio
1100 Aluminum	69	0.33
TiB_2	529	0.12
Void	0.069	0.33

In the simulations where non-linear properties are used, an incremental elastic-plastic constitutive model was used for the 1100 aluminum matrix with a nonlinear uniaxial stress-strain curve previously developed [16], as shown in Figure 5. Both the TiB_2 particles and voids remained modeled as elastic materials.

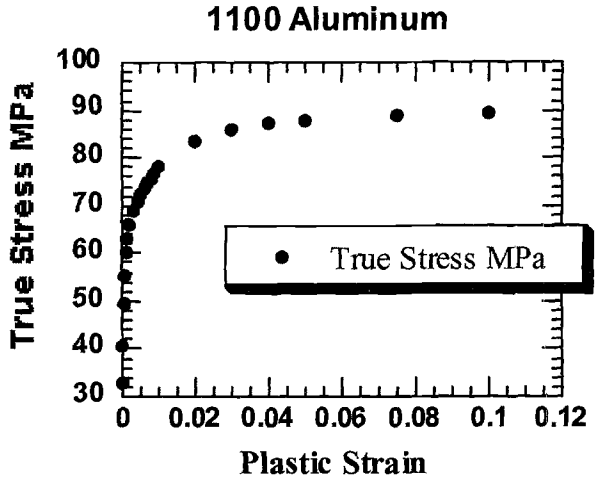

Figure 5 – *Non-linear input stress/strain response for 1100 aluminum.*

Boundary Conditions

The 20x20x20 and 50x50x50 3D finite element models were subjected to three displacement basis loading cases for both elastic analyses. The loading cases represented the three orthogonal tensile deformation basis loads in the x, y and z directions, respectively, as shown in Figure 6. For each of the three basis loading cases, uniform normal displacements were applied to the appropriate opposing sides of the model. These displacements were selected to produce an average strain of 0.002 across the model in the direction of loading. Zero normal displacement boundary conditions were applied to the remaining four sides of the model, as shown in Figure 6. These deformation states are equivalent to applying one-dimensional principle stretches on the axes of the model and they are appropriate for the subsequent linear superposition to construct arbitrary combined deformation states, which in turn are needed to construct the yield surface estimates.

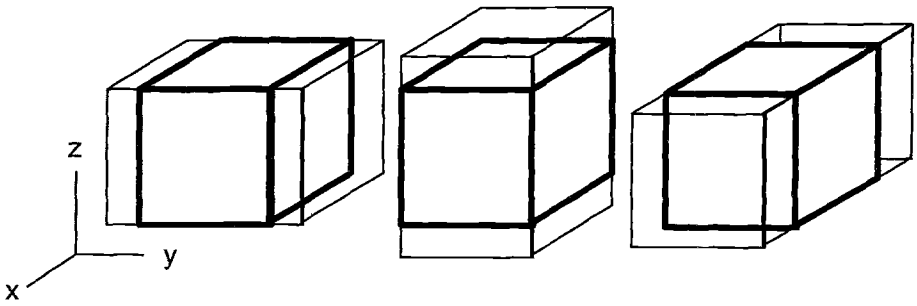

Figure 6 – *Schematic of tensile deformation basis loading cases used in this study.*

Since the percolation-based methodology produces only an estimate of the microstructurally-dependent yield surface, nonlinear finite element analyses of selected deformation states were also performed to compare to the percolation-based estimates. These nonlinear analyses are also used to evaluate how calibration factors could reconcile the linear estimations with the predicted nonlinear responses and to determine the time and resource savings using the linear estimates. Three nonlinear analyses were performed using the basis loading cases for each model to directly determine yield by load-displacement response.

Finite Element Results

All finite element analyses were performed using ABAQUS 5.8-1 on a Sun HPC GlobalWorks computer. The elastic basis loading case run times were on the order of 4.2 minutes for the 20x20x20 element models and 4.2 hours for the 50x50x50 element models using ABAQUS/Standard. These solutions are used in the subsequent analysis as the input for the database for percolation. Nonlinear elastic-plastic run times were on the order of 9.7 hours for the 20x20x20 element models, using ABAQUS/Standard, and 15.0 hours for the 50x50x50 element models, using ABAQUS/Explicit.

Typical finite element results are shown in Figure 7. This figure shows the von Mises stresses for the non-linear 50x50x50 cases tested in the same basis loading direction. It shows that the model with the TiB_2 particles exhibits higher average matrix stresses, while the model with the voids exhibits greater matrix stress non-uniformity (stress localization).

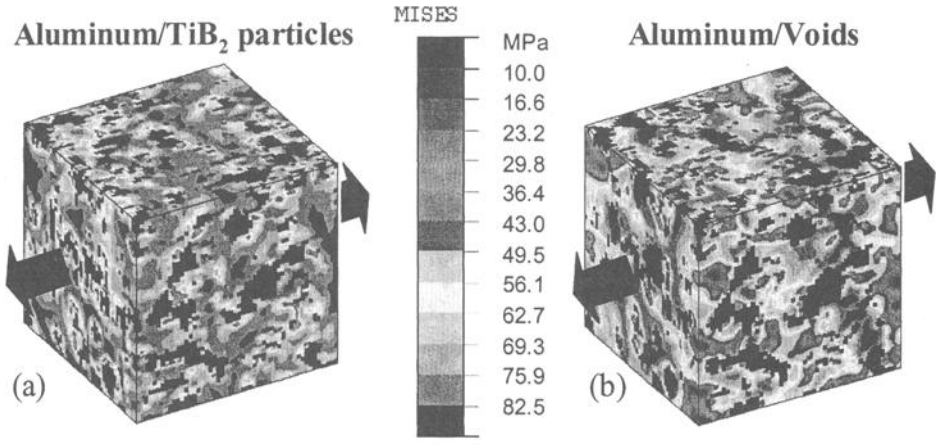

Figure 7 – *Von Mises stresses generated by elastic analyses using one-dimensional tensile basis load deformation for (a) aluminum/TiB2 composite model and (b) aluminum/void model.*

Yield Surface Estimation Using Percolation Analysis

The "classical" definition of percolation of one phase in a two-phase medium is a change in cluster length from finite to infinite length scales. The relevant "phases" for this investigation are elastic material and plastic material cells. The elastic phase elements have a von Mises equivalent stress less than the yield stress value. The plastic phase elements have von Mises equivalent stresses greater than or equal to the yield stress value. The von Mises stresses are calculated for each element from the basis loading cases and superposition defined from a given loading direction. In the case of voided material, the void elements are defined as part of the plastic phase since they offer no appreciable resistance to deformation.

In 2D models, plastic percolation across the model is associated with the "division" of the remaining elastic domain into two (or more) separate and smaller regions. The plastic phase can span the finite domain in the x direction, y direction or both x and y directions, and is associated with macroscopic plastic flow normal to these directions, as illustrated in Figure 1.

In 3D domains, such as are considered here, classical percolation is the "spanning" of the plastic phase across the domain. For phenomena such as dielectric breakdown, where curvilinear continuity of charge conduction paths across the domain is sufficient to make the transition from an insulator to a conductor, the classical definition is sufficient. In the case of plasticity, however, curvilinear spanning of a 3D domain by plasticity is not a sufficient condition for macroscopic plastic flow to occur across the volume. The more stringent criterion of volume "division" must be imposed in the spirit of the practical implications of 2D percolation, i.e., the elastic region must be divided into two or more regions by the plastic region for macroscopic plastic flow to occur. It follows that the relevant test for plastic flow in 3D is the loss of classical elastic material percolation in the direction in which macroscopic plastic flow will take place.

The multiaxial deformation state and the points on the yield surface estimate are constructed in 3D strain space using spherical coordinates. The deformation state is described by angle θ in the x-y deformation plane (as measured from the x-axis), angle ϕ as measured from the z-axis. A load factor λ was used to scale the basis loading cases while the yield surface is located along each radial loading path. Figure 8 illustrates the different yield definitions that can be calculated using the percolation analysis. The first yield definition is initial microscopic yield (λ init), which occurs when the first element reaches the yield criterion. This is similar to the experimental yield definition of the proportional limit stress. The second definition is first plastic percolation (λ pl perc min), where a plastic cluster percolates across the volume. A third percolation point can be defined as the last elastic percolation (λ el perc max), where there is still a continuity of elastic cells along the reference direction. The criterion used for material yield (λ yield), occurs when there is no longer continuity of the elastic cells along the reference direction. This is similar to elastic limit stress, which is the greatest stress a material can see without any permanent deformation. The final yield definition is plastic saturation (λ sat) that occurs when the entire model is plastic.

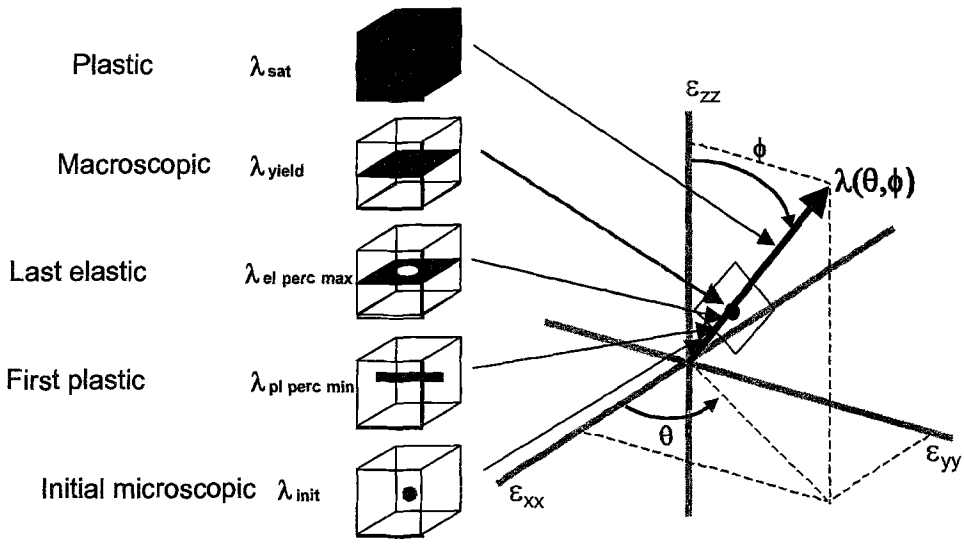

Figure 8 – *Schematic illustration of different yield conditions for a given 3D loading path.*

For the 20x20x20 element model a total of 482 multiaxial strain states, i.e. 32 values of angle θ and 17 values of angle ϕ (minus redundant values at the poles on the z-axis), were used to construct the yield surface. For the 50x50x50 element model a total of 722 multiaxial strain states, i.e. 40 values of angle θ and 20 values of angle ϕ (minus redundant values at the poles), were used to construct the yield surface.

Tension-compression inversion of strain states, represented by mapping θ into $\theta + 180^{\circ}$ and ϕ into $\phi + 180^{\circ}$ to account for symmetry about the origin, in principle reduces the number of unique strain states by a factor of two. These assumptions were used to calculate the complete set of values in order to demonstrate its general implementation. The TiB_2/aluminum microstructure morphology under study may lend itself to microbuckling type phenomena in the void model, so that yield surface points in tension-compression inverted strain states may be different. Likewise, this microstructure could respond to shear loading conditions differently than the calculations generated from the superposition of the three basis loading conditions. These effects could be included in the linear estimates, but it has not been included at this time.

For each value of θ and ϕ, linear superposition is used to calculate the local von Mises stress state in each element of the model. The λ scaling parameter needs to be determined that produces percolation for macroscopic yielding (Figure 8). In general, as the λ parameter is increased, a number of elastic phase elements are changed to plastic phase. This process can be repeated until the definition of percolation is met. Specifically, interval halving was used to solve for the λ scaling parameter, iterating to the λ value at which plastic flow percolation occurs and defines a point on the yield

surface. Initial values for the interval halving were calculated from the linear superposition database and λ values corresponding to the highest and lowest von Mises stress values in the model. The ratio of λ values associated with the first element to yield (i.e. first microyield) and the last eligible element to yield was typically on the order of 10^{-5}. The λ values for first and last yield were, of course, different for each strain loading path, reflecting the different responses of the microstructure to the applied multiaxial deformation state. Within these bounds, the onset of classical plastic percolation served as a refined lower bound threshold for yield, and the point at which to start testing for the yield as the absence of classical elastic percolation perpendicular to the direction of plastic flow.

Interval halving solutions for λ at each set of θ and ϕ was typically performed in 20 iterations per point on the yield surface. This produced a relative accuracy on the order of 10^{-6} times the range defined by typical values of highest and lowest von Mises stress values.

Percolation could occur across one or more of the three directions (i.e. x, y or z) defined by the model. Percolation will generally occur in more than one direction, but it need not occur simultaneously in all directions. Microstructural anisotropy, not a major feature in the TiB_2 aluminum material considered here, will strongly favor asynchronous plastic percolation. For the 20x20x20 element models, the analysis was performed using MATLAB Version 5.3 (1998) and executed on a Pentium 350 MHz personal computer. Each point on the yield surface required approximately 60 seconds of calculation time, and a total time of 8.0 hours to generate the set of 482 points defining the yield surface. For the 50x50x50 element model, the analysis was developed using Fortran 90 and executed on a Cray T90. Each point required approximately 35 seconds and the 722-point yield surface required 7.0 hours to construct. Both programs assessed percolation and constructed the yield surface estimates in an equivalent manner. In comparison, assuming the time taken in the non-linear basis loading cases, it would take 194 days and 451 days to calculate the equivalent yield surfaces for the 20x20x20 and 50x50x50 models, respectively.

Representative yield surfaces for the smaller and larger models with void properties are shown in Figures 9a and 9b, respectively. Both surfaces show anticipated general effects of hydrostatic stress in the triaxial tensile and compressive octants. The data could be used to establish parameters for an analytical model of the yield surface, or to generate a database for a multifaceted yield surface implemented with user subroutines. They also highlight regions of interest, where non-linear analyses may be run for a more detailed examination. Comparison of the two figures shows that the 50x50x50 model is more spherical than the 20x20x20 model and thus the effect of the voids are more homogenized over the volume of material.

The linear estimated yield points on the three basis loading axes fall between the proportional limit and the 0.2% yield definitions of the equivalent nonlinear simulations. Initial results show that the ratios of linear estimated yield strains to the nonlinear predicted yield points (based on a 0.2% yield definition) are 0.318, 0.319 and 0.422 for the x, y and z basis loading deformations. The values of the ratios are consistent with the engineering definition of the nonlinear predicted yield. The nonlinear runs can be used for the basis for practical calibration factors for the linear estimates. The development of

experimental techniques for calibration would also be appropriate, perhaps looking at XCMT data before and after deformation.

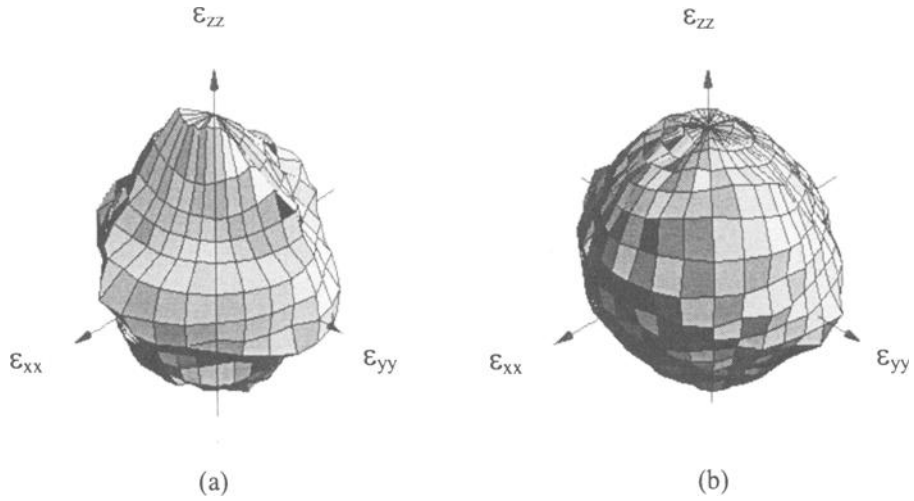

Figure 9 – *Three-dimensional yield surface estimate in strain space for (a) 20x20x20 model and (b) 50x50x50 model.*

Cluster Statistics Analysis

Reinforcement microstructure is known to affect the mechanical behavior of discontinuous composite materials. In the past, this issue was addressed with average values of microstructural variables such as global versus local volume fraction or mean nearest-neighbor distance. Yet these metrics cannot capture the true complexity of the micro-yield percolation process. From the occurrence of first cell yielding to the final global percolation of yield (mesoscale yield), microplastic clusters nucleate, grow and coalesce.

Developing and tracking metrics for these microplastic clusters allows a direct measure of the architecture's interplay between local and global length scales. Initially, we have focused on two easily accessed metrics of the microplastic clusters: the number of clusters and the maximum cluster size. These are measured in an attempt to assess the efficiency of the architecture (i.e., how much of the microstructure is participating in the mesoscale yield process) and the size of a dominant microstructural feature, which might define some "natural" length scale. We have tracked the development of these two parameters as a function of λ loading and load direction.

Figure 10a shows that, for the model with TiB_2 properties, the number of clusters initially increases extremely fast and then decreases with scaling, indicating the net coalescence of clusters. At the same time, the maximum cluster size does not initially change with scaling during the growth phase, indicating relatively uniform growth of smaller clusters. However, at some point, which varies with loading case, a single dominant cluster is formed and it grows until percolation is achieved. This scenario changes somewhat when we consider the void model, shown in Figure 10b. Initially, the number of clusters is large and continuously decreases with loading. This truncated nucleation phase most likely occurs due to the lack of load shedding to the reinforcement and the stress concentration factors at the void. As with the composite, a dominant cluster still forms.

The development of the metrics for the TiB_2 particle model is similar for different multiaxial loading directions. The primary difference being the maximum number of microplastic clusters was greater for triaxial than uniaxial loading. The maximum cluster size at percolation was also slightly lower for the triaxial case. Interestingly, in the void model, the maximum cluster size at percolation was larger for the triaxial case. The maximum and final number of microplastic clusters were similar in each loading case for the void model. However, if the microstructure were more anisotropic (e.g., aligned short fiber reinforcements or pores), the differences would likely be more pronounced.

Finally, it should be pointed out that these microplastic cluster metrics could be used for architecture optimization. However, without more detailed simulations, it is difficult to predict precisely which arrangements are beneficial. One supposes that increased cluster nucleation coupled with a delay of cluster coalescence (and percolation) would maximize the energy absorption.

Summary

A combination of micrometer resolution tomography, imaged based finite element models and percolation analysis has been used to demonstrate how 3D multiaxial yield surfaces can be estimated from microstructure morphology. Linear superposition of three elastic basis deformation loading cases was used to construct arbitrary strain states, from which plastic flow percolation was identified and associated with the onset of yield. This methodology was demonstrated using a TiB_2 particle reinforced 1100 aluminum composite with the limiting cases of perfectly bonded and perfectly debonded particles. Two orders of magnitude reductions in the time to construct the yield surface are seen using selected simulations and percolation based estimation versus direct simulation of the microstructure.

The broader implications of this effort are to construct techniques that evaluate complex microstructural performance and identify classes of microstructural features and deformation patterns that merit further detailed study. This combination of screening and focus activities can relate this information to practical engineering properties needed for component performance simulation and process development.

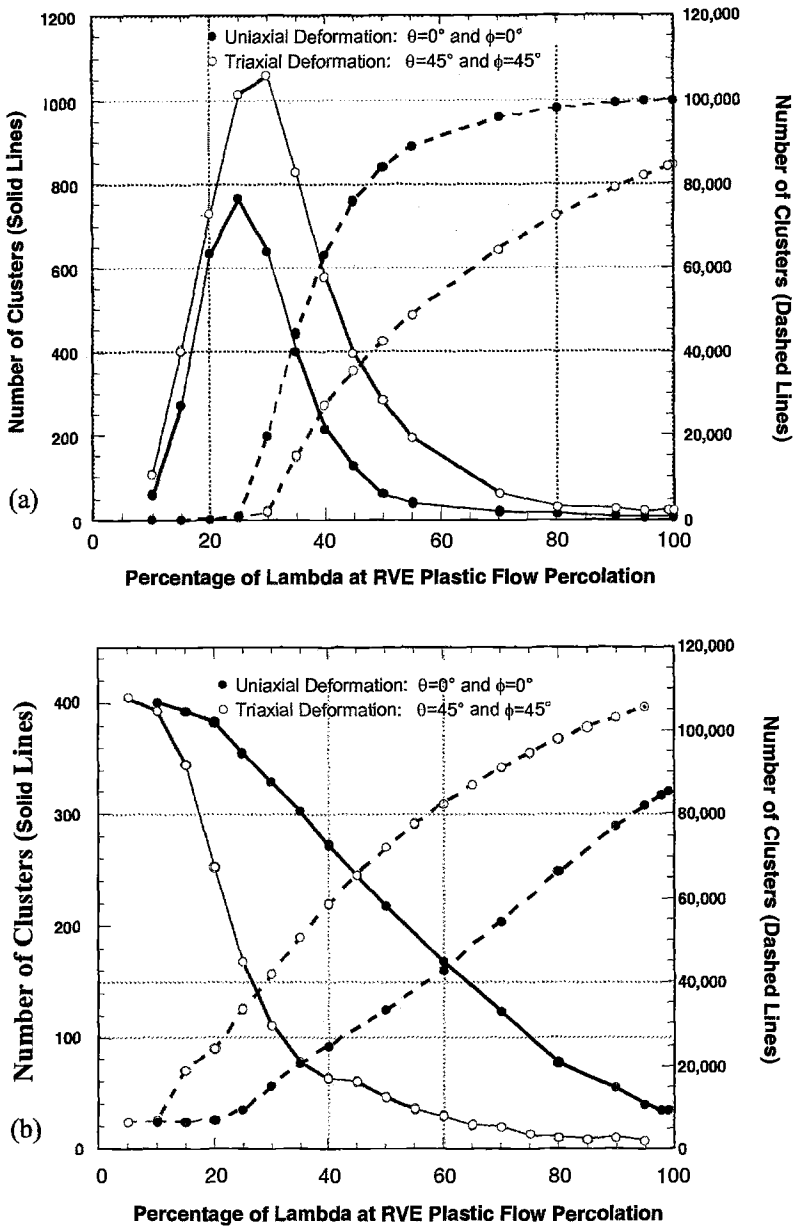

Figure 10 – *Cluster evolution graphs for (a) aluminum/TiB2 composite model and (b) aluminum/void model.*

References

[1] Jiang, M., Ostoja-Starzewski, M. and Jasiuk, I., "Scale-Dependent Bounds on Effective Elastoplastic Response of Random Composites," *Journal of the Mechanics and Physics of Solids*, Vol. 49, No. 3, 2001, pp. 655-673.

[2] Jiang, M., Jasiuk, I. and Ostoja-Starzewski, M., "Apparent Elastic and Elastoplastic Behavior of Periodic Composites," *International Journal of Solids and Structures*, Vol. 39, No. 1, 2002, pp. 199-212.

[3] Werwer, M., Cornec, A. and Schwalbe, K.-H., "Local Strain Fields and Global Plastic Response of Continuous Fiber Reinforced Metal-Matrix Composites under Transverse Loading," *Computational Materials Science*, Vol. 12, No. 2, 1998, pp. 124-136.

[4] Wienecke, H. A., Brockenbrough, J. R. and Romanko, A. D., "A Three-Dimensional Unit Cell Model with Application toward Particulate Composites," *Journal of Applied Mechanics – Transactions of the ASME*, Vol.62, No. 1, 1995, pp. 136-140.

[5] Li, C. and Ellyin, F., "A Micro-Macro Correlation Analysis for Metal Matrix Composites Undergoing Multiaxial Damage," *International Journal of Solids and Structures*, Vol. 35, No. 7-8, 1998, pp. 637-649.

[6] Brockenbrough, J. R., Hunt, W. H., Jr. and Richmond, O., "A Reinforced Material Model using Actual Microstructural Geometry," *Scripta Metallurgica et Materialia*, Vol. 27, No. 4, 1992, pp. 385-390.

[7] Baaklini, G. Y., Ramakrishna, T. B., Eckel, A. J., Engler, P., Castelli, M. G. and Rauser, R. W., "X-ray Microtomography of Ceramic and Metal Matrix Composites," *Materials Evaluation*, Vol. 53, No. 9, 1995, pp. 1040-1044.

[8] Everett, R. K., Simmonds, K. E. and Geltmacher, A. B., "Spatial Distribution of Voids in HY-100 Steel by X-ray Tomography," *Scripta Materialia*, Vol. 44, No. 1, 2001, pp. 165-169.

[9] Guvenilir, A., Breunig, T. M., Kinney, J. H. and Stock, S. R., "Direct Observation of Crack Opening as a Function of Applied Load in the Interior of a Notched Tensile Sample of Al-Li 2090," *Acta Materialia*, Vol. 45, No. 5, 1997, pp. 1977-1987.

[10] Hirano, T., Usami, K., Tanaka, Y. and Masuda, C., "*In Situ* X-ray CT under Tensile Loading using Synchrotron Radiation," *Journal of Materials Research*, Vol. 10, No. 2, 1995, pp. 381-386.

[11] Liu, X. and Bathias, C., "Defects in Squeeze-Cast Al_2O_3/Al Alloy Composites and Their Effects on Mechanical Properties," *Composites Science and Technology*, Vol. 46, No. 3, 1993, pp. 245-252.

[12] London, B., Yancey, R. N. and Smith, J. A., "High-Resolution X-ray Computed Tomography of Composite Materials," *Materials Evaluation*, Vol. 48, No. 5, 1990, pp. 604-608.

[13] Breunig, T. M., Stock, S. R., Guvenilir, A., Elliott, J. C., Anderson, P. and Davis, G. R., "Damage in Aligned-Fibre SiC/Al Quantified using a Laboratory X-ray Tomographic Microscope," *Composites*, Vol. 24, No. 3, 1993, pp. 209-213.

[14] Buffiere, J.-Y., Maire, E., Cloetens, P., Lormand, G. and Fougeres, R., "Characterization of Internal Damage in a MMC_p using X-ray Synchrotron Phase Contrast Microtomography," *Acta Materialia*, Vol. 47, No. 5, 1999, pp. 1613-1625.

[15] Dowd, B. A., Campbell, G. H., Marr, R. B.; Nagarkar, V. V., Tipnis, S. V., Axe, L., and Siddons, D. P., "Developments in Synchrotron X-ray Computed Microtomography at the National Synchrotron Light Source", *Proceedings of the SPIE Volume 3772 – Developments in X-ray Tomography II*, U. Bonse, Ed., The International Society for Optical Engineering, Bellingham, WA, 1999, pp. 224-236.

[16] Everett, R. K., "Mesoscale Effects on Strengthening Mechanisms in Particulate / Aluminum Metal Matrix Composites," Ph. D. Dissertation, University of Maryland, 1996, pp. 84-104.

Muhammad A. Qidwai,[1] Virginia G. DeGiorgi,[2] and Rick K. Everett[2]

Image-Based Characterization and Finite Element Analysis of Porous SMA Behavior

Reference: Qidwai, M. A., DeGiorgi, V. G., and Everett, R. K., "**Image-Based Characterization and Finite Element Analysis of Porous SMA Behavior**," *Predictive Material Modeling: Combining Fundamental Physics Understanding, Computational Methods, and Empirically Observed Behavior, ASTM STP 1429*, M. T. Kirk and M. Erickson Natishan, Eds., ASTM International, West Conshohocken, PA, 2003.

Abstract: Porous shape memory alloys (SMAs) are a relatively new group of materials that are of interest because of their potential use in the design of damping and shock mitigation systems. Benefits of the material include reduced weight, high level of energy absorption through phase transformation and possible increased energy absorption through wave scattering due to porosity. Essential to the use of these materials is an understanding of the structural and shock absorbing response of the material. Constitutive models that accurately represent these characteristics are necessary. The emphasis of this research is to develop a computational methodology that will bridge the mesostructural and macrostructural features of porous SMAs. The first step in the process involves the detailed characterization of the relevant mesostructure, i.e., information about pore shape, size, volume fraction and distribution. This representative characterization can be used to produce realistic image-based finite element models. Because the resultant models have large degrees of freedom they cannot be employed to analyze large-scale structural problems. However, simply designed boundary value problems such as the dynamic uniaxial compressive loading of a bar can be used as benchmarks for the verification of phenomenological macro-constitutive models, or models that are derived using averaging methods such as the Mori-Tanaka method or the self-consistent method. In this study, an attempt is made to analyze numerically porous SMA behavior under dynamic conditions based on the representative mesostructural features. Preliminary results are obtained for selected pore volume fractions and distinct trends in material behavior are observed.

Keywords: porous shape memory alloy, smart material, computational modeling, X-ray computed tomography, dynamic constitutive behavior, pseudoelasticity

Introduction

Most of the current shape memory alloy (SMA) applications utilize the shape memory and pseudoelastic effects in the quasi-static regime — (very low strain rates of

[1] Scientist, Geo-Centers, Inc., Washington Operations, P.O. Box 441340, Fort Washington, MD, 20749.
[2] Section Head, Code 6353 and 6352, respectively, Multifunctional Materials Branch, Naval Research Laboratory, 4555 Overlook Avenue, S.W., Washington, DC, 20375.

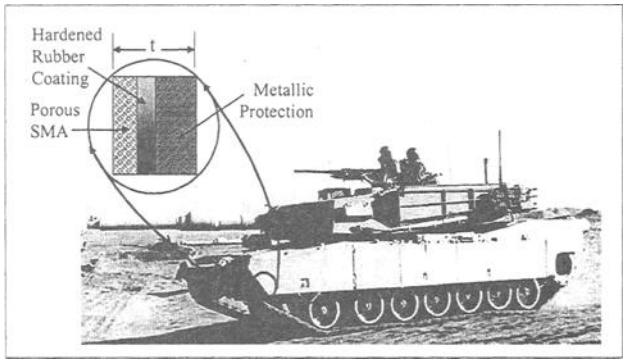

Figure 1 -- *Conceptual hybrid porous SMA composite wheel-chain skirt for protection.*

10^{-5} /s to 10^{-1} /s). However, SMAs may be a valuable material in shock and impact damage mitigation. A recent study by Jimenez-Victory [1] suggests that SMAs possess significant energy absorption and damping characteristics at higher strain-rates (>> 10^{-1} /s). Jimenez-Victory conducted numerical simulations of stress pulse impact on one-dimensional semi-infinite dense SMA bar using a rate-independent constitutive model. The results predicted that 90% of the input impact energy would be absorbed during the first few hundred microseconds through phase transformation.

In addition to the work by Jimenez-Victory there are a few studies on the constitutive modeling of the dynamic SMA behavior. Chen and Lagoudas [2] have provided a closed-form solution of the coupled thermomechanical one-dimensional phase propagation problem in a semi-infinite dense SMA bar by using the theory of Riemann invariants and characteristic curves. Escobar and Clifton [3] have carried out pressure-shear plate impact experiments on Cu-14.44Al-4.19Ni single crystals to study the kinetics of stress-induced phase transformation. Abeyaratne and Knowles [4] have determined the values of phase boundary velocity and driving force according to their one-dimensional constitutive model [5], which is based on a Helmholtz free energy function, a kinetic relation and a nucleation criterion.

As mentioned earlier, dense SMA may have important shock mitigation features. When the advantages of a porous material are added to SMA these features may become of even greater interest for the design of new shock and impact resistance systems. The advantages of pores in an otherwise dense SMA include reduced weight and the possibility for mechanical impedance matching through the ability to customize the porosity level. These advantages are in addition to the energy absorption capability. Potential application areas for porous SMA can be protective armor for both structures and personnel, self-healing structural materials and vibration control. Figure 1 shows one conceptual schematic of protective structural armor in the form of a hybrid porous SMA composite wheel-chain skirt.

Quasi-static constitutive modeling of porous SMA based on averaging techniques taking into account both periodic pore distribution (using unit cell FEM) and random pore distribution (using Mori-Tanaka averaging method) have been presented in [6, 7, 8]. Similarly, the effects of pore distribution on the material behavior at the mesoscale have

been investigated [9]. In all cases the spatial relationships between pores, especially in the case of non-uniform pore distributions, was seen as critical to the overall bulk material response. Accelerated phase transformation was observed based on pore spacing as well as pore orientation. These analyses indicate that the closer the analytical model is to the actual porous material microstructure, the more accurate the computational material performance predictions. This effect is apparent in quasi-static analysis performed. It is considered that it will be even more critical in dynamic analysis.

In this study, the notion of assumed pore distribution is abandoned by representing as accurately as possible the actual mesostructure in the finite element models of the material specimen. The mesostructural information such as pore shape, size, distribution and volume fraction is obtained from X-ray computed micro-tomography (XCMT) images. The dynamic constitutive behavior of porous SMA is obtained by simulating the compressive split-Hopkinson bar test. It is assumed that porous SMA is a two-phase material consisting of pores and dense SMA material. The dense SMA behavior is described by an existing rate-independent thermomechanical constitutive model [10, 11].

The work presented here includes preliminary information on XCMT based material modeling; a brief overview of the compressive split-Hopkinson bar test; numerical modeling details; and finally conclusions on the simulations performed are presented.

Material and Experimental Model

Material Description of Porous SMA Based on X-Ray Computed Micro-Tomography (XCMT)

With the advent of X-ray computed micro-tomography (XCMT), it is possible to obtain three-dimensional digital images of material specimen [12]. The size of the material specimen that can be analyzed by this technique is limited by the size and the intensity of the X-ray beam used for probing. Once the images are obtained, useful graphical as well as statistical information on the shapes, sizes, volume fractions and distributions of the pores can be obtained. Standard image analysis programs are used to determine these characteristics.

There are two conventional methods to convert the information obtained using XCMT techniques into realistic finite element models. In the first method, the digital data from the images is directly converted into finite element models. In the other method, the statistical parameters that are retrieved from the imagery are employed with the help of distribution algorithms to generate near-realistic finite element models. The drawback of the direct conversion method is the computational cost due to the large number of finite elements that may be required to attain true resolution. On the other hand, it may not be practical to retrieve useful statistical variables such as variation of size, shape and distribution to represent the actual material morphology accurately. The choice of the method by a user may depend upon the material at hand, computational cost involved and simplicity of obtaining related statistical information. And in some cases neither method may be appropriate or feasible.

In the case of porous SMA neither conventional approach resulted in FE models that were suitable for analysis. The material characteristics and method used to create the FE models used are described here. Figure 2 shows examples of porous SMA created by three different fabrication techniques that use elemental powders. It exhibits a porous

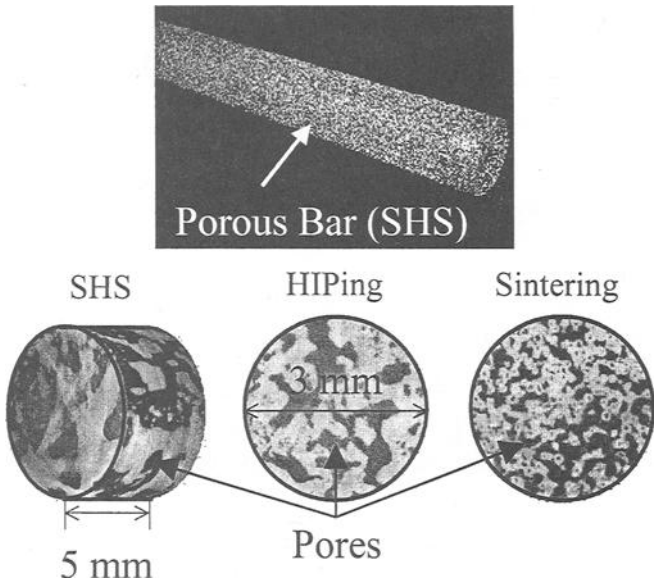

Figure 2 -- *Porous SMA bar made by high-temperature synthesis. X-ray computed micro-tomography images of three different specimens made using high-temperature synthesis (SHS), HIPing and sintering, respectively.*

SMA bar produced by self-propagating high-temperature synthesis (SHS) and XCMT images of specimens made by SHS, hot isostatic pressing (HIPing) and conventional sintering. Detailed description and relevant literature review of these methods can be found in [7] and [13]. It is found out from the analysis of the images that the average smallest pores, approximately 200 μm characteristic in-plane length, are produced in conventional sintering, whereas the average largest pores, approximately 2000 μm characteristic in-plane length, are produced in SHS.

Further study of the micro-tomographs shown in Figure 2 reveals that all specimens possess an intricate network of open pores with dendritic features. This arrangement is not conducive to generating reasonably sized direct-correspondence finite element meshes and also does not allow for obtaining "unique" statistical information on the three-dimensional pore shape, size and distribution. In fact, the only definite information easily available is the pore volume fraction, which is in between 50-60% for all the specimens shown in Figure 2. Therefore, the following material characterization strategy for numerical modeling has been adopted in this study.

Porous SMA specimen made by sintering is chosen because of its reasonable pore size. The specimens made by SHS and HIPing are ignored because their respective characteristic pore lengths are of the same order of magnitude as a split-Hopkinson bar specimen that may result in structural response rather than constitutive response under dynamic loading. It is assumed that the pore related parameters in the sintering specimen shown in Figure 3 such as shape, size and distribution pattern are independent of pore volume fraction. It is further deduced from image analysis that the average characteristic in-plane length of the pores in sintering specimen is 200 μm with a standard deviation of

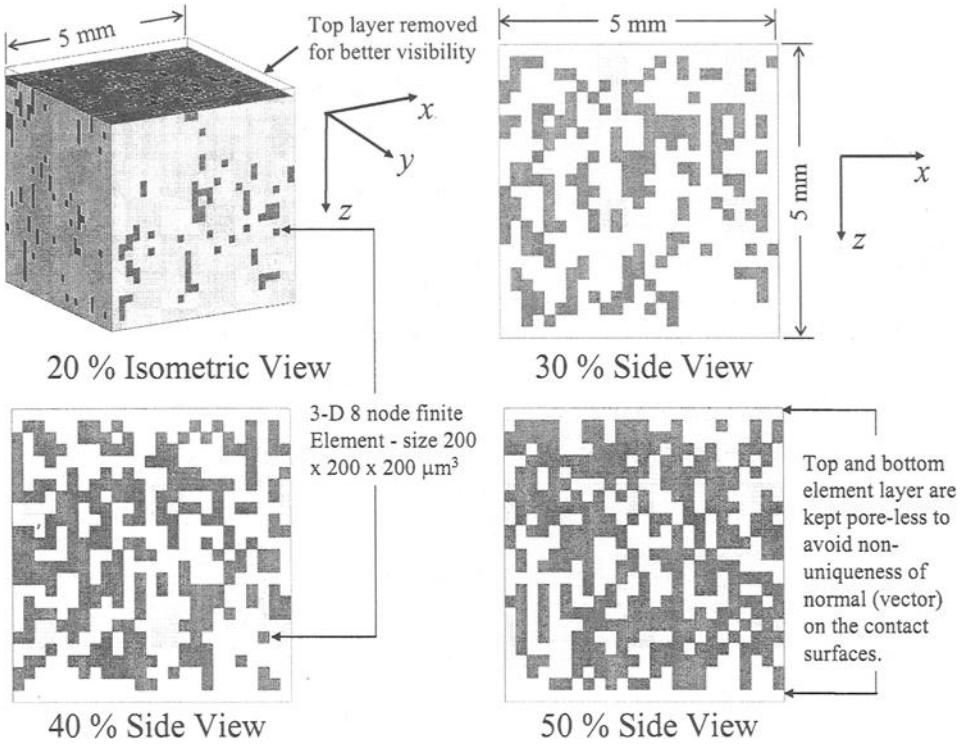

Figure 3 -- *Finite element meshes for specimens containing different pore volume fractions. pores are obtained based on average size and standard deviation and are distributed randomly in the specimen domain.*

200 μm. Normal Gaussian distribution is employed to generate pores based on this information for a given pore volume fraction and constraints of specimen geometry. Afterwards, an algorithm is used to place the pores randomly within the finite element mesh . The algorithm does not allow the pores to intersect but they can sit adjacent to each other. Consequently, large convoluted and randomly shaped pores may possibly form even if the average pore characteristic in-plane length is chosen to be 200 μm. This simple algorithmic arrangement results in effective finite element meshes, which bear a close morphological arrangement to the specimen. One isometric view and three planar views of meshes for pore volume fractions of 20%, 30%, 40% and 50% developed by this methodology are shown in Figure 3, respectively.

Compressive Split-Hopkinson Bar Test

The compressional split-Hopkinson bar test is a commonly used experimental method to determine one-dimensional material behavior at intermediate strain rates (10^2-10^4/s). A schematic of a typical test set-up is shown in Figure 4. A striker bar impacts the incident bar, thereby imparting in it a square pulse with a length that is large with respect to the specimen length, L, to ensure one-dimensional equilibrium conditions in the specimen.

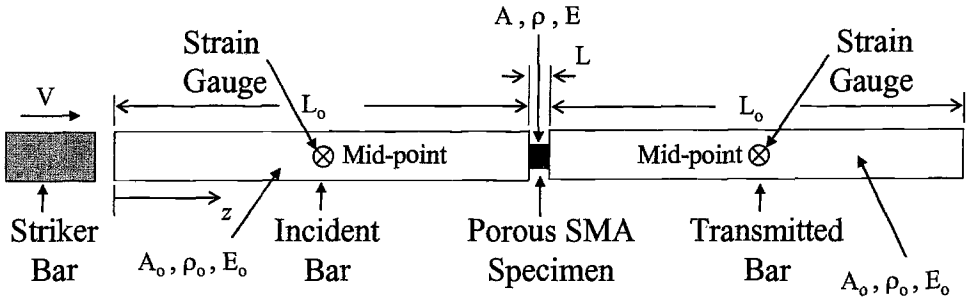

Figure 4 -- *Schematic of a compressional split-hopkinson bar test.*

The material of the incident bar is chosen so that an elastic wave travels through it and reaches the specimen, which is sandwiched between the incident and transmitted bar. The amplitude of the pulse is such that inelastic deformation is imparted to the specimen and the pulse proceeds through the transmitted bar. Recordings of the incident pulse, reflected pulse and transmitted pulse are made at strain gauges positioned at mid-points of the bars away from the interface to reduce noise as shown in Figure 4. The following relations are then obtained for average stress, σ, average strain rate, $\dot{\varepsilon}$, and average strain, ε, in the specimen in terms of the reflected and transmitted strain pulses as a function of time [14]

$$\sigma(t) = E_o \frac{A_o}{A} \varepsilon_T(t), \tag{1}$$

$$\dot{\varepsilon}(t) = -\frac{2C_o}{L} \varepsilon_R(t), \tag{2}$$

$$\varepsilon(t) = -\frac{2C_o}{L} \int_0^t \varepsilon_R(t)\, dt, \tag{3}$$

where E_o, A_o and C_o are the Young's modulus, cross-sectional area and elastic wave speed of the incident and transmitted bars, respectively; A and L are the cross-sectional area and length of the specimen; and $\varepsilon_R(t)$ and $\varepsilon_T(t)$ are the strains as a function of time at mid-points of the bars due to reflected and transmitted pulses, respectively.

Numerical Modeling

For the simulations, the incident and transmitted bars are both assumed to be maraging steel of square (12.5 x 12.5 mm^2) cross-section and 1 m in length. The Young's modulus, E_o, and density, ρ_o, of the bars are 210 GPa and 7900 Kg/m^3, respectively. These material properties are sufficient to maintain an elastic response in the incident and transmitted bars for medium strain-rate tests. The striker bar is not modeled--instead, a square axial velocity pulse of amplitude 5 m/s and time span of 100 μs is applied as a boundary condition at the left end of the incident bar. The amplitude of the velocity pulse is chosen to ensure an effective stress in the specimen sufficient for full phase transformation.

The specimen has a square cross-section of 5 x 5 mm^2 and length of 5 mm. Five specimens with pore volume fractions of 0%, 20%, 30%, 40% and 50%, respectively, are analyzed. The pore volume fraction of 0% implies fully dense SMA specimen. It is analyzed for verification and comparison purposes. As mentioned earlier, porous SMA is modeled as a two-phase material composed of pores and dense SMA. Initially, the dense SMA material in all specimens is in the austenitic state at the austenitic finish temperature, $A^{of} = 315$ K. For simplicity, the temperature is assumed constant. Transformation to martensite is stress-induced. A rate-independent constitutive model [10, 11] is used to describe the dense SMA material behavior. Material parameters and their values required by the model are given in Table 1 and are taken from the aforementioned references.

Table 1 – *Material parameters for dense SMA constitutive model*[3].

Material Parameters	Values
E^A	70.0×10^9 Pa
E^M	30.0×10^9 Pa
α^A	$22.0 \times 10^{-6} \frac{1}{K}$
α^M	$10.0 \times 10^{-6} \frac{1}{K}$
$\nu^A = \nu^M$	0.33
$\rho\Delta c$	$0.0 \frac{J}{m^3 K}$
H	0.05
$\frac{\rho b^A}{H} = \frac{\rho b^M}{H}$	140×10^6 Pa
$-\frac{\rho\Delta\eta_o}{H}$	$7.0 \times 10^6 \frac{Pa}{K}$
A^{of}	315.0 K
A^{os}	295.0 K
M^{os}	291.0 K
M^{of}	271.0 K

[3] See [10, 11].

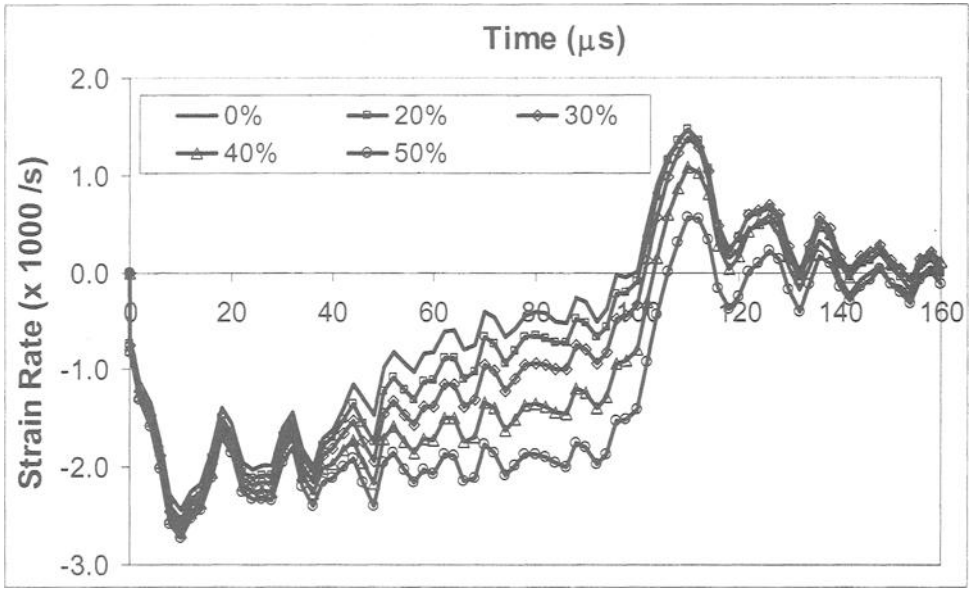

Figure 5 – *Evolution of strain rate in specimens carrying pore volume fractions of 0%, 20%, 30%, 40% and 50%. Note the change in strain rate at 100 μs.*

The commercial finite element software ABAQUS Explicit [15] is employed in simulating the dynamic problem. The SMA constitutive model is numerically implemented using the return mapping algorithm [11] in a user subroutine facility VUMAT available in ABAQUS Explicit. The bars and the specimen are all modeled using reduced integration 8-node brick elements. The automatic time incrementation option is used. The interfaces between the bars and the specimen are modeled using a contact surface option, where both the bars and the specimen are given equal weight in determining the master surface-slave surface relationship. The two layers of elements in each porous SMA specimen at the interface are kept pore-less to avoid non-uniqueness of the normal (vector) on the contact surfaces (see Figure 4). Overall time of each analysis is fixed to be 450 μs, sufficient for the pulse to reach the end of transmitted bar.

Results

The interpretation of results from split-Hopkinson bar test of porous SMA at temperatures greater than austenitic start temperature is more complicated due to recoverability than that of non-transforming metals that undergo dislocation plasticity. That is, at the end of the input pulse, there is an unloading in the porous SMA specimen resulting in reverse phase transformation from martensite to austenite. This can be observed in the evolutionary plot of strain rate for different pore volume fractions in Figure 5 obtained by using Equation (2). The time shown in the figure is calibrated to the start of loading on the specimen. The compressive strain rate in each specimen is in the order of 10^3 /s. The strain rate rises in the beginning as compressive and by the end of 100 μs changes into tensile due to recovery. Even though the applied loading pulse is

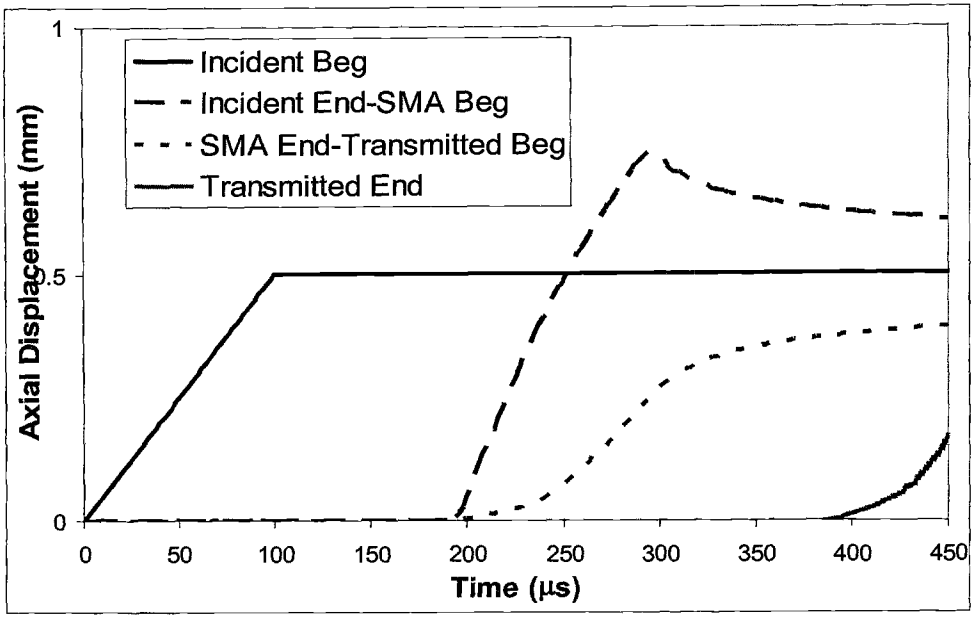

Figure 6 -- *Displacement profile of four locations in the simulation for a given pore volume fraction with respect to time indicating the passage of applied pulse.*

square in shape, there is a rise time in the beginning due to contact conditions. Similarly, at the end of the loading at 100 μs, the unloading rate decreases in amplitude unevenly due to complex multiple interactions at the interface.

A clear picture of the passage of applied pulse with time can be observed in Figure 6, where displacement at four different locations is plotted as function of time for a given pore volume fraction. The locations are the beginning of the incident bar, the incident bar-porous SMA specimen interface, the porous SMA specimen-transmitted bar interface, and the end of transmitted bar.

The evolution of total axial strain at mid-points of the incident bar and transmitted bar, away from the interface is plotted in Figure 7 for all specimens. The recording in the incident bar provide evolutionary information of both incident and reflected pulses. The pulse reaches mid-point of the incident bar in each case at about 97 μs consistent with the elastic wave speed of $\sqrt{E_o/\rho_o} = 5156$ m/s. As expected, it lasts until around 197 μs. By the end of 194 μs, the pulse reaches the interface between the incident bar and the SMA specimen. A reflected pulse of opposite sign and a transmitted pulse of the same sign are generated at that point in time. The reflected pulse reaches the mid-point of the incident bar at 291 μs, and almost at the same time the mid-point of the transmitted bar experiences the originally transmitted pulse.

Both reflected and the transmitted pulses are actually a combination of various interactions at the leading and ending interfaces, and therefore, are different in shape from the incident pulse, which is almost constant in amplitude (see Figure 7). Note that

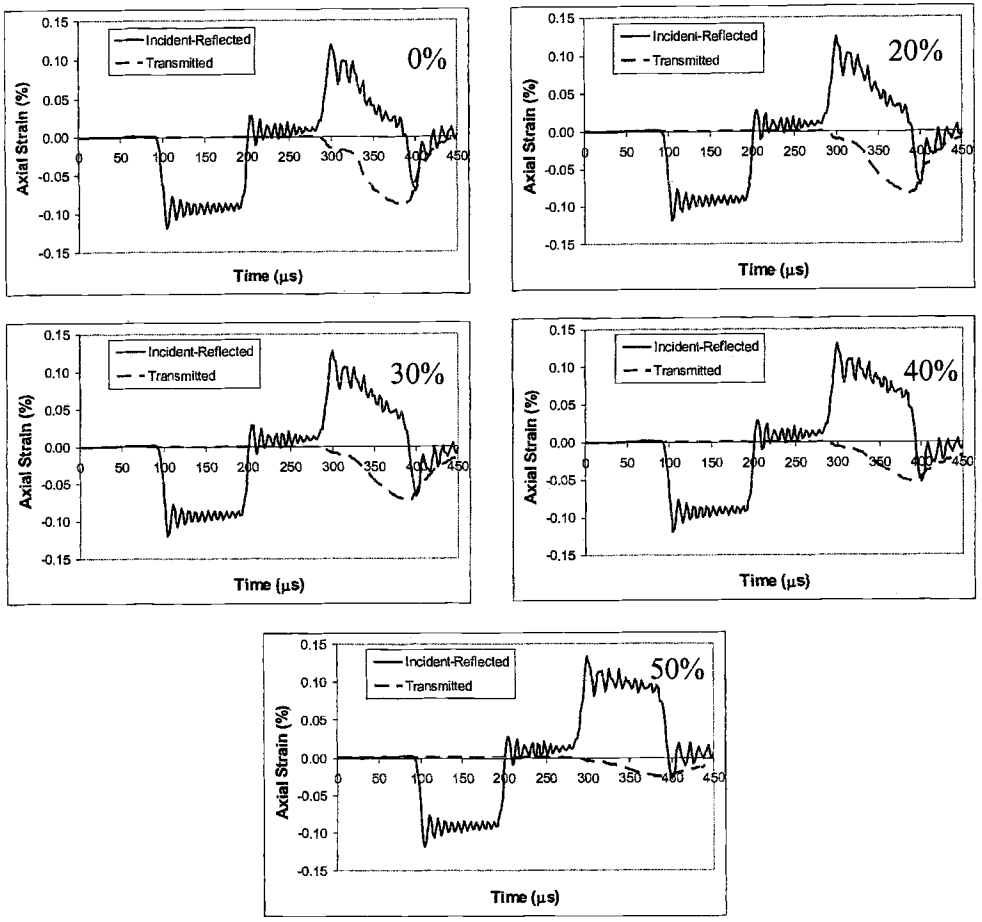

Figure 7 -- *Evolution of axial strain at mid-points in the incident bar and transmitted bar with time for pore volume fractions of 0%, 20%, 30%, 40% and 50%. The point on the incident bar provides information on both the incident and reflected pulse.*

in each case, the reflected pulse changes sign at around 391 μs and the transmitted pulse also reaches a peak from which it gradually decreases. This is attributed to the unloading of the specimen that should result in recovery. In fact, the peak and the area of the reflected pulse should be greater than the calculated value in each case after 391 μs (when the sign changes) as they directly relate to total axial strain experienced by the porous SMA specimen [see Equation (3)]. For the total strain to be zero at the end of the analysis, total area under the reflected strain pulse must be equal to zero. The consequence of this discrepancy will be seen in the stress-strain behavior later. Similarly, the magnitude of the transmitted pulse should be equal to zero at the end of the analysis.

Despite the above-mentioned discrepancy, certain valuable trends can be obtained from the series of results shown in Figure 7. First of all, the amplitude of the reflected pulse and corresponding area increases with increasing pore volume fraction during loading signifying larger total strain for large pore volume fractions. On the other hand,

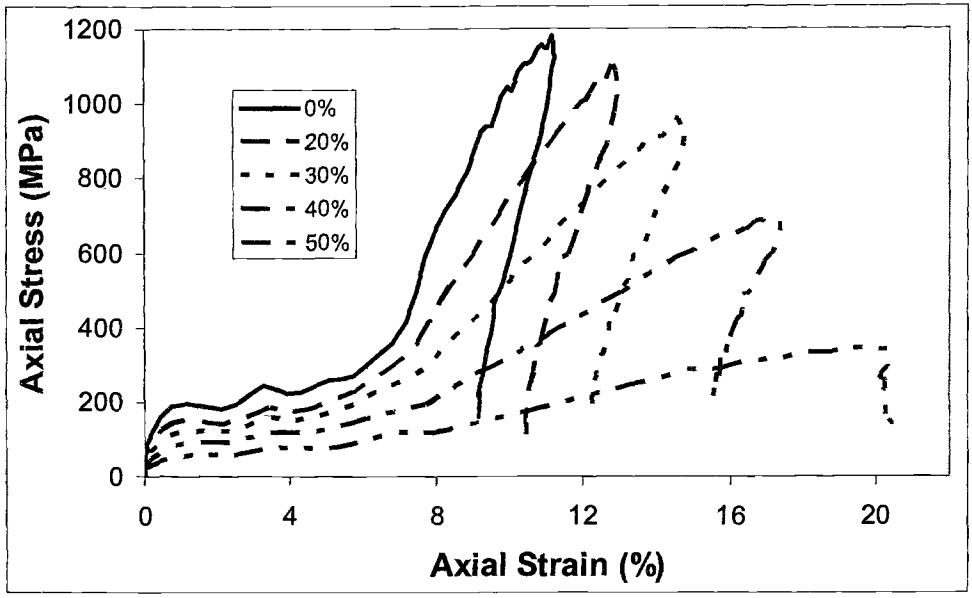

Figure 8 -- *Average stress-strain behavior of porous sma specimen for pore volume fractions of 0%, 20%, 30%, 40% and 50%.*

both the amplitude and the area after the change in sign decrease signifying lesser recovery with increasing pore volume fraction. The transmitted pulse is directly related to average stress in the specimen [see Equation (1)]. The maximum value at the end of loading (391 μs) of this pulse decreases with increasing pore volume fraction, indicating decreasing average stress in the specimen.

Using Equations (1) and (3), the absolute values of average stress and average strain in each specimen is plotted in Figure 8. The curves confirm the observations described above based on results shown in Figure 7. That is, the magnitude of average applied critical stresses needed to initiate phase transformation from austenite to martensite and full transformation, respectively, decrease with increasing pore volume fraction. Also, there is distinct softening in the material with an increased number of pores, and the same applied load results in larger average total strain but lesser average stress. During loading, there are distinct phases of elastic loading of austenite, phase transformation and then elastic loading of martensite. The loading part of the simulations is verified by noting that the critical stresses for beginning and ending the phase transformation in dense SMA (0%) are correct. The discrepancy mentioned in the discussion of Figure 7 is again noted in evaluation of results shown in Figure 8. Elastic unloading does not follow the path of loading and the typical pseudoelastic stress-strain response is not obtained. The problem may be a result of FE techniques used in this analysis; specifically incorrect numerical interface conditions. Currently this is under investigation with plans for subsequent improvements in the algorithms used.

Conclusion

The importance of spatial relationships between pores had been determined in previous work on quasi-static response of porous SMA material. It seemed probable that discrepancies in modeling due to assumptions of uniform or purely random pore orientation would be of greater importance in the evaluation of dynamic material response. Therefore, an approach to modeling in which the actual porous material mesostructure is represented in the finite element models used is adopted. The meso and macromechanical scales are attempted to be bridged by the use of X-ray computed micro-tomography (XCMT) to define characteristics at the mesoscale. Conventional methods for converting information from the data analysis of XCMT images to finite element models resulted in models that were unwieldy and of no practical use. An alternative approach is presented for creating usable finite element models that provide a good estimate of the actual mesostructure. Probabilistic algorithms are used to develop realistic finite element meshes to reduce the approximations usually incorporated in assuming periodic arrangement of pores or adopting micromechanical averaging techniques. These finite element models are then used to investigate the dynamic behavior of porous SMA.

The constitutive behavior of porous SMA is obtained by assuming the material to be composed of two phases, pores and dense SMA material. Numerical simulations of the split-Hopkinson bar test are employed to produce one-dimensional average dynamic porous SMA stress-strain response. The procedure is successfully carried out for pore volume fractions of 0%, 20%, 30%, 40% and 50%. It is observed that required magnitudes of applied stress to initiate and complete phase transformation decrease with increasing pore volume fraction. Also, there is a distinct increase in softening in the material due to increase in pore volume fraction. Typical pseudoelastic stress-strain response is not obtained for any specimen and this discrepancy is currently attributed to incorrect implementation of interface conditions in the simulations. Further investigations are being carried out in this regard. Experimental work is also currently being conducted at other institutions investigating porous SMA response. Once confidence is gained in the numerical simulations and processes, calculated results will be compared with experimental results.

Acknowledgment

The computations preformed by V.G. DeGiorgi and M.A. Qidwai are supported in part by a grant of HPC time from the DoD HPC Center at the Naval Research Laboratory, Washington, DC. The contribution of Dr. A.B. Geltmacher in the rendering of finite element meshes that appear in this work is also greatly appreciated.

References

[1] Jimenez-Victory, J.C., "Dynamic Analysis of Impact Induced Phase Transformation in Shape Memory Alloys Using Numerical Techniques," *Master's Thesis*, Texas A&M University, College Station, TX 77843-3141, 1999.

[2] Chen, Y.-C., and Lagoudas, D.C., "Impact Induced Phase Transformation in Shape Memory Alloys," Journal *for the Mechanics and Physics of Solids*, Vol. 48, No. 2, 2000, pp. 275-300.

[3] Escobar, J.C., and Clifton, R.J., "Pressure-Shear Impact Induced Phase Transformations in Cu-14.44Al-4.19Ni Single Crystals," *Journal of Material Science and Engineering*, Vol. A170, 1993, pp. 125-142.

[4] Abeyaratne, R., and Knowles, J.K., "On the Kinetics of an Austenite $\longrightarrow$ Martensite Phase Transformation Induced by Impact in a Cu-Al-Ni Shape-Memory Alloy," *Archives of Mechanics*, Vol. 45, 1997, pp. 1671-1683.

[5] Abeyaratne, R., and Knowles, J.K., "A Continuum Model of a Thermoelastic Solid Capable of Undergoing Phase Transitions," *Journal for the Mechanics and Physics of Solids*, Vol. 41, 1993, pp. 541-571.

[6] Lagoudas, D.C., Entchev, P.B., Qidwai, M.A., and DeGiorgi, V.G., "Micromechanics of Porous Shape Memory Alloys," *Proceedings of Adaptive Structures and Material Systems, ASME*, J. Redmond, and J. Main, Eds., Vol. AD-60, 2000, pp. 40-50.

[7] Lagoudas, D.C., Entchev, P.B., Vandygriff, E.L., Qidwai, M.A., and DeGiorgi, V.G., "Modeling of Thermomechanical Response of Porous Shape Memory Alloys," *Proceedings of Active Materials: Behavior and Mechanics, SPIE*, C.S. Lynch, Ed., Vol. 3992, 2000, pp. 496-508.

[8] Qidwai, M.A., Entchev, P.B., Lagoudas, D.C., and DeGiorgi, V.G., "Estimate of Porous Shape Memory Alloy Material Behavior," *International Journal of Solids and Structures*, Vol. 38, 2001, pp. 8653-8671.

[9] DeGiorgi, V., and Qidwai, M.A., "Mesoscale Analysis of Porous Shape Memory Alloys", *Proceedings of Adaptive Structures and Material Systems, ASME*, J. Redmond, and J. Main, Eds., Vol. AD-60, 2000, pp. 33-39.

[10] Lagoudas, D.C., Bo, Z., and Qidwai, M.A., "A Unified Thermodynamic Constitutive Model for SMA and Finite Element Analysis of Active Metal Matrix Composite," *Mechanics of Composite Materials and Structures*, Vol. 3, 1996, pp. 153-179.

[11] Qidwai, M.A., and Lagoudas, D.C., "Numerical Implementation of a Shape Memory Alloy Thermomechanical Constitutive Model using Return Mapping Algorithms," *International Journal for Numerical Methods in Engineering*, Vol. 47, 2000, pp. 1123-1168.

[12] Dowd, B.A., Campbell, G.H., Marr, R.B., Nagarkar, V., Tipnis, S.V., Axe, L., and Siddons, D.P., "Developments in Synchrotron X-Ray Computed Microtomography at the National Synchrotron Light Source," *Proceedings of Developments in X-Ray Tomography II*, SPIE, Vol. 3772.

[13] Vandygriff, E.C., Lagoudas, D.C., Thangaraj, K., Chen, Y.-C., "Porous Shape Memory Alloys, Part I: Fabrication and characterization," *Proceedings of ASC 15th Annual Technical Conference,* College Station, TX, 2000.

[14] Meyers, M.A., *Dynamic Behavior of Materials*, John Wiley & Sons, Inc., 1994.

[15] HKS, *ABAQUS/Explicit User's Manual*, Hibbit, Karlsson & Sorensen, Inc., 1998.